

Vol. 50 No. 4  
December 2000

ISSN: 0263-8223

# COMPOSITE STRUCTURES

EDITOR: I.H. MARSHALL

*Special Issue*

Experimental Validation of Theoretical Predictions  
for Composite Structures

*Guest Editors*

R. Jones & T. D. Kim

20010122149

ELSEVIER

<http://www.elsevier.com/locate/compstruct>



# COMPOSITE STRUCTURES

The past few decades have seen outstanding advances in the use of composite materials in structural applications. There can be little doubt that, within engineering circles, composites have revolutionised traditional design concepts and made possible an unparalleled range of new exciting possibilities as viable materials of construction. *Composite Structures*, an International Journal, disseminates knowledge between users, manufacturers, designers and researchers involved in structures or structural components manufactured using composite materials.

The journal publishes papers which contribute to knowledge in the use of composite materials in engineering structures. Papers may be on design, research and development studies, experimental investigations, theoretical analyses and fabrication techniques relevant to the application of composites in load-bearing components for assemblies. These could range from individual components such as plates and shells to complete composite structures.

## Editor

### PROFESSOR I. H. MARSHALL

Monash University, Department of Mechanical Engineering, Clayton Campus, Clayton 3168, Australia,

Fax: +61 (0) 3 9905 1825,

E-mail: [ian.marshall@eng.monash.edu.au](mailto:ian.marshall@eng.monash.edu.au)

### Administrative Address

For submission of papers: Professor I. H. Marshall, 36 Gogosside Road, Largs,

Ayrshire KA30 9LX, UK, Tel./Fax: +44 (0) 1475 687444

E-mail: [ian\\_marshall@talk21.com](mailto:ian_marshall@talk21.com)

## Editorial Board

### S. Adali

University of Natal, Republic of South Africa

### W. M. Banks

University of Strathclyde, Glasgow, UK

### P. Beardmore

Ford Motor Co., Dearborn, Michigan, USA

### W. Becker

University of Siegen, Siegen, Germany

### C. W. Bert

University of Oklahoma, Norman, USA

### H. F. Brinson

University of Houston, Texas, USA

### A. R. Bunsell

Ecole Nationale Supérieure des Mines de Paris, France

### R. Byron Pipes

Rensselaer Polytechnic Institute, Troy, USA

### Lien-Wen Chen

National Cheng Kung University, Tainan, Taiwan

### A. H. Cardon

Free University of Brussels, Pleinlaan, Belgium

### P. Gaudenzi

Università di Roma La Sapienza, Rome, Italy

### R. Jones

Monash University, Clayton, Victoria, Australia

### D. G. Lee

KAIST, Taejeon-shi, Korea

### A. W. Leissa

The Ohio State University, Columbus, USA

### F. L. Matthews

Imperial College, London, UK

### A. Miravete

University of Zaragoza, Spain

### K. Moser

Universität Innsbruck, Austria

### Y. Narita

Hokkaido Institute of Technology,

Sapporo, Japan

### A. N. Palazotto

Air Force Institute of Technology,

Dayton, Ohio, USA

### G. J. Turvey

University of Lancaster, Bailrigg, UK

### J. F. M. Wiggensraad

National Aerospace Laboratory, Emmeloord,

The Netherlands

## Publishing Office

Elsevier Science Ltd, The Boulevard, Langford Lane, Kidlington, Oxford OX5 1GB, UK

[Tel: (+44) (0)1865 843730; Fax: (+44) (0)1865 843969]

## Advertising information

Advertising orders and enquiries can be sent to: **Europe and ROW:** Rachel Leveson-Gower, Elsevier Science Ltd., Advertising Department, The Boulevard, Langford Lane, Kidlington, Oxford OX5 1GB, UK; phone: (+44) (1865) 843565; fax: (+44) (1865) 843976; e-mail: [r.leveson-gower@elsevier.co.uk](mailto:r.leveson-gower@elsevier.co.uk). **USA and Canada:** Elsevier Science Inc., Mr Tino DeCarlo, 655 Avenue of the Americas, New York, NY 10010-5107, USA; phone: (+1) (212) 633 3815; fax: (+1) (212) 633 3820; e-mail: [t.decarlo@elsevier.com](mailto:t.decarlo@elsevier.com). **Japan:** Elsevier Science K.K., Advertising Department, 9-15 Higashi-Azabu 1-chome, Minato-ku, Tokyo 106, Japan; phone: (+81) (3) 5561-5033; fax: (+81) (3) 5561 5047.

## Subscriptions

**Publication information:** *Composite Structures* (ISSN 0263-8223). For 2001, volumes 51-54 are scheduled for publication. Subscription prices are available upon request from the Publisher or from the Regional Sales Office nearest you or from this journal's website (<http://www.elsevier.com/locate/compstruct>). Further information is available on this journal and other Elsevier Science products through Elsevier's website: (<http://www.elsevier.com>). Subscriptions are accepted on a prepaid basis only and are entered on a calendar year basis. Issues are sent by standard mail (surface within Europe, air delivery outside Europe). Priority rates are available upon request. Claims for missing issues should be made within six months of the date of dispatch.

**Orders, claims, and product enquiries:** please contact the Customer Support Department at the Regional Sales Office nearest you:

**New York:** Elsevier Science, PO Box 945, New York, NY 10159-0945, USA; phone: (+1) (212) 633 3730 [toll free number for North American customers: 1-888-4ES-INFO (437-4636)]; fax: (+1) (212) 633 3680; e-mail: [usinfo-f@elsevier.com](mailto:usinfo-f@elsevier.com)

**Amsterdam:** Elsevier Science, PO Box 211, 1000 AE Amsterdam, The Netherlands; phone: (+31) 20 4853757; fax: (+31) 20 4853432; e-mail: [nlinfo-f@elsevier.nl](mailto:nlinfo-f@elsevier.nl)

**Tokyo:** Elsevier Science K.K., 9-15 Higashi-Azabu 1-chome, Minato-ku, Tokyo 106, Japan; phone: (+81) (3) 5561 5033; fax: (+81) (3) 5561 5047; e-mail: [info@elsevier.co.jp](mailto:info@elsevier.co.jp)

**Singapore:** Elsevier Science, No. 1 Temasek Avenue, #17-01 Millenia Tower, Singapore 039192; phone: (+65) 434 3727; fax: (+65) 434 3727; e-mail: [asiainfo@elsevier.com.sg](mailto:asiainfo@elsevier.com.sg)

**Rio de Janeiro:** Elsevier Science: Rua Sete de Setembro 111/16 Andar, 20050-002 Centro, Rio de Janeiro - RJ, Brazil; phone: (+55) (21) 509 5340; fax: (+55) (21) 507 1991; e-mail: [elsevier@campus.com.br](mailto:elsevier@campus.com.br) [Note (Latin America): for orders, claims and help desk information, please contact the Regional Sales Office in New York as listed above]

## Back Issues

Back issues of all previously published volumes are available direct from Elsevier Science Offices (Oxford and New York). Complete volumes and single issues can be purchased for 1995-1999. Earlier issues are available in high quality photo-duplicated copies as complete volumes only.

Periodicals postage paid at Rahway, New Jersey. *Composite Structures* (ISSN 0263-8223) is published (Monthly in January to December as three volumes per year, four issues per volume) by Elsevier Science Ltd., The Boulevard, Langford Lane, Kidlington, Oxford OX5 1GB, UK. The annual subscription in the USA is \$3168.

*Composite Structures* is circulated by Mercury International Limited, 365 Blair Road, Avenel, NJ 07001, USA.

**POSTMASTER:** Please send address corrections to: *Composite Structures*, c/o Customer Services, Elsevier Science Inc., 655 Avenue of the Americas, New York, NY 10010, USA.

© 2000 Elsevier Science Ltd. All rights reserved

REPORT DOCUMENTATION PAGE					Form Approved OMB No. 0704-0188	
<p>The public reporting burden for this collection of information is estimated to average 1 hour per response, including the time for reviewing instructions, searching existing data sources, gathering and maintaining the data needed, and completing and reviewing the collection of information. Send comments regarding this burden estimate or any other aspect of this collection of information, including suggestions for reducing the burden, to Department of Defense, Washington Headquarters Services, Directorate for Information Operations and Reports (0704-0188), 1215 Jefferson Davis Highway, Suite 1204, Arlington, VA 22202-4302. Respondents should be aware that notwithstanding any other provision of law, no person shall be subject to any penalty for failing to comply with a collection of information if it does not display a currently valid OMB control number.</p> <p><b>PLEASE DO NOT RETURN YOUR FORM TO THE ABOVE ADDRESS.</b></p>						
1. REPORT DATE (DD-MM-YYYY) 08-01-2001		2. REPORT TYPE Conference Proceedings		3. DATES COVERED (From - To) 18-19 Nov 99		
4. TITLE AND SUBTITLE  Composite Structures Workshop held 18-19 Nov 99, at Monash University, Melbourne, Australia; Special Issue: Experimental Validation of Theoretical Predictions for Composite Structures (Volume 50, No. 4, December 2000)				5a. CONTRACT NUMBER F6256299M9218		
				5b. GRANT NUMBER		
				5c. PROGRAM ELEMENT NUMBER		
				5d. PROJECT NUMBER		
6. AUTHOR(S)  Conference Committee				5e. TASK NUMBER		
				5f. WORK UNIT NUMBER		
7. PERFORMING ORGANIZATION NAME(S) AND ADDRESS(ES) Monash University Department of Mechanical Engineering Clayton 3168, VIC Australia				8. PERFORMING ORGANIZATION REPORT NUMBER  N/A		
9. SPONSORING/MONITORING AGENCY NAME(S) AND ADDRESS(ES)  AOARD UNIT 45002 APO AP 96337-5002				10. SPONSOR/MONITOR'S ACRONYM(S)  AOARD		
				11. SPONSOR/MONITOR'S REPORT NUMBER(S) CSP-99-08		
12. DISTRIBUTION/AVAILABILITY STATEMENT  Approved for public release; distribution is unlimited.						
13. SUPPLEMENTARY NOTES						
14. ABSTRACT Conference Proceedings to Include the Following: "Experience With the Finite Element Modelling of a Full-Scale Test of a Composite Aircraft Control Surface" "Material Characterization of Laminated Composite Plates Via Static Testing" "Evaluating the Soundness of Bonding Using Shearography" "Combined Numerical-Experimental Model for the Identification of Mechanical Properties of Laminated Structures" "Control of Beam Vibrations by Means of Piezoelectric Devices: Theory and Experiments" "Impact Energy Absorption Characteristics of Composite Structures" "Experimental and Computer Natural Frequencies of Square Pultruded GRP Plates: Effects of Anisotropy, Hole Size Ratio, and Edge Support Conditions" "Optical Fibre Sensors for Health Monitoring of Bonded Repair Systems" "On the Analysis of Composite Structures With Material and Geometric Non-Linearities" "Smart Structure Application in Bonded Repairs"						
15. SUBJECT TERMS  Aircraft Structures, Composite Structures						
16. SECURITY CLASSIFICATION OF:			17. LIMITATION OF ABSTRACT	NUMBER OF PAGES 126	19a. NAME OF RESPONSIBLE PERSON Thomas D. Kim	
a. REPORT	b. ABSTRACT	c. THIS PAGE			19b. TELEPHONE NUMBER (Include area code) +81-3-5410-4409	
U	U	U	UU			

# COMPOSITE STRUCTURES

VOL. 50 2000

*Special Issue*

Experimental Validation of Theoretical Predictions  
for Composite Structures

*Guest Editors*

R. Jones & T. D. Kim

*EDITOR*

I. H. MARSHALL

Journal homepage: <http://www.elsevier.com/locate/compstruct>



ELSEVIER

DTIC QUALITY INSPECTED 4  
20010122 149



This journal and the individual contributions contained in it are protected under copyright by Elsevier Science Ltd, and the following terms and conditions apply to their use:

### **Photocopying**

Single photocopies of single articles may be made for personal use as allowed by national copyright laws. Permission of the publisher and payment of a fee is required for all other photocopying, including multiple or systematic copying, copying for advertising or promotional purposes, resale, and all forms of document delivery. Special rates are available for educational institutions that wish to make photocopies for non-profit educational classroom use.

Permissions may be sought directly from Elsevier Science Global Rights Department, PO Box 800, Oxford OX5 1DX, UK; phone (+44) 1865 843830, fax: (+44) 1865 853333, e-mail: [permissions@elsevier.co.uk](mailto:permissions@elsevier.co.uk). You may also contact Global Rights directly through Elsevier's home page (<http://www.elsevier.nl>), by selecting 'Obtaining Permissions'.

In the USA, users may clear permissions and make payments through the Copyright Clearance Center, Inc., 222 Rosewood Drive, Danvers, MA 01923, USA; phone: (978) 7508400, fax: (978) 7504744, and in the UK through the Copyright Licensing Agency Rapid Clearance Service (CLARCS), 90 Tottenham Court Road, London W1P 0LP, UK; phone: (+44) 20 7631 5555; fax: (+44) 20 7631 5500. Other countries may have a local reprographic rights agency for payments.

### **Derivative Works**

Subscribers may reproduce tables of contents or prepare lists of articles including abstracts for internal circulation within their institutions. Permission of the publisher is required for resale or distribution outside the institution.

Permission of the publisher is required for all other derivative works, including compilations and translations.

### **Electronic Storage**

Permission of the publisher is required to store electronically any material contained in this journal, including any article or part of an article.

Except as outlined above, no part of this publication may be reproduced, stored in a retrieval system or transmitted in any form or by any means, electronic, mechanical, photocopying, recording or otherwise, without prior written permission of the publisher.

Address permissions requests to: Elsevier Science Global Rights Department, as the mail, fax and e-mail addresses noted above.

### **Notice**

No responsibility is assumed by the Publisher for any injury and/or damage to persons or property as a matter of products liability, negligence or otherwise, or from any use or operation of any methods, products, instruction or ideas contained in the material herein. Because of rapid advances in the medical sciences, in particular, independent verification of diagnoses and drug dosages should be made.

Although all advertising material is expected to conform to ethical (medical) standards, inclusion in this publication does not constitute a guarantee or endorsement of the quality or value of such product or of the claims made of it by its manufacturer.

© The paper used in this publication meets the requirements of ANSI/NISO Z39.48-1992 (Permanence of Paper).

Typeset in India by Scientific Publishing Services Ltd, Chennai

Printed by Nuffield Press, Abingdon, Oxon.

## Foreword

The present volume comprised of a collection of invited papers from outstanding international composite specialist during Composite Specialist Workshop held in Melbourne, Australia, on 18 November 1999. This one-day workshop was held after the 10th International Conference on Composite Structures (ICCS-10). The focus of this workshop was on the "Experimental Validation of Theoretical Predictions for Composite Structures." Many papers in this volume reflect new trends and present work carried out on a global scale.

Although composite technology has been around for more than 40 years, it is rapidly transitioning from advanced aerospace materials into civil, sporting, and even medical industry. For the past 10 years, there has been a phenomenal increase in the production of composite structures. At the same time, manufacturing cost has been decreasing as improvements in processing methods have emerged. All these enhancements in the composites industry are largely due to advances in analytical tools for analyzing composite structures before production of a part. However, many analytical predictors have not been matched by equivalent experimental corroboration. There are increasing trends towards theoretical solutions to problems in structural application of composites with an opposite trend in experimental studies. This in effect raises questions on the appropriateness and validity of such analytical predictors along with accuracy that can reasonably be expected when applied to the design or assessment of composite structures. This is especially evident in study of long-term durability of composite structures.

This workshop redressed aforementioned imbalances by focussing on experimental methodology that has been employed to corroborate theoretical studies on

composite structures. I believe this workshop provided a good summary on the present status of experimental methodology applied to composite structures from an international perspective.

The Asian Office of the Aerospace Research and Development (AOARD), a detachment of US Air Force Office of Scientific Research (AFOSR), located in Tokyo, Japan, co-sponsored both ICCS and the Specialist Workshop. Throughout the year, AFOSR/AOARD sponsors many technical conferences in Asia to promote science and technology. We hope that supporting a conference and publishing a special issue such as this will further advance the composite materials and structures technology. It is one of our main tasks of AOARD to bring together material experts, space scientists, and theorists from different fields and to give them the opportunity to discuss and compare their results. We feel that this will contribute to the achievement of a deeper understanding and increase value to those results through multi-disciplinary research in various fields of international co-operation.

A special acknowledgement of gratitude is extended to *Professors Ian H. Marshall and Rhys Jones* at Monash University, Melbourne, who worked tirelessly to organize the ICCS, Specialist Workshop and to publish this work. My many thanks to all those individuals at Melbourne; who made the workshop a success.

Thomas D. Kim

*Asian Office of Aerospace Research and Development  
(AFOSR/AOARD), 7-23-17 Roppongi, Minato-ku  
Tokyo 106, Japan*

*E-mail address: kimt@aoard.af.mil*

## Preface <sup>☆</sup>

This Issue forms the *Proceedings of the International Workshop on Experimental Validation of Theoretical Predictions for Composite Structures*, held at Monash University, Melbourne, Australia on 18 November 1999. The Workshop was sponsored by the Department of Mechanical Engineering of Monash University with the support of US Air Force Office of Scientific Research – AOARD. Composite structures specialists from nine countries, namely Australia, Italy, Korea, The Netherlands, Portugal, Singapore, Taiwan, UK and USA brought a wide geographical perspective to the theme of the Workshop.

Clearly, the topic of experimental validation embraces a broad area of study with manifold interpretations. However, the central thrust focuses on the need for a degree of confidence, by those charged with the design or assessment of composite structures, on increasingly sophisticated analytical predictions. There is no doubt that theoretical and computational tools have been dramatically enhanced in the last decade or so thereby allowing greater flexibility and increasing accuracy of solution. Although the benefits are inescapable, theoretical predictions are to some extent entering uncharted ground, which a generation ago would have been corroborated by experimental evidence. However, it is often extremely difficult to design an experiment

that adequately reflects a complex situation without resorting to full scale testing, which is in many cases impractical. The corollary being a level of uncertainty amongst those at the frontiers of theoretical or computational knowledge.

This is further exacerbated by a growing tendency towards theoretical advances in the general area of composite structures over the last decade or so.

The present International Workshop aims to redress this imbalance in some small way and thereby assist in putting present analytical capabilities into perspective. It is hopeful that the present volume will act as a catalyst for future developments in this area and underline a need for theory and experiment to work in parallel.

We wish to thank the Air Force Office of Scientific Research – AOARD for their contribution to the success of this Workshop:

Finally, a word of gratitude to the contributors and participants, without whom the Workshop would not have been possible.

Ian H Marshall, Thomas D. Kim, Rhys Jones  
*Asian Office of Aerospace Research and Development*  
7-23-17 Roppongi, Minato-ku  
Tokyo 106, Japan  
E-mail address: kimt@aoard.af.mil

<sup>☆</sup> Note. A special word of welcome to Alun Jones, son of Rhys and Sue Jones who was born on the day of the Workshop.

# Experience with the finite element modelling of a full-scale test of a composite aircraft control surface

Rodney S. Thomson <sup>a,1</sup>, Murray L. Scott <sup>b,\*</sup>

<sup>a</sup> Cooperative Research Centre for Advanced Composite Structures Limited, 506 Lorimer Street, Fishermens Bend, Vic. 3207, Australia

<sup>b</sup> Sir Lawrence Wackett Centre for Aerospace Design Technology, Department of Aerospace Engineering, Royal Melbourne Institute of Technology, GPO Box 2476V, Melbourne, Vic. 3001, Australia

## Abstract

A full-scale, co-cured, carbon fibre composite control surface representative of those found on mid-size, jet transport aircraft has been designed and tested. It was designed as a postbuckling blade-stiffened structure to reduce weight and improve operational performance compared with a honeycomb sandwich panel design traditionally used in such structures. The purpose of the tests was to demonstrate the validity of the design methodology by applying static limit and ultimate loads to the structure. The control surface, manufactured from prepreg tape, was successfully loaded to the ultimate design load without evidence of failure. Buckling initiated at approximately 48% of ultimate load with significant out-of-plane displacements observed. The global behaviour predicted by the finite element (FE) model of the test arrangement was in close agreement with the experimental results. Good agreement was also demonstrated with the local behaviour, as evidenced by the strain and buckling results. The inability of the FE analysis to capture complex snap-through mode change behaviour at 89% of ultimate load was identified as a limitation. The success of the testing program demonstrated the suitability of the design methodology for this type of structure. © 2000 Elsevier Science Ltd. All rights reserved.

**Keywords:** Aileron; Finite element analysis; Postbuckling; Full-scale testing; Integral stiffeners

## 1. Introduction

Stiffened panels in semi-monocoque construction have been extensively employed in metallic aerospace structures for many years. Incorporating postbuckling design concepts into such structures has further optimised their structural performance. However, the progressive introduction of advanced carbon fibre composites into aerospace structures presents new challenges in the design and manufacture of these components. Carbon fibre reinforced composites in honeycomb sandwich panels have now been widely used in control surfaces for commercial transport aircraft for well over a decade. Typical design configurations for components, such as ailerons, incorporate carbon fibre/epoxy ribs and spars which are mechanically fastened to honeycomb sandwich skins. Poor impact resistance, water ingress,

skin/core delamination and costly repair of damaged skins are the most common causes of problems raised by operators of aircraft with this type of construction.

In recent years, the imperative to reduce the manufacturing cost of advanced fibre composite components and wherever possible improve their operational performance has led to innovative design concepts being proposed which do not rely on honeycomb sandwich construction techniques [1–5]. The most promising concept for the relatively lightly loaded components found in control surface structures is that characterised by thin, integrally stiffened, composite skins, which buckle below limit load levels in a similar manner to their metallic counterparts.

The design and manufacturing technology associated with composite/honeycomb sandwich panels was considered the baseline for the new composite control surface design presented here. The structure studied represents the aileron of a mid-sized, commercial, jet transport aircraft. In order to demonstrate the weight and cost saving potential of thin buckling skins with integral blade-stiffening, a complete aileron has been designed which incorporates many innovative features.

\* Corresponding author. Tel.: +61-3-9647-3064; fax: +61-3-9647-3050.

E-mail addresses: rodney@duigen.dsto.defence.gov.au (R.S. Thomson), m.scott@rmit.edu.au (M.L. Scott).

<sup>1</sup> Tel.: +61-3-9646-0581; fax: +61-3-9646-8352.

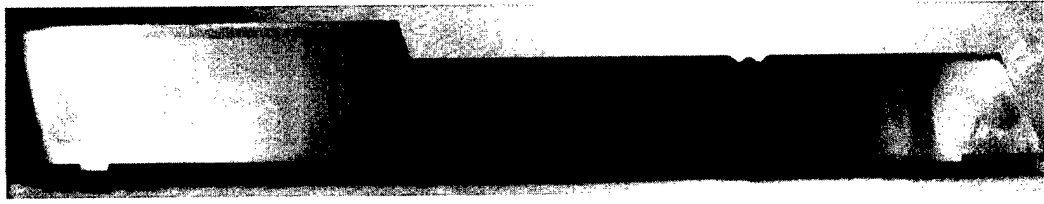


Fig. 1. Control surface configuration.

Central to this task was the selection of a one-piece composite manufacturing process which enabled the blade-stiffened skin, rear spar and ribs to be co-cured.

The primary objectives for the new design were as follows: to reduce the mass of the control surface box structure by 30%; reduce manufacturing costs; to achieve or exceed existing requirements for quality, durability and damage tolerance; and to achieve existing requirements for environmental degradation and stiffness criteria. The design was performed using Catia and structural analysis was performed using MSC.Nastran and MSC.Patran. Full-scale tests were undertaken to validate the design which highlighted the strengths and weaknesses of current finite element (FE) codes.

## 2. New aileron design

### 2.1. Aileron configuration

The overall dimensions of the aileron are  $2.8 \text{ m} \times 0.4 \text{ m}$ , with a local sweep angle of  $16^\circ$ , as shown in Fig. 1. There are four hinges supporting the aileron through its front spar. A 1.7-m long balance tab is located at the trailing edge extending from the inboard end of the structure. The aileron is actuated by a single control rod next to the inboard hinge.

The baseline honeycomb structure has been redesigned, while maintaining the stiffness, by using thin buckling skins incorporating multiple, co-cured blade-stiffeners. Since similar front and rear spars to the baseline control surface were used, bending stiffness was not significantly altered. To match the torsional stiffness of the baseline control surface, a total of nine ribs and 12 stiffeners were incorporated, which were positioned chordwise along the span as shown in Fig. 2. The thin skins consisted of two pairs of  $\pm 45^\circ$  plies to resist the torsional loading, two  $0^\circ$  (spanwise plies) and one  $90^\circ$  (chordwise plies) to transfer the air loading to the surrounding structure, as shown in Fig. 3. Local skin build-ups were incorporated at the front and rear spars and around major hinge ribs.

### 2.2. Design and manufacturing model

Catia was the computer aided design and manufacturing environment chosen for the project due to its

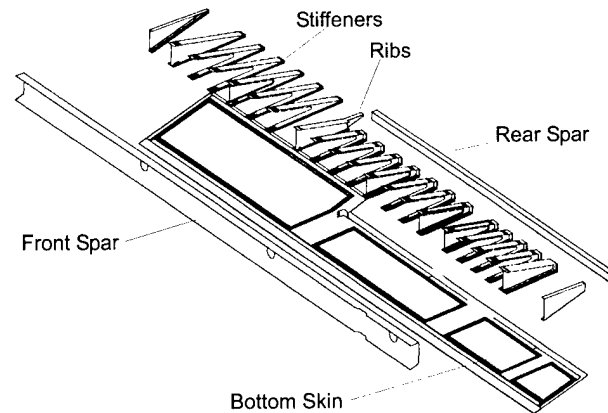


Fig. 2. Exploded view of the new aileron design.

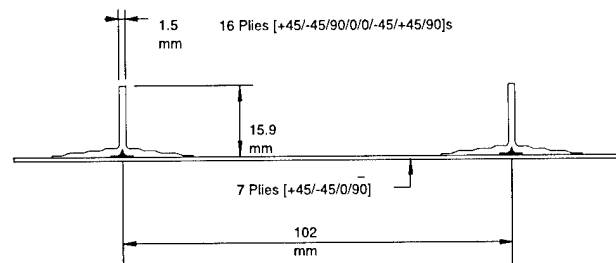


Fig. 3. Typical skin-stiffener interface.

extensive use in the aerospace industry. The Catia design database was used as the sole design authority and was transferred digitally between the design centre and the manufacturing centre. Catia is a powerful software tool that consists of geometric 3D modelling, drafting and analysis capabilities that can be combined with the Catia geometry interface and Catia mathematical subroutines package to access and modify the model database [6]. Data from Catia was translated into the MSC.Patran and MSC.Nastran environment for FE analysis purposes.

### 2.3. Critical load cases

The loads acting on the aileron were divided into three groups: distributed surface pressures resulting from the airloads; secondary pressure loads resulting from the trim tab, mass balance and leading edge; and

induced bending loads. The pressure profiles resulting from airloads applied to the top and bottom skins of the aileron are shown in Fig. 4. They were assumed to be distributed evenly, with 50% on the upper and lower surfaces.

Secondary airloads originated from the mass balance panel, leading edge (D-nose) and trim tab. The mass balance load was generated by the differential pressure between the slots on the top and bottom skin of the wing. This load was resolved as a moment and a force at the front spar. Loads due to the D-nose were resolved to the front spar and were evenly distributed along the span, while moments were applied as couples on the spar web.

It was assumed that the wing induced bending load was reacted mostly by the front spar of the control surface. Since the front spar design had not changed significantly, the same reaction load was assumed for the new design. Such an assumption was considered conservative since the bending stiffness of the postbuckling

design was slightly less than the current honeycomb structure, leading to lower hinge reaction loads.

#### 2.4. Design features

To achieve significant weight savings over the honeycomb sandwich baseline structure, emphasis was placed on a thin-skinned postbuckling design. Buckling was only permitted in the skins of the box structure. The front and rear spars, which carry the bending loads on the aileron, were not permitted to buckle nor cripple at ultimate load. Likewise, ribs were designed to be non-buckling. Some sections of the upper and lower skins however, were reinforced to prevent buckling to allow attachment of a fairing to the lower skin for the tab control rods. Multiple chordwise blade-stiffeners were incorporated to stiffen the thin, buckling skin.

The upper and lower skin, blade-stiffeners, rear spar and internal ribs were co-cured. This eliminated the use of fasteners and pad-ups, which reduces weight and cost. The closure ribs, front spar and rib shear ties were cured separately and mechanically fastened to the box structure. This manufacturing method allowed forward removal of the tooling. The aluminium internal mandrels were machined to the inner mould line profile by numerical controlled machinery. They were designed to apply pressure to the composite laminates for compaction and consolidation by thermal expansion. Steel caul plates which reacted the expansion of the internal aluminium tools were clamped to the outer surface of the box structure and vacuum bagged.

The blade-stiffeners were required to be terminated, or “run-out”, at the front spar which required careful design to prevent stiffener disbonding. Local skin ply build-ups were used to inhibit skin buckling at the stiffener run-outs. All stiffening members were double flanged and blade “softening” or local blade ply “drop-offs” were incorporated to prevent buckling at the skin interface and reduce peel stresses. At the trailing edge and rear spar locations, the upper and lower surface blade-stiffeners were joined together to form a “semi-rib” which avoided stiffener run-outs and improved torsional stiffness.

The ribs were typically constructed using a similar web-skin interface as the stiffener, with two C-sections combined back-to-back to form an I-section. The in-board ribs were connected to the rear spar by wrapping the rib web towards the rear spar web to form a pair of rib flanges. The two closure ribs were mechanically fastened to the structure, as was the front spar. Special attention was focussed on the design of the “kink” rib, which is located outboard of the rear spar termination. A shear-tie between the web of the rib and the web of the rear spar improves stiffness and load transfer. Doublers were added to the flanges of the rib at the kink joint in order to add strength. Additional skin ply

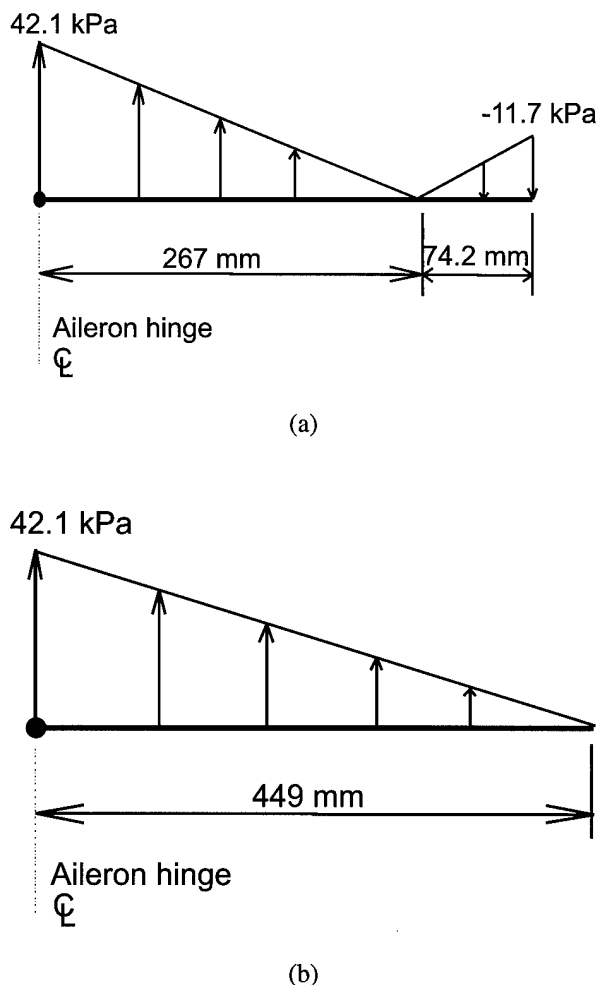


Fig. 4. Chordwise pressure distribution (ultimate airload) in: (a) the tab region; (b) the no-tab region.

build-ups were incorporated to prevent buckling of the skin near the trailing edge of the kink rib.

### 3. Full-scale aileron test

The aileron design was substantiated by means of a full-scale static test, the results of which were used in validation of the analysis and design techniques.

#### 3.1. Loading

For the purpose of the structural tests, an approximation of the airload used for the design was required. The shear loads resulting from the pressure distribution were resolved at each rib by assuming that the airload applied to any given bay was carried equally by the ribs enclosing that bay. The loads carried by the leading edge of the control surface and the tab loads were similarly resolved to the nearest ribs to give the best approximation to the pressure loading.

The chordwise location of the load on each rib was chosen to approximate the spanwise hinge moment distribution caused by the airloads. Hence, in the tab region, the rib loads were applied close to, in some cases forward of, the hinge line because the tab relieved the hinge moment. Conversely, outboard of the tab the loads were higher and acted further aft of the hinge line. It was in this outboard region that most of the airload and hinge moment was developed. After small adjustments to individual rib loads and moment arms, an acceptable approximation to the pressure loading was obtained. The individual rib loads and moment arms corresponding to the ultimate design load are shown in Table 1.

Displacements for the wing bending case were also based on the same aileron design load case and determined by applying induced bending loads at the middle two hinges in the FE model and observing the displacement of these hinges. These displacements were then applied during the test, and were 7.5 and 9.9 mm at Hinges 2 and 3, respectively.

#### 3.2. Structural test arrangement

The test article was mounted in a purpose built test rig as shown in Figs. 5 and 6. The test article was positioned with its chord in the vertical plane to enable observation of the top and bottom skins under load as

extensive buckling was anticipated. The test article was mounted to the test rig at the four hinge points and a link from the control surface to the test rig at the actuator location resisted all hinge moment.

The two middle hinge fittings on the test rig were capable of being displaced normal to the chord line to enable wing bending displacement to be applied to the test article. These two hinge fittings also incorporated a load cell each to measure the normal-to-chord hinge reaction load during the tests. These hinge fittings were calibrated by applying known normal-to-chord loads directly to the hinge pins prior to installing the control surface in the test rig.

Instrumentation consisted of 52 strain channels, mainly back-to-back rosettes on the upper and lower skins with some linear gauges on selected stiffeners, eight load channels (six actuators and two hinges), the calibrated control rod to measure hinge moment and a linear variable differential transformer (LVDT) was positioned at each of five locations (three positioned along the trailing edge of the control surface and two normal to the top skin to measure out-of-plane displacements).

Two shadow moiré grid panels were placed over the bottom skin, one at the inboard end beside the actuator rib and one outboard where the tab region ends; photographs of each panel were taken at each load level. It was anticipated that the outboard area would buckle first and the inboard area would record the highest strains. It was subsequently found that significant buckling over most of the specimen was highly visible even without the aid of a moiré grid.

#### 3.3. Load application

Simulated air loads were applied to the test article through nine form boards, one located at each rib. Application of the loads at the ribs permitted the skin to buckle freely. The alternative loading method, using pressure pads, would have inhibited buckling and also risked damaging the thin skins, as well as complicating the loading system. These form boards were loaded using six electric screw jack actuators fitted with load cells and were controlled through a closed loop control system to a specified maximum load at a specified rate. At three locations, two ribs were loaded using a single actuator via a whiffle tree arrangement, as the spacing of the ribs did not permit an actuator per rib to be used.

Table 1  
Rib loads and moment arms at DUL used in the structural test

Rib	1	2	3	4	5	6	7	8	9
Load (N)	934	1681	1802	2140	3149	4377	4897	3265	1032
Moment arm (mm) <sup>a</sup>	50.8	10.7	−50.3	−26.4	−25.4	78.7	129.5	170.2	307.3

<sup>a</sup> A negative moment arm indicates the load is applied forward of the hinge line.

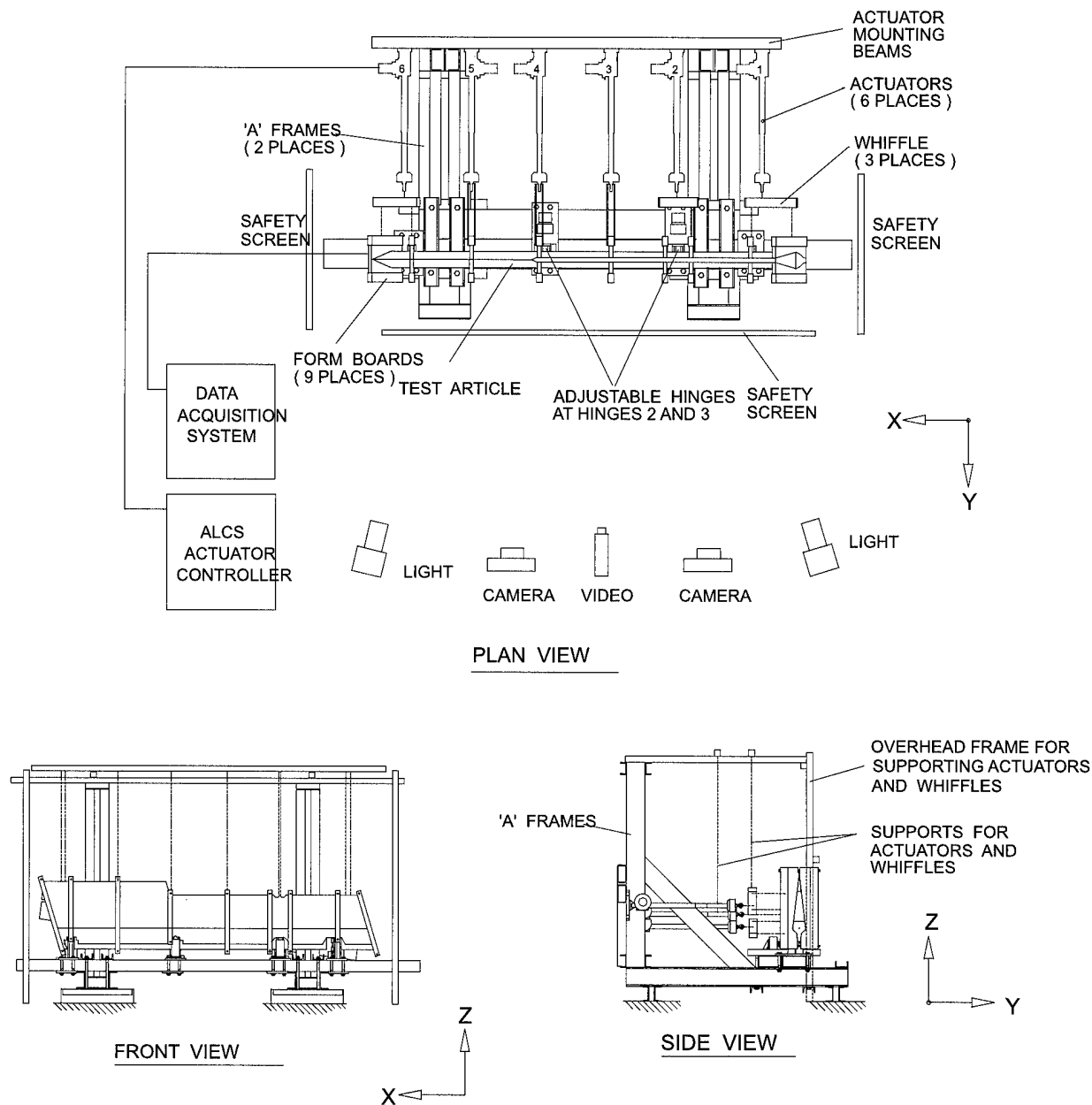


Fig. 5. Test arrangement.

No drag loads (parallel to the control surface chord) were applied in the tests because such loads would have contributed little to the buckling of the structure and likewise to the strains measured. The internal loading in the structure is primarily caused by torsion and normal-to-chord bending. It was determined that this approach would enable adequate comparisons with the FE model.

Due to the geometry of the form boards used to load each rib, the hinge moment arms were significantly reduced as the control surface deflected under load. This was particularly evident at the ribs outboard of the tab region, as these ribs experienced the largest deflections. Consequently, the relationship between rib load and

hinge moment during the tests was nonlinear. The hinge moment arms were positioned to simultaneously achieve the ultimate design hinge moment and ultimate design rib loads in the maximum deflected position.

### 3.4. Test procedure

The tests were conducted in the following order to ensure they progressed from least to most severe: limit airloads only; limit airloads and wing bending displacement; ultimate airloads only; ultimate airloads and wing bending displacement. The airloads, applied through the rib form boards, were increased in 5% of



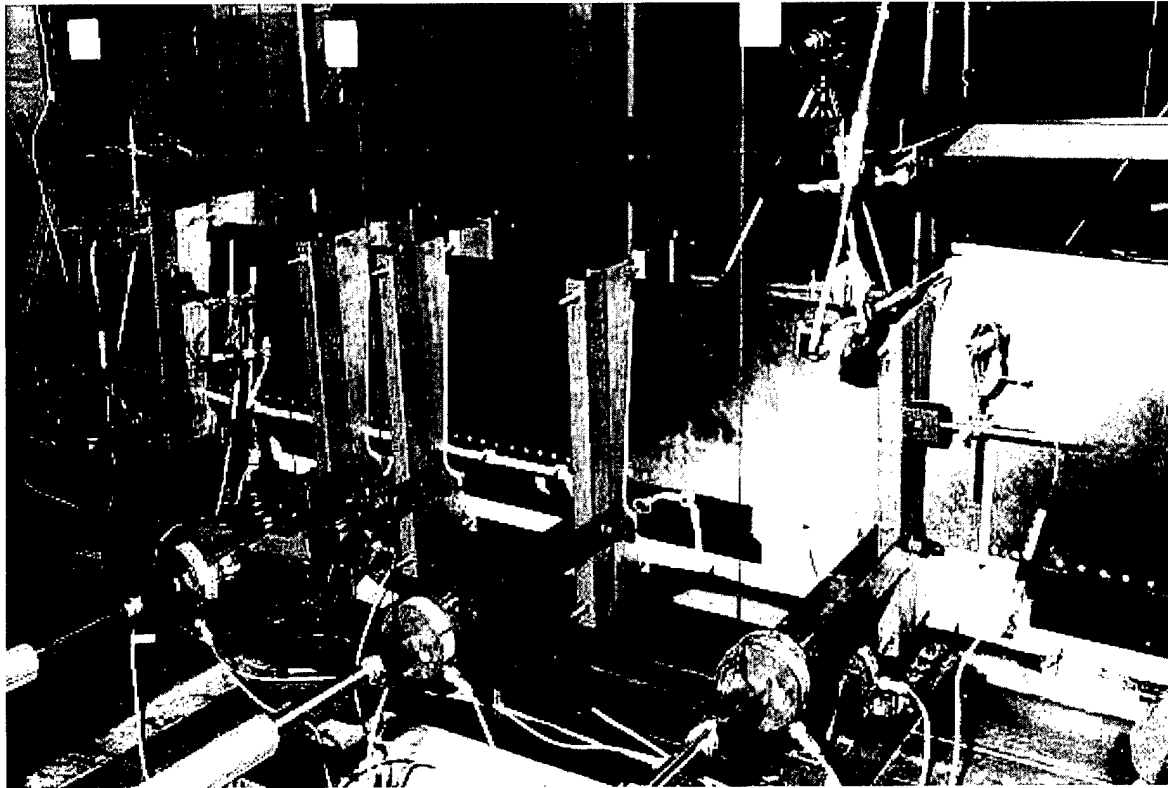


Fig. 6. Detailed view of the test arrangement (looking at top skin).

design ultimate load (DUL) increments with photographs of each moiré panel taken at each load level. Data acquisition was continuous at two seconds per scan, pausing while photographs were taken, and videos were rolling continuously, focused on the top and bottom skins. For the ultimate load cases, a 200s loading ramp was used. The ultimate load was held for approximately 2 min while photographs were taken, after which the specimen was unloaded at the same rate. No failure of the test articles occurred during the tests and only results from the final load case have been presented.

#### 4. FE model configuration

Two separate FE analyses of the aileron were conducted. Firstly, it was used as a design tool where airloads were applied to the skins. Secondly, the test arrangement was modelled where the loads were applied discretely at the ribs.

##### 4.1. FE model description

The FE model of the control surface was constructed using the pre- and post-processor MSC.Patran. The basic geometry of the aileron was translated from Catia into MSC.Patran. This created points and lines defining

the aileron geometry from which surfaces were generated in MSC.Patran. This enabled each region to be meshed separately with the basic quadrilateral shell elements suitable for analysis using MSC.Nastran. The model, shown in Fig. 7, contained 14,000 four-noded CQUAD4 elements and a total of 70,000 degrees of freedom. It has been found from previous analytical postbuckling work that a minimum of six quadrilateral elements between each stiffener bay is sufficient to capture the buckling mode shapes [7]. In this model, seven quadrilateral elements between stiffeners were used to provide minimum mesh density and adequate element geometry.

Metallic hinges and fixtures were modelled using 4-noded shell elements. Due to the 3D geometry of the model, four local coordinate frames were produced to aid defining the material axes for the complicated ply lay-ups.

##### 4.2. Stiffener model

In order to control the size of the FE model, blade-stiffeners were modelled using 2D beam elements where appropriate laminate properties were calculated and applied to the elements. These elements could not be offset due to a limitation in MSC.Nastran involving off-sets and the calculation of differential stiffness required in a geometric nonlinear analysis. The neutral axis of stiff-

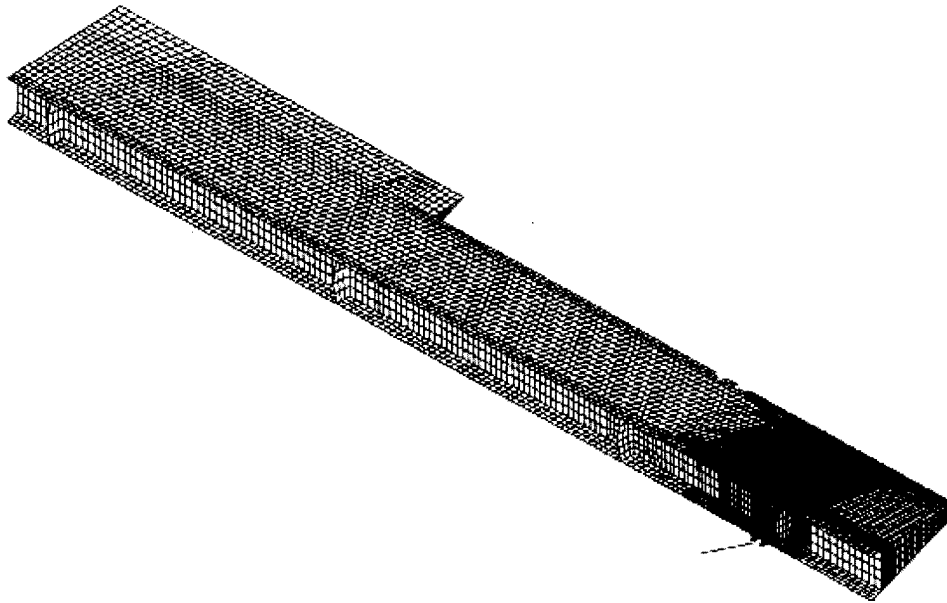


Fig. 7. The FE model.

eners represented by beam elements was therefore located in the plane of the skin. The error induced by this approximation was not expected to be large as the stiffeners were designed not to buckle. Shell elements were used in the region where the stiffeners joined to form a semi-rib near the trailing edge and rear spar.

#### 4.3. Detailed regions

The FE mesh was refined locally to model the critically loaded region near the actuator rod hinge, as shown in Fig. 8. Blade-stiffeners were accurately modelled using shell elements allowing more details to be incorporated such as stiffener run-outs and ply build-ups or drop-offs. Modelling of the stiffeners correctly using shell elements required at least four rows of elements along the height of the stiffener, otherwise an artificially high stiffness would result [8].

Hinge 1 and the actuator rod fitting were also modelled in detail to enable a realistic load transfer from the actuator rod to the front spar. The connection of the actuator rod to the hinge fitting consisted of two beam elements which had relatively large section properties, as rigid elements could be used in the geometric nonlinear analysis. Individual fasteners connecting the hinge assembly to the front spar were modelled as common nodes (perfect connection at the fastener locations).

#### 4.4. FE model of the test arrangement

To validate the design process, an analysis was performed with loading that simulated the test situation. This enabled an accurate comparison between the FE model and the experimental results. It should be pointed

out that the nose cover, which was fastened to the spar and covered the hinges, was not modelled despite being included in the test. It was determined that this part of the structure would not carry any significant amount of the torsion load applied to the aileron.

The form boards were modelled using a number of beam elements which connected the nodes along the bottom of the rib to the load application point, as shown in Fig. 9. This ensured that the load application point rotated in the manner experienced during testing and thus the variation in hinge moment would be accurately represented. The beam elements were relatively stiff resulting in no significant bending of the “form boards”. In addition, follower forces were not used so as to represent the test situation. The loads and moment arms corresponded to those presented in Table 1. The variation of hinge moment with applied rib loads proved to be almost identical to that experienced during testing.

The analysis was performed on the tape version of the aileron for the load case that included wing bending and DUL. The loads were applied in three subcases, as shown in Table 2. It should be noted that the entire wing sympathetic bending displacements were applied in the first subcase along with one-third of the airloads. This differed from the test in which the displacements were applied prior to the application of any airloads. As a result, comparison between the test and the analysis only valid at loads in excess of 33% of the applied air loads.

Difficulty was experienced in gaining convergence, hence the use of the “ITER” option for the second and third subcases. In addition, the error tolerances on convergence were relaxed from the default values. The MSC.Nastran FE analysis took approximately 26 h to

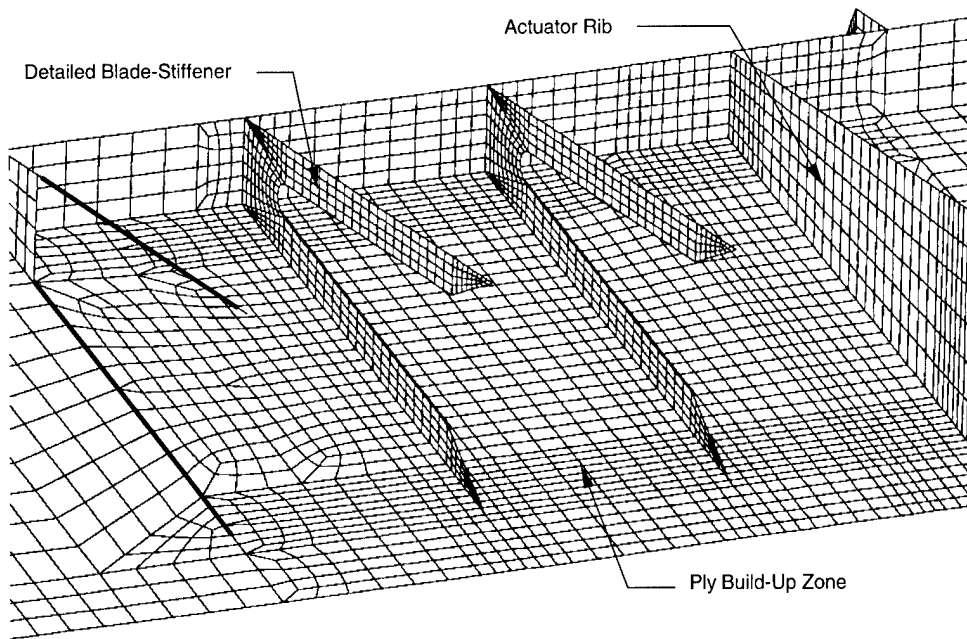


Fig. 8. Detailed region of the FE model (front spar and top skin not shown).

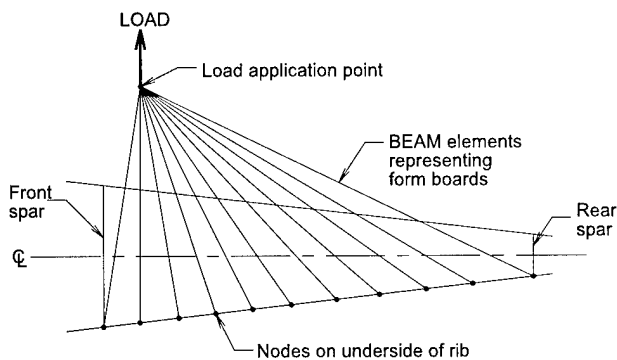


Fig. 9. Load application method in FE model of the test arrangement.

complete on an IBM RS/6000 3AT workstation. This was considerably longer than for the pressure loading used in the design of the aileron.

## 5. Results and comparison with analysis

### 5.1. Buckling behaviour

Buckling was observed to initiate during testing at approximately 48% DUL, although some bays did not

buckle until over 70% DUL. This was followed by a change in buckling mode by means of snap-through at 89% DUL. In the FE analysis, buckling was predicted to initiate at 45% DUL. No significant mode change was predicted to occur.

The buckling behaviour of individual bays of the aileron was observed through the moiré screens positioned as shown in Fig. 10. The development of buckling with increasing load through the outboard moiré screen is shown in Fig. 11. Buckling was first observed adjacent to Rib 6 at approximately 40% of ultimate load as shown in Fig. 11(b), with the extent of buckling increasing with load level until the entire panel was extensively buckled (refer to Fig. 11(c) and (d)). The buckling mode at the ultimate load consisted of five half-wavelengths in the chordwise direction, as shown in Fig. 11(d).

The development of buckling with increasing load through the inboard moiré screen is shown in Fig. 12. Between Ribs 2 and 3 on the bottom skin where the highest strains were expected, buckling was not significant until approximately 60% DUL, at which load load fringing in the moiré panel commenced adjacent to Rib 3. With increasing load, further buckling between Ribs 2 and 3 occurred up to DUL, as shown in Fig. 12(b) and (c).

Table 2  
MSC.Nastran nonlinear solution strategy

Subcase	% Air load	% Sympathetic bending	Stiffness update method	Number of load steps
1	33	100	SEMI	3
2	67	100	ITER	11
3	100	100	ITER	11

A comparison of the general buckling pattern experienced during test and that predicted by the FE analysis at 100% DUL is presented in Fig. 13. A photograph taken at ultimate load during testing is shown in

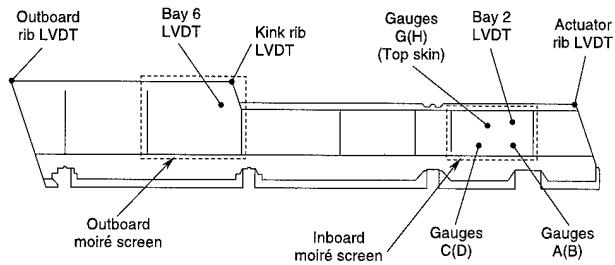


Fig. 10. Location of LVDTs, moiré screens and selected strain gauges used during testing (viewed from bottom skin). Gauge letter in parentheses indicates rosette applied to the inner surface of the skin.

Fig. 13(a), while the rendered displacement result from FE analysis is shown in Fig. 13(b). Buckling patterns are clearly visible over the entire aileron and the comparison between the analytical and experimental buckling modes is generally good. The diagonal buckling shape due to shear dominated loading in the stiffened skins is clearly observed in both images. However, it is apparent that the order of the buckling mode is different in the bay between Ribs 7 and 8 on the right of the Fig. 13. During testing, five half-waves per stiffener bay were present in this region at a load factor of 1.0, while the analysis predicted only three.

### 5.2. Trailing edge displacements

The displacements of the trailing edge at three locations, shown in Fig. 10, were measured during the tests.

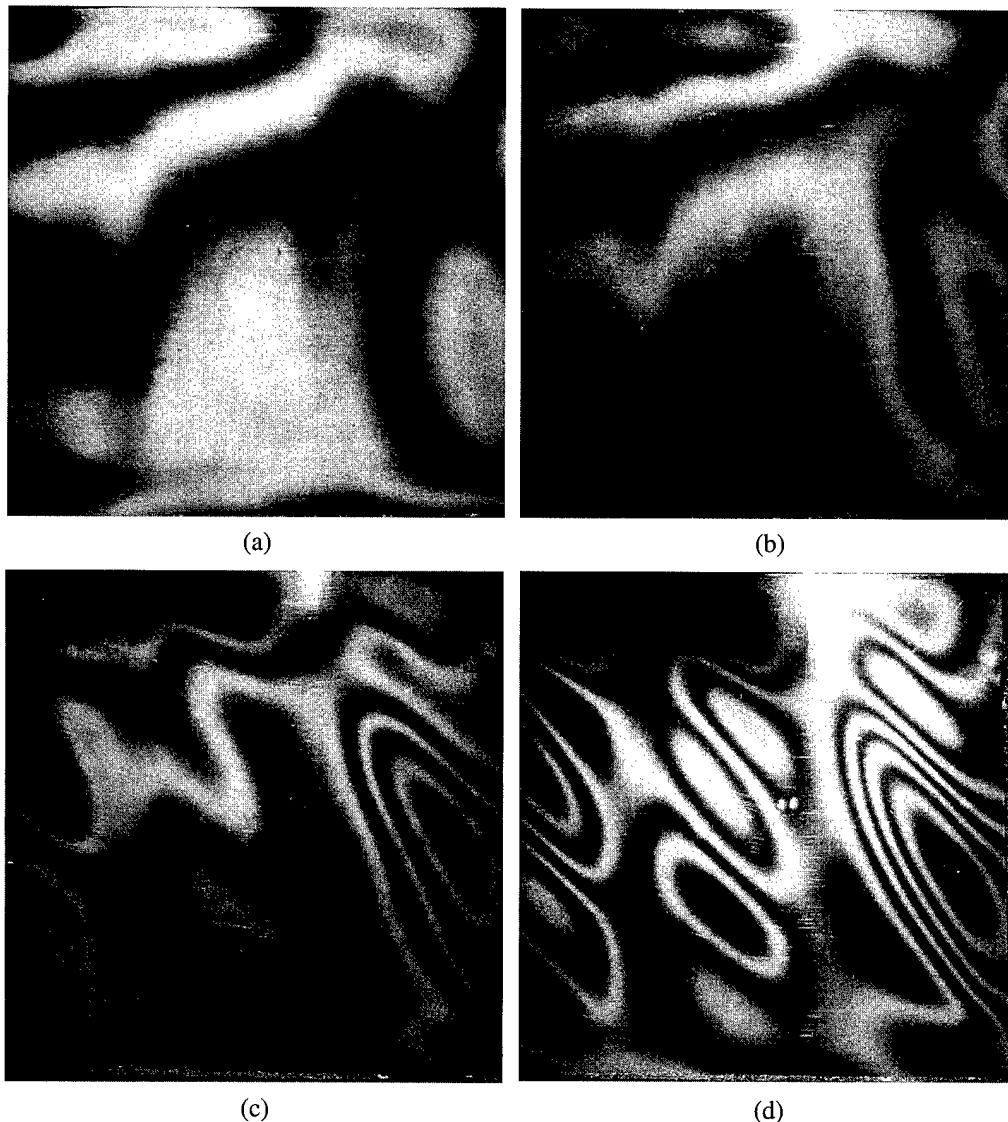


Fig. 11. Moiré fringe pattern at outboard bay at: (a) 0; (b) 40%; (c) 70%; (d) 100% DUL.

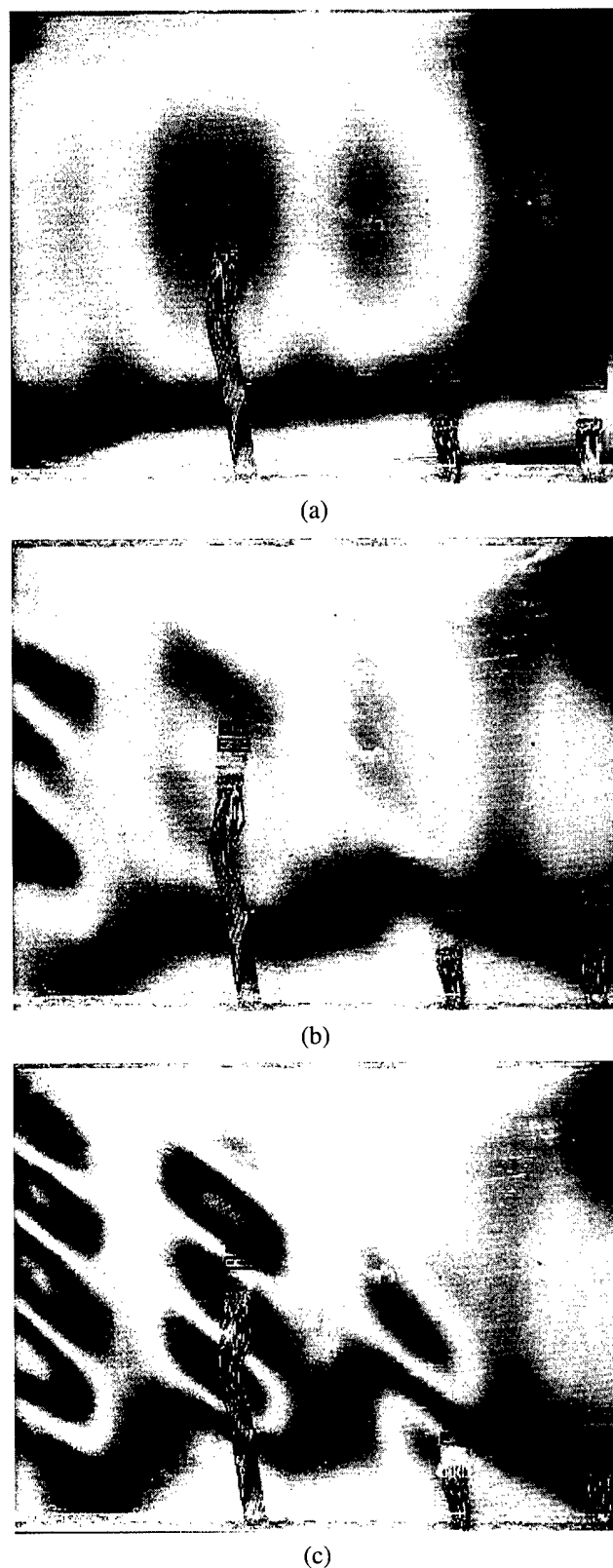


Fig. 12. Moiré fringe pattern at inboard end at: (a) 0; (b) 70%; (c) 100% DUL.

The measured displacements were relative to the test rig framework and so include that attributable to flexure of the control rod and its attachment pins. This was found to be significant at the ultimate load and, in fact, permanent bending of the high tensile steel bolt attaching the control rod to the control surface occurred after several load cases had been tested. It should be noted that the control rod components and attachment pin were not aircraft quality parts.

The measured trailing edge displacements at each location are shown in Fig. 14. The initial displacements in Fig. 14 are due to the wing bending displacements applied to Hinges 2 and 3 prior to applying the rib loads. The initial unsteadiness evident in the plot at approximately 10% rib load is characteristic of the test rig at low load levels. As the displacement at the trailing edge is primarily dependent on the hinge moment, the displacements are plotted against load factor based on hinge moment.

The displacements of nodes corresponding to the positions of the three trailing edge LVDTs were extracted and are compared in Fig. 14. While the comparison of the raw displacements is reasonable, it is more appropriate to compare the relative displacement or twist that the aileron experiences as this eliminates the influence of test rig deflections. A summary of the values at a load factor of 1.0 are presented in Table 3. These results demonstrate the excellent comparison between test and the FE analysis with only 2% difference at 100% DUL.

### 5.3. Skin out-of-plane displacements

The locations of LVDTs in Bays 2 and 6, shown in Fig. 10, were selected based on expected areas of significant buckling. These were mounted from the nearest form boards to measure skin out-of-plane displacement, and as such were very sensitive to movement of the form board relative to the control surface. While results from these two instruments can only be loosely interpreted, both these LVDTs clearly highlight onset and change in the buckling mode as shown by the sudden displacement changes evident in Fig. 15.

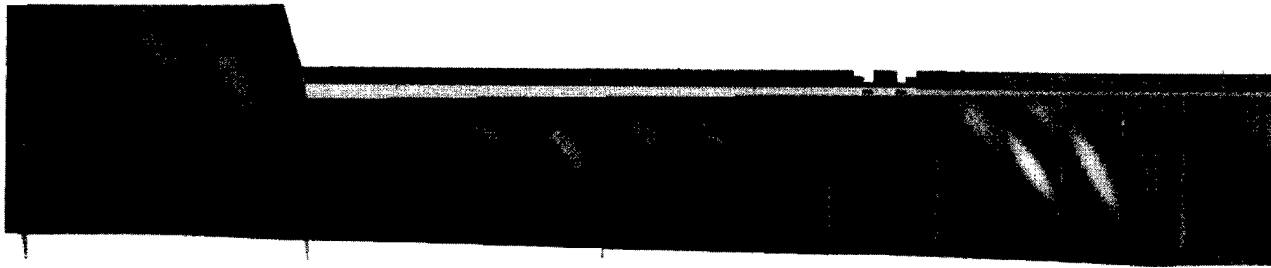
The skin out-of-plane displacements due to buckling were difficult to compare with the analysis because the instrumentation was very sensitive to movement of the form board relative to the control surface, to compression of the felt between the form board and control surface, or even small lateral movements of the form board. Hence, no comparisons are presented.

### 5.4. Strain measurements

The strains recorded during the test at various locations are compared with analytical strains determined



(a)



(b)

Fig. 13. Comparison of buckling patterns at DUL between: (a) test; (b) FE analysis.

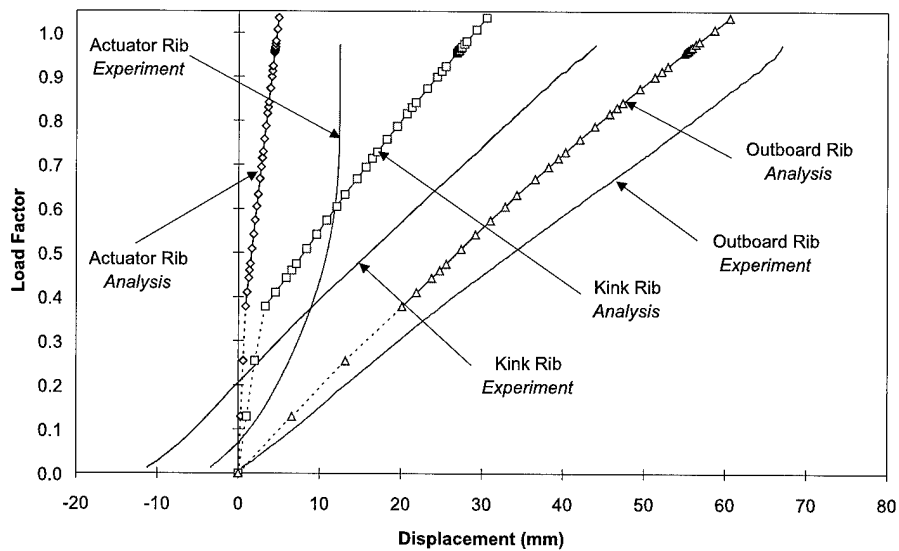


Fig. 14. Comparison of trailing edge displacements from test and FE analysis.

from the ply strain output from MSC.Nastran. The analytical strains are output at the mid-plane of each ply, so they were extrapolated to give the surface strains

necessary for comparison with strain gauge data. The ply shear strains were derived from the strains measured in all three elements.

Table 3  
Comparison between test and FE analysis at a load factor of 1.0

	Actuator rib		Outboard rib		Relative	
	Displacement (mm)	Angular rotation (°)	Displacement (mm)	Angular rotation (°)	Twist (°)	Error
Test	12.4	2.14	68.1	8.71	6.57	–
FE analysis	4.8	0.84	60.5	7.74	6.69	2%

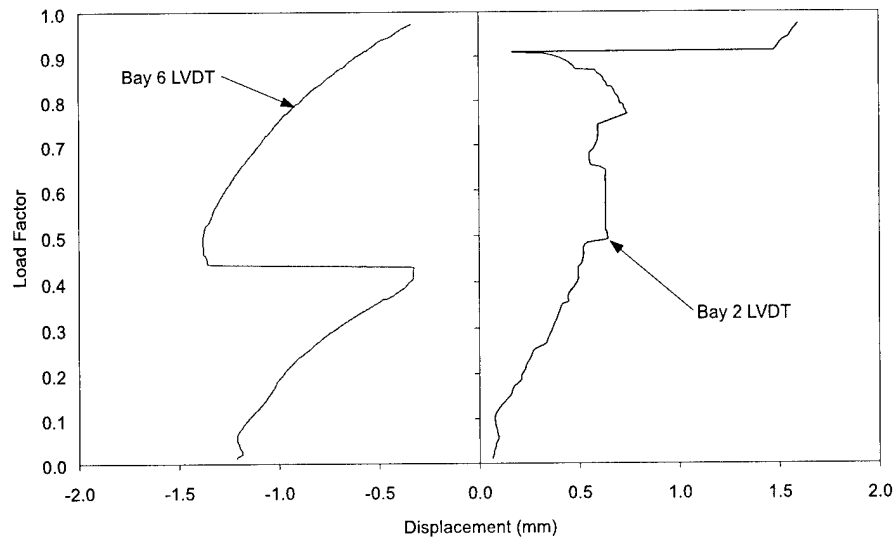


Fig. 15. Skin out-of-plane displacements recorded from test.

In general, the results demonstrated good agreement between analysis and test data. Due to the different method of applying the wing bending loads, the results should only be compared at load factors in excess of 0.38. Gauges located in regions in which large strains were introduced though application on the wing bending compare less well than the others. The test and analysis results remain off-set indicating that strains due to wing bending did not compare well.

Comparisons between experimental and analytical strains are presented for the gauges at the locations shown in Fig. 10. The back-to-back longitudinal and transverse ply strains at Gauge C(D) on the bottom skin from test and analysis are presented in Fig. 16. The strains compare very well up to 80% DUL when the experimental strains diverge somewhat. Similar behaviour was noted in the back-to-back shear strains at Gauges A(B), as shown in Fig. 17. It is apparent that the slope of the predicted load-strain curve was lower leading to an overestimation of the strains. More complex buckling behaviour was evident in the back-to-back shear strains at Gauges G(H), as shown in Fig. 18. The comparison above 38% DUL was very good despite the complex buckling behaviour. However, at 89% DUL the mode change experienced in the test is clearly evident as the experimental strains on the inner and outer surface “swap over”. This behaviour was not predicted by the analysis.

### 5.5. Discussion

Comparing the FE analysis results with the test results showed that the global behaviour, such as the nonlinear loading effect and the resulting displacements, were accurately modelled. The local behaviour, such as buckling initiation, was also well represented, although the accuracy of strains measured at several locations varied significantly. Errors in the strain measurements ranged from 10% to over 100%, or up to a maximum of 1500  $\mu\epsilon$  at 100% DUL. This highlights the way in which small variations in the buckling mode or the location of a buckling peak can lead to dramatic changes in the measured strain. The buckling mode could have been affected by such factors as manufacturing variations, initial imperfections in the skins or through variations in the load introduction through the form boards. In addition, nose covers which were not included in the model may have carried some of the applied loads.

Comparisons between test and analysis were made more difficult due to limitations of the FE modelling technique. Typically, the strain output from the FE model was averaged over a larger area (one element) than that covered by the strain gauges in the test. In addition, due to the size of the elements, they did not always coincide exactly with the strain gauge locations and were sometimes over 12 mm from the correct

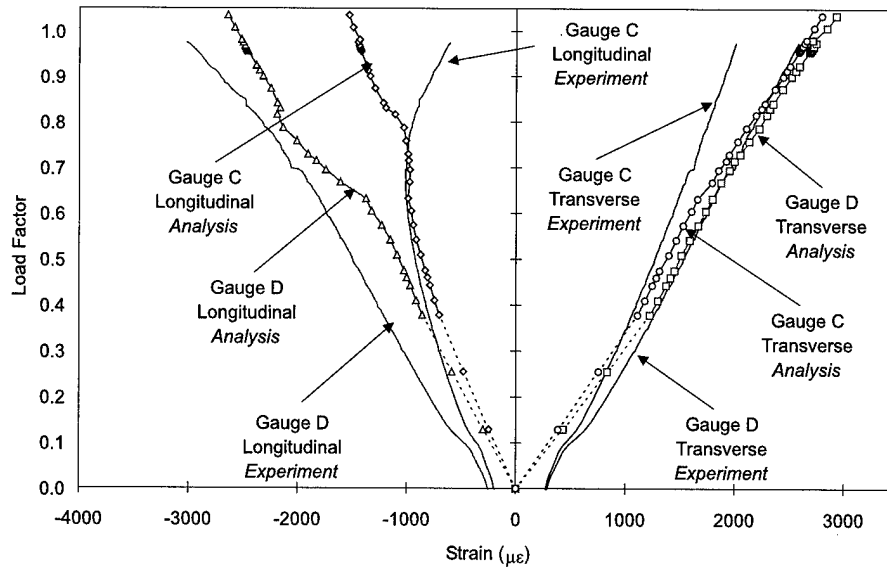


Fig. 16. Comparison between test and experimental back-to-back longitudinal and transverse ply strains in the bottom skin at Gauges C(D).

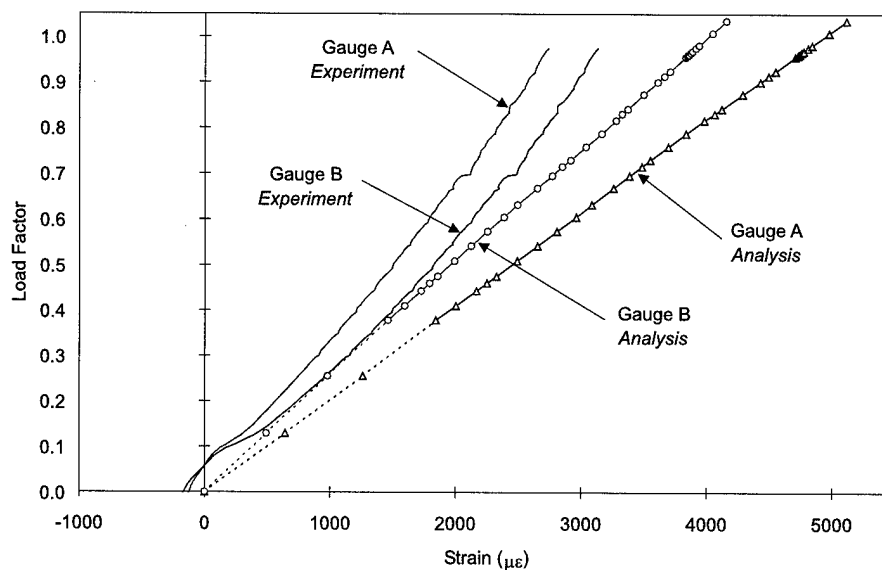


Fig. 17. Comparison between test and experimental back-to-back shear strains in the bottom skin at Gauges A(B).

location. This effect would be very significant in thin, postbuckling structures.

Difficulty in achieving convergence in the FE analysis was experienced, as evidenced by the long run-time and the need to relax the convergence error tolerances. This has the potential to adversely affect the accuracy of the solution in extreme cases [9]. From past experience, the levels to which the convergence error tolerances were relaxed should not have affected the solution, although this is difficult to prove.

It was also evident that the analysis failed to capture the complicated snap-through buckling mode change

that occurred at 89% of DUL. At a load factor of 0.95, problems with convergence were experienced during the analysis which could have indicated that a snap-through phenomenon was likely. From other experience, MSC.Nastran geometric nonlinear analysis is unlikely to predict a snap-through buckling event when using a standard load increment approach [10]. Introduction of the arc-length technique, where the load steps are determined based on the resulting displacements, is more likely to predict such behaviour. However, the use of applied displacements to represent the wing bending prevented use of the arc-length method.



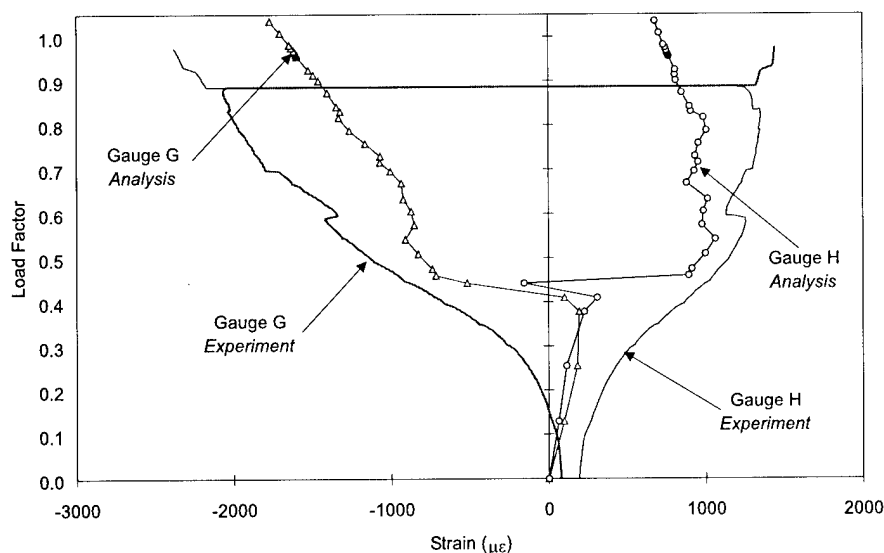


Fig. 18. Comparison between test and experimental back-to-back shear strains in the top skin at Gauges G(H).

## 6. Conclusions

Full-scale static testing of a co-cured carbon fibre composite control surface has been performed and the results compared with FE analysis. The control surface, which is representative of those found on mid-size jet transport aircraft, is designed as a postbuckling blade-stiffened structure to reduce weight and improve operational performance compared with a traditional honeycomb sandwich panel design. The purpose of the tests was to demonstrate the validity of the design by applying static limit and ultimate loads to the structure.

The control surface was successfully loaded to the ultimate design load, including wing bending displacement, without evidence of failure. Buckling initiated at approximately 48% of ultimate load with out-of-plane displacements observed in most panels. The postbuckling behaviour of the aileron was complicated by a sudden mode change which occurred at 89% of DUL. Following this change, higher order buckling modes were evident in several bays.

A FE analysis of the aileron was conducted under loading which simulated the test conditions. The global behaviour, such as overall twist of the aileron, was predicted with great accuracy. The local behaviour, such as buckling behaviour and strains, was predicted accurately in most locations. Some localised variation in the buckling mode shape was experienced at very high load levels which affected the position of the buckle peaks and thus the strains in these areas. In particular, the analysis failed to capture a buckling mode change which occurred in some areas of the aileron at 89% of DUL. This illustrated the importance of conducting full-scale testing of structures operating at loads well in excess of buckling. The success of the testing program demon-

strated the suitability of the methodology used in the design of a postbuckling, carbon fibre composite aileron.

## Acknowledgements

The authors gratefully acknowledge the contributions to this work of Messrs Alan Cheung and Shane Craddock in the design and analysis, and Messrs Paul Newman and Mark McVilley in the testing of the ailerons.

## References

- [1] Hart-Smith LJ. Lessons learned from the DC-10 carbon epoxy rudder program. Douglas Aircraft Paper 7734, Long Beach, 1986.
- [2] Hawley AV. Ten years of flight service with DC-10 composite rudders – a backward glance. Douglas Aircraft Paper 7733. In: Proceedings of the SAE Aerotech '86, Long Beach, California, USA, 13–16 October 1986.
- [3] Schneider CW, Gibson DC. Design and certification of a composite control surface. In: Composites: Design and Manufacturing for General Aviation Aircraft, SAE SP-623, Wichita, Kansas, USA, 16–19 April 1985.
- [4] Hart-Smith LJ. Innovative concepts for the design and manufacture of secondary composite aircraft structures. McDonnell Douglas Paper MDC 93K0081. In: Proceedings of the Fifth Australian Aeronautical Conference, Melbourne, Australia, 13–15 September 1993.
- [5] Ashizawa M, Toi Y. Unique features and innovative application of advanced composites to the MD-11. In: Proceedings of the AIAA/AHS/ASCE Aircraft Design, Systems and Operations Conference, AIAA-90-3217, Dayton, OH, USA, 17–19 September 1990.
- [6] Catia Version 3: Interactive user access, 3D design, solids geometry, mathematical subroutine package and geometry interface manuals. 3rd ed. vol. 6, IBM Corporation, 1990. p. 511–8.

- [7] Trentin C, Scott ML, Alesi H. Postbuckling behaviour of blade-stiffened fibre composite panels. In: Proceedings of the Ninth International Conference on Composite Materials, Madrid, Spain, 12–16 July 1993.
- [8] Lee JM, editor. MSC.Nastran common questions and answers. 2nd ed. LA, USA: MacNeal-Schwendler, 1993.
- [9] Lee SH, editor. MSC.Nastran handbook for nonlinear analysis (Draft) (Version 67). LA, USA: MacNeal-Schwendler, 1992.
- [10] Thomson RS, Scott ML. The effect of delaminations in post-buckling stiffened composite shear panels, *Computational Mechanics* (in press).

# Material characterization of laminated composite plates via static testing

W.T. Wang, T.Y. Kam \*

*Department of Mechanical Engineering, National Chiao Tung University, 1001 Ta Hsueh Road, Hsin-Chu 300 50, Taiwan, ROC*

## Abstract

A minimization method for material characterization of laminated composite plates using static test results is presented. Mechanical responses such as strains and displacements are measured from the static tests of the laminated composite plates. The finite element method is used to analyse the deformation of the laminated composite plates. An error function is established to measure the differences between the experimental and theoretical mechanical responses of the laminated composite plates. The identification of the material elastic constants of the laminated composite plates is formulated as a constrained minimization problem in which the elastic constants are determined by making the error function a global minimum. A number of examples are given to illustrate the feasibility and applications of the proposed method. © 2000 Elsevier Science Ltd. All rights reserved.

**Keywords:** Composite laminate; Material characterization; Identification; Minimization method; Finite element method

## 1. Introduction

Recently composite laminates have been used extensively in the mechanical and aerospace industries, especially for the fabrication of high performance structures. To ensure high reliability of the structures, the actual behaviors of the laminated composite parts in service must be accurately predicted and carefully monitored. The attaining of the actual behavioral predictions of the structures depends on the correctness of the elastic constants of the structures. As well-known, there are many methods for manufacturing laminated composite components [1,2] and different manufacturing or curing processes may yield different mechanical properties of the components. Furthermore, the material properties determined from standard specimens tested in laboratory may deviate significantly from those of actual laminated composite components manufactured in factory. On the other hand, laminated composite structures subject to dynamic loads or used in severe environments may experience progressive stiffness reduction or material degradation which will finally lead to the failure of the structures. It has been pointed out that accurate de-

termination of current stiffness or material properties of a laminated composite structure can help prevent sudden failure of the structure [3]. Therefore, the determination of realistic material or mechanical properties of laminated composite components has become an important topic of research. In the past two decades, a number of non-destructive evaluation techniques have been proposed for the determination of material properties of or damages in laminated composite parts [4–7]. Nevertheless, these techniques have their own limitations or specific difficulties when in use. On the other hand, a number of researchers have presented methods to identify or improve the analytical system matrices of a structure using vibration test data [8–12]. For instance, Berman and Nagy [8] developed a method which used measured normal modes and natural frequencies to improve an analytical mass and stiffness matrix model of a structure. Their method could find minimum changes in the analytical model to make it exactly agree with the set of measured modes and frequencies. Kam and his associates [9–12] developed methods to identify the element bending stiffnesses of beam structures using measured natural frequencies and mode shapes or displacements alone.

In this paper, a non-destructive evaluation method is presented for the determination of material elastic constants of laminated composite plates. The method is

\*Corresponding author. Tel.: +886-3-5725-634; fax: +886-3-5728-504.

E-mail address: tykam@cc.nctu.edu.tw (T.Y. Kam).

based on the minimization of the sum of the differences between the predicted and measured mechanical responses of a composite plate. A global minimization technique together with an appropriate bounding method for determining the starting points and the search direction are used to solve the minimization problem from which the material constants can be identified. Static tests of several laminated composite plates have been performed and the results used to verify the accuracy and illustrate the applications of the method.

## 2. Deformation analysis of laminated composite plate

Consider a rectangular plate of area  $a \times b$  and constant thickness  $h$  subject to transverse load  $p(x, y)$  as shown in Fig. 1. The plate is composed of a finite number of layer groups in which each layer group contains several orthotropic layers of same fiber angle and uniform thickness. The  $x$  and  $y$  coordinates of the plate are taken in the mid-plane of the plate. The displacement field is assumed to be of the form:

$$\begin{aligned} u_1(x, y, z) &= u_0(x, y) + z \cdot \psi_x(x, y), \\ u_2(x, y, z) &= v_0(x, y) + z \cdot \psi_y(x, y), \\ u_3(x, y, z) &= w(x, y), \end{aligned} \quad (1)$$

where  $u_1, u_2, u_3$  are displacements in the  $x, y, z$  directions, respectively, and  $u_0, v_0, w$  the associated mid-plane displacements;  $\psi_x$  and  $\psi_y$  are shear rotations.

The constitutive equations of a shear deformable laminated composite plate can be written as

$$\begin{bmatrix} N_1 \\ N_2 \\ Q_y \\ Q_x \\ N_6 \\ M_1 \\ M_2 \\ M_6 \end{bmatrix} = \begin{bmatrix} A_{11} & A_{12} & 0 & 0 & A_{16} & B_{11} & B_{12} & B_{16} \\ A_{12} & A_{22} & 0 & 0 & A_{26} & B_{12} & B_{22} & B_{26} \\ 0 & 0 & A_{44} & A_{45} & 0 & 0 & 0 & 0 \\ 0 & 0 & A_{45} & A_{55} & 0 & 0 & 0 & 0 \\ A_{16} & A_{26} & 0 & 0 & A_{66} & B_{16} & B_{26} & B_{66} \\ B_{11} & B_{12} & 0 & 0 & B_{16} & D_{11} & D_{12} & D_{16} \\ B_{12} & B_{22} & 0 & 0 & B_{26} & D_{12} & D_{22} & D_{26} \\ B_{16} & B_{26} & 0 & 0 & B_{66} & D_{16} & D_{26} & D_{66} \end{bmatrix} \begin{bmatrix} u_{0,x} \\ v_{0,y} \\ w_{,y} + \psi_y \\ w_{,x} + \psi_x \\ u_{0,y} + v_{0,x} \\ \psi_{x,x} \\ \psi_{y,y} \\ \psi_{x,y} + \psi_{y,x} \end{bmatrix}, \quad (2)$$

where  $N_1, N_2, \dots, M_6$  are stress resultants;  $A_{ij}, B_{ij}$  and  $D_{ij}$  are material components; the comma before a subscript denotes the partial derivative with respect to the subscript. The material components are given by

$$\begin{aligned} (A_{ij}, B_{ij}, D_{ij}) &= \int_{-h/2}^{h/2} Q_{ij}^{(m)}(1, z, z^2) dz \\ (i, j &= 1, 2, 6) \end{aligned} \quad (3a)$$

and

$$\begin{aligned} A_{ij} &= k_x \cdot k_y \cdot \bar{A}_{ij}, \quad \bar{A}_{ij} = \int_{-h/2}^{h/2} Q_{ij}^{(m)} dz \\ (i, j &= 4, 5; \alpha = 6 - i; \gamma = 6 - j). \end{aligned} \quad (3b)$$

The stiffness coefficients  $Q_{ij}^{(m)}$  depend on the material properties and orientation of the  $m$ th layer group. The parameters  $k_i$  are shear correction factors which are

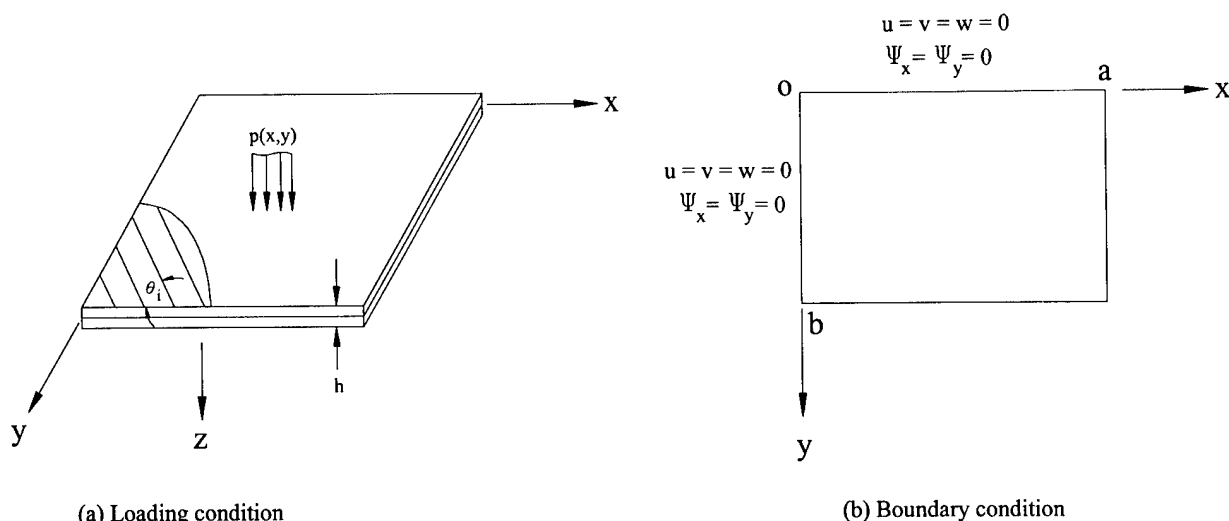


Fig. 1. Laminated composite plate.

determined using the expressions given by Whitney [13]. In the plate analysis, the finite element developed by Kam and Chang [14] is adopted to evaluate the deformation of the plate. The element contains five degrees-of-freedom (three displacements and two slopes, i.e., shear rotations) per node. In the evaluation of the element stiffness matrix, a quadratic element of a serendipity family and the reduced integration are used. The element has been used in the static analysis of both thin and moderately thick laminated composite plates and very good results for strains and displacements can be obtained. The accuracy of the finite element in predicting strains was also investigated via an experimental approach [15]. A square  $[0_2^\circ/90_2^\circ/0_2^\circ/90_2^\circ]_s$  graphite/epoxy laminate with clamped edges was loaded at the center and strains at the center of the bottom surface of the laminate were measured in the experiment. The strain data were compared with those predicted by the finite element method. It was found that the use of a  $3 \times 3$  mesh over a quarter plate could yield very good results. In the following identification of material constants, strains and deflections at some particular points on a plate are defined as deformational parameters.

### 3. Determination of material constants

The problem of material constants identification is formulated as a minimization problem. In mathematical form it is stated as

$$\begin{aligned} &\text{Minimize } e(\underline{x}) = (\underline{D}^*)'(\underline{D}^*) \\ &\text{subject to } x_i^L \leq x_i \leq x_i^U, \quad i = 1, \dots, 5, \end{aligned} \quad (4)$$

where  $\underline{x} = [E_1, E_2, \nu_{12}, G_{12}, G_{23}]$  the material constants;  $\underline{D}^*$  is an  $N \times 1$  vector containing the differences between the measured and predicted values of the deformational parameters;  $e(\underline{x})$  is an error function measuring the sum of differences between the predicted and measured data;  $x_i^L, x_i^U$  are the lower and upper bounds of the material constants. It is noted that the lower and upper bounds of the material constants are chosen in such a way that the lower bound of  $E_1$  is larger than the upper bounds of  $E_2$  and  $G_{12}$ . The elements in  $\underline{D}^*$  are expressed as

$$D_i^* = \frac{D_{pi} - D_{mi}}{D_{mi}}, \quad i = 1, \dots, N, \quad (5)$$

where  $D_{pi}$ ,  $D_{mi}$  are predicted and measured values of deformation parameters, respectively. The above problem of Eq. (4) is then converted into an unconstrained minimization problem by creating the following general augmented Lagrangian:

$$\bar{\Psi}(\tilde{\underline{x}}, \underline{\mu}, \underline{\eta}, r_p) = e(\underline{x}) + \sum_{j=1}^5 [\mu_j z_j + r_p z_j^2 + \eta_j \phi_j + r_p \phi_j^2] \quad (6)$$

with

$$\begin{aligned} z_j &= \max \left[ g_j(\tilde{x}_j), \frac{-\mu_j}{2r_p} \right], \\ g_j(\tilde{x}_j) &= \tilde{x}_j - \tilde{x}_j^U \leq 0, \\ \phi_j &= \max \left[ H_j(\tilde{x}_j), \frac{-\eta_j}{2r_p} \right], \\ H_j(\tilde{x}_j) &= \tilde{x}_j^L - \tilde{x}_j \leq 0, \quad j = 1, \dots, 5, \end{aligned} \quad (7)$$

where  $\mu_j, \eta_j, r_p$  are multipliers;  $\max[*,*]$  takes on the maximum value of the numbers in the bracket. The modified design variables  $\tilde{\underline{x}}$  are defined as

$$\tilde{\underline{x}} = \left[ \frac{E_1}{\alpha_1}, \frac{E_2}{\alpha_2}, \nu_{12}, \frac{G_{12}}{\alpha_3}, \frac{G_{23}}{\alpha_4} \right], \quad (8)$$

where  $\alpha_i$  are the normalization factors. The update formulas for the multipliers  $\mu_j, \eta_j$  and  $r_p$  are

$$\begin{aligned} \mu_j^{n+1} &= \mu_j^n + 2r_p^n z_j^n, \\ \eta_j^{n+1} &= \eta_j^n + 2r_p^n \phi_j^n, \quad j = 1, \dots, 5, \\ r_p^{n+1} &= \begin{cases} \gamma_0 r_p^n & \text{if } r_p^{n+1} < r_p^{\max}, \\ r_p^{\max} & \text{if } r_p^{n+1} \geq r_p^{\max}, \end{cases} \end{aligned} \quad (9)$$

where the superscript  $n$  denotes iteration number;  $\gamma_0$  is a constant;  $r_p^{\max}$  is the maximum value of  $r_p$ . The parameters  $\mu_j^0, \eta_j^0, r_p^0, \gamma_0$  and  $r_p^{\max}$  are chosen as

$$\begin{aligned} \mu_j^0 &= 1.0, \quad \eta_j^0 = 1.0, \quad j = 1, \dots, 5, \\ r_p^0 &= 0.4, \quad \gamma_0 = 1.25, \quad r_p^{\max} = 100. \end{aligned} \quad (10)$$

The constrained minimization problem of Eq. (6) has thus become the solution of the following unconstrained problem:

$$\text{Minimize } \bar{\Psi}(\tilde{\underline{x}}, \underline{\mu}, \underline{\eta}, r_p). \quad (11)$$

The solution of the above unconstrained optimization problem is obtained by using the previously proposed unconstrained multi-start global optimization algorithm [16,17]. In the adopted optimization algorithm, the objective function to be minimized is treated as the potential energy of a traveling particle and the search trajectories for locating the global minimum are derived from the equation of motion of the particle in a conservative force field. The design variables, i.e., material constants, that make the potential energy of the particle, i.e., objective function, the global minimum constitute the solution of the problem. In the minimization process, a series of starting points are selected at random from the region of interest and the lowest local minimum along the search trajectory initiated from each starting point is determined. A Bayesian argument is then used to establish the probability of the current overall minimum value of the objective function being the global minimum, given the number of starts and the number of times this value has been achieved. The

multi-start procedure is terminated once a target probability, typically 0.99, has been exceeded.

#### 4. Experimental investigation

The composite materials under consideration are T300/2500 graphite/epoxy produced by Torayca, Japan. The properties of the graphite/epoxy material are first determined experimentally in accordance with the relevant ASTM specifications [18]. Each material constant was determined from tests using five specimens. The mean values and coefficients of variation of the experimentally determined material constants are given as follows:

$$\begin{aligned} E_1 &= 124.68 \text{ GPa (2.75\%)}, & E_2 &= 9.6 \text{ GPa (3.24\%)}, \\ G_{12} &= 8.64 \text{ GPa (2.8\%)}, & G_{23} &= 2.32 \text{ GPa (6.82\%)}, \\ \nu_{12} &= 0.33 \text{ (5.1\%)}. \end{aligned} \quad (12)$$

For experimental investigation, a number of square symmetric laminates, namely,  $[45_2^\circ/0_3^\circ/-45_2^\circ/0_3^\circ/45_2^\circ]_s$  and  $[0_2^\circ/90_2^\circ/0_2^\circ/90_2^\circ]_s$  of dimensions 14 cm  $\times$  14 cm were manufactured and subjected to static tests in accordance with the test procedure described in Ref. [19]. The lamina thickness for the laminated plates is 0.125 mm. A schematic description of the experimental setup is shown in Fig. 2 in which the laminate is clamped at all edges and the actual dimensions of the laminate are

10 cm  $\times$  10 cm. The laminated plates were subjected to two types of loadings, namely, a center point load or a uniformly distributed load. A number of displacement transducers (LVDT) and strain gauges were placed beneath the bottom surface of the laminate for measuring the deformational parameters of the laminate. The load–displacement and load–strain curves of the laminates were constructed using the data measured from the displacement transducer (LVDT) and strain gauges, respectively. The points on the bottom surface of the laminated plate at which the displacements and strains were measured is shown in Fig. 3.

#### 5. Results and discussions

The aforementioned non-destructive evaluation method will be applied to the material characterization of the laminated composite plates which have been tested. The upper and lower bounds of the material constants are chosen based on experience.

$$\begin{aligned} 40 &\leq E_1 \leq 400 \text{ GPa}, & 0 &\leq E_2 \leq 40 \text{ GPa}, \\ 0 &\leq G_{12} \leq 40 \text{ GPa}, & 0 &\leq G_{23} \leq 40 \text{ GPa}, \\ 0 &\leq \nu_{12} \leq 0.5. \end{aligned} \quad (13)$$

The modified design variables are obtained via the use of the following normalization factors:

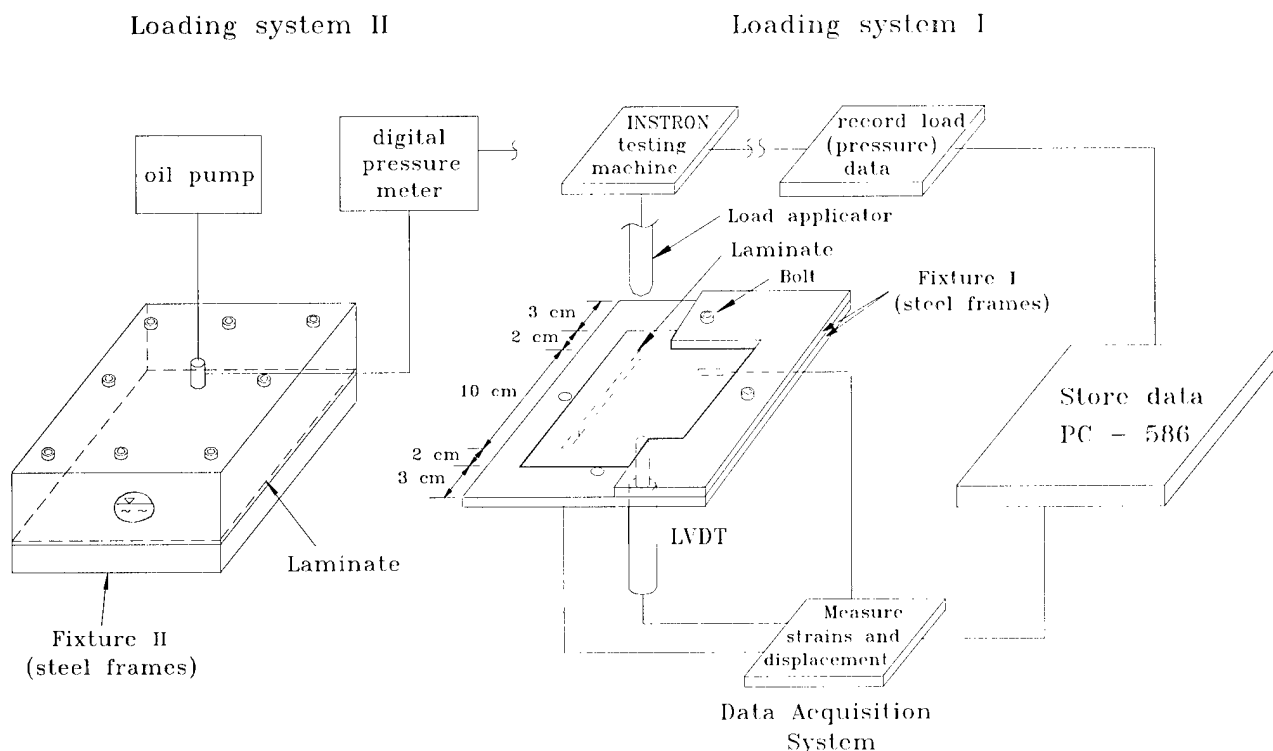


Fig. 2. A schematic description of the experimental setup.

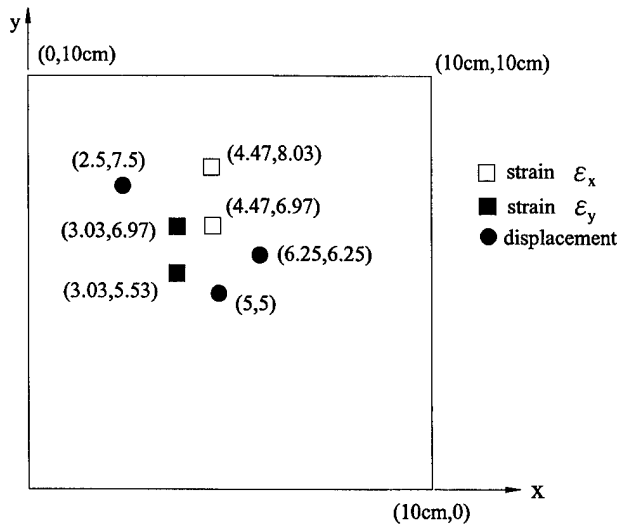


Fig. 3. Locations on laminated plates for the measurements of displacements and strains.

$$\alpha_1 = 1000, \quad \alpha_i = 100 \quad (i = 2, 3, 4). \quad (14)$$

Three deformational parameters are used in the present identification method to determine the material constants of the laminated composite plates. About eight

starting points have been randomly selected to obtain the global minimum in the identification process. The predicted material constants as well as the percentage differences between the theoretically predicted and experimentally determined material constants for different cases are listed in Tables 1 and 2. It is noted that the present method can produce results of acceptable accuracy for the cases under consideration. In particular, for the laminated plates subjected to a point load, excellent results can be obtained for the predictions of the material constants and in general their errors are equal to or less than 9%. As for the  $[0_2^\circ/90_2^\circ/0_2^\circ/90_2^\circ]_s$  plates subjected to uniform loads, the error for the prediction of  $G_{23}$  can be as large as 26.7%. The cause of the relatively large errors in the prediction of  $G_{23}$  is due to the small contribution of transverse shear deformation to the magnitudes of the deformational parameters when the plate is under uniform load. Due to the facts that the value of Poisson's ratio is small and it has small effects on the deformation of the laminated composite plates, the error in the prediction of  $\nu_{12}$  tend to be large when compared with those of  $E_1, E_2$  and  $G_{12}$ . After all it is obvious that point load is more appropriate than uniform load for use in the identification of the five material constants. It is also noted that if the present normalization and

Table 1  
Material constant identification of laminated composite plates subjected to a uniform load

Plate lay-up	Measured deformational parameters	Identified material constants
$[45_2^\circ/0_3^\circ/-45_2^\circ/0_3^\circ/45_2^\circ]_s$	$d(5 \text{ cm}, 5 \text{ cm})^a = 0.12 \text{ mm}$ $\epsilon_x(4.47 \text{ cm}, 6.97 \text{ cm}) = 0.112 \times 10^{-3}$ $\epsilon_y(3.03 \text{ cm}, 5.53 \text{ cm}) = 0.14 \times 10^{-3}$	$E_1 = 125.1 \text{ GPa}$ (0.34%) <sup>b</sup> , $E_2 = 9.6 \text{ GPa}$ (0%) $G_{12} = 8.6 \text{ GPa}$ (0.46%), $G_{23} = 2.5 \text{ GPa}$ (7.8%) $\nu_{12} = 0.294$ (10.9%)
$[0_2^\circ/90_2^\circ/0_2^\circ/90_2^\circ]_s$	$d(5 \text{ cm}, 5 \text{ cm}) = 0.348 \text{ mm}$ $\epsilon_x(4.47 \text{ cm}, 6.97 \text{ cm}) = 0.368 \times 10^{-3}$ $\epsilon_y(3.03 \text{ cm}, 5.53 \text{ cm}) = 0.33 \times 10^{-3}$  $d(2.5 \text{ cm}, 7.5 \text{ cm}) = 0.125 \text{ mm}$ $d(5 \text{ cm}, 5 \text{ cm}) = 0.348 \text{ mm}$ $d(6.25 \text{ cm}, 6.25 \text{ cm}) = 0.275 \text{ mm}$	$E_1 = 123.67 \text{ GPa}$ (0.8%), $E_2 = 9.74 \text{ GPa}$ (1.46%) $G_{12} = 8.65 \text{ GPa}$ (0.12%), $G_{23} = 2.79 \text{ GPa}$ (20.2%) $\nu_{12} = 0.36$ (9%)  $E_1 = 124.7 \text{ GPa}$ (0.016%), $E_2 = 9.57 \text{ GPa}$ (0.33%) $G_{12} = 7.87 \text{ GPa}$ (8.9%), $G_{23} = 2.94 \text{ GPa}$ (26.7%) $\nu_{12} = 0.39$ (18.2%)

<sup>a</sup> The values in the parentheses denote coordinates.

<sup>b</sup> The values in the parentheses denote percentage difference between predicted and measured data.

Table 2  
Material constant identification of laminated composite plates subjected to a point load

Plate lay-up	Measured deformational parameters	Identified material constants
$[45_2^\circ/0_3^\circ/-45_2^\circ/0_3^\circ/45_2^\circ]_s$	$d(5 \text{ cm}, 5 \text{ cm})^a = 0.595 \text{ mm}$ $\epsilon_x(4.47 \text{ cm}, 8.03 \text{ cm}) = 3.5 \times 10^{-4}$ $\epsilon_y(3.03 \text{ cm}, 6.97 \text{ cm}) = 1.03 \times 10^{-4}$	$E_1 = 124.3 \text{ GPa}$ (0.3%) <sup>b</sup> , $E_2 = 9.8 \text{ GPa}$ (2.1%) $G_{12} = 8.7 \text{ GPa}$ (1.1%), $G_{23} = 2.13 \text{ GPa}$ (8.2%) $\nu_{12} = 0.3$ (9%)
$[0_2^\circ/90_2^\circ/0_2^\circ/90_2^\circ]_s$	$d(5 \text{ cm}, 5 \text{ cm}) = 1.63 \text{ mm}$ $\epsilon_x(4.47 \text{ cm}, 6.97 \text{ cm}) = 1.506 \times 10^{-3}$ $\epsilon_y(3.03 \text{ cm}, 5.53 \text{ cm}) = 1.89 \times 10^{-3}$  $d(2.5 \text{ cm}, 7.5 \text{ cm}) = 0.352 \text{ mm}$ $d(5 \text{ cm}, 5 \text{ cm}) = 1.63 \text{ mm}$ $d(6.25 \text{ cm}, 6.25 \text{ cm}) = 1.01 \text{ mm}$	$E_1 = 124.2 \text{ GPa}$ (0.41%), $E_2 = 9.8 \text{ GPa}$ (2.1%) $G_{12} = 8.2 \text{ GPa}$ (4.68%), $G_{23} = 2.3 \text{ GPa}$ (0.9%) $\nu_{12} = 0.325$ (1.5%)  $E_1 = 125.1 \text{ GPa}$ (0.34%), $E_2 = 9.82 \text{ GPa}$ (2.3%) $G_{12} = 7.89 \text{ GPa}$ (8.7%), $G_{23} = 2.13 \text{ GPa}$ (8.2%) $\nu_{12} = 0.31$ (6%)

<sup>a</sup> The values in the parentheses denote coordinates.

<sup>b</sup> The values in the parentheses denote percentage difference between predicted and measured data.

bounding techniques were not adopted in the material constants identification process, erroneous results would be obtained or there would be difficulties in making the solution converge.

## 6. Conclusion

A method for non-destructive evaluation of material constants of laminated composite structures was presented. Five material constants were identified via the minimization of the error function which was used to measure the differences between the theoretical and experimental deformations. A global minimization algorithm together with an appropriate normalization technique were used to determine the global minimum. A number of laminated composite plates subjected to different loading conditions were tested and three measured deformational parameters were used in the present method for material constants identification. The study showed that the present method could produce reasonably good results. It was also demonstrated that loading condition could affect the accuracies of the identified values of the material constants and the use of point load was better than the use of uniform load. The present method is general and can be extended to the material constants identification of other types of structures.

## Acknowledgements

This research work was supported by the National Science Council of the Republic of China under Grant No. NSC 87-2218-E009-021. Their support is gratefully appreciated.

## References

- [1] Lubin G. Handbook of composites. London: van Nostrand Reinhold; 1982.
- [2] Schwartz MM. Composite materials handbook. New York: McGraw-Hill; 1983.
- [3] Salkind MJ. Fatigue of composites, composite materials: testing and design, Second Conference. ASTM STP, vol. 497, 1972. p. 143–69.
- [4] Crema LB, Castellani A, Coppotelli G. Damage localization in composite material structures by using eigenvalue measurements. ASME Mater Design Technol 1995;PD-71:201–05.
- [5] Bar-Cohen Y. NDE of fiber reinforced composites – a review. Mater Eval 1986;44:446–54.
- [6] Erdmann-Jesnitzer F, Winkler T. Application of the holographic nondestructive testing method for evaluation of disbonding in sandwich plates. Adv Composite Mater 1980;ICCM3(2):1029–39.
- [7] Wells DR. NDT of sandwich structures by holographic interferometry. Mater Eval 1969;27:225–6.
- [8] Berman A, Nagy EJ. Improvement of a large analytical model using test data. AIAA J 1983;21:1168–73.
- [9] Kam TY, Lee TY. Crack size identification using an expanded mode method. Int J Solids Struct 1994;31:925–40.
- [10] Kam TY, Lee TY. Detection of cracks from modal test data. Int J Engrg Fract Mech 1992;42:381–7.
- [11] Kam TY, Lee TY. Identification of crack size via an energy approach. J Nondestr Eval 1994;13:1–11.
- [12] Kam TY, Liu CK. Stiffness identification of laminated composite shafts 1998;40:927–36.
- [13] Whitney JM. Shear correction factors for orthotropic laminates under static load. J Appl Mech 1973;40:302–4.
- [14] Kam TY, Chang RR. Finite element analysis of shear deformable laminated composite plates. J Energy Res Technol, ASME 1993;115:41–6.
- [15] Kam TY, Sher HF, Chao TN, Chang RR. Predictions of deflection and first-ply failure load of thin laminated composite plates via the finite element approach. J Solids Struct 1995 [to appear].
- [16] Snyman JA, Fatti LP. A multi-start global minimization algorithm with dynamic search trajectories. J Optim Theory Appl 1987;54:121–41.
- [17] Kam TY, Chang RR. Design of laminated composite plates for maximum axial buckling load and vibration frequency. J Comput Meth Appl Mech Engrg 1993;106:65–81.
- [18] ASTM standards and literature references for composite materials, 2nd ed., 1990.
- [19] Kam TY, Lai FM. Experimental and theoretical predictions of first-ply failure strength of laminated composite plates. J Solids Struct 1999;36:2379–95.



## Evaluating the soundness of bonding using shearography

Y.Y. Hung<sup>a,\*</sup>, W.D. Luo<sup>a</sup>, L. Lin<sup>a</sup>, H.M. Shang<sup>b</sup>

<sup>a</sup> Department of Mechanical Engineering, Oakland University, Rochester Hills, Michigan MI 48309, USA

<sup>b</sup> Department of Mechanical and Production Engineering, National University of Singapore, Kent Ridge, Singapore

### Abstract

Shearography is an optical measurement technique invented to overcome several limitations of holography. One distinct advantage is that it alleviates the stringent environmental stability demanded by holography, rendering the technique practical for industrial applications. There are two modes of shearography, one for measuring surface displacement and the other for measuring surface displacement derivatives. This paper discusses the underlying principle of shearography and its application in nondestructive testing, in particular, of laminated composite structures. In flaw characterization, a thin-plate model is used for back-calculating the shape, size and location of debonds. Shearographic nondestructive testing relies on measuring the response of a defect to stresses. Two practical types of stressing for revelation of debonds are described – static loading using vacuum stressing, and dynamic stressing by means of vibrational excitation. In vibrational stressing, both single frequency excitation and broadband excitation can be used. While vacuum stressing is limited to detecting debonds with closed boundaries, the vibrational excitation can be used for detecting debonds with closed as well as opened boundaries. A major drawback associated with the use of single excitation frequency is the need for vibrating the test object within an appropriate frequency range, as otherwise the test data obtained will not readily reveal the debonds. This paper also describes a new method that uses multiple frequency sweep (equivalent to broadband excitation) which fosters rapid detection and unambiguous assessment of the soundness of adhesive bonding. © 2000 Elsevier Science Ltd. All rights reserved.

**Keywords:** Shearography; Laminated composite structures

### 1. Introduction

Adhesive-bonded structures are found in nearly all sectors of the manufacturing and repair industries. A common defect that undermines the service life of these structures is the separation of adherends, known also as debond or delamination, caused by factors such as weak bonding during fabrication, and degradation in adhesion strength with time especially in thermal and humid environment. Many nondestructive testing techniques have thus been developed to detect and assess the embedded debonds, using radioactive devices (such as X-ray), acoustics (such as ultrasound), and optics (such as moiré, projection grating, holography and shearography). These optical methods, which were developed initially for surface profiling and displacement/strain measurements, are based on the general principle that, when load-increment is applied on the object, the reduction in local stiffness at its defective region will

manifest as an anomalously deformed area in comparison with a defect-free object. The characteristics of the anomalous area are also a function of the size and location of the defect, in addition to the manner in which the incremental load is applied. Optical nondestructive testing may therefore be perceived as the process of identification, in a methodical manner, of anomalous regions of response of the test object under external stimuli (e.g., load-increment), and back-calculation from the anomalous response, using the laws of mechanics, for quantifying the shape, size and location of defects.

The use of the projection grating method [1–4] requires projecting a reference grating of known distribution onto the object surface, and measuring the distribution of the distorted grating appearing on the object surface when viewed at an angle – subsequent use of the method of triangulation enables calculation of the deformed profile and, hence, identification and assessment of defective regions. The well-known moiré techniques [3,4] measure surface profiles from the low-frequency fringes that are reconstructed from the interference of the high-frequency reference grating and the high-frequency distorted grating that is diffracted by the

\* Corresponding author.

E-mail addresses: hung@oakland.edu (Y.Y. Hung), mpeshm@nu.edu.sg (H.M. Shang).

object surface. In double-exposure holography [1,4–9] and in double-exposure shearography [4,7,10–13], two successive recordings of the state of the object surface are made – one before, and another after, the application of an incremental load on the test object. The reconstructed fringe pattern represents contour lines of displacements (in holography) and displacement-derivatives (in shearography), thus enabling the detection of debonds and other forms of defects (e.g., cracks) from regions of perturbed fringes. The main advantage of shearography over other optical techniques is that environmental stability during testing need not be stringently enforced. Moreover, the ability of shearography to measure directly displacement-derivatives results in it being more sensitive than many other optical methods in detecting slight anomalous changes in the surface profile. With these advantages, shearography has offered itself as a viable NDT tool for use in the plant environment. The discussion in this paper, therefore, is focused on shearographic nondestructive evaluation of the soundness of bonding.

## 2. Basic principles of conventional shearography

The technique of shearography [10–13] requires the use of an image-shearing device placed in front of an ordinary camera so that two laterally displaced images of the object surface are focused at the image plane of the camera. For convenience, separation of the two images are taken to be along the reference  $x$ -axis by the amount  $\delta x$ . A point  $H$  on the overlapped images that is recorded with the camera may be construed as light wavefronts scattered from two points  $P(x, y, Z)$  and  $Q(x + \delta x, y, Z + \delta Z)$  on the object surface being brought to interfere at  $H$ . A small glass wedge [7,10–12] or a modified Michelson interferometer [13] is commonly used as the image-shearing device although other means [4,7] of achieving image-shearing have been found successful. Fig. 1(a) shows a simple optical layout for shearography – the illuminated object surface is focused on the image plane (the location of the photographic plate) of an image-shearing camera which comprises a glass wedge and an ordinary camera. It is worth noting that the sensitivity in fringe formation may be enhanced with the use of large wedge-angle, as the amount of image-shearing  $\delta x$  is proportional to the wedge-angle. By rotating the glass wedge about the axis of the camera lens, the direction of image-shearing may be varied at will in the  $xy$ -plane – this enables determination of displacement-gradients with respect to any direction specified by the direction of image-shearing.

The complex amplitude  $U_P$  and  $U_Q$  of light wavefronts propagated from the laser to the camera image plane via the two neighboring points  $P$  and  $Q$  on the

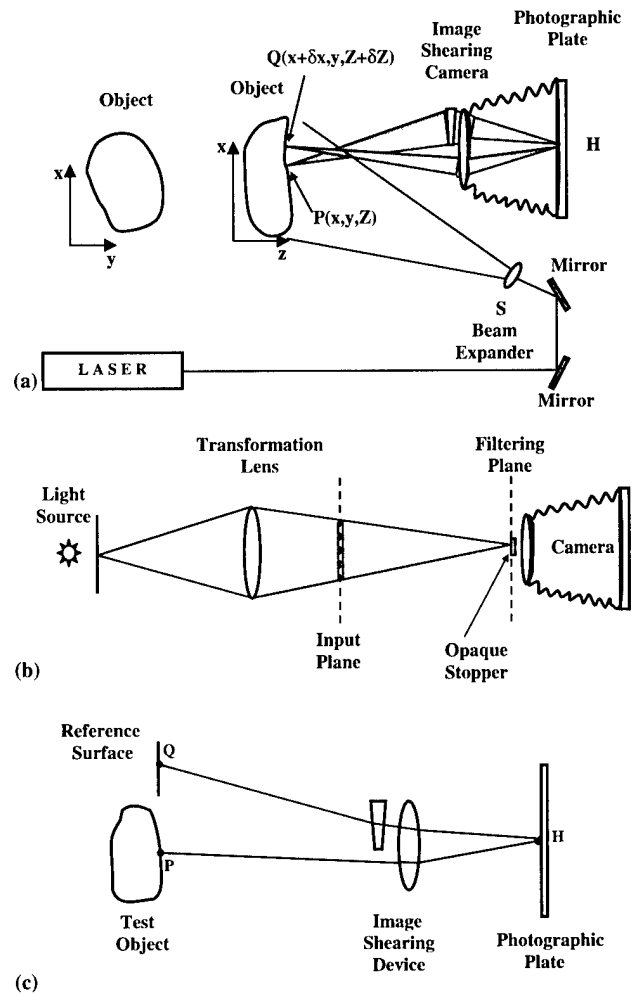


Fig. 1. Optical layout for film-based shearography. (a) Small image-shearing shearography. (b) Shearographic fringe reconstruction. (c) Large image-shearing shearography.

object surface are commonly described using the following expressions [1,3–13]:

$$\begin{aligned} U_P &= Ae^{i\phi_P}, \\ U_Q &= Ae^{i\phi_Q}, \end{aligned} \quad (1)$$

where  $A$  is the real amplitude of light wavefront and, for simplicity, it is assumed to be a constant value along the object surface;  $\phi$  is the phase related to the optical path length measured from the laser to the camera image plane via the object surface; and the subscripts  $P$  and  $Q$  represent the two neighboring points on the object surface.

When a high resolution photographic plate is placed at the image plane of the camera, the intensity distribution  $I_1$  on the object surface that is recorded is given by  $[(U_P + U_Q)(U_P^* + U_Q^*)]$ , where  $U^*$  denotes the complex conjugate of  $U$ . Thus, the following expression is obtained:

$$I_1 = 2A^2 [1 + \cos(\phi_P - \phi_Q)]. \quad (2)$$

The term  $(\phi_P - \phi_Q)$  may be regarded as the reference phase-difference, or the reference relative phase, between the two neighboring points  $P$  and  $Q$ . Denoting  $(\phi_P - \phi_Q)$  by the symbol  $\alpha$ , Eq. (2) may be rewritten as follows:

$$I_1 = 2A^2[1 + \cos \alpha]. \quad (3)$$

Slight deformation of the object surface changes the positions of points  $P$  and  $Q$  to the new positions  $P'$  and  $Q'$  (not shown in Fig. 1(a)), and, hence, causes a change in the respective optical path lengths. The corresponding phase-change  $\Delta$  gives rise to a new intensity distribution  $I_2$  to be recorded on the same photographic plate during the second exposure. Again, by assuming the real amplitude  $A$  of light wavefront (Eqs. (1)–(3)) to remain unchanged, the mathematical expression for  $I_2$  may be written in the same manner as Eq. (3), that is

$$I_2 = 2A^2[1 + \cos(\alpha + \Delta)]. \quad (4)$$

The resulting intensity distribution  $I_{\text{sum}}$  that is recorded on the same photographic film is the summation of  $I_1$  and  $I_2$ . The use of Eqs. (3) and (4) subsequently yields the following expression:

$$I_{\text{sum}} = 4A^2 + 4A^2 \left[ \cos \left( \alpha + \frac{\Delta}{2} \right) \right] \cos \frac{\Delta}{2}. \quad (5)$$

As seen in Eq. (5),  $I_{\text{sum}}$  comprises a high-dc term (denoted by  $4A^2$ ), a high-frequency varying term (containing the random phase  $\alpha$  and the deformation phase-change  $\Delta$ ) modulated by a low-frequency varying term that is related only to  $\Delta$ . The resulting fringe pattern is not readily visible, but it can be reconstructed using an optical high-pass Fourier filtering technique whose optical set-up [10–12] is illustrated in Fig. 1(b). With this simple optical arrangement, the following equation [14] is readily derived which shows that phase-fringes representing loci of constant phase-change  $\Delta$  may be reconstructed from a doubly exposed shearogram

$$I_{\text{recon}} = \kappa \cos^2 \left( \frac{\Delta}{2} \right), \quad (6)$$

where  $\kappa$  is a constant related to the set-up of the optical high-pass filter. A visible fringe-line [1,3–14] is formed when  $\Delta = N\pi$ , where  $N$  is the fringe order with  $N = \pm(0, 2, 4, 6, \dots)$  being attached to bright fringes and  $N = \pm(1, 3, 5, 7, \dots)$  being attached to dark fringes. The use of optical high-pass filtering gives a theoretical fringe visibility of 100%; but if fringe visibility is not a major concern, shearographic fringes are also reconstructed when the shearogram is viewed against a strong light source [14].

The magnitude of phase-change  $\Delta$  is related to the wavelength  $\lambda$  of the laser, the refractive index  $n$  of the media through which the laser beam propagates, and the geometrical path-change  $\delta L$  caused by surface deformation [1,3–13]. If  $n$  and  $\lambda$  are both held constant

when the two exposures are made, the phase-change  $\Delta$  is given by the following expression:

$$\Delta = \left( \frac{2\pi n}{\lambda} \right) \delta L, \quad (7)$$

where, with reference to Fig. 1(a), the geometrical path-change  $\delta L$ , which corresponds to the point  $P$  being shifted to  $P'$ , and the point  $Q$  to  $Q'$ , is given by the following expression:

$$\delta L = [(SQ' + Q'H) - (SQ + QH)] - [(SP' + P'H) - (SP + PH)]. \quad (8)$$

The amount of image-shearing  $\delta x$  is governed by the magnitude of the wedge-angle. The use of small wedge-angle results in small image-shearing (Fig. 1(a)), so that Eq. (8) prevails – this forms the basis of conventional shearography [10–12] in which the following expression related to displacement-derivatives is obtained:

$$\Delta = -\frac{2\pi}{\lambda} \left( \sin \theta \frac{\partial u}{\partial x} + \sin \beta \frac{\partial v}{\partial x} + (1 + \cos \theta) \frac{\partial w}{\partial x} \right) \delta x \equiv N_x \pi, \quad (9)$$

where  $\lambda$  is the wavelength of the laser used;  $u$ ,  $v$ , and  $w$  the displacement components along the reference  $x$ -,  $y$ -, and  $z$ -axis, respectively;  $\theta$  and  $\beta$  the angles of illumination with respect to the  $yz$ -plane and the  $xz$ -plane;  $\delta x$  the amount of image-shearing that is directed along the reference  $x$ -axis; and  $N_x$  is the fringe order with even integers denoting bright fringes and odd integers denoting dark fringes. Suppose image-shearing is directed along an arbitrary  $\zeta$ -axis by the amount  $\delta \zeta$ , the phase-change  $\Delta_\zeta$  that is equivalent to Eq. (9) is now given by the following expression:

$$\Delta_\zeta = -\frac{2\pi}{\lambda} \left( \sin \theta \frac{\partial u}{\partial \zeta} + \sin \beta \frac{\partial v}{\partial \zeta} + (1 + \cos \theta) \frac{\partial w}{\partial \zeta} \right) \delta \zeta \equiv N_\zeta \pi, \quad (10)$$

where  $N_\zeta$  is the fringe order of the resulting fringe pattern.

The use of large wedge-angle, on the other hand, gives rise to large image-shearing so that, with reference to Fig. 1(c), the point  $Q$  lies on a reference surface external to the test object, or on a point within the object surface where deformation there is negligible. The geometrical path-change  $\delta L$  is now caused by point  $P$  being shifted to  $P'$  and it is given by the following expression:

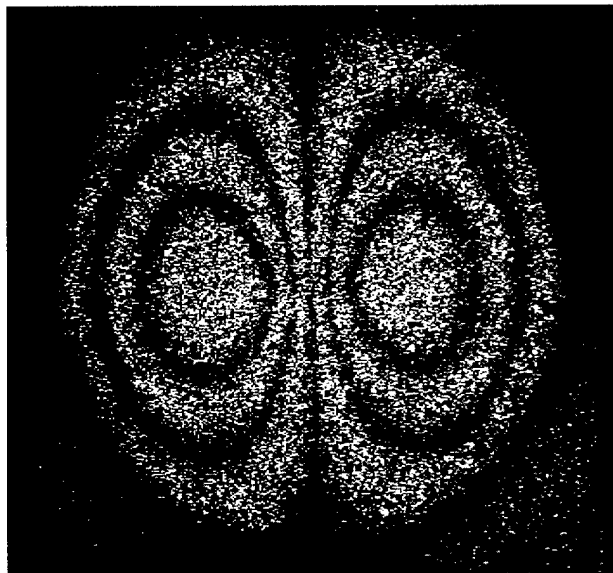
$$\delta L = (SP' + P'H) - (SP + PH). \quad (11)$$

It is noted that Eq. (11) also represents the geometrical path-change  $\delta L$  in conventional holography [1,4–9] that yields the following displacement-related expression:

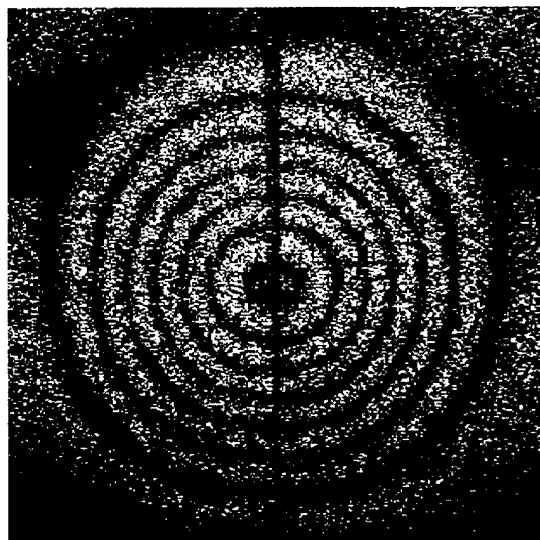
$$\Delta = -\frac{2\pi}{\lambda} [(\sin \theta)u + (\sin \beta)v + (1 + \cos \theta)w] \equiv N\pi, \quad (12)$$

where  $N$  is the fringe order of the resulting holographic fringe pattern.

Eqs. (9) and (12) have thus led to the suggestion [15] that shearography, in broad sense, may be perceived as an optical technique that encompasses both conventional shearography and conventional holography, depending on the amount of image-shearing used during testing. As an illustration, a circular plate with fully clamped boundary is subjected to central point load-increment between two exposures. With the use of small image-shearing, Fig. 2(a) shows the typical butterfly-shaped fringes that depict loci of constant displacement-gradients (shearographic fringes). On the other hand, when large image-shearing is used, Fig. 2(b) shows



(a)



(b)

Fig. 2. Typical fringe pattern for a centrally point-loaded circular plate. (a) Formation of butterfly-shaped shearographic fringes due to small image-shearing. (b) Formation of concentric circular holographic fringes due to large image-shearing.

concentric circular fringes that represent loci of constant out-of-plane displacements (holographic fringes).

### 3. Basic principles of digital shearography

With the rapid advancement of computer technology and image-processing techniques, digital shearography was developed using either a Michelson shearing interferometer [4,7,13,16,17] or a birefringent crystal [15,18–20] as the image-shearing device. The use of these devices is generally confined to small-image shearing that is equivalent to conventional shearography. Nonetheless, as shown in Fig. 2(b) as well as results reported earlier [15,18], the use of a birefringent prism with large image-shearing also produces displacement-related holographic fringes. In Fig. 3 is shown a typical layout for small image-shearing digital shearography using a birefringent prism. The prism splits an incoming laser beam into two beams that are orthogonally plane-polarized, hence the formation of two overlapping images of the test object. The degree of overlap depends on the amount of image-shearing provided by the birefringent prism. Light wavefront scattered from a point on the overlapped region may therefore be viewed as the superposition of light wavefronts scattered from two points  $P$  and  $Q$  on the object surface. The additional use of a polarizer in front of the video camera is to ensure interference of the two light wavefronts. Where need arises, a phase-shifter may be placed between the test object and the birefringent prism in order to facilitate multiple-frame phase-shifting [15,18–20].

The intensity distributions recorded using the digital camera system during the first and second exposures are expressed by Eqs. (3) and (4). Instead of image-addition that takes place in film-based shearography, image-

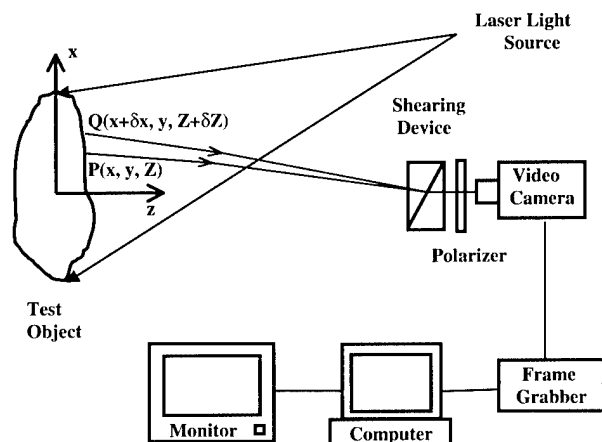


Fig. 3. Optical layout for digital shearography using a birefringent prism.

subtraction is generally performed in digital shearography [15,18–20] that leads to the following expression:

$$I_{\text{diff}} = \left| -4A^2 \left[ \sin \left( \alpha + \frac{\Delta}{2} \right) \right] \sin \frac{\Delta}{2} \right|. \quad (13)$$

In Eq. (13), numerical values of  $I_{\text{diff}}$  are chosen as intensities and quantified digitally in terms of gray level, which, for 8-bit digitization hardware, ranges from 0 (darkest) to 255 (brightest). Although Eq. (13) comprises a high-frequency varying term (containing  $\alpha$  and  $\Delta$ ) modulated by a low-frequency varying term (containing only  $\Delta$ ), visible fringes are displayed on the computer monitor, with the deformation phase-change  $\Delta$  defined by Eq. (9) for small image-shearing and by Eq. (12) for large image-shearing.

Unlike film-based shearography, which relies on visible fringes for quantitative interpretation of test data, digital shearography extracts deformation-related phases  $\Delta$  directly from the measured intensities using computer programs. The measured phases are then related to deformation for subsequent interpretation. The multiple-frame phase-shifting (such as four-frame phase-shifting) and Fast Fourier Transform methods are commonly used for extracting and unwrapping the phases [2,13,15–20]. A simple approach [2,15] is, instead of using Eq. (13) to directly calculate the phase-change  $\Delta$ , Eqs. (3) and (4) are used to determine separately the phases  $\alpha$  and  $(\alpha + \Delta)$  using multiple-frame phase-shifting technique or Fast Fourier Transform technique; the difference of the two determined phases subsequently gives the values of  $\Delta$ .

#### 4. Shearographic nondestructive testing

Shearographic nondestructive testing is the process of identification and quantitative interpretation of fringe-phase anomalies appearing on the illuminated surface of the test object when it is subjected to load-increment between exposures. The incremental load is generally either static or vibrational [1,4–9,12,19–23]. With static loading, the resulting fringe pattern is described by Eq. (9) for small image-shearing or by Eq. (12) for large image-shearing.

When the test object is subjected to steady-state out-of-plane vibration with amplitude variation given by  $z(x, t) = Z(x) \sin \omega t$ , the recording device, which is either film-based (Fig. 1) or digital-based (Fig. 3), integrates light intensity diffracted from the vibrating object with an integration time exceeding several vibrational periods. For near normal illumination and recording, the resulting intensity distribution is related to zero-order Bessel function of the first kind so that nodal points appear as bright spots [1,4–9,21–23] on the reconstructed fringe pattern. With small image-shearing, the nodal point corresponds to  $\partial Z(x)/\partial x = 0$ , but with large

image-shearing, the nodal point corresponds to  $Z(x) = 0$ . This method of recording fringe patterns is commonly known as time-average, or time-integrated, holography and shearography [1,4–9,21–23]. As the scope of shearography also covers holography [15], this technique may conveniently be named as Time-Integrated Shearography. Whilst the principle of time-integrated shearography will be presented later in this paper, the following section illustrates the use of static loading for the detection and quantitative assessment of closed-boundary debonds in laminates.

#### 5. Detecting and assessing debonds in laminates

Debonds with closed boundaries are readily revealed when the load-increment applied between exposures is in the form of heating, vacuum stressing or single frequency vibrational excitation [1,4–9]. With vacuum stressing, Fig. 4(a) shows typical small image-shearing

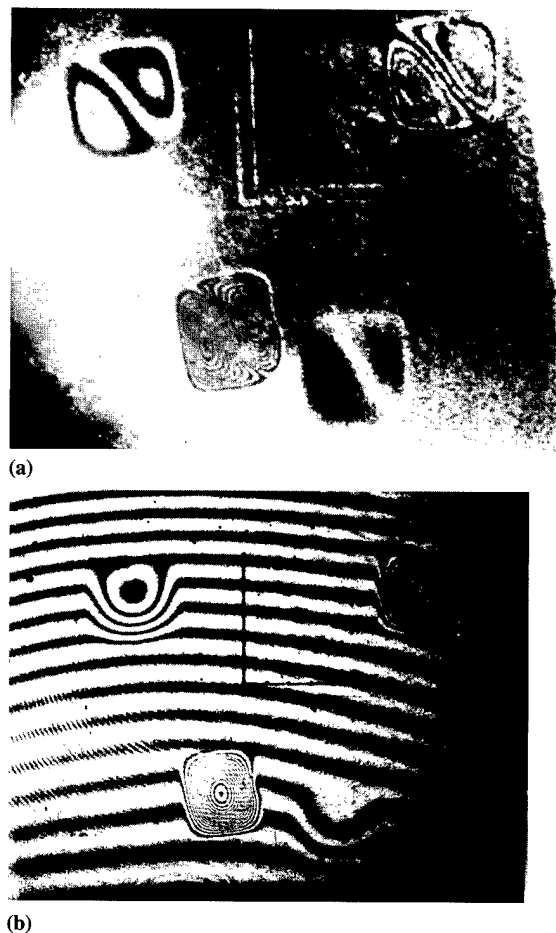


Fig. 4. Typical perturbed fringe patterns of a layered panel containing debonds embedded at various depths. (a) Shearographic fringes due to small image-shearing. (b) Holographic fringes due to large image-shearing.

shearographic fringe patterns of a layered plate structure containing square debonds embedded at different depths from the illuminated surface; and Fig. 4(b) shows the corresponding holographic (equivalent to large image-shearing) fringe patterns. It is observed that (i) the shape of the boundary of perturbed fringes is similar to that of the debond; (ii) the perturbed fringe-density decreases with increasing depth of debond; and (iii) with nonresilient adhesive layers, the boundary of perturbed fringes is nearly of the same size as the debond.

For quantitative assessment of the shape, size and depth of debonds in laminates bonded using nonresilient or brittle adhesives, a thin-plate model [24–26] based on these observations was thus developed. In this model, a fully clamped plate, whose boundary and size are identical with those of the region of perturbed fringes and whose thickness is equal to the depth of debond, is subjected to uniform lateral pressure-increment of magnitude equal to the applied vacuum pressure-increment. Invoking elastic plate-bending theory, the actual depth of debond may be back-calculated from the measured debond size (equal to the size of the anomalous fringe area) and the fringe distribution appearing within the debonded region. For adhesives exhibiting pronounced elastic behavior, this simple model was subsequently modified [27] to account for the over-estimated debond size due to the resilience of the adhesive layers, which may be assumed as of Winkler type. In performing quantitative assessment of defect geometry, degradation with time and service environment of the bonding agents frequently makes it extremely difficult for the analyst to define accurately the boundary conditions of the entire test structure as well as those of the defective region. Thus, the foundation modulus at the boundary of debond, and the actual size and depth of debond are parameters used in the iteration algorithm for back-calculation; the minimum discrepancy between theoretical and experimental fringe distribution corresponds to the actual debond size and depth. The main advantage of this modified thin-plate model therefore lies in not having to pre-determine the foundation modulus of the adhesive layers, or the edge conditions, before back-calculation is made – a simple iteration procedure rapidly yields the size and depth of the debond with good accuracy.

The fringes for fully overlapping identical debonds are visually similar to those for single debonds, as are shown in Fig. 5, where defects in the form of a single debond (Flaw #1), two fully overlapping identical debonds (Flaw #2), and two partially overlapping identical debonds (Flaw #3) are embedded [28]. By recording the fringe patterns on both sides of the test plate (Fig. 5(a) and (b)) and using the foregoing thin-plate model, it is possible to ascertain the presence of only one debond, or the presence of two or multiple debonds that are fully overlapped. Thus, the size and depths of two fully

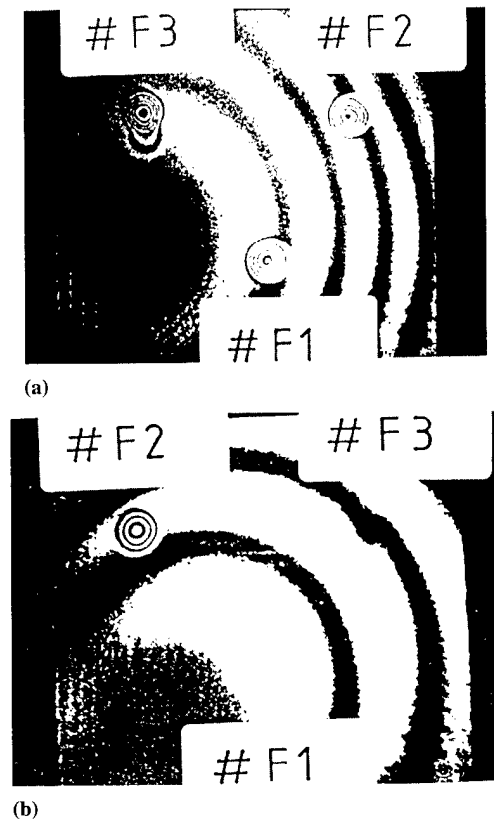


Fig. 5. Typical holographic fringe patterns [28] (equivalent to large image-shearing) revealing the presence of a single debond (Flaw #1), two fully overlapping identical debonds (Flaw #2), and two partially overlapping identical debonds (Flaw #3) in a laminated plate tested using vacuum stressing. (a) Fringe pattern on one side of the test plate. (b) Fringe pattern on the opposite side of the same test plate.

overlapping debonds, as well as those of two partially overlapping debonds, may also be accurately back-calculated [28] using the thin-plate model [24–26] or the modified model [27] that was developed initially for single debonds.

In Figs. 4(b) and 5 are seen thick fringes sparsely spreading across the entire plate surface, together with concentrated dense fringes in the form of near-concentric circles at the locations of the debonds. The sparse fringes, which are attributed to slight deflection of the glass cover of the vacuum chamber during vacuum stressing, therefore, act as carrier to the dense circular fringes, resulting in the formation of a distinct C-shaped fringe pattern. By introducing a set of linear holographic carrier fringes onto the thin-plate model, the theoretical fringe pattern represented by the family of solid lines in Fig. 6 is of C-shape [29] which is similar to the experimental fringe patterns in Figs. 4(b) and 5. It is noted that, in Fig. 6, the dotted circle represents the circular debond, whose center coincides with the origin of the reference axes that have been normalized by the radius  $R$  of debond. In Fig. 5 is seen dense anomalous fringes for Flaw #2; thus the effect of the sparse carrier is not

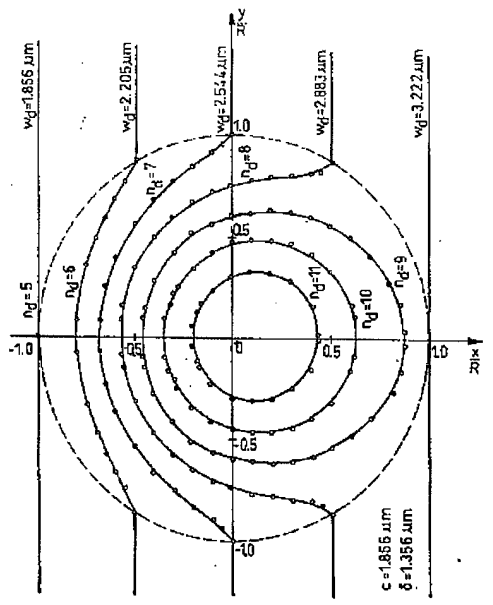


Fig. 6. Theoretical holographic fringe pattern [29] illustrating the effect of vertical carrier fringes on the circular deformation fringes.

prominent enough for opening-up the dense fringes to attain C-shaped. With a fringe pattern including the effect of carrier, a simple method was developed to back-calculate the geometry and depth of debonds [29].

In Fig. 5, the peculiar shape of the fringes (resembling the numeric 8) corresponding to two partially overlapping debonds (Flaw #3) may easily be explained in the light of the thin-plate model [28] that is illustrated schematically in Fig. 7(a). Upon eliminating the effect of the carrier fringes and ignoring localized effects at the boundary of the debonded area, the resulting deflection of two equivalent plates (with their respective thickness equal to the debond depths  $h_1$  and  $h_2$ ) that are partially overlapping is calculated using this model. As shown in Fig. 7(b), the two dotted circles represent the two overlapping circular debonds and the solid curves represent the theoretical fringes that depict loci of constant out-of-plane deflection. It is readily seen that the theoretical fringe pattern is similar to the experimental fringe pattern for Flaw #3 in Fig. 5. Hence, the geometry and depths of two partially overlapping debonds may also be back-calculated [28].

## 6. Digital time-integrated shearography

Initially, time-integrated shearography was developed using photographic films as the recording media: nodal points thus appear as bright spots on the reconstructed fringe pattern [1,4–9,21,22]. With rapid advancements in computer technology and image processing techniques, digital time-integrated shearography is now readily

achieved [23]. The optical set-up and the underlying principle of this technique are similar to those of conventional digital shearography (Fig. 3). During the first exposure when the test object is stationary, the intensity distribution recorded using the CCD camera is expressed by Eq. (3). The second recording is made at any time  $t$  when the object is subjected to periodic excitation  $z(x, t) = Z(x) \sin \omega t$ , where  $Z(x)$  denotes the amplitude and  $\omega$  denotes the excitation frequency. With small image-shearing, the corresponding intensity distribution  $I_t$  recorded using the digital camera is given by the following equation:

$$I_t = 2A^2 \left\{ 1 + \cos \left[ \alpha - \frac{4\pi}{\lambda} \frac{\partial Z(x)}{\partial x} \delta x \sin \omega t \right] \right\}, \quad (14)$$

where  $\lambda$  denotes the wavelength of the laser; and  $\delta x$  denotes the amount of image-shearing along the reference  $x$ -axis.

Recording the response of the test object over a period of time  $T$  that exceeds several vibrational periods, the time average of intensity over  $T$  may be derived to be

$$\begin{aligned} I_T &= \frac{1}{T} \int_0^T I_t dt \\ &= 2A^2 \left\{ 1 + (\cos \alpha) J_0 \left[ \frac{4\pi}{\lambda} \frac{\partial Z(x)}{\partial x} \delta x \right] \right\}, \end{aligned} \quad (15)$$

where

$$J_0 \left[ \frac{4\pi}{\lambda} \frac{\partial Z(x)}{\partial x} \delta x \right]$$

is known as the zero-order Bessel function of the first kind.

As in digital shearography, subtracting Eq. (3) from Eq. (15) yields the following expression:

$$I_T - I_1 = 2A^2 \cos \alpha \left\{ J_0 \left[ \frac{4\pi}{\lambda} \frac{\partial Z(x)}{\partial x} \delta x \right] - 1 \right\} \equiv \delta I_T. \quad (16)$$

Thus, corresponding to  $\partial Z(x)/\partial x = 0$ , a dark area (that is,  $\delta I_T = 0$  or zero gray level) indicating the nodal point will appear on the  $\delta I_T$ -map. With large image-shearing, which is equivalent to conventional time-average digital holography, the  $\delta I_T$ -map obtained using image-subtraction is still described by Eq. (16) except that the Bessel function is now written as

$$J_0 \left[ \frac{4\pi}{\lambda} Z(x) \right].$$

Again, the darkest spot on the  $\delta I_T$ -map represents the nodal point with  $Z(x) = 0$ .

As an illustration, Fig. 8 shows a wide flat plate that is adhesive-bonded (represented by the shaded region along the horizontal direction) to a rigid C-channel. At the center of the C-channel, an area of debond (non-shaded region along the horizontal direction) is deliberately created. The optical arrangement for conducting this test resembles that shown in Fig. 3, except that a

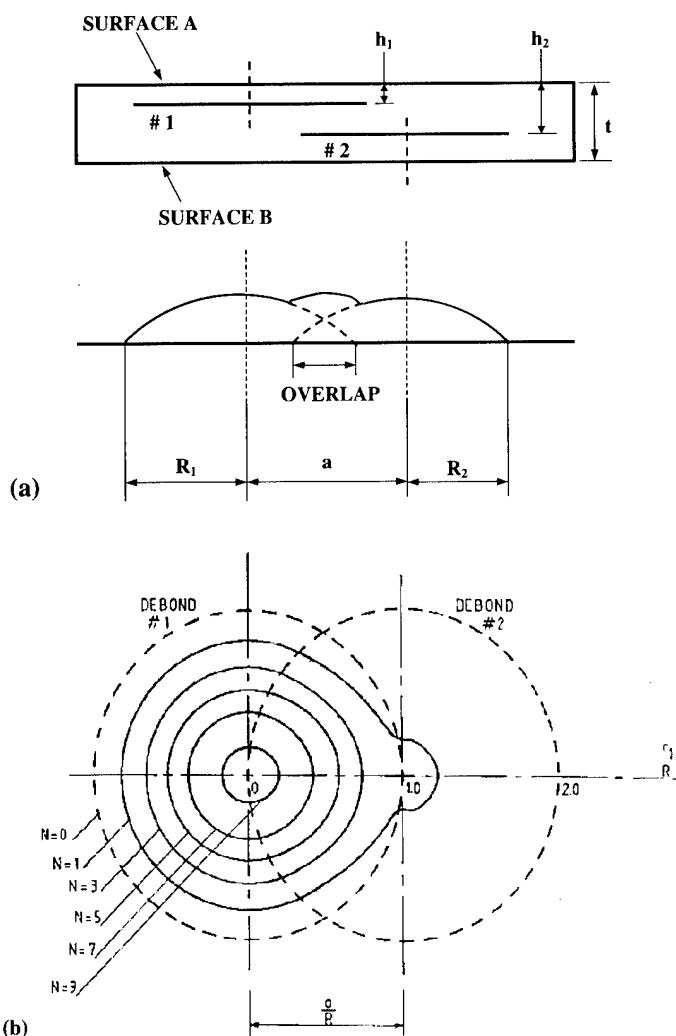


Fig. 7. Quantitative assessment of overlapping debonds [28]. (a) A simple model for two partially overlapping identical circular debonds. (b) Comparison between theoretical fringe pattern and experimental fringe pattern for Flaw #3 in Fig. 5.

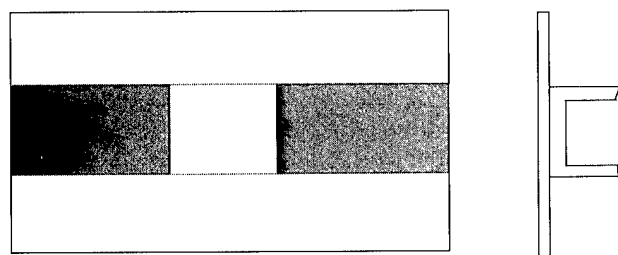


Fig. 8. Shearographic NDT of a flat wide plate adhesive-bonded to a rigid C-channel. The nonshaded area along the central region of the C-channel denotes an artificial debond.

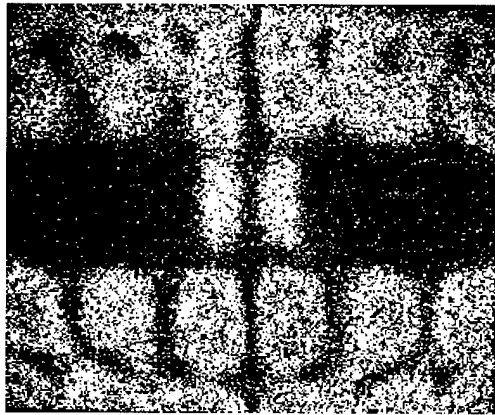
high-powered loudspeaker is placed behind the test plate. The desired frequency of excitation is achieved using a computer-controlled wavefront generator and amplifier. As shown in Fig. 9(a) and (b), the white patch on the  $\delta I_T$ -map along the central region of the C-channel readily reveals the debonded area when the structure

is tested at 4.13 and at 8.68 kHz. However, as shown in Fig. 9(c), when the frequency of 7.48 kHz is used, the debonded area is not revealed since a dark patch appears along the entire C-channel on the  $\delta I_T$ -map. Thus, a major drawback of using single excitation frequency lies with the difficulty in pre-selecting the appropriate excitation frequency that will reveal the debonded area. To alleviate this drawback, it is necessary to test the structure within a range of excitation frequencies. This subsequently leads to the development of time-integrated shearography combined with multiple frequency sweep, which is described as follows:

## 7. Digital time-integrated shearography with multiple frequency sweep

The foregoing equations (e.g., Eq. (16)) for time-integrated shearography were derived using a single exci-

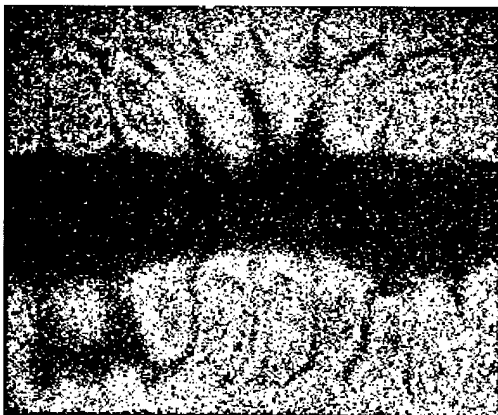




(a)



(b)



(c)

Fig. 9. Detection of debond using small image-shearing Time-Integrated Shearography with single excitation frequency. (a) The debond is revealed when excited at 4.13 kHz. (b) The debond is revealed when excited at 8.68 kHz. (c) The debond is not revealed when excited at 7.48 kHz.

tation frequency  $\omega$ . In examining the soundness of bonded layers using multiple-frequency sweep with frequencies  $\omega_a, \omega_b, \omega_c, \dots, \omega_n$ , it would be desirable if the improperly bonded area appears as an anomalous patch on the final  $\delta I_T$ -map. For this purpose, a computer al-

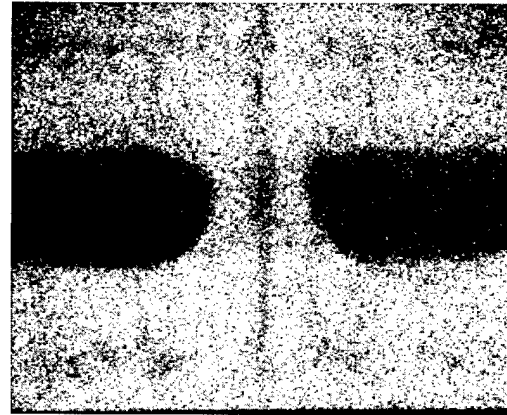


Fig. 10. Detection of debond using small image-shearing Time-Integrated Shearography with multiple frequency sweep (2.51–8.68 kHz).

gorithm is written which takes into account of the individual intensity distributions (Eq. (16)) for  $\omega_a, \omega_b, \omega_c, \dots, \omega_n$ , so that the resulting intensity distribution on the  $\delta I_T$ -map will correspond to the maximum gray level over the test frequency-spectrum. Thus, a properly bonded area will manifest as a dark patch whilst an unsound area of bonding, or debond, will appear as white.

As an illustration of this technique, the same bonded structure in Fig. 8 is tested with a multiple-frequency sweep ranging from 2.51 to 8.68 kHz. The resulting white patch in Fig. 10 at the central region along the C-channel readily reveals the debonded area; elsewhere along the C-channel is shown dark, indicating sound bonding.

## 8. Concluding remarks

Shearography was developed initially for direct measurement of surface strains but was later extended to other applications such as flaw detection. Being whole-field and noncontacting, this technique is particularly useful for revealing debonds in composite structures. As a separate reference beam is not needed in shearography, the requirement for environmental stability during testing is less stringent than many other optical techniques such as moiré and holography. Whilst conventional shearography uses a small image-shearing device to give displacement-gradients on the object surface, deliberate use of a large image-shearing device enables direct measurement of surface displacements. Thus, shearography may also be perceived as an optical technique that measures both surface displacements and surface strains, depending on the amount of image-shearing used in the set-up.

Shearographic flaw detection requires the use of suitable stressing techniques that readily reveals defects.

Vacuum stressing and steady-state vibration are effective for detecting debonds with closed-boundaries. Interpretation of test results with reference to mechanics equations further facilitates back-calculation for the geometry and location of the debonds that are detected. If steady-state vibration is applied to the test object, the use of single excitation frequency may give erroneous conclusion on the soundness of the bonding unless an appropriate range of excitation frequency is selected. This paper also demonstrates that the use of multiple frequency sweep alleviates the difficulties encountered in using single excitation frequencies.

### Acknowledgements

The research reported in this paper was supported by a National Science Foundation grant (Grant No. CMS9601778). The support of Dr. Ken Chong is appreciated.

### References

- [1] Vest CM. Holographic interferometry. New York: Wiley; 1979.
- [2] Hung YY, Lin L, Shang HM, Park BG. Practical 3D computer vision techniques for full-field surface measurement. *Opt Engng* 2000;139(1):143–9.
- [3] Post D, Han B, Ifju P. High sensitivity moiré – experimental analysis for mechanics and materials. Germany: Springer; 1994.
- [4] Rastogi PK. Optical measurement techniques and applications. USA: Artech House; 1997.
- [5] Collier RJ, Burckhardt CB, Lin LH. Optical holography. New York: Academic Press; 1971.
- [6] Erf RK. Holographic nondestructive testing. New York: Academic Press; 1974.
- [7] Erf RK. Speckle metrology. New York: Academic Press; 1978.
- [8] Ostrovsky YI, Butusov MM, Ostrovskaya GV. Interferometry by holography. New York: Springer; 1980.
- [9] Jones R, Wykes C. Holographic and speckle interferometry: a discussion Of the theory, practice and application of the techniques, second ed. UK: Cambridge University; 1989.
- [10] Hung YY. A speckle-shearing interferometer. *Opt Commun* 1974;11:132–5.
- [11] Hung YY, Liang CY. Image-shearing camera for direct measurement of surface strains. *Appl Opt* 1979;10(7):1046–50.
- [12] Hung YY. Shearography: a new optical method for strain measurement and nondestructive testing. *Opt Engng* 1982;21(3):391–5.
- [13] Leendertz JA, Butters JN. An image-shearing speckle pattern interferometer for measuring bending moments. *J Phys E: Sci Instrum* 1973;6:1107–10.
- [14] Toh SL, Tay CJ, Shang HM, Lin QY. Analysis of shearogram reconstruction. *Appl Opt* 1993;32(25):4929–33.
- [15] Shang HM, Hung YY, Luo WD, Chen F. Surface profiling using shearography. *Opt Engng* 2000;139(1):23–31.
- [16] Huang JR, Ford HD, Tatam RP. Slope measurement by two-wavelength electronic shearography. *Opt Lasers Engng* 1997;27(3):321–33.
- [17] Rastogi PK. Determination of surface strains by speckle shear photography. *Opt Lasers Engng* 1998;29(2–3):103–16.
- [18] Hung MYY, Long KW, Wang JQ. Measurement of residual stress by phase shift shearography. *Opt Lasers Engng* 1997;27(1):61–73.
- [19] Hung YY. Computerized shearography and its applications for nondestructive evaluation of composites. Society of Experimental Mechanics; 1998 [a chapter in manual on experimental techniques for testing of composites].
- [20] Hung YY, Luo WD, Lin L, Shang HM. Shearography for rapid nondestructive evaluation of bonded composite structures. SAE Technical Paper 1999-01-0947, SAE International Congress and Exposition, Detroit, Michigan; 1–4 March 1999.
- [21] Hovanesian JD, Hung YY, Durelli AJ. New optical method to determine vibration induced strains with variable sensitivity after recording. Proceedings of the Conference on Experimental Stress Analysis, Smolenice, Czechoslovakia; 16–18 October 1978.
- [22] Toh SL, Shang HM, Chau FS, Tay CJ. Flaw detection in composites using time-average shearography. *Opt Laser Technol* 1991;23(1):25–30.
- [23] Hung YY, Griffen CT. Digital Shearography versus TV-Holography for Vibration Measurement. In: Proceedings of the 15th Biennial Conference on Mechanical Vibration and Noise, 1995 ASME Design Engineering Technical Conferences, vol. 3, Part C, Boston, Massachusetts; 17–20 September 1995. p. 1461–470.
- [24] Shang HM, Chau FS, Tay CJ, Toh SL. Estimating the depth and width of arbitrarily oriented disbands in laminates using shearography. *J Nondestruct Eval* 1990;9(1):19–26.
- [25] Shang HM, Toh SL, Chau FS, Shim VPW, Tay CJ. Locating and sizing disbands in glassfibre-reinforced plastic plates using shearography. *ASME Trans J Engng Mater Technol* 1991;113:99–103.
- [26] Shang HM, Soh CC, Chau FS. The use of carrier fringes in shearography for locating and sizing debonds in GRP plates. *Compos Engng* 1991;1(3):157–65.
- [27] Shang HM, Tham LM, Chau FS. Shearographic and holographic assessment of defective laminates with bond-lines of different elasticities. *ASME Trans J Engng Mater Technol* 1995;117(3):322–9.
- [28] Shang HM, Toh SL, Chau FS, Tay CJ, Tay TE. Holographic inspection of laminated plates containing two fully overlapping identical debonds. *J Nondestruct Eval* 1991;10(1):7–17.
- [29] Shang HM, Lim EM, Lim KB. Estimation of size and depth of debonds in laminates from holographic interferometry. *ASME Trans J Engng Mater Technol* 1992;114:127–31.

## Combined numerical–experimental model for the identification of mechanical properties of laminated structures

A.L. Araújo<sup>a</sup>, C.M. Mota Soares<sup>b,\*</sup>, M.J. Moreira de Freitas<sup>c</sup>, P. Pedersen<sup>d</sup>,  
J. Herskovits<sup>e</sup>

<sup>a</sup> ESTIG, Campus de Sta., Instituto Politécnico de Bragança, Apolónia, Apartado 134, 5301-857 Bragança, Portugal

<sup>b</sup> IDMEC, Instituto de Engenharia Mecânica, I.S.T., Av. Rovisco Pais, 1049-001 Lisboa, Portugal

<sup>c</sup> ICEMS-UME, Dept. Eng. Mecânica, I.S.T., Av. Rovisco Pais, 1049-001 Lisboa, Portugal

<sup>d</sup> Department of Solid Mechanics, Building 404, Technical University of Denmark, DK-2800 Lyngby, Denmark

<sup>e</sup> COPPE, Universidade Federal do Rio de Janeiro, Caixa Postal 68503, 21945-970 Rio de Janeiro, Brazil

### Abstract

A combined numerical–experimental method for the identification of six elastic material modulus of generally thick composite plates is proposed in this paper. This technique can be used in composite plates made of different materials and with general stacking sequences. It makes use of experimental plate response data, corresponding numerical predictions and optimisation techniques. The plate response is a set of natural frequencies of flexural vibration. The numerical model is based on the finite element method using a higher-order displacement field. The model is applied to the identification of the elastic modulus of the plate specimen through optimisation techniques, using analytical sensitivities. The validity, efficiency and potentiality of the proposed technique is discussed through test cases. © 2000 Elsevier Science Ltd. All rights reserved.

**Keywords:** Identification; Mechanical properties; Numerical–experimental vibrations; Sensitivity analysis; Optimisation

### 1. Introduction

The dynamic free vibration behaviour of a structure made of anisotropic materials depends on its geometry, density, boundary conditions and elastic constants. Hence, a non-destructive method for the determination of the elastic constants of the materials that make up the structure can be developed. The method combines experimental results of a free vibration test with a numerical model capable of predicting the dynamic free vibration behaviour of the structure and makes use of optimisation techniques.

Thus, it becomes necessary to use an error measure that expresses the difference between experimental and numerical eigenvalues. This error measure is then minimised with respect to the elastic modulus of the different materials.

This work is a generalisation of the work presented by Mota Soares and coworkers (see e.g., [1,2]) using the

Mindlin plate theory along with a finite element model, and Araújo et al. [3] using a higher-order displacement finite element model. It has the innovative aspect of contemplating identification of mechanical parameters of specimens having layers made up of several materials and general stacking sequences. It is closely related to the developments presented by Pedersen [4] for thin plates using the classical plate theory and Frederiksen [5] for thick plates using a higher-order theory associated to a numerical model based on the Rayleigh–Ritz approach for symmetric lay-ups and specimens made of a single material. Other research works that also use the Rayleigh–Ritz method along with the classical plate theory were presented by Wilde and Sol [6], Sol [7] and Wilde [8], using Bayesian estimation instead of optimisation techniques for symmetric single material laminates. Lai and Ip [9] presented a method, using the Kirchhoff plate theory, which takes into account both the confidence associated with mathematical modelling and parameter estimates. This last technique has been validated satisfactorily on symmetric single material laminates. In fact, in more recent works, priority is given to assessment of uncertainties. In [10], these questions are addressed based on statistics.

\*Corresponding author. Tel.: +351-21841-7455; fax: +351-21841-7915.

E-mail address: cmmsoares@alfa.ist.utl.pt (C.M. Mota Soares).

More recently, a method based on response surfaces has been used by Rikards and coworkers (see e.g., [11,12]) and Bledzki et al. [13]. This technique commonly called planning of experiments was used successfully to identify elastic properties in unidirectional laminates.

The use of model updating techniques for the identification of mechanical properties of laminates was also presented by Cunha and Piranda [14], applied to sandwich composite structures.

An overview of different approaches on combined numerical-experimental identification methods with the goal of obtaining material stiffness for composite structures, based on eigenfrequencies and optimisation, is carried out by Pedersen [15].

## 2. Numerical model

The eigenvalue problem and the sensitivity analysis are carried out using a third-order shear deformation theory whose pioneering works are described in [16,17] and has been applied to discrete finite element models by Mallikarjuna and Kant [18], among others. Full details regarding the model development and implementation for dynamics can be found in [19,20].

Fig. 1 shows a rectangular plate of constant thickness  $h$  and plane dimensions  $a$  and  $b$ . A Cartesian coordinate system  $(x, y, z)$  is located at the middle plane as shown.

The assumed displacement field is a third-order expansion in the thickness coordinate for the in-plane displacements and a constant transverse displacement:

$$\begin{aligned} u(x, y, z, t) &= u_0(x, y, t) + z\theta_x(x, y, t) \\ &\quad + z^2u_0^*(x, y, t) + z^3\theta_x^*(x, y, t), \\ v(x, y, z, t) &= v_0(x, y, t) + z\theta_y(x, y, t) \\ &\quad + z^2v_0^*(x, y, t) + z^3\theta_y^*(x, y, t), \\ w(x, y, z, t) &= w_0(x, y, t), \end{aligned} \quad (1)$$

where  $u_0$ ,  $v_0$  and  $w_0$  are the in-plane displacements in the  $x$ -,  $y$ - and  $z$ -directions and  $\theta_x$  and  $\theta_y$  are the rotations of

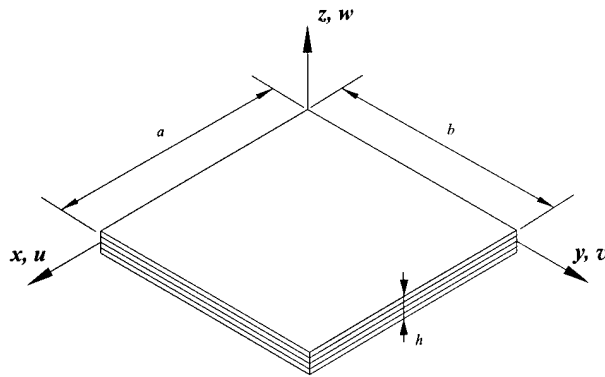


Fig. 1. Plate global coordinate system  $(x, y, z)$  and associated displacement field  $(u, v, w)$ .

normals to the midplane about the  $y$ -axis (anticlockwise) and  $x$ -axis (clockwise), respectively. The functions  $u_0^*$ ,  $v_0^*$ ,  $\theta_x^*$  and  $\theta_y^*$  are higher-order terms in the Taylor series expansion, defined also in the midplane of the plate.

As for the constitutive relations, considering a plane stress analysis and a linear elastic material, it can be shown that, for a laminae of orthotropic material in the  $(1, 2, 3)$  coordinate system (Fig. 2), the stress-strain relation is

$$\sigma_{(1,2,3)} = \mathbf{Q}\epsilon_{(1,2,3)} \quad (2)$$

with the following constitutive matrix:

$$\mathbf{Q} = \frac{E_1}{8\alpha_0} \begin{bmatrix} 8 & \alpha_4 - \alpha_3 & 0 & 0 & 0 \\ \alpha_4 - \alpha_3 & 8 - 2\alpha_2 & 0 & 0 & 0 \\ 0 & 0 & \alpha_8 - \alpha_9 & 0 & 0 \\ 0 & 0 & 0 & \alpha_8 + \alpha_9 & 0 \\ 0 & 0 & 0 & 0 & \frac{1}{2}(8 - \alpha_2 - 3\alpha_3 - \alpha_4) \end{bmatrix}. \quad (3)$$

The non-dimensional parameters in Eq. (3) are defined as [5,21]

$$\begin{aligned} \alpha_2 &= 4 - 4E_2/E_1, \\ \alpha_3 &= 1 + (1 - 2\nu_{12})E_2/E_1 - 4\alpha_0G_{12}/E_1, \\ \alpha_4 &= 1 + (1 + 6\nu_{12})E_2/E_1 - 4\alpha_0G_{12}/E_1, \\ \alpha_8 &= 4(G_{13} + G_{23})\alpha_0/E_1, \\ \alpha_9 &= 4(G_{13} - G_{23})\alpha_0/E_1, \end{aligned} \quad (4)$$

where  $\alpha_0 = 1 - \nu_{12}^2 E_2/E_1$  and  $E_1$ ,  $E_2$  are Young's modulus in  $(1, 2)$ -direction (Fig. 2),  $G_{12}$ ,  $G_{23}$  and  $G_{13}$  are the transverse shear modulus in planes 1–2, 2–3 and 1–3 (3 perpendicular to 1–2 plane), respectively, and  $\nu_{12}$  is the major Poisson's ratio.

The inverse relations of Eq. (4) can be written as

$$\begin{aligned} E_2/E_1 &= (4 - \alpha_2)/4, \\ G_{12}/E_1 &= (8 - \alpha_2 - 3\alpha_3 - \alpha_4)/(16\alpha_0), \\ \nu_{12} &= (\alpha_4 - \alpha_3)/(8 - 2\alpha_2), \\ G_{13}/E_1 &= (\alpha_8 + \alpha_9)/(8\alpha_0), \\ G_{23}/E_1 &= (\alpha_8 - \alpha_9)/(8\alpha_0), \\ \alpha_0 &= 1 - ((\alpha_4 - \alpha_3)^2/(16(4 - \alpha_2))). \end{aligned} \quad (5)$$

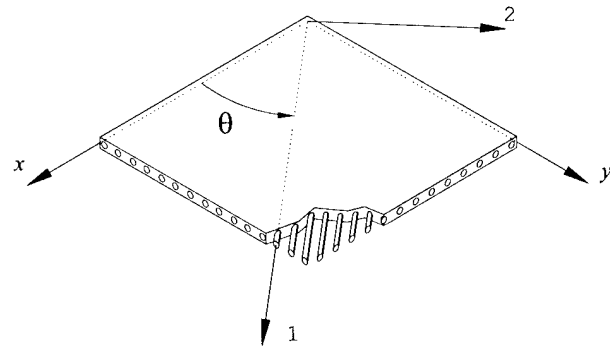


Fig. 2. Orthotropic material laminae; principal  $(1, 2)$  and global  $(x, y)$  coordinate system.

For a laminae in the  $(x, y, z)$  coordinate system (Fig. 2), the stress-strain relations are

$$\sigma_{(x,y,z)} = \frac{E_1}{8\alpha_0} \mathbf{c} \cdot \epsilon_{(x,y,z)}, \quad (6)$$

where

$$\mathbf{c} = \begin{bmatrix} c_{11} & c_{12} & 0 & 0 & c_{16} \\ c_{12} & c_{22} & 0 & 0 & c_{26} \\ 0 & 0 & c_{44} & c_{45} & 0 \\ 0 & 0 & c_{45} & c_{55} & 0 \\ c_{16} & c_{26} & 0 & 0 & c_{66} \end{bmatrix} \quad (7)$$

with

$$\begin{aligned} c_{11} &= 8 - \alpha_2(1 - \cos 2\theta) - \alpha_3(1 - \cos 4\theta), \\ c_{12} &= \alpha_4 - \alpha_3 \cos 4\theta, \\ c_{16} &= \frac{1}{2} \alpha_2 \sin 2\theta + \alpha_3 \sin 4\theta, \\ c_{22} &= 8 - \alpha_2(1 + \cos 2\theta) - \alpha_3(1 - \cos 4\theta), \\ c_{26} &= \frac{1}{2} \alpha_2 \sin 2\theta - \alpha_3 \sin 4\theta, \\ c_{44} &= \alpha_8 - \alpha_9 \cos 2\theta, \\ c_{45} &= \alpha_9 \sin 2\theta, \\ c_{55} &= \alpha_8 + \alpha_9 \cos 2\theta, \\ c_{66} &= \frac{1}{2} (8 - \alpha_2 - \alpha_3 - \alpha_4) - \alpha_3 \cos 4\theta. \end{aligned} \quad (8)$$

Assuming small displacements and using Hamilton's variational principle along with an eight node isoparametric plate element with nine degrees of freedom per node, corresponding to the nine expansion terms in the displacement equation (1), we obtain the following equilibrium equation for free harmonic vibrations at the element level:

$$\mathbf{K}^e \mathbf{a}_i^e - \lambda_i^e \mathbf{M}^e \mathbf{a}_i^e = 0, \quad (9)$$

where  $\mathbf{K}^e$  and  $\mathbf{M}^e$  are the element stiffness and mass matrices, respectively, and  $\mathbf{a}_i^e$  are the eigenvectors associated to the eigenvalues  $\lambda_i^e$ , at the element level. Second degree *serendipity* shape functions were used to interpolate the displacement field within an element [22].

The equilibrium equation for the whole discretised plate assumed free in space is therefore [23]

$$(\mathbf{K} + \beta \mathbf{M}) \mathbf{a}_i - (\lambda_i + \beta) \mathbf{M} \mathbf{a}_i = 0, \quad (10)$$

where  $\mathbf{K}$  and  $\mathbf{M}$  are the stiffness and mass matrices of the plate, and  $\mathbf{a}_i$  the eigenvector associated to the numerical eigenvalue  $\lambda_i$ . In order for the stiffness matrix to be positive definite, a shift  $\beta \mathbf{M}$  is applied to it (usually  $\beta$  is of the same magnitude as the first non-zero eigenvalue).

### 3. Experimental method

The experimental eigenfrequencies of a completely free plate are obtained using the experimental setup shown in Fig. 3.

In practice a truly free support cannot be provided. However, a suspension which closely approximates this condition can be achieved by supporting the test plate on light elastic bands so that the rigid body modes have very low natural frequencies in relation to those of the bending modes. These elastic bands were simply glued to the plate edge (approximately at the mid points of two neighbour edges).

The simplest and fastest way to excite the vibration modes of a plate is the impulse technique, so a hand held hammer was used to impact the plate and the force transducer attached to the hammer head measures the input force.

A condenser microphone was used to measure the plate response. The microphone is placed in a small table stand perpendicular to the plate.

The analog signals from the impact hammer and microphone were fed into a dual channel signal analyser. Both signals are low-pass filtered, sampled and subjected to appropriate time weighting functions. The weighting is important in order to reduce noise and avoid a leakage error caused by the truncation of the sampled time signal. The signals are fast Fourier transformed and divided to obtain the frequency response function (FRF). All of these steps are handled by the signal analyser.

The digital process described above results in a discrete spectrum which contains a finite number of values for the FRF. The FRF is generally a complex valued function and a peak usually indicates the presence of a natural frequency, however, the frequency of maximum response is not an accurate estimate of the natural frequency. First of all, the spectrum is discrete with a certain resolution and the peak value may not rely entirely on a single point. The second most serious reason is that neighbouring modes contribute a certain amount to the total response at the resonance of the mode being analysed. Finally, the third reason is that the values of the FRF include damping, which affects slightly the resonant frequencies. To deal with these problems,

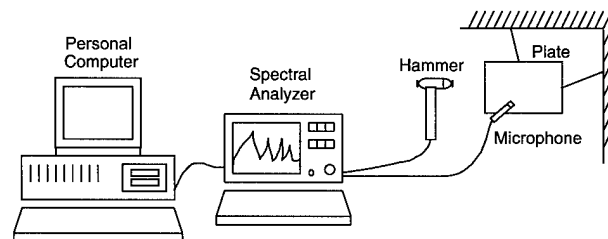


Fig. 3. Schematic representation of experimental setup.

refined modal analysis methods have been developed. In this work the rational fraction polynomial (RFP) method as described in [24] was used for the curve fitting process on a personal computer suited with an interface card.

#### 4. The identification method

The problem of identifying mechanical properties of composite plate specimens involves the comparison of the experimental results described in the previous section with the results produced by the numerical method. In a laminate made out of  $M$  different materials the mechanical properties that are to be identified for material  $i$  are  $E_1^i$ ,  $E_2^i$ ,  $G_{12}^i$ ,  $\nu_{12}^i$ ,  $G_{23}^i$  and  $G_{13}^i$ . The experimental results that are used in this process are the first  $I$  natural frequencies of the free plate.

This problem is solved using optimisation techniques by minimising an error estimator  $\Phi$ , which expresses the difference between the response of the numerical model and the corresponding experimental results. In Fig. 4, a schematic representation of the identification method is presented, where index  $k$  represents the current iteration and  $\mathbf{r}_e$  represents the experimental response:

$$\mathbf{r}_e = \{\tilde{\lambda}_1, \dots, \tilde{\lambda}_I\}^T, \quad (11)$$

where  $\tilde{\lambda}_i = \tilde{\omega}_i^2$  are the experimental eigenvalues and  $I$  is the total number of measured experimental eigenfrequencies.

The response of the numerical model is  $\mathbf{f}(\mathbf{p}) = \{\lambda_1, \dots, \lambda_I\}^T$ , where  $\lambda_i = \omega_i^2$  are the eigenvalues obtained through this model and  $\mathbf{p}$  is the vector of design variables:

$$\mathbf{p} = \{\bar{\alpha}^1, \dots, \bar{\alpha}^{MT}\}^T, \quad (12)$$

in which  $\bar{\alpha}^i$  contains the non-dimensional material parameters for material  $i$ ,

$$\bar{\alpha}^i = \{\bar{\alpha}_1^i, \dots, \bar{\alpha}_6^i\}^T. \quad (13)$$

The non-dimensional material parameters for material  $i$  are defined using Eq. (4):

$$\begin{aligned} \bar{\alpha}_1^i &= E_1^i / {}^0E_1^i, \\ \bar{\alpha}_2^i &= \alpha_2^i, \\ \bar{\alpha}_3^i &= \alpha_3^i, \\ \bar{\alpha}_4^i &= \alpha_4^i, \\ \bar{\alpha}_5^i &= \alpha_8^i, \\ \bar{\alpha}_6^i &= \alpha_9^i. \end{aligned} \quad (14)$$

It should be noted that, in Eq. (14), the superscript  $i$  was added to the non-dimensional parameters of Eq. (4) with the purpose of referencing the different materials in the laminate. In Eq. (14),  ${}^0E_1^i$  is the initial guess for the longitudinal Young's modulus of material  $i$ .

##### 4.1. Error measure

In order to establish an effective comparison between experimental results and the response of the numerical model it is necessary to define an error measure that, in general, can be of the following form [25]:

$$\Phi = (\mathbf{r}_e - \mathbf{f}(\mathbf{p}))^T \mathbf{W}_r (\mathbf{r}_e - \mathbf{f}(\mathbf{p})) + (\mathbf{p}^{(0)} - \mathbf{p})^T \mathbf{W}_p (\mathbf{p}^{(0)} - \mathbf{p}). \quad (15)$$

The weighting matrix  $\mathbf{W}_r$  expresses the confidence on the measured natural frequencies while the weighting matrix  $\mathbf{W}_p$  takes into consideration the reliability of the initial estimate  $\mathbf{p}^{(0)}$ . Of the two terms in Eq. (15), the first one represents the gap between the model response and the experimental one and the second one represents the deviation between the initial guess for the non-dimensional parameters and the real parameters that are to be determined. Each one of these terms is an L2 error estimator, weighted by  $\mathbf{W}_r$  and  $\mathbf{W}_p$ .

For the sake of simplicity it was decided to use only the first term of Eq. (15), with  $\mathbf{W}_p = \mathbf{0}$  and with the following response weighting matrix:

$$\mathbf{W}_r = \begin{bmatrix} w_1 / \tilde{\lambda}_1^2 & & 0 \\ & \ddots & \\ 0 & & w_I / \tilde{\lambda}_I^2 \end{bmatrix}, \quad (16)$$

in which  $w_i \in [0, 1]$  are weighting factors that express the confidence level in each eigenfrequency  $i$ , the error measure in Eq. (15) can be rewritten as

$$\Phi = \sum_{i=1}^I w_i \left( \frac{\tilde{\lambda}_i - \lambda_i}{\tilde{\lambda}_i} \right)^2. \quad (17)$$

Eq. (17) can easily be identified as a weighted least-squares error estimator.

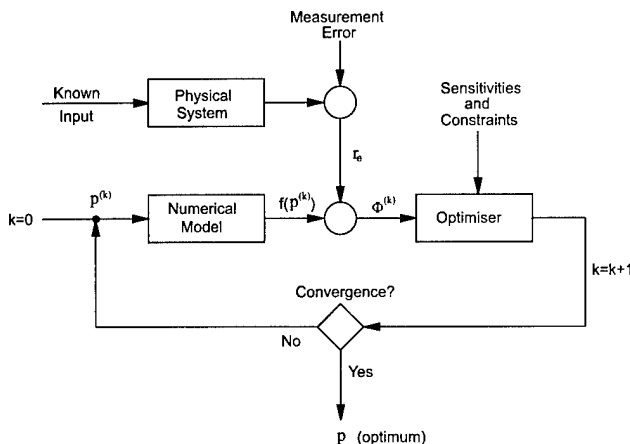


Fig. 4. Schematic representation of the identification method.

## 4.2. The minimisation problem

The problem of identifying mechanical properties of composite materials can be formulated as a minimisation problem:

$$\begin{aligned} \min \quad & \Phi(\mathbf{p}) \geq 0 \\ \text{s.t.} \quad & \mathbf{g}(\mathbf{p}) \leq \mathbf{0}, \\ & \mathbf{p}' \leq \mathbf{p} \leq \mathbf{p}'' \end{aligned} \quad (18)$$

where  $\mathbf{p}'$  and  $\mathbf{p}''$  are the side constraints on the design variables  $p$ ,  $\mathbf{g}$  is the vector of the imposed constraints on the design variables in order for the constitutive matrix for each material in Eq. (3) to be positive definite [5,21],

$$\mathbf{g} = \{\mathbf{g}^{1T}, \dots, \mathbf{g}^{MTT}\}^T, \quad (19)$$

in which  $\mathbf{g}^i$  are the vectors that contain the six constraints associated with material  $i$ ,

$$\mathbf{g}^i = \{g_1^i, \dots, g_6^i\}^T, \quad (20)$$

with the following components:

$$\begin{aligned} g_1^i &= -\bar{\alpha}_1^i, \\ g_2^i &= \frac{\bar{\alpha}_2^i}{\bar{\alpha}_2^i - 4}, \\ g_3^i &= \frac{8 - \bar{\alpha}_2^i - 3\bar{\alpha}_3^i - \bar{\alpha}_4^i}{-16\bar{\alpha}_0^i}, \\ g_4^i &= \left| \frac{\bar{\alpha}_4^i - \bar{\alpha}_3^i}{8 - 2\bar{\alpha}_2^i} \right| - \sqrt{\frac{4}{4 - \bar{\alpha}_2^i}}, \\ g_5^i &= \frac{\bar{\alpha}_5^i - \bar{\alpha}_6^i}{-8\bar{\alpha}_0^i}, \\ g_6^i &= \frac{\bar{\alpha}_5^i + \bar{\alpha}_6^i}{-8\bar{\alpha}_0^i}, \end{aligned} \quad (21)$$

which can be expressed in terms of the physical constants:

$$\begin{aligned} g_1^i &= -\frac{E_1^i}{E_1^i}, \\ g_2^i &= E_2^i - E_1^i, \\ g_3^i &= -\frac{G_{12}^i}{E_1^i}, \\ g_4^i &= |v_{12}^i| - \sqrt{E_1^i/E_2^i}, \\ g_5^i &= -\frac{G_{23}^i}{E_1^i}, \\ g_6^i &= -\frac{G_{13}^i}{E_1^i}. \end{aligned} \quad (22)$$

The minimisation problem formulated above is solved using non-linear mathematical programming techniques. To carry out the constrained minimisation a *feasible directions non-linear interior point algorithm* developed by Herskovits [26] is used. The choice of this

algorithm was made by one very important reason: the objective function cannot be defined at infeasible points, since the stiffness matrix is only positive definite at interior points.

## 4.3. Sensitivity analysis

The minimisation described in the previous section demands the sensitivities of the objective function  $\Phi$ . Sensitivity analysis consists in determining, for a given perturbation  $\delta\mathbf{p}$  in the design variables, the variation  $\delta\Phi$  of the objective function:

$$\delta\Phi = \frac{\partial\Phi}{\partial\mathbf{p}} \cdot \delta\mathbf{p}. \quad (23)$$

If we differentiate Eq. (17) with respect to  $\mathbf{p}$  we obtain

$$\frac{\partial\Phi}{\partial\mathbf{p}} = -2 \sum_{i=1}^I \mathbf{w}_i \left( 1 - \frac{\lambda_i}{\bar{\lambda}_i} \right) \frac{1}{\bar{\lambda}_i} \frac{\partial\lambda_i}{\partial\mathbf{p}}. \quad (24)$$

The problem of sensitivity evaluation is therefore reduced to the evaluation of the derivatives of the eigenvalues  $\lambda_i$  in order to design variables  $\mathbf{p}$ . From the equilibrium equation (10) (with  $\beta = 0$ ) it is possible to obtain the components of  $\partial\lambda_i/\partial\mathbf{p}$  (with the eigenvectors  $\mathbf{a}_i$  mass-normalised):

$$\frac{\partial\lambda_i}{\partial p_j} = \mathbf{a}_i^T \left( \frac{\partial\mathbf{K}}{\partial p_j} - \lambda_i \frac{\partial\mathbf{M}}{\partial p_j} \right) \mathbf{a}_i. \quad (25)$$

In the present case the mass matrix does not depend on the design variables, hence

$$\frac{\partial\lambda_i}{\partial p_j} = \mathbf{a}_i^T \frac{\partial\mathbf{K}}{\partial p_j} \mathbf{a}_i. \quad (26)$$

It is desirable, for the sake of computational efficiency, to evaluate Eq. (26) at the element level, adding the contribution of all the elements:

$$\frac{\partial\lambda_i}{\partial p_j} = \sum_{e=1}^{\text{NE}} \mathbf{a}_i^{eT} \frac{\partial\mathbf{K}^e}{\partial p_j} \mathbf{a}_i^e, \quad (27)$$

where NE is the total number of elements in which the plate is discretised.

The evaluation of the derivatives of the element stiffness matrix is performed analytically, considering that only the elasticity matrices depend on the design variables.

Results showing the quality of sensitivities for a plate made up of two different materials have been published by Araújo et al. [27]. These results show that the technique described here can be applied with confidence in the optimisation of material parameters of composite materials.

Table 1

Experimentally measured frequencies (Hz) and residuals (%) obtained after identification for specimens in Example 1

	<i>I</i>	1	2	3	4	5	6	7	8	9	10	11	12	13
S1.1	$\tilde{\omega}_i$	125.05	203.50	331.30	446.65	493.55	603.80	650.75	818.70	951.35	990.65	1256.75	1343.80	–
	$r_i$	0.09	–0.05	0.14	0.15	–0.07	0.06	0.06	–0.14	–0.10	–0.11	0.00	0.14	–
S1.2	$\tilde{\omega}_i$	167.70	198.65	414.20	480.70	–	633.90	738.50	909.20	1016.5	1176.3	1300.60	1388.70	1418.70
	$r_i$	–0.03	–0.07	0.02	0.02	–	0.07	0.02	0.10	–0.07	0.03	–0.01	–0.10	0.02
S1.3	$\tilde{\omega}_i$	129.85	218.70	–	395.10	459.75	630.45	722.20	878.50	1000.20	1026.50	1167.40	1261.05	1402.00
	$r_i$	0.07	–0.28	–	0.24	0.45	–0.07	0.50	–0.53	–0.07	0.19	–0.03	0.25	–0.57
S1.4	$\tilde{\omega}_i$	137.65	221.50	403.05	430.75	472.90	642.45	758.30	879.50	1035.30	1119.40	1250.30	1340.00	–
	$r_i$	0.01	–0.01	0.02	–0.03	–0.04	0.12	0.03	–0.04	–0.02	–0.04	–0.03	0.03	–

## 5. Applications

The following examples illustrate the application of the method described in the previous sections. For each example the experimental eigenfrequencies are presented, as well as the corresponding percentage residuals at the optimum:

$$r_i = \frac{\tilde{\omega}_i - \omega_i}{\tilde{\omega}_i} \times 100. \quad (28)$$

Each identification set of results is compared with strain gauge measurements.

It is assumed that weight factors  $w_i = 1$  were used in all examples, except otherwise specified. A  $12 \times 12$  finite element mesh is used for all the examples.

**Example 1.** Four IM7 carbon fibre reinforced epoxy resin 977-2 (Fiberite) plate specimens (S), made of unidirectional fibres with a nominal thickness of 0.135 mm for 60%  $V_f$ , with stacking sequences

- $[45^\circ_3, 0^\circ_3, -45^\circ_3, 90^\circ_3]_s$  (S1.1),
- $[45^\circ, 0^\circ, -45^\circ, 90^\circ, 45^\circ_2, 0^\circ_2, -45^\circ_2, 90^\circ_2]_s$  (S1.2),
- $[45^\circ_4, -45^\circ_4, 0^\circ_3, 90^\circ]_s$  (S1.3) and
- $[45^\circ_3, -45^\circ_3, 0^\circ_5, 90^\circ]_s$  (S1.4)

were studied. The specimens dimensions and masses are:

- S1.1:  $a = 210.5$  mm,  $b = 311$  mm,  $h = 3.06$  mm,  $m = 0.3225$  kg;
- S1.2:  $a = 210.5$  mm,  $b = 311$  mm,  $h = 3.07$  mm,  $m = 0.3232$  kg;
- S1.3:  $a = 210$  mm,  $b = 311$  mm,  $h = 3.04$  mm,  $m = 0.320$  kg;
- S1.4:  $a = 210.5$  mm,  $b = 310.5$  mm,  $h = 3.09$  mm,  $m = 0.3252$  kg.

The initial guess for the elastic constants corresponds to a typical unidirectional layer of carbon fibre reinforced epoxy resin with 50%  $V_f$ :

$${}^0E_1 = 117.2 \text{ GPa}, \quad {}^0E_2 = 8.8 \text{ GPa},$$

$${}^0G_{12} = {}^0G_{23} = {}^0G_{13} = 3.1 \text{ GPa}, \quad {}^0\nu_{12} = 0.35.$$

In Table 1 it can be seen that, for specimens S1.2 and S1.3, there are some experimental frequencies that were

not detected. So, the weighting factor associated with these were  $w_i = 0$ .

Identification results are presented in Table 2 along with strain gauge test results on specimens with unidirectional layers made of the same material. All the identified properties are in good agreement with the tensile test results, except for the major Poisson's ratio  $\nu_{12}$ , whose values present a pronounced oscillation and do not agree satisfactorily with the strain gauge test results.

**Example 2.** Two E glass fibre reinforced epoxy resin R368 (Structil) plate specimens (S), made of unidirectional fibres with a nominal thickness of 0.130 mm for 60%  $V_f$ , with stacking sequences  $[(0^\circ, 90^\circ)_2, 90^\circ, 0^\circ, 90^\circ]_s$  (S2.1) and  $[0^\circ_2, 90^\circ_2, 0^\circ_2, 90^\circ]_s$  (S2.2) were studied. The specimens dimensions and masses are:

- S2.1:  $a = 191$  mm,  $b = 283$  mm,  $h = 2.89$  mm,  $m = 0.2571$  kg;
- S2.2:  $a = 191$  mm,  $b = 282$  mm,  $h = 2.87$  mm,  $m = 0.2511$  kg.

The initial guess for the elastic constants corresponds to a typical unidirectional layer of E glass reinforced epoxy resin with 50%  $V_f$ :

$${}^0E_1 = 45 \text{ GPa}, \quad {}^0E_2 = 4.5 \text{ GPa},$$

$${}^0G_{12} = {}^0G_{23} = {}^0G_{13} = 3.7 \text{ GPa}, \quad {}^0\nu_{12} = 0.28.$$

Identification results are presented in Table 3. Some tensile test results are presented and compared with

Table 2

Identified properties and strain gauge results for Example 1 (modulus in GPa)<sup>a</sup>

Specimen	S1.1	S1.2	S1.3	S1.4	Strain gauge
$E_1$	161.1	162.3	164.8	159.6	$170 \pm 1^{(T)}$ , $150 \pm 5^{(C)}$
$E_2$	9.3	8.9	9.6	9.8	$10 \pm 1^{(T)}$
$G_{12}$	6.8	6.0	6.8	6.2	5.8
$G_{13}$	3.1	2.4	2.6	3.0	–
$G_{23}$	3.2	2.4	1.4	4.4	–
$\nu_{12}$	0.166	0.249	–0.036	0.264	0.35

<sup>a</sup> (T) – Tension; (C) – compression.



Table 3  
Identified properties for Example 2 (modulus in GPa)

Specimen	S2.1	S2.2
$E_1$	28.8	29.4
$E_2$	8.6	7.2
$G_{12}$	2.7	2.7
$G_{13}$	3.9	1.3
$G_{23}$	3.9	1.3
$\nu_{12}$	0.287	0.407

Table 4  
Comparison between identified and tensile global  $E_y$  (GPa) for Example 2

Specimen	Identified	Tensile test
S2.1	20.3	22.5
S2.2	17.0	17.5

global identified results in Table 4. The global identified mechanical properties are obtained using the procedure described in Appendix A.

The values obtained in this example for the mechanical properties are in relatively good agreement with each other, except for the major Poisson's ratio  $\nu_{12}$  and the transverse shear modulus  $G_{13}$  and  $G_{23}$ . A good agreement is obtained between the global identified and the tensile test results, with very low residual level as shown in Table 5.

**Example 3.** A mixed glass/carbon (g/c) fibre reinforced epoxy plate specimen with plies made of unidirectional fibres, respectively, of E glass in a R368 resin (Structil) with a nominal thickness of 0.130 mm for 60%  $V_f$  and T300 carbon fiber in an epoxy resin R367 (Structil) with a nominal thickness of 0.327 mm for 60%  $V_f$ , with a stacking sequence  $[0^\circ_c, 90^\circ_g, 0^\circ_c, 90^\circ_{2g}, 0^\circ_c, 90^\circ_g]_s$  was studied. The specimen dimensions and mass are:

- $a = 192.5$  mm,  $b = 292$  mm,  $h = 3.83$  mm,  $m = 0.3369$  kg.

The prepregs used to build these specimens are: Structil 200 g/m<sup>2</sup> VEE<sub>2</sub>20 R368 for glass plies and Structil 350 g/m<sup>2</sup> CTE<sub>2</sub>35 R367 for carbon plies. Hence, the initial guess for the elastic constants of the glass plies corresponds to a typical layer of this unidirectional glass with 50%  $V_f$ :

$${}^0E_1 = 45 \text{ GPa}, \quad {}^0E_2 = 4.5 \text{ GPa},$$

$${}^0G_{12} = {}^0G_{23} = {}^0G_{13} = 3.7 \text{ GPa}, \quad {}^0\nu_{12} = 0.28,$$

while the initial guess for the elastic constants of the carbon plies corresponds to a typical layer of this unidirectional carbon with 50%  $V_f$ :

$${}^0E_1 = 117.2 \text{ GPa}, \quad {}^0E_2 = 8.8 \text{ GPa}$$

$${}^0G_{12} = {}^0G_{23} = {}^0G_{13} = 3.1 \text{ GPa}, \quad {}^0\nu_{12} = 0.35.$$

The first step was to obtain the global properties of the specimen, using in the numerical model only one equivalent single layer (ESL).

The second step was to calculate the fibre volume for carbon and glass plies as well as the epoxy matrix volume, using the nominal and actual thickness of the specimen and data available from Structil. With the obtained data it is then possible to estimate the correct thickness for each material ply, as well as relative densities, based on the assumption that the epoxy matrix distribution is proportional to the nominal thickness of each layer.

Finally a complete model (CM) of the plate specimen was used in order to identify the properties of each material layer.

Results for global properties using the ESL and the CM are presented in Table 6, while individual layer results are presented in Table 7.

The measured natural frequencies and residuals obtained after identification for the two described situations are presented in Table 8.

It can be seen that the identified  $E_x$  for the ESL model is quite good when compared with the equivalent one determined through tensile testing of a specimen using a strain gauge. Concerning the results for the CM, the values of the global  $E_x$ , which were calculated using the identified properties for each layer in accordance with the procedure described in Appendix A, present a worst agreement with the tensile test results than those obtained through the global model (ESL). We think that this is due to the uncertainties in determining the correct thickness, and consequently the matrix and fibre volume distribution of the glass and carbon plies on hybrid composite panels, that affect the ply elastic properties and density.

Although one could conclude that the number of experimental natural frequencies is not enough for the 12 design variables involved, it can be seen in Fig. 5 that this might not be the case.

Table 5  
Experimentally measured frequencies (Hz) and residuals (%) obtained after identification for specimens in Example 2

	$I$	1	2	3	4	5	6	7	8	9	10	11	12
S2.1	$\tilde{\omega}_i$	72.78	121.00	191.38	286.78	315.12	340.40	400.12	433.84	634.81	653.56	712.43	789.97
	$r_i$	0.27	-0.24	0.04	0.04	-0.04	0.11	-0.08	-0.25	-0.35	0.30	0.03	0.15
S2.2	$\tilde{\omega}_i$	72.22	108.57	182.73	293.94	308.74	343.48	369.41	442.62	586.17	623.61	649.79	845.90
	$r_i$	0.08	-0.48	0.00	0.32	-0.10	0.30	0.18	-0.23	0.13	-0.20	-0.04	0.02

Table 6  
Identified global properties using ESL, CM and strain gauge results for Example 3 (modulus in GPa)

	Identified (ESL)	Identified (CM)	Strain gauge
$E_x$	76.2	69.7	77.0
$E_y$	15.3	20.7	—
$G_{xy}$	3.7	4.0	—
$G_{xz}$	1.8	1.8	—
$G_{yz}$	3.3	3.4	—
$\nu_{xy}$	0.183	0.132	0.15–0.17

Table 7  
Identified properties (CM) in Example 3 (modulus in GPa)

Ply type	Glass	Carbon
$E_1$	43.1	103.3
$E_2$	4.6	8.7
$G_{12}$	3.8	4.1
$G_{13}$	3.7	1.0
$G_{23}$	3.4	3.2
$\nu_{12}$	0.280	0.402

Table 8  
Experimentally measured frequencies and residuals obtained after identification through ESL and CM for Example 3

$i$	$\bar{\omega}_i$ (Hz)	$r_i$ (ESL; %)	$r_i$ (CM; %)
1	112.40	0.02	0.01
2	316.25	0.05	0.05
3	337.75	-0.13	-0.13
4	392.70	-0.01	-0.01
5	401.05	-0.08	-0.08
6	650.85	0.04	0.04
7	881.90	-0.00	-0.01
8	907.75	0.19	0.19
9	933.45	-0.27	-0.27
10	977.95	0.00	0.00
11	1160.15	0.07	0.07
12	1177.30	0.15	0.15
13	1623.80	-0.02	-0.02
14	1713.55	-0.21	-0.21
15	1754.30	0.61	0.61
16	1775.40	-0.40	-0.40
17	1814.45	0.22	0.22
18	1947.54	-0.14	-0.13
19	2007.40	0.21	0.21
20	2356.90	-0.34	-0.34

## 6. Conclusions

A non-destructive numerical-experimental method for the identification of up to six elastic constants per material on composite plate specimens made up of different materials has been discussed. The method is based on a numerical higher-order finite element model, using analytical sensitivities, as well as on experimental non-destructive free vibration analysis.

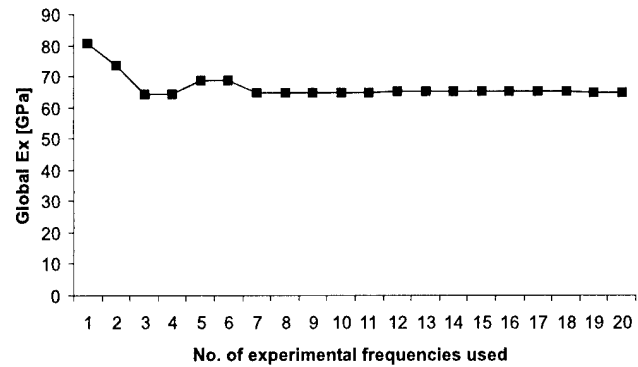


Fig. 5. Example 3, complete model: graph showing the dependence of global  $E_x$  with respect to the number of experimental frequencies used.

The mechanical properties evaluated through this technique are valid on average for the entire specimen, whereas the classical tensile test measurements are only valid in a specific point of the test specimen.

The mechanical properties  $E_1$ ,  $E_2$  and  $G_{12}$  are always evaluated without major discrepancies in single-material plates.

As for the transverse shear modulus  $G_{13}$  and  $G_{23}$ , the plates tested in this work are not thick enough for them to be correctly identified. Thus, the identified values of the transverse shear modulus can be disregarded as the sensitivity to these modulus is very low. As for the major Poisson's ratio  $\nu_{12}$ , some discrepancies are found in the test cases. This can be explained if we consider the results of a sensitivity analysis carried out by Frederiksen [5], according to which the sensitivity of  $\nu_{12}$  is very small when compared to the sensitivities of the other in-plane mechanical properties. This is specially pronounced for the most strongly anisotropic specimens presented, as can be seen in specimen S1.3.

Regarding the identification of mechanical properties in composite plates made up of layers with different materials, more tests are required in order to explain the discrepancies found.

Finally, the non-linear interior point algorithm used in the optimisation phase proved to be very robust and efficient. The CPU times involved in the overall process of identification are of the order of 10–20 min using a personal computer equipped with a 450 MHz Pentium II processor and 128 MB RAM.

## Acknowledgements

The authors thank Fundação para a Ciência e Tecnologia (FCT) for the financial support, through project PRAXIS/P/EME/12028/1998 and FCT/ICCTI (Portugal) and CNPq (Brazil).

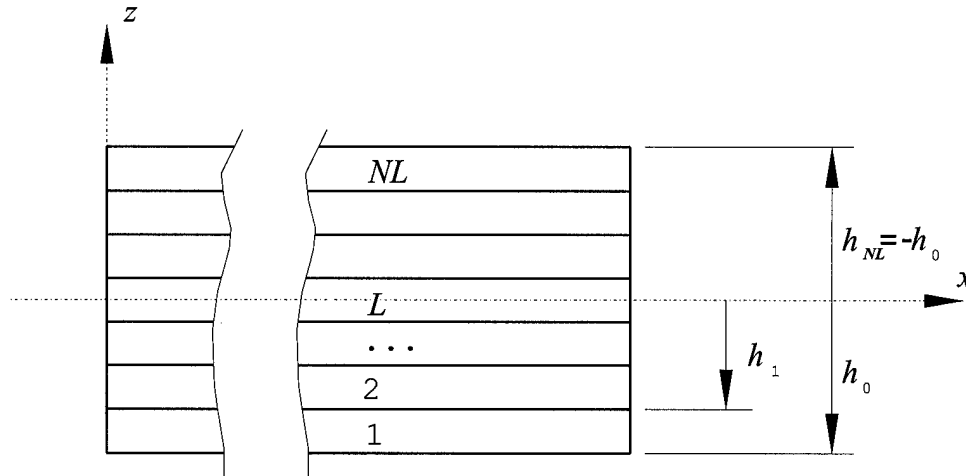


Fig. 6. Layer numbering used for a typical laminate.

## Appendix A

The global properties of a laminate, in the  $(x, y, z)$  coordinate system, can be obtained using the procedure described herein [19,21].

Let  $\mathbf{C}$  be the matrix that relates membrane and transverse shear forces with the corresponding membrane deformations and distortions:

$$\mathbf{C} = \sum_{L=1}^{NL} (h_L - h_{L-1}) \left( \frac{E_1}{8\alpha_0} \mathbf{c} \right)^{(L)}, \quad (\text{A.1})$$

where  $L$  is the layer number,  $NL$  the total number of layers and  $h_L$  can be depicted from Fig. 6. Matrix  $\mathbf{c}$  is the same as defined in Eqs. (7) and (8).

By inverting  $\mathbf{C}$  and pre-multiplying the inverse by the thickness of the laminate we obtain

$$\mathbf{S} = h\mathbf{C}^{-1}$$

$$= \begin{bmatrix} 1/E_x & -\nu_{xy}/E_x & 0 & 0 & \eta_{x,xy}/G_{xy} \\ -\nu_{yx}/E_y & 1/E_y & 0 & 0 & \eta_{y,xy}/G_{xy} \\ 0 & 0 & 1/G_{yz} & \mu_{yz,xz}/G_{xz} & 0 \\ 0 & 0 & \mu_{xz,yz}/G_{yz} & 1/G_{xz} & 0 \\ \eta_{xy,x}/E_x & \eta_{xy,y}/E_y & 0 & 0 & 1/G_{xy} \end{bmatrix}, \quad (\text{A.2})$$

where  $E_x$  and  $E_y$  are the global Young modulus in the  $x$ - and  $y$ -directions, respectively,  $G_{xy}$ ,  $G_{xz}$  and  $G_{yz}$  the transverse shear modulus in planes  $xy$ ,  $xz$  and  $yz$ , respectively and  $\nu_{xy}$  and  $\nu_{yx}$  are Poisson's ratios in the  $xy$  plane. As for the remaining quantities, they are the mutual influence and Chentsov coefficients [21].

## References

- [1] Mota Soares CM, Moreira de Freitas M, Araújo AL, Pedersen P. Identification of material properties of composite plate specimens. *Compos Struct* 1993;25:277–85.
- [2] Mota Soares CM, Moreira de Freitas MJ, Meira Afonso JM. Identificação de propriedades mecânicas de materiais compósitos utilizando técnicas de otimização. *Rev Internac Métod Numér Cálculo* 1993;9(4):357–73.
- [3] Araújo AL, Mota Soares CM, Moreira de Freitas MJ. Characterization of material parameters of composite plate specimens using optimization and experimental vibrational data. *Composites: Part B* 1996;27B:185–91.
- [4] Pedersen P. Optimization method applied to identification of material parameters. In: Eschenauer HA, Thierauf G, editors. *Discretization methods and structural optimization – procedures and applications*. Berlin: Springer; 1989. p. 277–83.
- [5] Frederiksen PS. Identification of material parameters in anisotropic plates – a combined numerical/experimental method. Ph.D. Thesis, Department of Solid Mechanics, The Technical University of Denmark, 1992.
- [6] Wilde WP, Sol H. Anisotropic material identification using measured resonant frequencies of rectangular composite plates [vol. 2] *Compos Struct* 1987;4:2317–24 [London: Elsevier].
- [7] Sol H. Identification of the complex moduli of composite materials by a mixed numerical/experimental method. In: Wilde WP, Blain WR, editors. *Composite materials design and analysis*. Berlin: Springer, 1990. p. 267–79.
- [8] Wilde WP. Identification of the rigidities of composite systems by mixed numerical/experimental methods. In: Vautrin A, Sol H, editors. *Mechanical identification of composites*. Amsterdam: Elsevier; 1991. p. 1–15.
- [9] Lai TC, Ip KH. Parameter estimation of orthotropic plates by Bayesian sensitivity analysis. *Compos Struct* 1996;34:29–42.
- [10] Frederiksen PS. Parameter uncertainty and design of optimal experiments for the estimation of elastic constants. *Int. J Solids and Structures* 1998;35:1241–60.
- [11] Rikards R, Chate A. Identification of elastic properties of composites by method of planning of experiments. *Compos Struct* 1998;42:257–63.
- [12] Rikards R, Chate A, Steinchen W, Kessler A, Bledzki AK. Method for identification of elastic properties of laminates based on experiment design. *Composites: Part B* 1999;30:279–89.
- [13] Bledzki AK, Kessler A, Rikards R, Chate A. Determination of elastic constants of glass/epoxy unidirectional laminates by the vibration testing of plates. *Compos Sci Technol* 1999;59:2015–24.
- [14] Cunha J, Piranda J. The use of model updating techniques in dynamics for identification of stiffness properties of sandwich composite structures. *J Braz Soc Mech Scis* 1999;XXI(2):313–21 [in Portuguese].

- [15] Pedersen P. Identification techniques in composite laminates. In: Mota Soares CA, Mota Soares CM, Freitas MJM, editors. *Mechanics of composite materials and structures*. Dordrecht: Kluwer Academic Publishers; 1999. p. 443–52.
- [16] Lo KW, Christensen RM, Wu EM. A higher-order theory for deformations. Part 1: Homogeneous plates. *J Appl Mech Trans ASME* 1977;44(4):663–8.
- [17] Lo KW, Christensen RM, Wu EM. A higher-order theory for deformations. Part 2: Laminated plates. *J. Appl Mech* 1977;44(2):669–76.
- [18] Malikarjuna, Kant T. A critical review and some results of recently developed theories of fibre-reinforced laminated composites and sandwiches. *Compos Struct* 1993;23:293–312.
- [19] Araújo AL. Método numérico/experimental para caracterização mecânica de materiais compósitos. M.Sc. Thesis, Mec. Eng. Dept, IST, Technical University of Lisbon, April 1995 [in Portuguese].
- [20] Moita JS, Mota Soares CM, Mota Soares CA. Buckling and dynamic behaviour of laminated composite structures using a discrete higher-order displacement model. *Comput Struct* 1999;73:407–23.
- [21] Jones RM. *Mechanics of composite materials*. New York: McGraw-Hill; 1975.
- [22] Bathe KJ. *Finite element procedures in engineering analysis*. Englewood Cliffs, NJ: Prentice-Hall; 1982.
- [23] Zienkiewicz OC. *The finite element method in engineering science*. New York: McGraw-Hill; 1971.
- [24] Richardson MH, Formenti DL. Parameter estimation from frequency response measurements using rational fraction polynomials. In: *Proceedings of the IMAC I*. Orlando (FL, USA), Nov 8–10, 1982.
- [25] Beck JV, Arnold KJ. *Parameter estimation in engineering and science*. New York: Wiley; 1977.
- [26] Herskovits J. A feasible directions interior point technique for nonlinear optimization. *J Optim Theory Appl* 1998;99(1):121–46.
- [27] Araújo AL, Mota Soares CM, Freitas MJM, Pedersen P. Identification of mechanical properties of composite plate specimens using a discrete higher-order displacement model and experimental vibration data. In: Topping BHV, editor. *Advances in analysis and design of composites*. Edinburgh: Civil-Comp Press; 1996. p. 101–11.

# Control of beam vibrations by means of piezoelectric devices: theory and experiments

Paolo Gaudenzi <sup>\*</sup>, Rolando Carbonaro, Edoardo Benzi

*Dipartimento Aerospaziale, Univeristà di Roma "La Sapienza", Via Eudossiana 16, 00184 Rome, Italy*

## Abstract

The problem of the attenuation of the vibration effects in active cantilever beams has been approached by two strategies, position and velocity control, which have been simulated numerically and analysed experimentally. The numerical simulation has been developed by means of a finite element approach based on an Euler–Bernoulli model and subsequent modal factorisation. Each device as well as each electronic circuit, present in the single-input single-output control system has been modelled and the results of the numerical simulations have been compared with the ones obtained in the experimental tests. A good correspondence has been obtained in all the examined cases. © 2000 Elsevier Science Ltd. All rights reserved.

**Keywords:** Piezo-patch; Position control; Velocity control

## 1. Introduction

The attenuation of vibrations is a problem of primary importance in many engineering fields, among which aerospace applications. In the past, the attainment of the desired vibration levels was pursued by increasing the stiffness and the mass of the structure with respect to the initial scheme in order to increase the damping effect. However, this solution implied an inevitable rise in the weight of the structure causing a lot of heavy drawbacks.

From some years, a new approach of this problem has been considered. In this one, the structure is seen as a system with disturbance loads applied at its input. Then the problem is carried out in the form of a control strategy: the reduction of the undesired output effects by means, for an example, of a classic feedback closed loop with its sensing and actuating devices. Piezoelectric devices, as in particular PZT piezo-patches, seem very attractive to carry out the function of sensor and actuator. Referring to aforesaid old approach, the aim of reducing the vibrations may now be reached with a lower increase of weight.

A structure in which the damping action is realised by automatic control techniques is named “controlled

structure” and it is a particular case about a more general class named “active structures”, for which either a sensitive or an actuative component is present. Considerable research activity has been recently focussed on this field [1], and while some applications are already being studied and simulated, still some fundamental issue on modelling and implementation of a real active structure has to be considered.

Bailey and Hubbard [2] proposed the use of a “poly vinylidene fluoride” patch as a distributed actuator for controlling the vibrations of a cantilever beam.

Hagood et al. [3] have used PZT patches to couple the structural response with a electrical circuitry which can be tuned to optimally control a cantilevered beam test article. The Ritz–Galerkin approach is used for the simulation of the electro-mechanical behaviour of the system.

Hanagud et al. [4] formulated a control technique based on the minimisation of a quadratic performance index. In their experimental tests, the piezoelectric sensor was electrically connected with a zero input impedance circuit; in this way the sensor ideally becomes a pure current source.

Denoyer and Kwaak [5] presented a theoretical study and experimental results by using surface bonded piezoelectric sensors and actuators, and by proposing a linear quadratic control as controlling techniques.

The present research is the continuation of two previous experimental studies [6,7] by the same authors.

<sup>\*</sup> Corresponding author. Tel.: +39-06-4458-5304; fax: +39-06-4458-5670.

E-mail address: paolo@gaudenzi.ing.uniroma1.it (P. Gaudenzi).

These last ones were finalised to demonstrate the feasibility of the vibration suppression in aluminium and composite cantilever beams by a simple single-input single-output control that utilises PZT piezo-patches as actuator and sensor. Two control strategies, that are position control and velocity control, were tested and compared during the experimental researches. Their diversity consists in the different way by which the actuating action is carried out. In the former type of control, it is function of position quantities (the rotations of the extremities) detected by the piezo-sensor, whereas in the latter, the actuation depends by the time derivative of the same quantities.

In the present work, the two control strategies have been numerically simulated and experimentally analysed. The numerical simulation has been developed by a FEM approach based on an Euler–Bernoulli model and modal factorisation. Each device and electronic circuit, present in the single-input single-output control system, have been modelled and the results of the numerical simulations have been compared to those ones previously obtained in the experimental tests. The study not only offers a possible numerical approach for studying the problem but also allows the validation of the theory with experimental results.

## 2. Finite element modelling

Let us consider the laminated cantilever beam of Fig. 1. Two identical piezo-patches are perfectly and symmetrically attached to the two sides of the isotropic (aluminium) beam. The piezo-patch on the upper side is utilised as an actuator, while the other, in the lower side, as a sensor. Moreover, an accelerometer and a disc, the latter with a diameter of few millimetres and made of ferromagnetic material, are attached in proximity of the beam tip, respectively, on the upper and lower side. The function of the little disc is to interact with an electro-magnetic exciter in such a way as to produce a bending

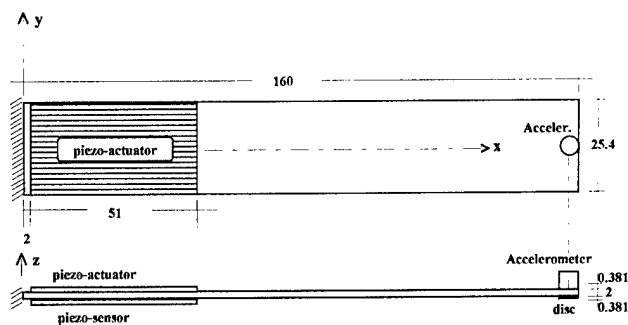


Fig. 1. Geometry and layout of the active cantilever beam (all the measures are in mm).

load. The function of the accelerometer is to measure to response at beam tip under dynamic load.

An Euler–Bernoulli (EB) model is considered for the finite elements analysis of the whole structure. In particular the beam section between the two piezo-patches is modelled as a laminated beam, while the remainder as an isotropic beam. Besides, the accelerometer and the bending load are considered as a concentrated mass and a concentrated load, respectively, located and applied to the beam tip.

### 2.1. Beam and piezo-patches finite element

Let us consider the laminated beam element represented in Fig. 2. The stacking sequence consists of two PZT piezoelectric layers symmetrically located to an aluminium central layer. The piezo-layers have isotropic and linear elastic characteristics.

From an electrical point of view, the piezo-patch is a planar capacitor with a polarised dielectric. The direction of polarisation is normal to metal plates of the capacitor and corresponds to  $z$ -axis direction as shown in Fig. 2. When a voltage is applied to its plates, the piezo-patch, because of the *converse piezoelectric effect*, is subjected to deformations along the coordinate axes. The sign of these deformations depends on the sign of the applied voltage. On the contrary, if the piezo-patch is mechanically deformed, a voltage can be measured across the metal plates; this is the *direct piezoelectric effect*. Since an EB model has been adopted for the whole structure, then the two piezoelectric effects can be, respectively, represented by the following relations:

$$\text{converse} \quad \varepsilon_x = \frac{\sigma_x}{E_{PZ}} + \frac{d_{xz}}{t_{PZ}} V, \quad (2.1)$$

$$\text{direct} \quad D_z = E_{PZ} d_{xz} \varepsilon_x + \frac{\epsilon_{zz}}{t_{PZ}} V, \quad (2.2)$$

where  $\varepsilon_x$  and  $\sigma_x$  are, respectively, the strain and stress components along  $x$ -axis,  $E_{PZ}$  and  $t_{PZ}$  are the Young's module and thickness of piezo-patch,  $d_{xz}$  and  $\epsilon_{zz}$  are the piezoelectric and the dielectric constants of the PZT material and  $V$  is the voltage across the metal plates.

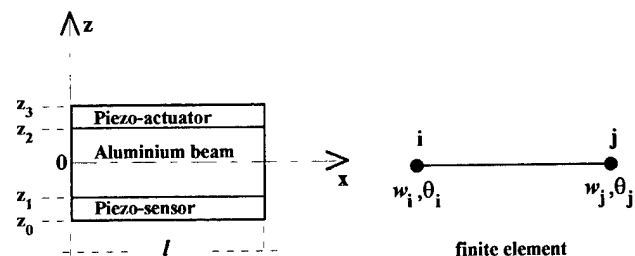


Fig. 2. Laminated beam element and corresponding finite element.

Following the hypothesis illustrated in [4], if no external voltage is applied to the piezo-patch, the second term  $\epsilon_{zz}V/t_{PZ}$  in the right-hand side of the equation of the direct effect (2.2) can be neglected being much smaller than the first one. As a consequence of this simplifying hypothesis, the two effects can be considered coupled only in the converse equation (2.1) and not in the second one Eq. (2.2).

The equilibrium of the active laminated beam element in dynamic condition can be represented by principle of virtual works in the following way:

$$\sum_{i=1}^3 \int_{v_i} \tilde{\epsilon}_x^i(x, z, t) \sigma_x^i(x, z, t) dv_i + \sum_{i=1}^3 \int_{v_i} \tilde{w}_i(x, t) \rho_i \ddot{w}_i(x, t) dv_i = 0. \quad (2.3)$$

In Eq. (2.3), the quantities associated to the generic  $i$ th layer,  $\tilde{\epsilon}_x^i(x, z, t)$  and  $\sigma_x^i(x, z, t)$ ,  $\tilde{w}_i(x, t)$  and  $\rho_i$ , represent, respectively, the virtual strain and the stress components along the  $x$ -axis, the virtual normal displacement and the density. In particular, the stress components are represented with the next equations, which incorporate Euler–Bernoulli beam hypothesis:

$$\sigma_x^1(x, z, t) = E_{PZ} z \chi(x, t), \quad \sigma_x^2(x, z, t) = E_A z \chi(x, t), \\ \sigma_x^3(x, z, t) = E_{PZ} z \chi(x, t) - E_{PZ} \frac{d_{xz}}{t_{PZ}} V(t),$$

where  $E_A$  and  $\chi(x, t)$  are the Young's module of the aluminium layer and the curvature, respectively.

On the basis of the usual finite element procedure, the normal displacement  $w_i(x, t)$  can be represented in terms of nodal displacement and shape functions

$$w_i(x, t) = [N(x)] \{\delta(t)\}_e \quad (2.4)$$

$$\text{with } \{\delta(t)\}_e^T = \{w_i(t) \theta_i(t) w_j(t) \theta_j(t)\}.$$

The relation between curvature and nodal displacements can be derived from Eq. (2.4):

$$\chi(x, t) = -\frac{\partial^2}{\partial x^2} [N(x)] \{\delta(t)\}_e = [B(x)] \{\delta(t)\}_e. \quad (2.5)$$

By substituting the relations (2.4) and (2.5) into the relation (2.3), after some simplifications, we obtain the final relation which represents the dynamics for the present element

$$[K]_e \{\delta(t)\}_e + [M]_e \{\ddot{\delta}(t)\}_e = \{P\}_e V(t). \quad (2.6)$$

In Eq. (2.6), the  $[K]_e$  and  $[M]_e$  and  $\{P\}_e$  are the stiffness and the mass matrices of element and the piezoelectric local load vector, respectively, they are represented by the following relations:

$$[K]_e = \left[ E_{PZ} \frac{z_1^3 - z_0^3}{3} + E_A \frac{z_2^3 - z_1^3}{3} + E_{PZ} \frac{z_3^3 - z_2^3}{3} \right] \\ \times \int_l [B]^T [B] dx \\ [M]_e = [\rho_{PZ}(z_1 - z_0) + \rho_A(z_2 - z_1) + \rho_{PZ}(z_3 - z_2)] \\ \times \int_l [N]^T [N] dx \\ \{P\}_e = E_{PZ} \frac{z_3^2 - z_2^2}{2} \frac{d_{xz}}{t_{PZ}} \int_l [B]^T dx,$$

where  $\rho_{PZ}$  and  $\rho_A$  are the densities of the PZT material and aluminium, respectively. It would be easy to add a vector of nodal forces to the forcing term as usually done for the beam as . . . . . in the next section.

## 2.2. Beam finite element

The equation of the dynamics for this type of element is obtained in a way analogue to the previous one

$$[K]_e \{\delta(t)\}_e + [M]_e \{\ddot{\delta}(t)\}_e = 0, \quad (2.7)$$

where

$$[K]_e = E_A \frac{z_2^3 - z_1^3}{3} \int_l [B]^T [B] dx$$

and

$$[M]_e = \rho_A (z_2 - z_1) \int_l [N]^T [N] dx.$$

The global equation that represents the dynamics without damping of the whole structure is obtained by an assembling procedure of all local matrix and vectors; therefore the resultant equation is

$$[M] \{\ddot{\delta}(t)\} + [K] \{\delta(t)\} = \{F_c\} + \{P\} V(t). \quad (2.8)$$

The eigen-values ( $\omega_k$ ) and the eigen-vectors ( $\{W_k\}$ ) can be obtained by considering the eigen-equation joined to Eq. (2.8) and after the fixed end constrain conditions have been imposed in the latter.

## 3. The control system model

The block diagram of the vibration control system is shown in Fig. 3. As it can be noted, it is a typical single-input single-output feedback control system. The feedback signal is generated by the piezo-sensor. Then the signal is conditioned by an ad hoc electronic interface, subsequently filtered by a low pass filter. The signal is then amplified and applied to the piezo-actuator. Depending on the type of signal conditioning, the vibration control can be realised in two different ways: position and velocity. In the former type of control, the actuating action is function of position quantities detected by the piezo-sensor, whereas in the latter the actuation depends by the





the mesh, Eq. (3.7) can be rewritten from scalar to a vector form as follows:

$$\begin{aligned} V_{CV}(t) &= E_{PZZ_2} b d_{xz} R_{CV} \{A\}^T \frac{d}{dt} \{\delta(t)\} \\ &= K_{CV} \{A\}^T \{\dot{\delta}(t)\}. \end{aligned} \quad (3.8)$$

### 3.3. The model of the whole control system

To complete the representation of the whole control system, it is necessary to include the system damping. In order a proportional damping in the Reyleigh form is considered for the present analysis

$$[D] = \alpha[M] + \beta[K]. \quad (3.9)$$

Then, the complete representation is obtained by introducing the damping term in the smart structure representation (2.10) and considering as actuation signal the relation (3.5) for the position control

$$\begin{aligned} [M]\{\ddot{\delta}(t)\} + [D]\{\dot{\delta}(t)\} + [K]\{\delta(t)\} \\ = \{F_c(t)\} + \{P\}K_{CA}\{A\}^T\{\delta(t)\} \end{aligned} \quad (3.10)$$

or the relation (3.8) for the velocity control.

$$\begin{aligned} [M]\{\ddot{\delta}(t)\} + [D]\{\dot{\delta}(t)\} + [K]\{\delta(t)\} \\ = \{F_c(t)\} + \{P\}K_{CV}\{A\}^T\{\dot{\delta}(t)\}. \end{aligned} \quad (3.11)$$

An approach based on the modal analysis is convenient to represent the response of the control system. Let us express the nodal displacements as a function of modal coordinates  $q_k(t)$ .

$$\{\delta(t)\} = \sum_k \{W_k\} q_k(t), \quad (3.12)$$

where  $\{W_k\}$  is the generic  $k$ th eigen vector.

Using the usual procedure of the modal analysis and the Fourier-transform, we can represent the equation of the generic  $k$ th mode in the frequency domain:

for the *position control*

$$\begin{aligned} (-\omega^2 + j2\omega\zeta_k\omega_k + \omega_k^2)q_k(\omega) \\ = \frac{1}{m_k} \left( \{W_k\}^T \{F_c\} \right. \\ \left. + \{W_k\}^T \{P\}K_{CA}\{A\}^T \{W_k\} q_k(\omega) \right) \end{aligned} \quad (3.13)$$

and for *velocity control*

$$\begin{aligned} (-\omega^2 + j2\omega\zeta_k\omega_k + \omega_k^2)q_k(\omega) \\ = \frac{1}{m_k} \left( \{W_k\}^T \{F_c\} \right. \\ \left. + j\omega \{W_k\}^T \{P\}K_{CA}\{A\}^T \{W_k\} q_k(\omega) \right). \end{aligned} \quad (3.14)$$

In Eqs. (3.13) and (3.14),  $\zeta(k)$  is the damping ratio of the  $k$ th mode and  $m_k = \{W_k\}^T [M] \{W_k\}$  is the modal mass. At the right-hand side of both Eqs. (3.13) and (3.14) the contribution to the  $k$ th mode of the external forces and of the control forces is present.

## 4. Comparison between numerical simulation and experimental tests

In the following the description of the experimental tests is briefly recalled for the convenience of the reader and described in details in Ref. [6,7].

The experimental tests have been carried out by the experimental set up shown in Fig. 3.

Two identical PZT devices (type QP10N by ACX Inc.) with the principal characteristics indicated in Table 1 have been used. The characteristics of the aluminium beam are also indicated in the same table. The positioning of the piezos has been fixed based on the results presented in Ref. [8], where the optimal positioning of PZT actuators for the active control of a beam is discussed. Therefore, the positioning of the piezo-actuator, with the dimensions of Table 1, in proximity to the fixed-end appears to be the optimal position to control the damping of the 1st and 2nd mode.

Besides the above mentioned ones on signal conditioning, the feedback loop is provided of the following circuits:

1. A low-pass filter whit gain  $G_F = 0$  dB and bandwidth  $B_F = 0 \div 800$  Hz. The functions of this circuit are to make the controlled system stable and to limit its response so that only the first two modes can be observed.
2. An inverting power amplifier (type 1224/5 Quick Pack by ACX Inc.) with adjustable gain in the range  $G_{PW} = 0 \div 26$  dB and bandwidth  $B_{PW} = 0 \div 5$  KHz.

Table 1  
Principal characteristics of the aluminium beam and piezo-patch

	Aluminium beam	PZ QP10N
$E$ (GPa)	59.7	18.95
$\rho$ (kg/m <sup>3</sup> )	2637	5670
Dim.: $l \times w \times t$ (mm)	$160 \times 25.4 \times 2$	$50.8 \times 25.4 \times 0.381$
Piezo wafer size (mm)	–	$46 \times 20.6 \times 0.254$
$d_{xz}$ (m/V)	–	$4.47 \times 10^{-10}$
Operating voltage (V)	–	0 to $\pm 200$
Capacitance ( $\mu$ F)	–	0.06

The action of this amplifier is necessary because the voltage level at the output of the feedback loop is not sufficient for driving the piezo-actuator.

The acceleration at the beam tip has been assumed as output quantity in all the experimental tests and has been measured by an accelerometer (type 303A03 by PCB Piezotronics). The accelerometer signal is amplified by an opposite electronic interface, obtaining for this transducer a global sensibility of  $S_a = 10 \text{ mV}/(\text{m/s}^2)$ .

The transfer functions detected during the experimental tests have been measured by a FFT analyser (type SD375 by Scientific Atlanta) provided of two input channels. The same instrument can also generate a band-limited random signal, which has been always used as input in all the tests. This signal is put in the exciter (type 3930 by Bruel & Kjaer) after it has been amplified by an amplifier (type 2712 by Bruel & Kjaer).

The results of the experimental tests for the three cases, not-controlled system, position control and velocity control are illustrated in Table 2. As the not-controlled and position control, the same results are reported and compared in the graph shown in Fig. 6. Considering all these data, it is possible to note that the best control action is performed with the position control. Indeed, referring to the levels of the not-controlled system response, an attenuation of 17.1 dB for the first mode and 8.4 dB for the second mode are obtained at the resonance frequency with this control modality, while they become only 6.2 and 2 dB with velocity control. Besides, still referring at values of the not-controlled system response, changes of the two resonance frequencies are only noted for the position control which decrease from 60 to 40 Hz for the first mode and from 365 to 360 Hz for the second mode.

The damping ratios of the first two modes have been measured during the experimental tests, which have allowed to find the following values in the case of not-controlled system:

$$\text{1st mode, } \zeta_1 = 0.01371,$$

$$\text{2nd mode, } \zeta_2 = 0.00411.$$

These experimental values have been then utilised for the identification of the model used in the numerical simulation, which has been carried out based on three fundamental steps. First all the matrixes and vectors of the finite elements formulation are evaluated.

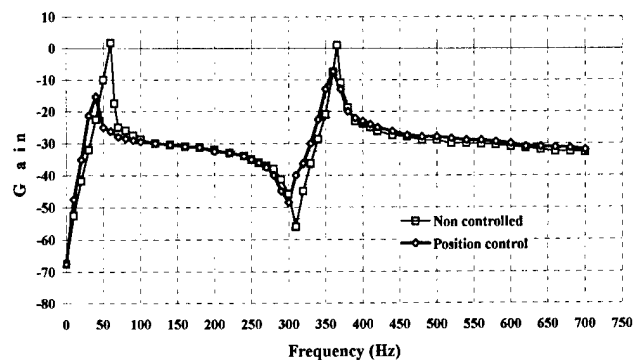


Fig. 6. Results of the experimental tests.

During the second step a finite element procedure calculates the eigen values and the eigen vectors, then it performs the modal factorisation by utilising these data according to the relations (3.13) and (3.14). The modal damping evaluated in the experiments are then included in the model.

In the third and last step the system transfer function  $H(\omega) = a(\omega)/F_c(\omega)$  are calculated, where  $a(\omega)$  and  $F_c(\omega)$  are, respectively, the acceleration and the bending load at beam tip, for the three cases, that is without control, with position and with velocity control. The power amplifier gains, fixed during all the tests are included in the constants  $K_{CA}$  and  $K_{CV}$ . In addition, the overall gain of the feedback loop, in the two cases of the controlled system, has been always assumed as a constant, because the upper cut-off frequencies of all the utilised circuits are greater than the maximum value of

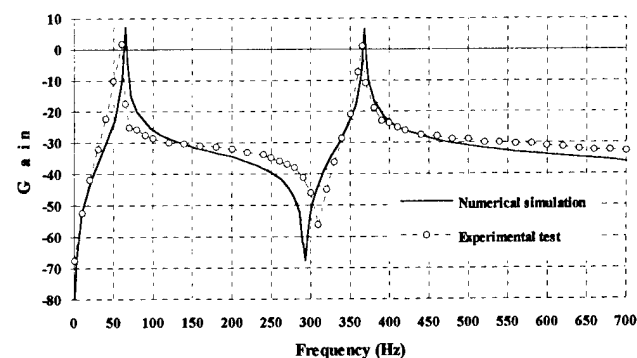


Fig. 7. Not-controlled system: comparison between experimental test and numerical simulation.

Table 2

Transfer function gains at resonance frequency obtained with numerical simulation and experimental tests

	Not controlled gain (dB)	Position control gain (dB)	Velocity control gain (dB)
1st mode numerical simulation	7.24	-14.3	0.7
1st mode experimental test	1.8	-15.3	-4.4
2nd mode numerical simulation	6.52	-4.15	-6.29
2nd mode experimental test	1	-7.4	-1

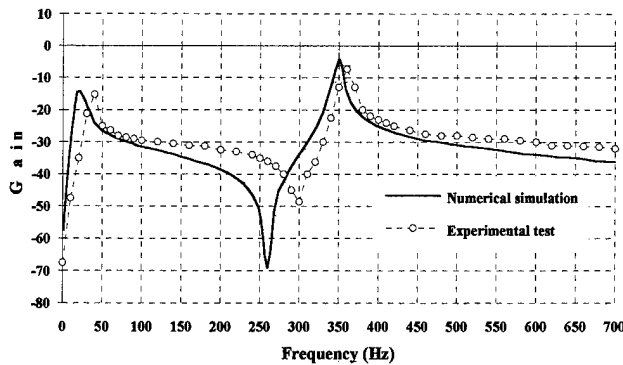


Fig. 8. Position control: comparison between experimental tests and numerical simulation.

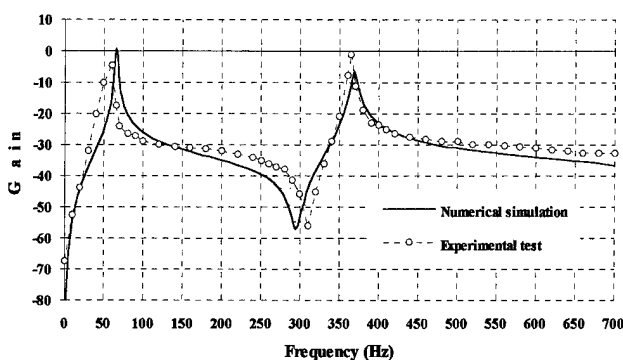


Fig. 9. Velocity control: comparison between experimental test and numerical simulation.

the frequency range (0–700) Hz considered in the numerical simulation.

The transfer functions obtained with the experimental measurements and numerical simulations are shown and compared in Figs. 7–9, respectively, for the three cases: not-controlled system, position control and velocity control. The transfer function gains at resonance frequency, obtained with the methods, are summarised in Table 2.

The analysis shows a better effectiveness in the vibration control for the examined cases for the position control, which allows a larger reduction in terms of amplitude with respect to the one obtained by means of velocity control.

## 5. Conclusions

The problem of vibration reduction for an active cantilever beam has been considered in the present research. A single-input single-output feedback closed

loop control system has been used for its solution. The sensing and actuating actions have been carried out by two identical PZT piezo-patches connected at the beam in a collocated way.

Two control strategies, position and velocity, characterised from different modes to detect the input of the feedback loop have been analysed.

A finite elements analysis, based on an Euler–Bernoulli model of the considered structure, and a modal approach have been taken into account to simulate the whole system response at a disturbance load in the three cases: not-controlled system, position and velocity control.

The results of the numerical simulation have been compared to those ones obtained with the experimental tests and a good correspondence has been obtained in the three cases. Besides, the analysis has demonstrated the better effectiveness of the position control respect to the velocity control as strategy to reduce the vibration levels in a cantilever beam.

## Acknowledgement

The present work has been developed in the frame of the PFMSTAZ-99.01797 the financial support of which is gratefully acknowledged.

## References

- [1] Gaudenzi P. Traditional and intelligent structures: a personal view. In: *Energy methods in vibroacoustics*, Polish Acoustical Society, Zakopane, Kiry, 24–27 April 1995, pp. 9–13.
- [2] Bailey T, Bubbard JE. Distributed piezoelectric-polymer active vibration control of a cantilever beam. *J Guidance Control* 1985;8(5):605–11.
- [3] Hagood NW, Chung WH, von Flotow A. Modelling of piezoelectric actuator dynamics for active structural control. *J Intell Mater Syst Struct* 1990;1:254–327.
- [4] Hangud S, Obal MW, Calise AJ. Optimal vibration control by the use of piezoceramic sensors and actuators. *J Guidance, Control Dynamics* 1992;15(5):1199–206.
- [5] Denoyer KK, Kwaak MK. Dynamic modeling and vibration suppression of a slewing structure utilizing piezoelectric sensors and actuators. *J Sound Vib* 1996;189(1):13–31.
- [6] Gaudenzi P, Carbonaro R, Barboni R. Vibration control of an active laminated beam. *Comp Struct* 1997;38(1–4):413–20.
- [7] Gaudenzi P, Barboni R, Carbonaro R, Accettella S. Direct position and velocity feedback control on an active beam with PZT sensors and actuators. *International Forum on aeroelasticity and structural dynamics*, Rome, Italy, June 1997;2:285–92.
- [8] Barboni R, Fantini E, Gaudenzi P, Mannini A. On the optimal placement of PZT actuators for the control of the dynamic response of a beam. In: *Proceedings of the 20th ICAS*, vol. 2, Sorrento, Italy, September 1996, pp. 1890–900.

# Impact energy absorption characteristics of composite structures

Dai Gil Lee<sup>\*</sup>, Tae Seong Lim, Seong Sik Cheon

*Department of Mechanical Engineering, Mechanical Design Laboratory with Advanced Materials, ME3221, Korea Advanced Institute of Science and Technology, 373-1, Gusong-dong, Yusong-gu, Taejeon-shi 305-701, South Korea*

---

## Abstract

The tensile and compressive tests of glass–epoxy composites with  $1\text{--}200\text{ s}^{-1}$  strain rates which are typical strain rate range during automobile crash accidents were performed in order to measure the strength variation with respect to strain rate. The tests were performed using both a horizontal type pneumatic impact tester and a conventional dynamic universal test machine with strain-rate-increase mechanisms. Also, the impact energy absorption characteristics of glass fiber reinforced composites were estimated using the newly proposed progressive impact fracture model. From the experiments and predictions, it was found that the proposed method predicted relatively well the experimental results. © 2000 Published by Elsevier Science Ltd. All rights reserved.

**Keywords:** Strain rates; Impact energy absorption; Progressive impact fracture model

---

## 1. Introduction

Fiber reinforced composites have been used for structural materials of aircraft and space vehicles thanks to their superior mechanical properties. In these days, their use is being increased in various industrial structures. As composite materials are increasingly employed in mechanical structures, the dynamic as well as static characteristics of composite structures should be considered for the reliable structures. Therefore, many researches on the impact behavior of composite materials have been carried out [1–10].

In the present study, in order to measure the strength variation with respect to strain rate, the tensile and compressive strengths of glass–epoxy composites were investigated under intermediate strain rates ( $1\text{--}200\text{ s}^{-1}$ ) which were the strain rates during automobile crash accidents. The tests were performed using a horizontal type pneumatic impact tester and a conventional dynamic universal test machine with strain-rate-increase mechanisms. Also, the impact energy absorption characteristics of glass fiber reinforced composites were estimated using the newly proposed progressive impact fracture model, whose basic scheme is to eliminate the fractured part of the composite at each divided loading stage.

Finally, the predicted impact energy absorption characteristics were compared with the experimental results obtained by the previous researchers [8–10].

## 2. Tensile and compressive tests under intermediate strain rates

Generally, the split Hopkinson bar tester was widely used to investigate dynamic properties of materials in the strain rate range between 100 and 1000 depending on the gauge length of specimens. However, the strain rates of automobile body during car crash accidents are  $1\text{--}200\text{ s}^{-1}$ , which are the comparable strain rates of impact speed of 5–13 m/s during impact tests. Therefore, the results of the split Hopkinson bar test have a limited applicability for the automotive material characterization during automobile crash accident.

In the present study, the effects of strain rate on the strength of glass fiber epoxy composite materials in the range of  $1\text{--}200\text{ s}^{-1}$  were investigated using two testing methods. For the range of  $1\text{--}20\text{ s}^{-1}$ , strain-rate-increase mechanisms with two hydraulic cylinders were designed and mounted on a conventional dynamic Instron machine (Instron 8032). By these mechanisms, test speed was increased 10 times both for tensile and compressive tests as shown in Fig. 1. Since the maximum test speed of the machine was 25 mm/s, the maximum test speed was increased to 250 mm/s. For the range of  $20\text{--}200\text{ s}^{-1}$ , horizontal type pneumatic impact tester was designed as

---

<sup>\*</sup>Corresponding author. Tel.: +82-42-869-3221; fax: +82-42-869-3210.

E-mail address: dglee@kaist.ac.kr (D.G. Lee).

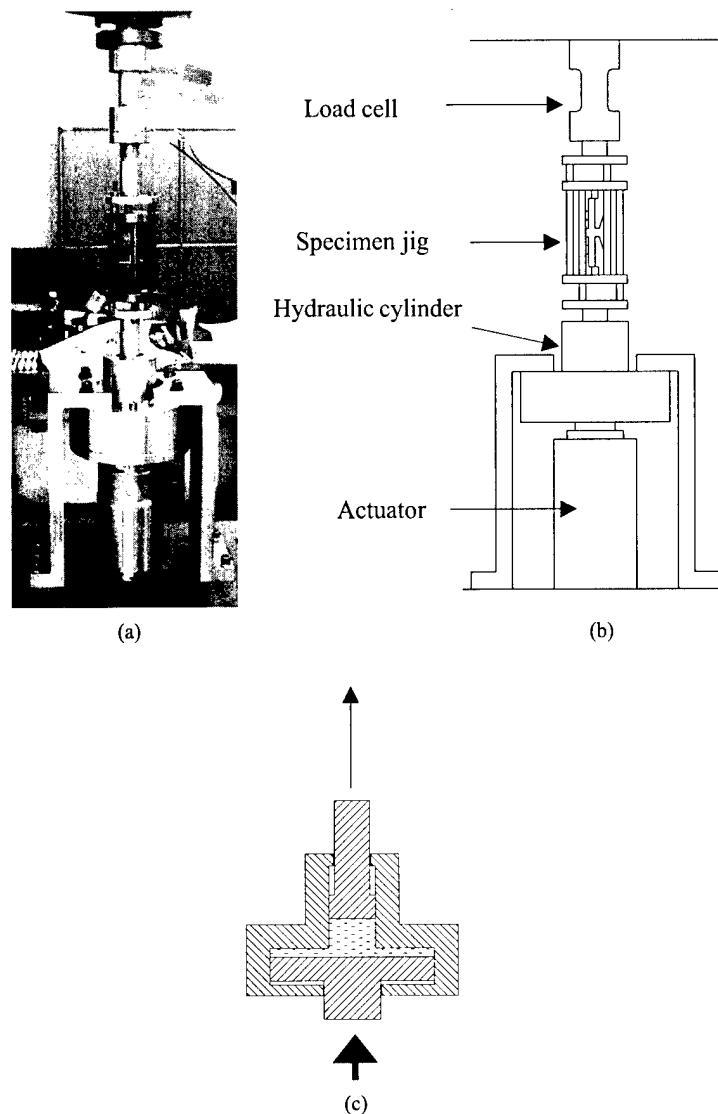


Fig. 1. Experimental setup for tensile and compressive tests with the strain-rate-increase mechanism: (a) photograph of the test equipment; (b) schematic diagram of the test equipment; (c) section of hydraulic cylinders.

shown Fig. 2. The mass and speed of the impactor were 5.6 kg and 0.25–3 m/s, respectively.

Fig. 3 shows the specimen shapes for the tests. The gauge lengths of both the tensile test type composite specimens and compressive type one were 2.5 mm. For the tests, a birdcage type jig was designed, which could insure alignment of compressive loads. And this jig could apply tensile loads to the specimens by pushing the outside cage of the jig as shown in Fig. 4. The columns of the compressive jig were properly lubricated with grease and their frictional loads were calibrated.

For the measurement of loads, the dog bone type load cell with four strain gauges was manufactured. And the load was measured using a DC type strain amplifier (AS2103, NEC, Japan). The measured data were transferred to the IBM-PC using an A/D converter. The measured strength data of the glass fiber epoxy com-

posites whose fiber volume fraction is 60% are shown in Fig. 5. The experiments were performed in the range of 1–200  $\text{s}^{-1}$  strain rate, whose results are shown in Fig. 6.

From the results of Fig. 6, it was found that the strength of glass-epoxy composites increased about 80% at the strain rate of up to 50  $\text{s}^{-1}$  compared to the strain rate of 0.01, which is a normal strain rate during material testing. Using the measured strength results, the energy absorption of glass fiber epoxy composites was calculated with the progressive impact fracture model.

### 3. Progressive impact fracture model [9]

In the present study, the dynamic external load and the energy absorption during the impact of composite were calculated using the progressive impact fracture

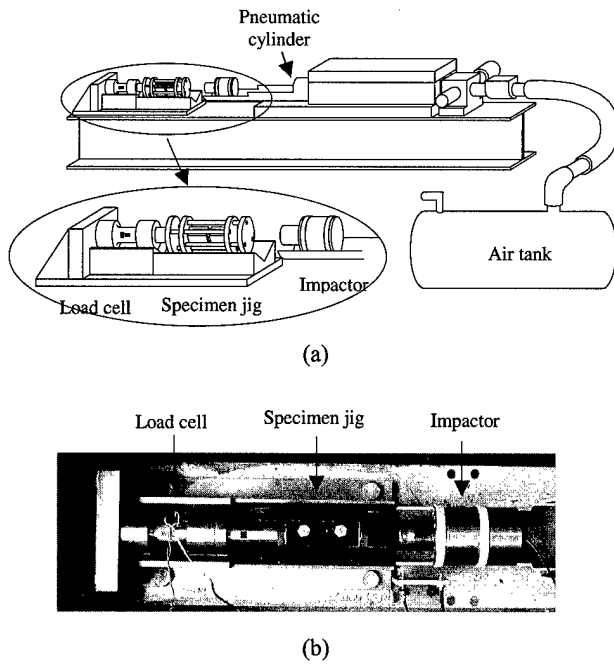


Fig. 2. Experimental setup of the horizontal type impact tester for tensile and compressive tests: (a) schematic diagram of the test equipment; (b) photograph of the main part.

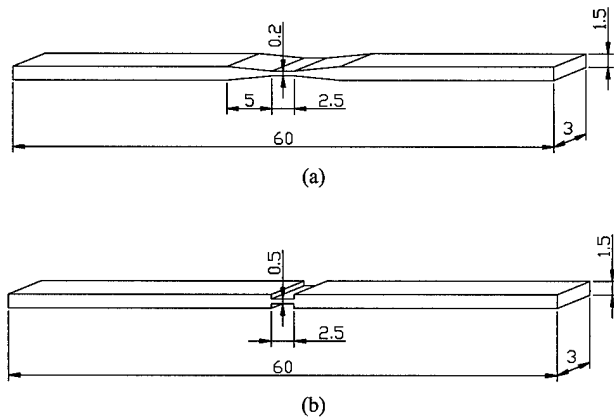


Fig. 3. Specimen dimensions for dynamic tensile and compressive tests: (a) tensile test specimen; (b) compressive test specimen.

model, whose basic scheme is to eliminate the fractured part of the specimen at each divided loading stage. The calculated results were compared with the instrumented Charpy test results (5.21 m/s of tup velocity) and the composite impact beam test results for passenger cars (13 m/s of tup velocity). The Hertzian contact between the composites and the impactor was included in the analysis to predict more accurately the initial slope and peak load during impact. Since the Hertzian contact occurred earlier than the bending fracture, it influenced only the initial dynamic force. The relationship between the Hertzian contact force  $P$  and the indentation  $\alpha$  during the impact of a cylinder on a flat or convex plane

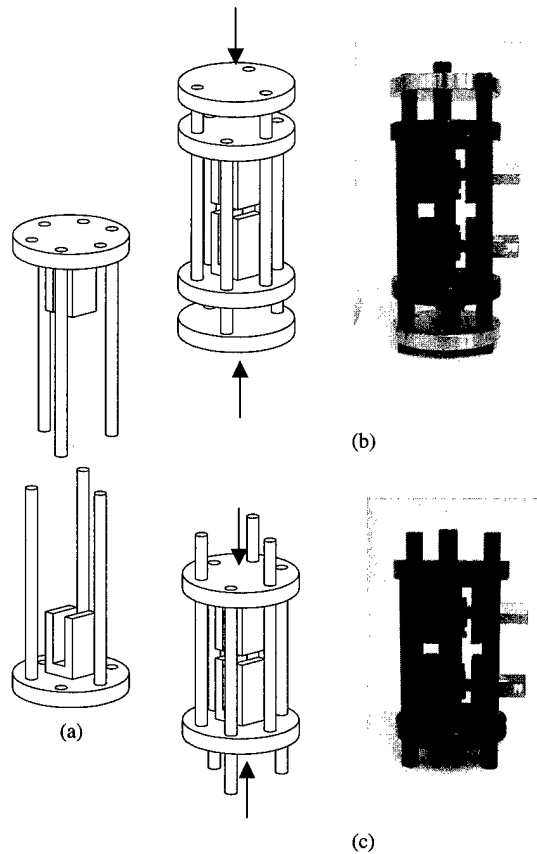


Fig. 4. Jig for tensile and compressive tests: (a) schematic diagram of the disassembled jig; (b) tensile test; (c) compressive test.

surface was approximated as a power index equation, which was the same formulation for the case of a ball on a flat or convex plane surface.

$$P = k_h \alpha^{1.5}. \quad (1)$$

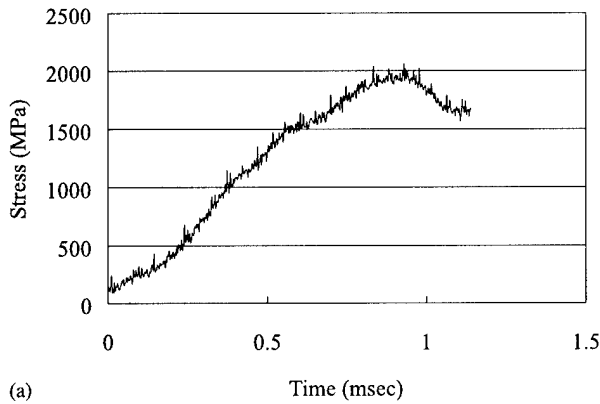
The actual values of  $k_h$  were obtained by the static indentation tests. The indentation amount was measured both by a dial gauge and by an linear variable differential transformer (LVDT) and the test results were fitted using Eq. (1). The nose radius of the loading cylinder for the composite Charpy specimens was 1.5 mm and that for the composite impact beams was 25 mm. During the impact tests, the same size radius tups were used. The Hertzian contact during impact was modeled as a serial connection of high stiffness nonlinear spring of stiffness  $k_h$  to the bending linear spring of stiffness  $k_b$  as shown in Fig. 7.

Using D'Alembert principle and geometric compatibility, Eqs. 2(a)–(c) were obtained.

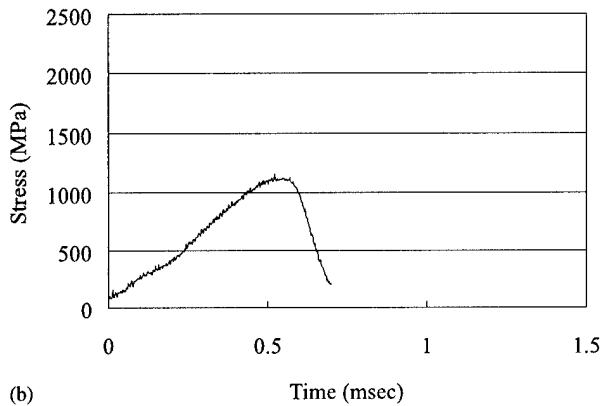
$$m\ddot{y} + k_h \alpha^{1.5} = 0, \quad (2a)$$

$$k_b \delta = k_h \alpha^{1.5}, \quad (2b)$$

$$y = \alpha + \delta, \quad (2c)$$



(a)



(b)

Fig. 5. Curves of dynamic tensile and compressive tests of the glass-epoxy composites: (a) tension ( $\dot{\epsilon} = 50 \text{ s}^{-1}$ ); (b) compression ( $\dot{\epsilon} = 50 \text{ s}^{-1}$ ).

where  $\alpha$  and  $\delta$  are the deflections due to the Hertzian contact and the bending, respectively.

For the simply supported center loading of a beam, the bending stiffness  $k_b$  can be obtained from the mechanics of materials method.

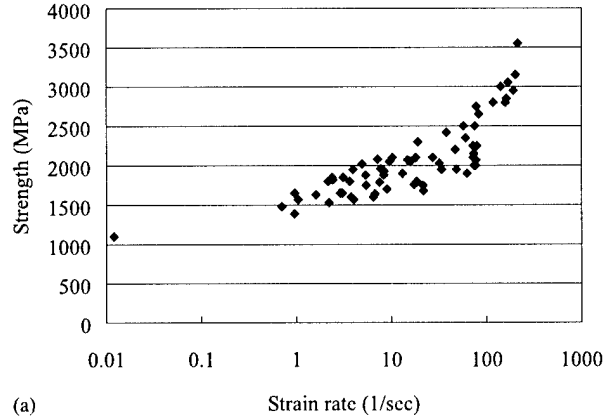
$$k_b = \frac{48EI}{L^3}, \quad (3)$$

where  $E$ ,  $I$  and  $L$  represent the Young's modulus, the second moment of inertia and the span length, respectively.

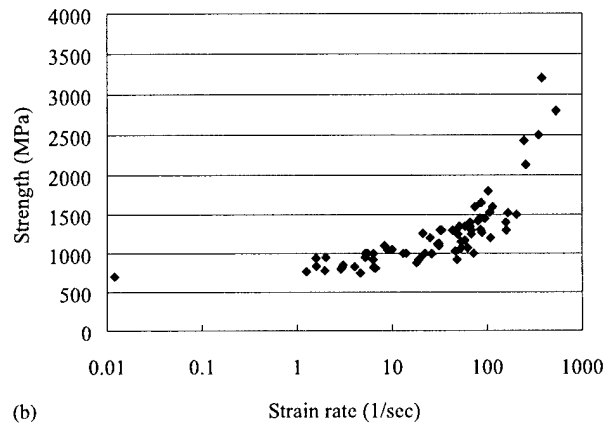
Using the numerical calculations of Eqs. 2(a) and (b), the values of  $\alpha$  and  $\delta$  were fitted as sinusoidal curves to be differentiable  $n$  times with respect to time.

The initial dynamic external load was obtained by multiplying the second derivative of  $y$  by the impactor mass  $m$  as shown in Eqs. 2(a)–(c). When the external load reached the critical value which could bring about the tensile fracture or the compressive fracture or delamination failure as shown in Fig. 8.

The critical loads for the tensile and compressive fractures with respect to strain rates were obtained in the previous chapter, and for the delamination failure the results obtained from the previous short beam shear tests were used [9,10].



(a)



(b)

Fig. 6. Strengths of the glass-epoxy composites w.r.t. strain rates: (a) tension; (b) compression.

After the first fracture of composite specimen, the Hertzian contact was no longer considered. Therefore, the impact test of composites was approximated as a simple spring mass system model as shown in Fig. 7(e) whose governing equation is shown in Eq. (4).

$$m\ddot{y} + k_b y = 0. \quad (4)$$

The analytical solution of Eq. (4) is as follows.

$$y = v \sqrt{\frac{m}{k_b}} \sin \left( \sqrt{\frac{k_b}{m}} t \right). \quad (5)$$

If the tensile or compressive stress in the composite specimen is more dominant than the interlaminar shear stress, the outer hatched regions of Fig. 8(a) would undergo failure, while the delamination failure would occur when the interlaminar shear stress is more dominant as shown in Fig. 8(c). Also, the tensile and compressive parts of specimens would not fail simultaneously because the glass fiber epoxy composite has a larger tensile strength than compressive strength as shown in Fig. 6. Therefore, the times  $t_t$  and  $t_c$  required for which the bending stress in the composite specimen reached the

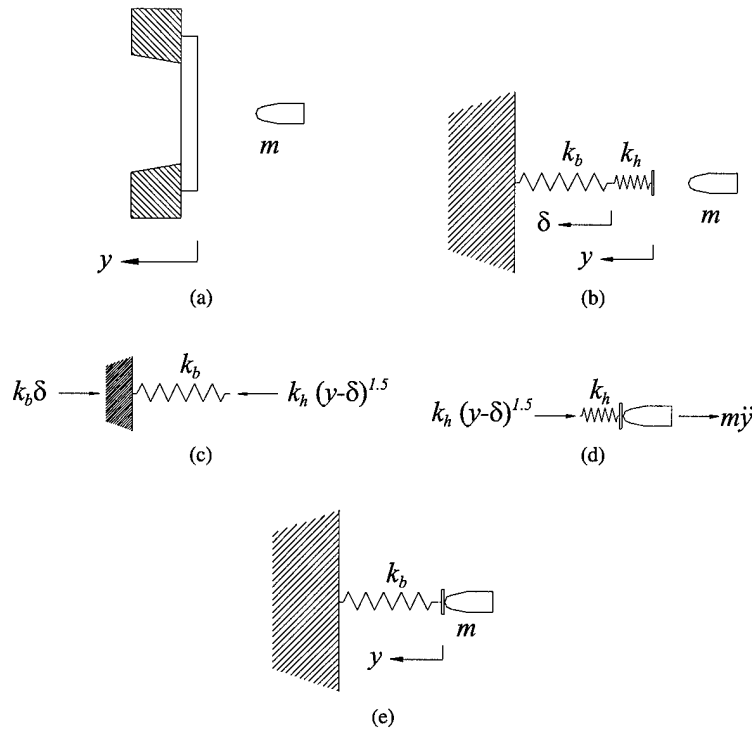


Fig. 7. Schematic diagram of impact between the impactor mass  $m$  and the beam with stiffness  $k_b$  and the Hertzian stiffness  $k_h$ : (a) real model; (b) approximated model; (c) dynamic equilibrium using D'Alembert principle; (d) external loads of the spring due to the Hertzian contact; (e) approximated model after first fracture occurred.

tensile strength and compressive strength, respectively and the time  $t_s$  required for which the interlaminar shear stress were calculated as follows:

$$t_t = \sqrt{\frac{m}{k_b}} \sin^{-1} \left( \frac{4\sigma_t Z}{vL\sqrt{mk_b}} \right), \quad (6a)$$

$$t_c = \sqrt{\frac{m}{k_b}} \sin^{-1} \left( \frac{4\sigma_c Z}{vL\sqrt{mk_b}} \right), \quad (6b)$$

$$t_s = \sqrt{\frac{m}{k_b}} \sin^{-1} \left( \frac{4\tau_d wh}{3v\sqrt{mk_b}} \right), \quad (6c)$$

where  $\sigma_t$ ,  $\sigma_c$  and  $\tau_d$  represent the tensile, compressive and interlaminar shear strengths of the glass-epoxy composite, respectively. Also,  $Z$  represents the sectional modulus (second moment of inertia/vertical length between neutral axis and fractured region),  $w$  and  $h$  the width and the height of specimen, respectively. Eqs. 6(a) and (b) were derived from the bending stress relation, and Eq. 6(c) was derived from the interlaminar shear stress relation. The next step is to choose the minimum time among  $t_t$ ,  $t_c$  and  $t_s$ . If  $t_t$  were selected, then the composite specimens would undergo the fracture of the base part. If  $t_c$  were selected, then the upper part fracture of the composite specimen would occur. If  $t_s$  were selected, then it would go through the interlaminar fracture as shown in Fig. 8(c). Since the dynamic stress-strain curves of composites show slight ductility within

10% strain during the fracture as depicted in Fig. 5, which was similar to the other previous research results [3,6], it was assumed that the real fracture of the composite specimens would initiate at  $1.1t_c$  rather than at  $t_c$  to make the eliminated part by fracture finite. As the fractured part of the composite specimen was eliminated, the Young's modulus, neutral axis, second moment of inertia of the composite specimen and the velocity of the impactor was updated in each iteration. To start the next iteration step, it is essential to determine the lower force ( $F_b$ ) as shown in Fig. 9. Since the displacement of the impactor at the end of the first step is equal to that of the start of the second step, the following relationship holds:

$$F_b = \frac{k_b}{k_a} F_a. \quad (7)$$

As explained above, the iterative procedure resulted in the dynamic load and the energy absorption versus time. The iterative equations for the velocity, displacement and energy absorption of the  $(i+1)$ th step were shown as follows:

$$v_{i+1} = v_i - \frac{F_i + F_{i+1}}{2m} \Delta t_{i+1}, \quad (8a)$$

$$\delta_{i+1} = \delta_i - \frac{v_i + v_{i+1}}{2} \Delta t_{i+1}, \quad (8b)$$

$$E_{i+1} = E_i - \frac{1}{2} m (v_{i+1}^2 - v_i^2). \quad (8c)$$



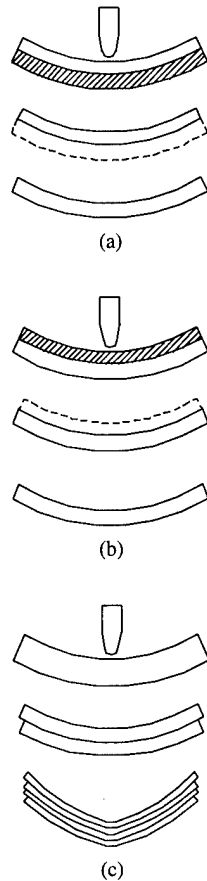
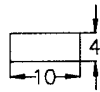
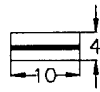
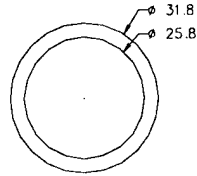
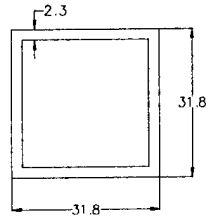


Fig. 8. Progressive impact fracture model of the composite specimen during impact load: (a) tensile fracture; (b) compressive fracture; (c) interlaminar shear stress dominant fracture.

Table 1  
Composite specimens for the impact test

Composite type	Length (mm)	Section (mm)	Experiment
Glass fiber epoxy composite specimen	55		Instrumented Charpy, $m = 12.07$ kg, $v = 5.21$ m/s, nose radius: 1.5 mm
Glass fiber epoxy composite specimen embedded with Kevlar 29 fiber	55		Instrumented Charpy, $m = 12.07$ kg, $v = 5.21$ m/s, nose, radius: 1.5 mm
Glass-epoxy composite beam (tubular type)	520		Pneumatic impact, $m = 13$ kg, $v = 13$ m/s, nose radius: 25 mm
Glass-epoxy composite beam (box type)	520		Pneumatic impact, $m = 13$ kg, $v = 13$ m/s, nose radius: 25 mm

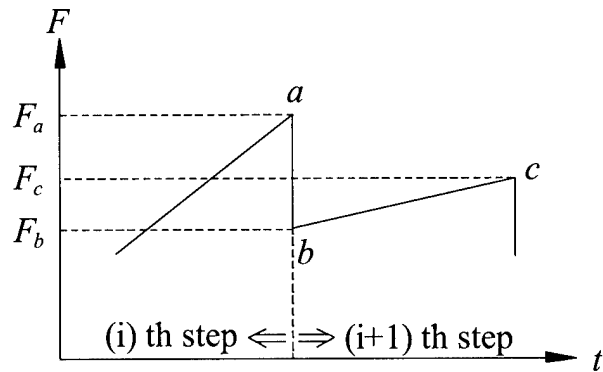


Fig. 9. Schematic force versus time diagram of the progressive impact fracture model for the composite specimen.

During each step of the iteration, the calculated displacement of the impactor was compared to the critical displacement of the impactor  $\delta_c$ , which was defined by the Pythagorean theorem as follows:

$$\delta_c = \sqrt{\left(\frac{L_s}{2}\right)^2 - \left(\frac{L}{2}\right)^2}, \quad (9)$$

where  $L_s$  and  $L$  are the specimen length and the span length, respectively. If the displacement of the impactor were larger than this critical value, the composite specimen would no longer support external load, but slip through the jig. At that time, the iteration would be terminated.

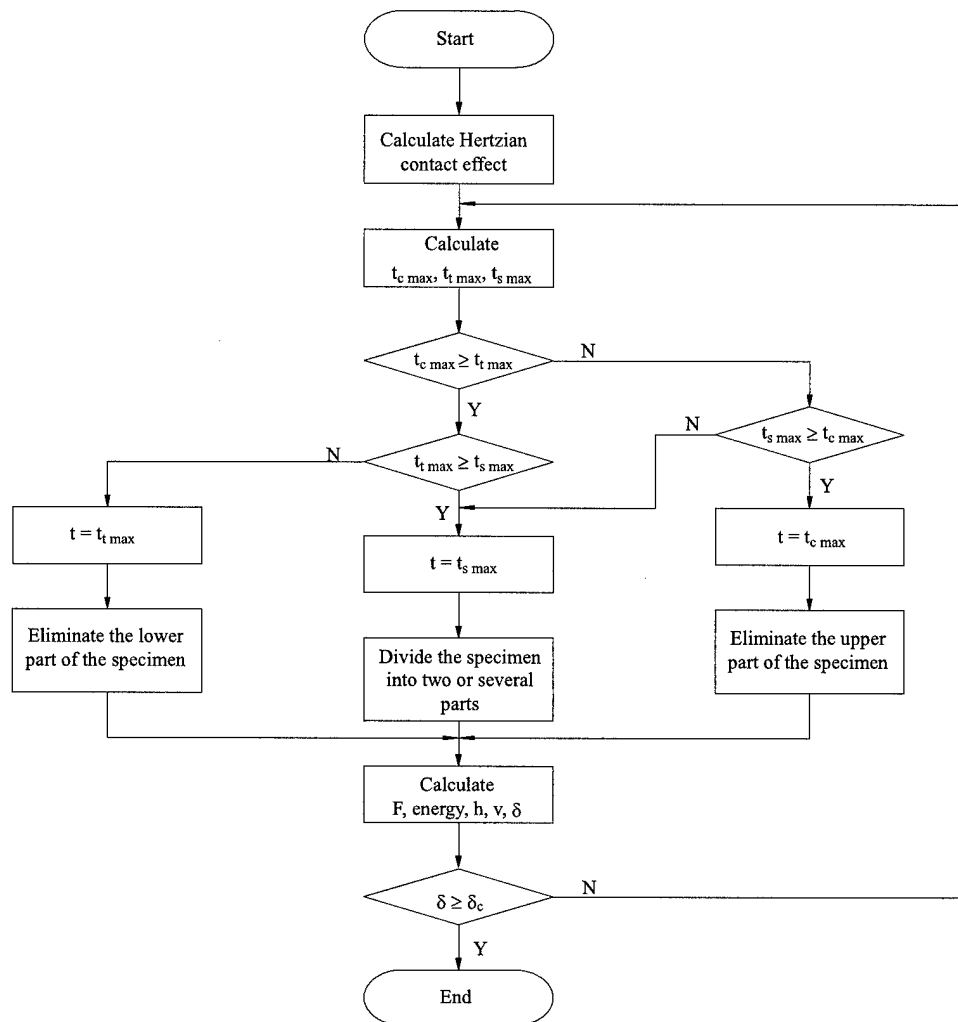


Fig. 10. Flow chart of the progressive impact fracture model.

Table 2  
Mechanical properties of the composite specimen

	Glass-epoxy composite (UGN 150)
Longitudinal tensile modulus (GPa)	43
Longitudinal tensile strength (GPa)	2.0
Longitudinal compressive strength (GPa)	1.2
Major Poisson's ratio	0.28

In the present work, this model was applied to several kinds of composites that were experimented as listed in Table 1. Fig. 10 shows the flow chart of the method. Also, Table 2 indicates the mechanical properties of glass-epoxy composites. The tensile and compressive strengths are the average values which were tested in the range of 10–100 s<sup>-1</sup> strain rate.

### 3.1. Glass-epoxy composite specimens

The static indentation tests were carried out to obtain the Hertzian stiffness and the values of  $k_h$  were obtained

for each specimen. Fig. 11 shows the static indentation test results for each glass-epoxy composite specimen. Then the estimated energy absorption characteristics of glass-epoxy composite specimens w.r.t. fiber volume fractions were compared to the previous test results by the instrumented Charpy impact test [10].

Fig. 12 shows the values  $\alpha$  and  $\delta$  calculated by substituting the experimentally obtained coefficients into Eqs. 2(a)–(c). The calculated values of  $\alpha$  and  $\delta$  were fitted by using sinusoidal functions.

Fig. 13 shows the experimental and estimated results when the fiber volume fraction is 60.6%.

### 3.2. Glass fiber reinforced hybrid composite [9]

In this case, Kevlar 29 fibers were embedded in the mid plane of the composite specimen. Therefore, Eqs. 6(a)–(c) should be modified to allow the embedded material because the neutral axis would not coincide with the centroid even with the symmetrically stacked

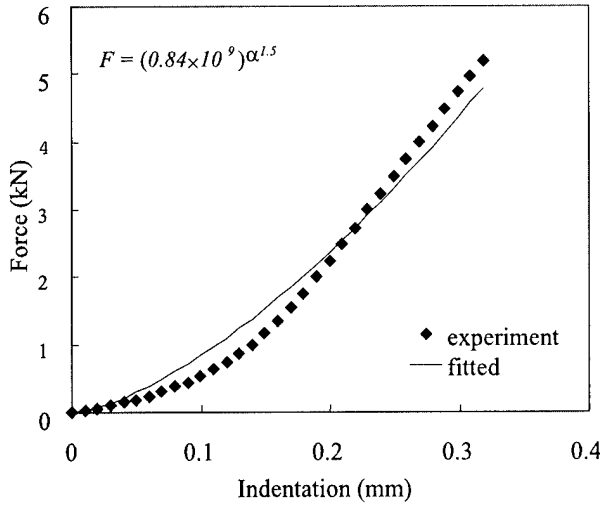
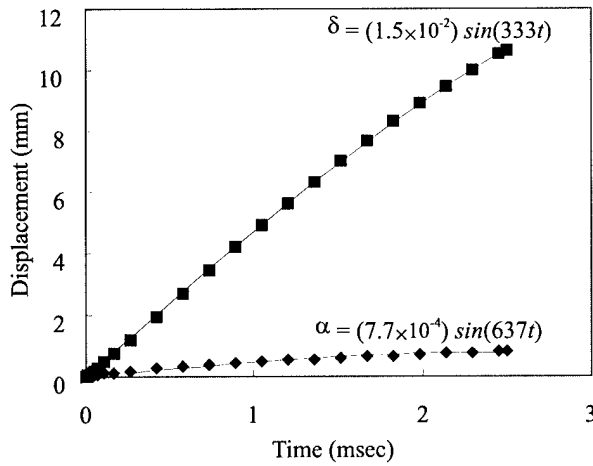
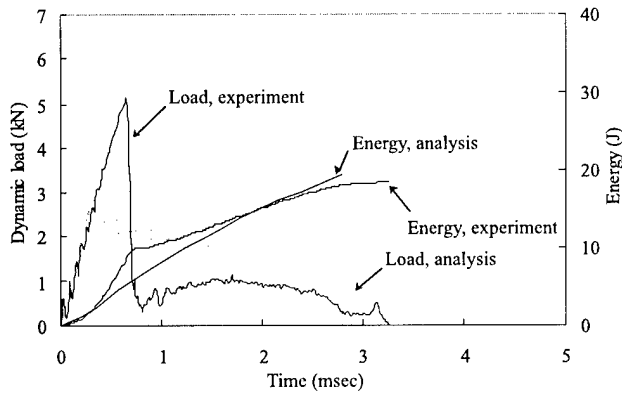
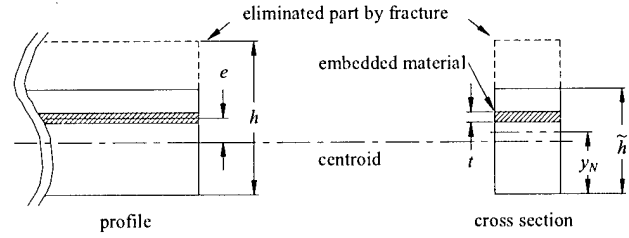
Fig. 11. Static indentation tests of glass-epoxy composites ( $v_f$ : 60.6%).Fig. 12. Static indentation tests of glass-epoxy composites ( $v_f$ : 60.6%).Fig. 13. Analytical and experimental results of the external load and energy absorption for glass-epoxy composites ( $v_f$ : 60.6%).

Fig. 14. Coordinate system for obtaining neutral axis of composite specimens which were embedded dissimilar materials.

laminates after fracture. If  $t$  and  $e$  represent the thickness of the embedded material and the distance from the centroid to the middle surface of the embedded material, respectively as shown in Fig. 14, the neutral axis  $y_N$  that is the distance between the base and the neutral axis of the partially fractured specimen is represented as follows:

$$y_N = \frac{\tilde{h}}{2} \left( \frac{1 - \frac{t}{\tilde{h}} - 2 \frac{et}{\tilde{h}^2} + \frac{tE_{fc}}{\tilde{h}E_{fg}} \left( 1 + 2 \frac{e}{\tilde{h}} \right)}{1 - \frac{t}{\tilde{h}} + \frac{tE_{fc}}{\tilde{h}E_{fg}}} \right), \quad (10)$$

where  $E_{fg}$  and  $E_{fc}$  represent the Young's moduli of glass-epoxy composites and embedded materials, respectively.

Then, the second moment of inertia  $I$  was calculated by the parallel axis theorem. When the middle surface of the embedded material is higher than the centroid,  $e$  is positive, otherwise it is negative. Therefore, the Eqs. 6(a)–(c) were modified as follows:

$$t_t = \sqrt{\frac{m}{k_b}} \sin^{-1} \left( \frac{4\sigma_t I}{vL y_N \sqrt{mk_b}} \right), \quad (11a)$$

$$t_c = \sqrt{\frac{m}{k_b}} \sin^{-1} \left( \frac{4\sigma_c I}{vL(\tilde{h} - y_N) \sqrt{mk_b}} \right), \quad (11b)$$

$$t_s = \sqrt{\frac{m}{k_b}} \sin^{-1} \left( \frac{4\tau_d w \tilde{h}}{3v \sqrt{mk_b}} \right). \quad (11c)$$

In the present study,  $t_c$  was the smallest in all cases of embedded materials. The composite specimen thickness after eliminating the fractured part by compression was calculated as follows:

$$\tilde{h} = y_N + \frac{4\sigma_c I}{Lv \sqrt{mk}} \csc \left( (1.1)t_c \sqrt{\frac{k}{m}} \right). \quad (12)$$

The removed outer part is of the pure glass-epoxy composites, which makes the relative portion of the embedded material increase because the embedded material is located at the middle surface. Accordingly, the Young's modulus, neutral axis, second moment of inertia of the composite specimen and the velocity of the impactor should be updated in each iteration as the

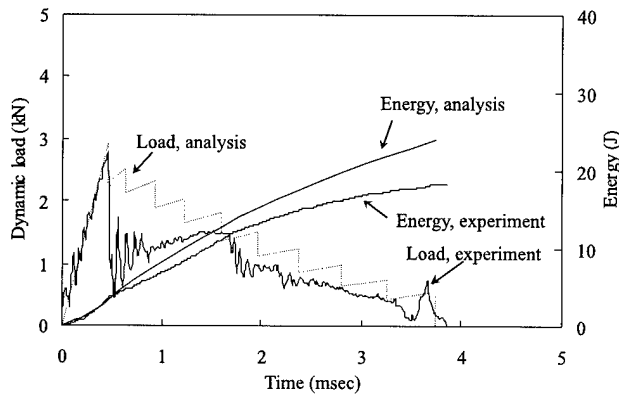


Fig. 15. Analytical and experimental results of the external load and energy absorption of the glass fiber hybrid composites (Kevlar 29,  $v_{f,Kevlar}$ : 8.9%,  $v_{f,Kevlar}$  means the volume fraction of the Kevlar 29 fiber, i.e.,  $v_f = V_{Kevlar}/V_{composite}$ ).

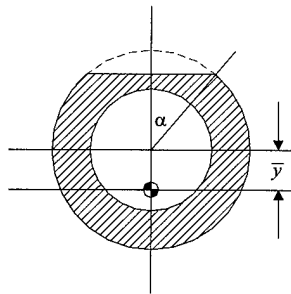


Fig. 16. Coordinate system to obtain the neutral axis of tubular type composite beams.

fractured part of the composite specimen was eliminated. Also, the static indentation tests were carried out to consider the Hertzian contact effect.

Fig. 15 shows the comparison between the Charpy impact test and the progressive impact fracture model.

### 3.3. Glass fiber epoxy composite beams

In this case, beams with two different sections such as tubular and box type as shown in Table 1 were tested. For these beams the centroid coincides with the neutral axis. The second moment of inertia of the tubular type beam as shown in Fig. 16 was calculated as follows:

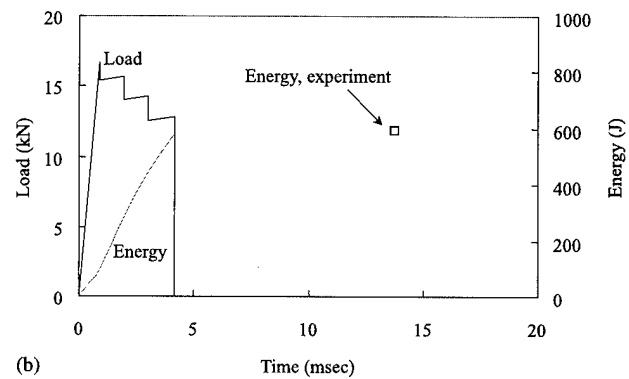
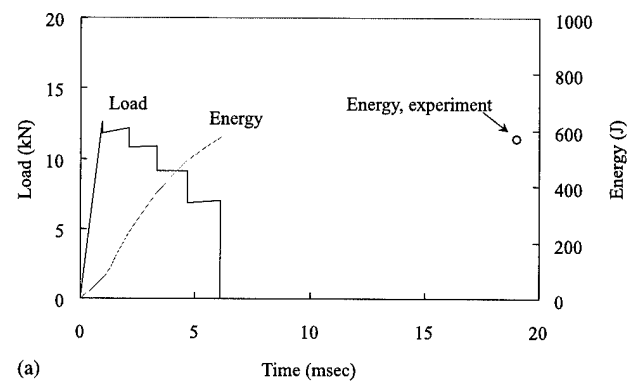


Fig. 17. Analytical results of the external load and energy absorption of the glass fiber epoxy composite beams: (a) tubular type section; (b) box type section.

$$I = \frac{\pi}{64} (d_0^4 - d_i^4) - \frac{d_0^4}{64} (\alpha - \sin \alpha \cos \alpha + 2 \sin^3 \alpha \cos \alpha) - \bar{y}^2 A, \quad (13)$$

where  $y$  and  $A$  can be shown as follows:

$$\bar{y} = \frac{d_0^3 \sin^3 \alpha}{3[4\pi t(d_0 - t) - d_0^2(\alpha - \sin \alpha \cos \alpha)]}, \quad (14a)$$

$$A = \pi t(d_0 - t) - \frac{d_0^2}{4} (\alpha - \sin \alpha \cos \alpha). \quad (14b)$$

The second moment of inertia for the box type beam can be obtained in an analogous manner without any difficulty.

These beams were tested with the specially designed pneumatic impact tester. The impactor mass and incident velocity were 13 kg and 13 m/s (30 mph),

Table 3

The comparison of the estimated impact energy absorption with the experimental ones

Composite beam type	Results	Model	Experiment
Tubular type	Impactor incident velocity, $V_i$ (m/s)	13	13.1
	Impactor final velocity, $V_f$ (m/s)	8.9	8.96
	Energy absorption ratio (%)	53.1	53.2
Box type	Impactor incident velocity, $V_i$ (m/s)	13	12.9
	Impactor final velocity, $V_f$ (m/s)	8.93	8.85
	Energy absorption ratio (%)	52.8	52.9

respectively [8]. Unfortunately the force versus time history during impact was not measured. Instead, the incident and final velocities of the impactor were observed with the help of optical sensors. Also, the static indentation tests were performed to consider the Hertzian contact effects.

Fig. 17 shows the estimated force versus time and the impact energy absorption results of each beam and Table 3 compares the estimated results with the experimental ones.

#### 4. Discussions

It was found that the progressive impact fracture model predicted relatively well the impact energy absorption characteristics of composite structures and the impact duration, however it was unable to predict the peak dynamic load during impact of composite structures. From the results of the modeling, the compressive fracture was predicted to be the dominant failure mode because the compressive strength of glass–epoxy composites is lower than the tensile one, while in the tests, the tensile, compressive and shear failures occurred simultaneously. From the experiments and estimation, it may be conjectured that the failure of fiber composites occurs at the moment the strain reaches the critical value rather than when the stress reaches the strength, because the real dynamic fractures of composites occur with slightly ductile behavior at high strain rate. Therefore, it may be helpful to investigate the failure strain of composites with respect to strain rates.

#### 5. Conclusion

In this work, the tensile and compressive strengths of glass fiber epoxy composite were measured with the strain rate of  $1\text{--}200\text{ s}^{-1}$  in order to investigate the effect of strain rate on the strength using strain-rate-increase mechanisms. From the experiments, it was found that the dynamic strength of glass–epoxy composites at the strain rate of  $50\text{ s}^{-1}$  was 80% higher than that of the static.

In order to estimate the impact energy absorption characteristics of fiber composite materials, the progressive impact fracture model was proposed. The model predicted relatively well the impact energy absorption characteristics of composites, however, it was unable to predict accurately the dynamic peak load during the impact of composite structures, which might be improved if the different failure strains of composites depending on the strain rate were considered.

#### Acknowledgements

This work was supported by KOSEF (Korea Science and Engineering Foundation) under Grant No. 98-0200-01-01-5 and in part by BK21 (Brain Korea 21) Project. Their support is gratefully acknowledged.

#### References

- [1] Adams DF, Miller AK. An analysis of the impact behavior of hybrid composite materials. *Mater Sci Engng* 1975;19:245–60.
- [2] Mallick PK, Broutman LJ. Static and impact properties of laminated hybrid composites. *J Testing and Evaluation* 1977;5:190–200.
- [3] Harding J, Welsh LM. A tensile testing technique for fibre-reinforced composites at impact rates of strain. *J Mater Sci* 1983;18:1810–26.
- [4] Arnold WS, Madjidi S, Marshall IH, Robb MD. Low velocity impact of inclined CSM composite laminates. In: *Proceedings of the International Conference on Advanced Composite Materials*. The Minerals, Metals & Materials Society, 1993. p. 617–22.
- [5] Jenq ST, Sheu SL. High strain rate compressional behavior of stitched and unstitched composite laminates with radial constraint. *Comp Struct* 1993;25:427–38.
- [6] Plastinin AV, Sil'vestrov VV. Dynamic compressive strength of epoxy composites. *Mech Comp Mater* 1995;31:549–53.
- [7] Sun CT, Potti SV. A simple model to predict residual velocities of thick composite laminates subjected to high velocity impact. *Int J Impact Engng* 1996;18:339–53.
- [8] Cheon SS, Lee DG, Jeong KS. Composite side door impact beams for passenger cars. *Comp Struct* 1997;38:229–39.
- [9] Cheon SS, Lim TS, Lee DG. Impact energy absorption characteristics of glass fiber hybrid composites. *Comp Struct* 1999;46:267–78.
- [10] Lee DG, Cheon SS. Impact characteristics of glass fiber composites with respect to fiber volume fraction. *J Comp Mater* (accepted).

# Experimental and computed natural frequencies of square pultruded GRP plates: effects of anisotropy, hole size ratio and edge support conditions

G.J. Turvey \*, N. Mulcahy, M.B. Widden

*Engineering Department, Faculty of Applied Sciences, Lancaster University, Bailrigg, Lancaster LA1 4YR, UK*

## Abstract

Experiments have been carried out to determine the free vibration frequencies and mode shapes of 3.2 mm thick, pultruded GRP, square plates with six combinations of clamped (C), simply supported (S) and free (F) edge supports. Comparison of experimental and theoretical/numerical frequencies confirms that thin homogeneous orthotropic/anisotropic plate theory provides a reasonable model for predicting the free vibration response of pultruded GRP plates. Additional vibration experiments were carried out on plates with central circular cutouts. The hole size ratios were varied from about 0.1 to 0.4 for three combinations of clamped (C) and simply supported (S) edge conditions. Finite-element (FE) frequency and mode shape predictions based on orthotropic plate theory were again shown to be in reasonable agreement with the experimental frequencies and modes. © 2000 Elsevier Science Ltd. All rights reserved.

## 1. Introduction

Over the past three decades many papers have been published on the free vibration behaviour of laminated composite plates. Their existence is due to the widespread use of laminated carbon fibre reinforced plastic (CFRP) and, to a lesser extent, glass reinforced plastic (GRP) plates in aerospace structures and components and the need to understand their free vibration response characteristics. The theoretical and experimental studies reported in these papers have shown that classical, first- and third-order laminated anisotropic plate theory may be used to model, with good accuracy, the free vibration response of both thin and moderately thick plates under a variety of edge support conditions. The fact that laminated anisotropic plate theory provides a sound basis for modelling the free vibration response of CFRP plates is, in no small measure, attributable to the rigorous quality control procedures used in their fabrication. Moreover, the high costs of these procedures can be justified in the aerospace context.

In the construction sector, however, low cost is one of the primary factors determining whether or not a par-

ticular type of material is used. Consequently, GRP is used more widely than CFRP. The manufacturing processes used to make GRP components for construction applications are generally simpler than for aerospace applications and variability in material properties is greater.

Pultrusion [1] is a low-cost process, which is used to make structural grade GRP profiles and plate for use in construction. The nature of the process dictates that it is much more difficult to achieve the same degree of control over the regularity and alignment of the fibre architecture than is possible with automated tape laying and other *leading edge* processes used in the manufacture of aerospace composites. Moreover, it is arguable that the types of glass reinforcement, viz., rovings (aligned fibre bundles) and continuous filament mat (CFM), used in pultruded GRP components do not produce such a well-defined laminated architecture, as in aerospace composites. In pultruded plate, especially, the discrete rovings have a lenticular cross-section, which causes undulations in the CFM. Furthermore, the undulations are not regular because the roving spacing tends not to be perfectly uniform due to friction-induced transverse movements between the CFM and rovings as they pass through the pultrusion die. These fibre architecture differences between composites used for aerospace and construction applications cast doubt on the

\* Corresponding author. Tel.: +44-01524-593088; fax: +44-01524-381707.

E-mail address: g.turvey@lancaster.ac.uk (G.J. Turvey).

adequacy of both laminated and homogeneous anisotropic plate theory as a suitable basis for modelling the free vibration response of pultruded GRP plates. To the best of the authors' knowledge, this matter has not been addressed. Therefore, in this paper, it is demonstrated, via a comparison of experimentally determined and theoretically predicted plate frequencies, that homogeneous anisotropic plate theory is indeed able to provide reasonable estimates of the free vibration frequencies of pultruded GRP plates under a variety of edge support conditions. Moreover, as little appears to have been published on the free vibration response of pultruded GRP plates, details are presented of a supplementary investigation, which explores the influence of several important factors on the vibration response of square plates. These factors are: edge support conditions, hole size ratio (for central circular cutouts) and anisotropy (defined in terms of the orientation of the pultrusion axis with respect to plate axes).

## 2. Pultruded GRP plate material properties

Structural grade GRP plate is manufactured by several pultruders in North America and Europe. The plate thicknesses vary from about 3.2 to 25.4 mm. The width of the plate is typically 1219 mm. It may be made to any required length, though it is usually supplied as 2438 mm  $\times$  1219 mm boards. Two forms of E-glass reinforcement are used in the plate. Rovings provide the longitudinal strength and stiffness and CFM, above and below the rovings, provides the transverse stiffness and strength. Polyester and vinylester resins are used as the primary matrix material, which supports the fibres and provides the means of load transfer between them. Some pultruders also use inert fillers, e.g., clay, to reduce the quantity of resin in their products. The pultruded plate used in the present plate vibration tests was 3.2 mm thick EXTREN<sup>®</sup> 525 Series plate manufactured by Strongwell of Bristol, Virginia, USA. (Note: reference to a product trade name in this paper is solely for the purposes of factual accuracy and does not imply endorsement of the product.) There are two roving layers in the 3.2 mm thick pultruded GRP plate – one near the upper and the other near the lower surface. The rovings

are clearly discernible by the small undulations, typically 0.1 mm high, they produce in the plate surfaces. Measurements between the centres of these undulations suggest that the roving spacing is not uniform and may vary between 10 and 20 mm.

Resin burn-off tests on 6.4 mm thick EXTREN<sup>®</sup> 500 Series plate have shown the volume percentages of glass, resin and filler to be approximately 30%, 60% and 10%, respectively. Although similar burn-off tests have not been undertaken on 3.2 mm thick material, it is assumed that the glass, resin and filler volume percentages would be similar.

Four strips – two longitudinal (parallel to the direction of the rovings) and two transverse – were cut from the 3.2 mm thick plate to provide coupons for tension testing. The nominal coupon size was 250  $\times$  25  $\times$  3.2 (all dimensions in mm). A biaxial strain gauge (with its sensitive axes along and normal to the length of the coupon) was bonded to the centre of one face and a uniaxial gauge (with its sensitive axis along the length of the coupon) was bonded to the centre of the other face. The longitudinal coupons were loaded in 1 kN increments to a maximum load of 7 kN and the transverse coupons were loaded to 3.2 kN in 0.4 kN increments. Strains were recorded immediately after the application of each increment of load. The longitudinal and transverse elastic moduli values and Poisson's ratios determined from the tension coupon tests are listed in Table 1 together with the values taken from the manufacturer's design manual [2].

It should be appreciated that the manufacturer's moduli values given in Table 1 are minimum values for use in design. Experience has shown that they may be up to 20% lower than the value measured in a single coupon test. Therefore, as an important aspect of the work presented here is to compare theoretical and experimental vibration frequencies, it is sensible to use moduli determined from coupon tests rather than design values. However, as no shear modulus tests were undertaken on the 3.2 mm thick pultruded plate, it has been necessary to use the manufacturer's value for the shear modulus in the numerical analyses.

The mass density per unit area of the pultruded GRP plate is required for the subsequent closed-form and finite-element (FE) orthotropic and anisotropic plate

Table 1  
Comparison of elastic moduli for 3.2 mm thick EXTREN<sup>®</sup> 525 series pultruded GRP plate

$E_L$ , longitudinal modulus (KN/mm <sup>2</sup> )	$E_T$ , transverse modulus (KN/mm <sup>2</sup> )	$G_{LT}$ , shear modulus (KN/mm <sup>2</sup> )	$\nu_{LT}$ , longitudinal Poisson's ratio	$\nu_{TL}$ , transverse Poisson's ratio	Comments
14.21	8.91		0.28	0.21	Tension coupon values
14.13	8.85		0.31	0.20	
12.40	4.83	2.93 <sup>a</sup>	0.31	0.29	Manufacturer's minimum values

<sup>a</sup> Value for a pultruded section.

analyses. The manufacturer's density value of  $1771.5 \text{ kg/m}^3$  given in [2] has been used to determine the mass density per unit area of the 3.2 mm thick GRP plate as  $5.67 \text{ kg/m}^2$ .

### 3. Parameters investigated in plate vibration tests

In this study, the effects of three principal types of parameter on the free vibration frequencies of 3.2 mm thick pultruded GRP square plates were investigated. The parameters were: the degree of material orthotropy (defined in terms of the orientation of the rovings with respect to one of the plate edges), the combination of plate edge support conditions and the diameter of the central circular cutout.

Three cases of orthotropy/anisotropy were investigated, viz., (1) longitudinal (rovings parallel to the  $x$ -axis), (2) transverse (rovings at  $90^\circ$  to the  $x$ -axis) and (3)  $45^\circ$  (rovings oriented at  $45^\circ$  to the  $x$ - and  $y$ -axes). These three cases are shown in Fig. 1. Cases (1) and (2) correspond to the two extremes of orthotropy and case (3) corresponds to the situation in which the plate's anisotropy is a maximum. The effects of the three orthotropy/anisotropy cases were investigated for six combinations of plate edge support conditions. The latter are illustrated in Fig. 2 and range from plates with all edges clamped (C–C–C–C) to cantilever plates (C–F–F–F).

The second part of the work was concerned with the effect of five central circular cutout sizes on the free vibration frequencies of square plates with all edges clamped (C–C–C–C), three edges clamped and one simply supported (C–C–C–S) and opposite pairs of edges clamped and simply supported (C–S–C–S). In all cases, the rovings were normal to one pair of clamped edges. The hole diameters range from 25 to 125 mm in steps of 25 mm, corresponding to hole size (hole diameter to plate side length) ratios of 0.083–0.417.

### 4. Details of the plate vibration test rig and the evaluation of natural frequencies and mode shapes

The plate vibration test rig was both conventional and simple in so far as an electrodynamic vibrator was

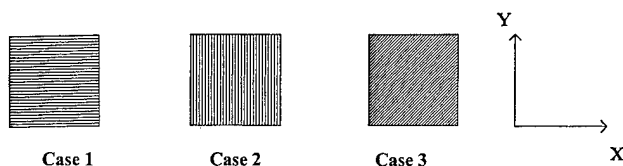


Fig. 1. Three cases of material orthotropy/anisotropy: (a) case (1) – longitudinal (rovings parallel to the  $x$ -axis); (b) case (2) – transverse (rovings parallel to the  $y$ -axis) and (c) case (3) –  $45^\circ$  (rovings equally inclined to the  $x$ - and  $y$ -axes).

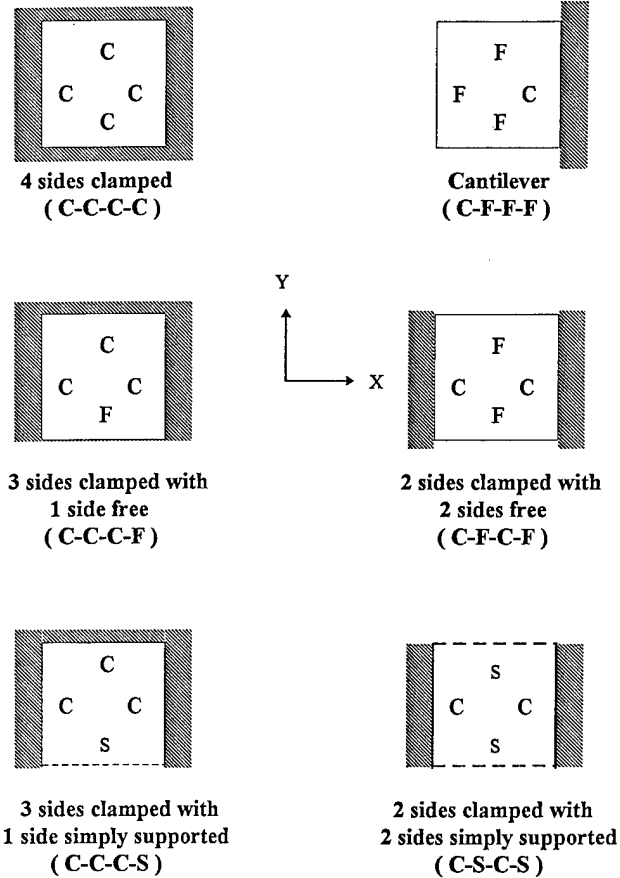


Fig. 2. Six combinations of clamped (C), simply supported (S) and free (F) edge conditions for 3.2 mm thick, pultruded GRP, square plates.

used to induce sinusoidal oscillations in the GRP plates. A variable frequency oscillator and power amplifier were used to adjust the frequency and amplitude of the plate vibrations. The vibration amplitudes were measured with an accelerometer connected to a charge amplifier and an oscilloscope. Plate 1 shows a view of the test apparatus mounted on a rigid cast iron bed plate which, in turn, was supported on mass concrete blocks.



Plate 1. Test rig for measuring the natural frequencies of pultruded GRP plates.



The plate support arrangement is of interest, because of its flexibility. It was designed to allow knife edges (representing simple support conditions) to be interchanged with rigid bars (representing clamped edges) so that six edge support combinations, including free edges, could be tested with the same rig. However, even though each plate had a span of 300 mm with respect to the  $x$ - and  $y$ -axes, their overall dimensions differed according to the particular combination of edge support conditions used and the need to allow for the 30 mm width of the rigid bars used to simulate clamped edges. Thus, for example, the cantilever plates (C–F–F–F) were  $330 \times 300$  mm, whereas plates with three clamped edges and one free edge (C–C–C–F) were  $360 \times 300$  mm overall.

The procedure used to identify the free vibration frequencies of each plate tested was simple and reasonably effective. The plate was vibrated at frequencies above and below the resonant frequency. The vibration amplitudes measured at each of these frequencies were plotted against frequency in order to bound the natural frequency. Knowing the natural frequency approximately, the procedure was repeated using smaller frequency increments above and below the natural frequency to allow more accurate bounds to the natural frequency to be determined. Fig. 3 shows an example of the type of frequency – vibration amplitude plot obtained with this simple technique. In general, it was found, providing reasonable care was taken with the

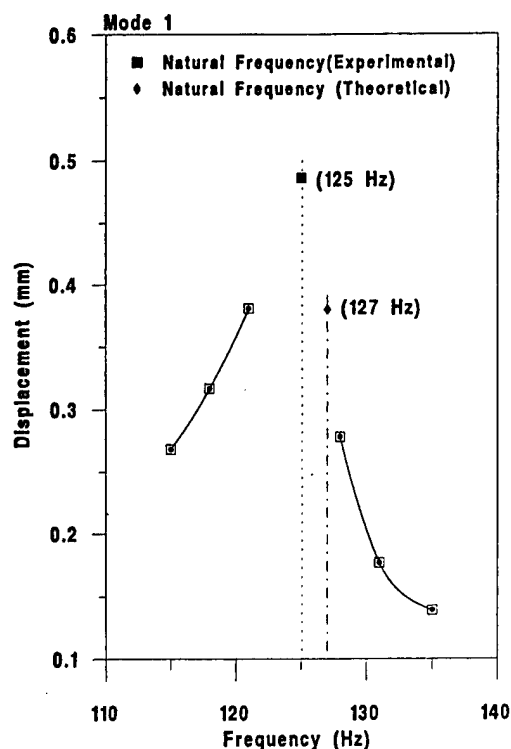


Fig. 3. Example of a frequency versus displacement plot used to determine the experimental free vibration frequencies (C–C–C–S (transverse)).

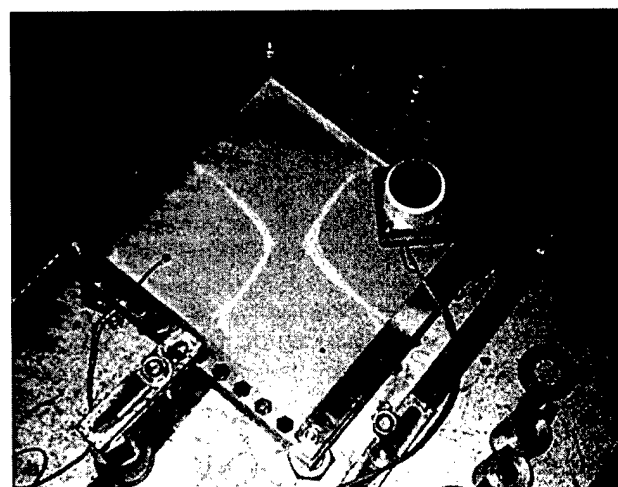
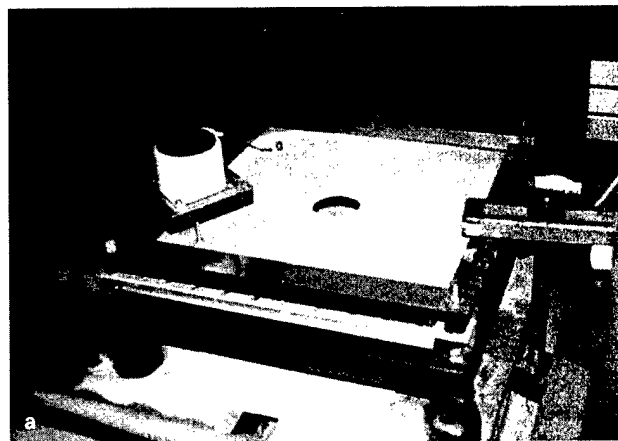


Plate 2. Identification of nodal lines through migration of fine sand: (a) plate with a central circular hole and (b) plate without a hole.

vibration tests, that only a few natural frequencies were missed (see Table 5), despite the simple nature of the procedures used.

The vibration modes were identified using Chladni's simple but effective method. With the plate vibrating at its resonant frequency, fine sand was scattered on its upper surface and allowed to migrate to the nodal lines. When the sand migration appeared to have stopped, the electrodynamic vibrator was switched off and the lines of sand, representing nodal lines, were sketched, measured and photographed. Plate 2 shows examples of the nodal lines obtained for two plates, one with and the other without a central circular cutout. Although this technique is far from perfect, it does provide a reasonable picture of the nodal lines, which, in general, may be correlated with the theoretical nodal lines without too much difficulty.

## 5. Computation of free vibration frequencies

The free vibration frequencies of the pultruded GRP, square plates have been computed on the basis of ho-

homogeneous orthotropic and anisotropic thin plate theory. Approximate closed-form expressions were used to compute the natural frequencies of the plates without free edges and central circular cutouts. For the plates with cutouts and/or free edges FE analysis was used to compute the natural frequencies. Further details of these two approaches for evaluating the plate vibration frequencies are given below.

### 5.1. Approximate closed-form frequency calculations

Hearmon [3] used Rayleigh's method to derive a closed-form expression for the free vibration frequency of homogeneous anisotropic rectangular plates with combinations of simply supported and clamped edges. The frequency formula obtained by Hearmon may be expressed as

$$\omega^2 = \frac{1}{\rho} \left( \frac{A^4 D_x^*}{a^4} + \frac{B^4 D_y^*}{b^4} + \frac{2CD_{xy}^*}{a^2 b^2} \right), \quad (1)$$

where  $\omega$  is the circular frequency,  $\rho$  the mass per unit area of the plate material,  $a$  the plate length,  $b$  the plate width,  $D_x^*$ ,  $D_y^*$  and  $D_{xy}^*$  the plate flexural stiffnesses with respect to the principal material axes and  $A$ ,  $B$ , and  $C$  are coefficients which depend on the number of longitudinal and transverse waves ( $m, n$ ) in the vibration mode. The expressions for the plate stiffnesses are

$$D_x^* = D_x = \frac{E_L t^3}{12(1 - \nu_{LT}\nu_{TL})};$$

$$D_y^* = \frac{E_T t^3}{12(1 - \nu_{LT}\nu_{TL})}; \quad D_{xy}^* = D_{xy} = D_x \nu_{TL} + 2D_k;$$

$$D_k = \frac{G_{LT} t^3}{12}.$$

In the above definitions of the plate stiffnesses,  $t$  denotes the plate thickness. These stiffness expressions apply to plates with rovings aligned parallel or transverse to the  $x$ -axis, i.e., cases (1) and (2) (see Fig. 1). For plates with

rovings at  $45^\circ$  to the  $x$ -axis, i.e., case (3), the following modified expressions have to be used

$$D_x^* = \frac{1}{4}(D_x + D_y + 2D_{xy}) = D_y^*;$$

$$D_{xy}^* = \frac{1}{4}(3D_x + 3D_y - 2D_{xy}).$$

The coefficients,  $A$ – $C$ , in Eq. (1) are defined in Table 2, which has been taken from [3]. Using a value of  $t = 3.2$  mm and average values for the longitudinal and transverse elastic moduli, given in Table 1, the plate flexural stiffnesses,  $D_x^*$  etc., have been evaluated. These have then been substituted into Eq. (1) to calculate the theoretical frequencies for plates with C–C–C–C, C–C–C–S and C–S–C–S edge conditions. The values obtained for the first 10 natural frequencies are listed in Table 3.

### 5.2. Finite-element frequency calculations

The MSC/NASTRAN FE software [4] has been used to compute the free vibration frequencies of the square pultruded GRP plates with and without cutouts. The plates were modelled with the CQUAD4 element [5], which is a four node, shear deformable general quadrilateral plate element with five degrees of freedom per node – three translations and two out-of-plane rotations. With this element, the clamped edge (C) condition is simulated by setting all five degrees of freedom to zero at a boundary node. Likewise, the simply supported edge (S) condition is defined by setting the three translations to zero at a boundary node. For the free edge (F) condition, all five degrees of freedom remain unconstrained at a boundary node.

The MSC/NASTRAN FE software was first used to compute the free vibration frequencies of a square simply supported isotropic thin plate for a range of uniform mesh sizes. The purpose of these computations was to establish a suitable mesh size for the subsequent

Table 2  
Coefficients used in Eq. (1) for various plate edge support combinations<sup>a</sup>

Plate edge support conditions	$A$	$B$	$C$	$m$	$n$
C–C–C–C	4.730	4.730	151.3	1	1
	4.730	$\varepsilon_2$	$12.30\varepsilon_2(\varepsilon_2 - 2)$	1	2, 3, 4, ...
	$\gamma_2$	4.730	$12.30\gamma_2(\gamma_2 - 2)$	2, 3, 4, ...	1
	$\gamma_2$	$\varepsilon_2$	$\gamma_2\varepsilon_2(\gamma_2 - 2)(\varepsilon_2 - 2)$	2, 3, 4, ...	1, 2, 3, 4, ...
C–C–C–S	4.730	$\varepsilon_1$	$12.30\varepsilon_1(\varepsilon_1 - 2)$	1, 2, 3, ...	1
	$\gamma_2$	$\varepsilon_1$	$\gamma_2\varepsilon_1(\gamma_2 - 2)(\varepsilon_1 - 2)$	1, 2, 3, ...	2, 3, 4, ...
C–S–C–S	4.730	$\varepsilon_0$	$12.30\varepsilon_0^2$	1	1, 2, 3, ...
	$\gamma_2$	$\varepsilon_0$	$\gamma_2\varepsilon_0^2(\gamma_2 - 2)$	2, 3, 4, ...	1, 2, 3, ...

<sup>a</sup> The terms  $\gamma_i$  and  $\varepsilon_i$  ( $i = 0, 1$  and  $2$ ) are defined as follows:

$$\gamma_0 = m\pi; \quad \gamma_1 = \left(m + \frac{1}{4}\right)\pi; \quad \gamma_2 = \left(m + \frac{1}{2}\right)\pi, \quad \varepsilon_0 = n\pi; \quad \varepsilon_1 = \left(n + \frac{1}{4}\right)\pi; \quad \varepsilon_2 = \left(n + \frac{1}{2}\right)\pi.$$

Table 3

Vibration frequencies (Hz) of 3.2 mm thick, pultruded GRP, square plates obtained from Eq. (1) for three cases of material orthotropy/anisotropy and three combinations of clamped (C) and simply supported (S) edge conditions

Mode No.	C-C-C-C	C-C-C-S		C-S-C-S		C-C-C-C	C-C-C-S	C-S-C-S
		Long.	Trans.	Long.	Trans.	45°	45°	45°
1	150.39	136.26	127.54	126.73	112.06	149.54	133.21	121.08
2	284.49	247.23	271.22	216.17	235.41	304.30	264.73	230.91
3	330.18	322.66	278.94	316.63	261.64	304.30	294.69	285.41
4	444.91	418.39	403.69	391.71	370.94	458.77	428.48	402.49
5	502.75	444.20	493.65	397.28	464.27	541.15	479.96	424.33
6	610.52	597.88	533.63	556.22	486.28	541.15	534.13	525.64
7	646.42	605.25	613.90	600.40	584.40	647.21	645.14	598.77
8	713.97	694.18	644.42	677.73	588.99	766.86	672.20	650.12
9	798.86	720.24	791.61	678.50	785.29	857.54	775.49	698.81
10	897.38	858.46	836.97	798.92	787.20	857.54	851.69	843.50

Table 4

Convergence of approximate FE frequencies (Hz) with mesh refinement for an isotropic, simply supported, square plate ( $a = b = 0.3$  m,  $t = 0.0032$  m,  $E = 210 \times 10^3$  N/mm<sup>2</sup>,  $\nu = 0.3$  and  $\rho = 7860$  kg/m<sup>3</sup>)

Uniform mesh size	Vibration mode number					
	1	2	3	4	5	6
2 × 2	207.7	11188.8	11188.8			
4 × 4	181.8	517.5	517.5	871.8	1311.7	1317.0
8 × 8	175.6	452.8	452.8	725.3	965.2	965.2
16 × 16	174.3	439.1	439.1	700.0	891.8	891.8
32 × 32	174.2	436.4	436.4	696.5	876.1	876.1
64 × 64	174.0	435.6	435.6	695.6	872.3	872.3
Exact solution <sup>a</sup>	174.7	436.8	436.8	698.9	873.6	873.6

<sup>a</sup> Based on thin (shear-rigid) plate theory.

pultruded plate vibration frequency analyses. The simply supported isotropic plate was chosen, because its natural frequency is known exactly. The frequency of this plate was determined using square meshes ranging from 2 × 2 (coarse) to 64 × 64 (fine) extending over the whole plate. The FE analysis frequencies for the first six vibration modes are shown in comparison to the exact

frequency values in Table 4. The rate of convergence with mesh refinement for the first mode of vibration is also shown in Fig. 4. It is evident from Table 4 that when an 8 × 8 mesh is used, the computed frequency differs by less than 1 Hz from the exact frequency. Furthermore, Fig. 4 shows that as the mesh is refined beyond 16 × 16, the FE analysis predicts a frequency lower than the exact value. This is because the exact frequency is based on thin and *not* shear deformation plate theory. Based on the results of this frequency convergence study for the simply supported, isotropic, square plate, it was decided to use a uniform 32 × 32 mesh for all of the FE free vibration analyses of pultruded GRP plates without holes. 32 × 32 meshes were also used for the free vibration analyses of the pultruded GRP plates with central circular cutouts. For the analyses, the meshes were not uniform, but each mesh was arranged so that the elements were roughly similar in shape and did not have any large obtuse angles.

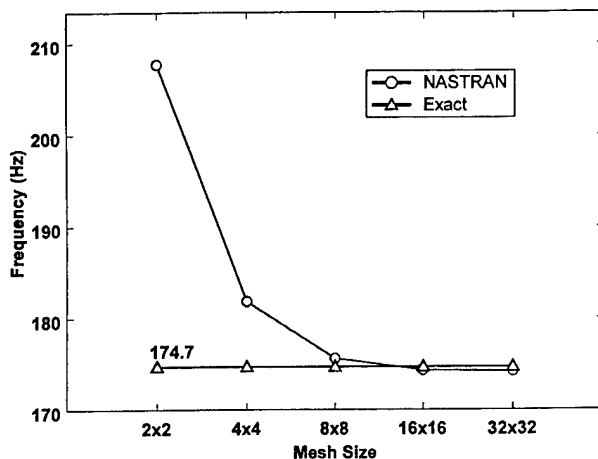


Fig. 4. Convergence of the FE first mode free vibration frequency with mesh refinement (isotropic, simply supported, square plate ( $a = b = 0.3$  m,  $t = 0.0032$  m,  $E = 210 \times 10^9$  N/mm<sup>2</sup>,  $\nu = 0.3$  and  $\rho = 7860$  kg/m<sup>3</sup>)).

## 6. Comparison of experimental and computed frequencies

The results for the free vibration frequencies of square GRP plates without cutouts are presented first. The results encompass the three levels of orthotropy/

Table 5

Comparison of theoretical/numerical and experimental free vibration frequencies (Hz) for 3.2 mm thick, pultruded GRP, square plates for three cases of material orthotropy/anisotropy and six combinations of clamped (C), simply supported (S) and free (F) edge conditions

Support conditions	Anal./Exp.	Vibration mode number						
		1	2	3	4	5	6	7
C–C–C–C (Long./Trans.)	Theor.	150.39	284.49	330.18	444.91	502.75	610.52	646.42
	NASTRAN	149.09	281.87	327.51	439.11	499.82	607.41	638.27
	Exp.	140.00	268.00	305.00	441.00	497.00		
	LUSAS	149.70	283.00	328.40	442.30	500.20		
C–C–C–S (Long.)	Theor.	136.26	247.23	322.66	418.39	444.20	597.88	605.25
	NASTRAN	135.13	245.01	320.37	413.85	441.73	591.01	602.89
	Exp.	132.00	232.00		376.00	400.00	521.00	
	LUSAS	135.70	246.00		416.70	441.90		
C–C–C–S (Trans.)	Theor.	127.54	271.22	278.94	403.69	493.65	533.63	613.90
	NASTRAN	126.66	269.43	277.22	400.25	491.96	531.87	609.80
	Exp.	125.00	261.00		385.00	465.00	555.00	
	LUSAS	127.30	270.40		403.10	492.10		
C–S–C–S (Long.)	Theor.	126.73	216.17	316.63	391.71	397.28	556.22	600.40
	NASTRAN	125.79	213.84	315.10	388.85	393.06	549.13	599.27
	Exp.	125.00		203.00	344.00	370.00	506.00	
	LUSAS	126.30	214.80	315.10	389.10	395.50		
C–S–C–S (Trans.)	Theor.	112.60	235.41	261.64	370.94	464.27	486.28	584.40
	NASTRAN	111.36	233.72	260.61	367.97	462.50	485.95	579.56
	Exp.	113.00	214.00		352.00	446.00		529.00
	LUSAS	111.90	234.50	261.40	370.60	423.80		
C–C–C–C (45°)	Theor.	149.54	304.30	304.30	458.77	541.15	541.15	647.21
	NASTRAN	146.80	289.77	306.77	442.26	530.33	538.67	652.28
	Exp.	150.00	292.00		428.00	505.00		616.00
	LUSAS	147.60	291.30		445.70		532.30	
C–C–C–S (45°)	Theor.	133.21	264.73	294.69	428.48	479.96	534.13	645.14
	NASTRAN	130.56	257.06	290.99	412.93	474.55	527.86	612.48
	Exp.	129.00	240.00		390.00	437.00	556.00	
	LUSAS	131.30	258.40		415.90	476.20		
C–S–C–S (45°)	Theor.	121.08	230.91	285.41	402.49	424.33	525.64	598.77
	NASTRAN	119.09	224.63	282.73	386.04	422.16	522.14	571.57
	Exp.	114.00	207.00		375.00	397.00	543.00	
	LUSAS	119.70	225.80	284.10	388.40	423.80		
C–F–C–F (Long.)	NASTRAN	105.82	117.37	172.89	292.20	303.44	308.14	368.60
	Exp.	70.00	94.00		172.00	208.00	230.00	
	LUSAS	105.90	117.80	174.20	292.00	305.00		
	NASTRAN	83.63	97.82	172.74	231.07	251.09	238.93	346.23
C–F–C–F (Trans.)	NASTRAN	86.80	106.89	180.79	240.36	268.81	323.38	365.85
	Exp.	94.00	111.00	181.00	258.00		322.00	
	LUSAS	87.28	107.60	182.10	241.30	270.40		
	NASTRAN	110.61	161.48	292.97	297.67	348.05	465.58	508.68
C–C–C–F (Long.)	Exp.	76.00	152.00	246.00	287.00	305.00		
	LUSAS	110.80	162.50	294.30	297.70	349.80		
	NASTRAN	90.27	161.21	238.32	306.10	337.10	462.15	465.74
	NASTRAN	95.02	168.84	250.34	308.22	335.36	475.94	485.32
C–C–C–F (45°)	Exp.	98.00	161.00	241.00	296.00	331.00		
	LUSAS	95.57	165.90	251.50	309.90	337.70		
	NASTRAN	16.61	32.92	96.89	107.86	130.29	209.07	244.23
	Exp.	15.00	32.00	77.00	114.00		210.00	
C–F–F–F (Long.)	LUSAS	16.60	33.20	97.00	108.00	131.00		
	NASTRAN	13.11	30.72	81.40	113.90	119.38	207.74	231.89
	NASTRAN	13.48	36.17	81.51	108.98	129.15	222.89	241.13
	Exp.	27.00	38.00	85.00	110.00	125.00		
C–F–F–F (45°)	LUSAS	13.56	36.29	82.04	109.40	129.80		

anisotropy defined in terms of the orientation of the rovings, i.e., longitudinal, transverse and 45°, with respect to the  $x$ -axis of the plate, and the six combinations of edge support conditions. Frequencies for the first

seven modes of vibration are presented in Table 5. For plates with combinations of clamped (C) and simply supported (S) edges, generally four frequencies are listed for each vibration mode, viz., the theoretical frequency

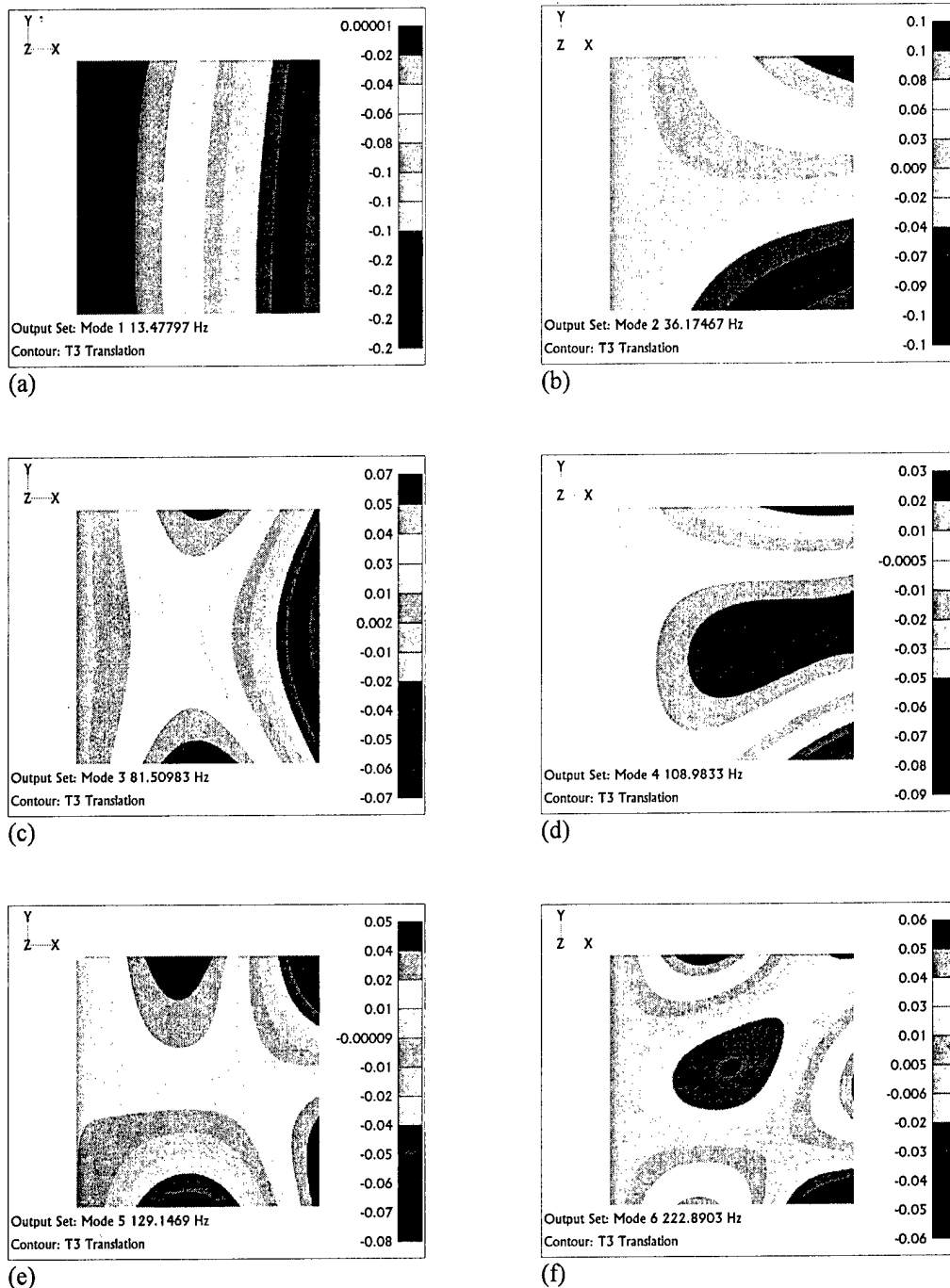
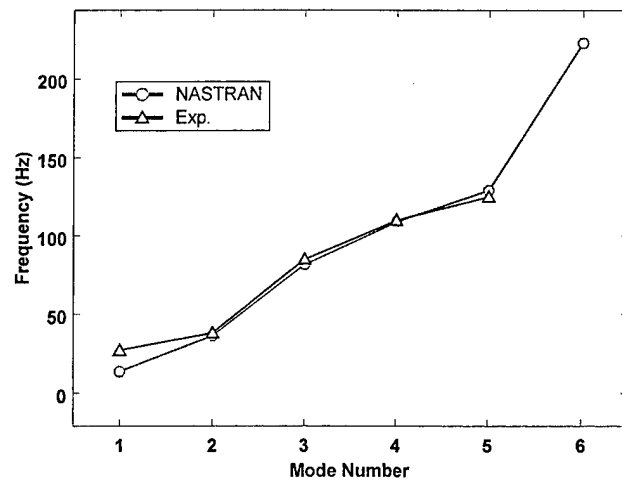


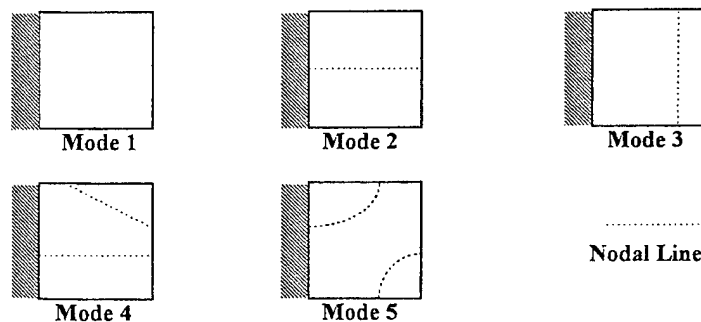
Fig. 5. MSC/NASTRAN mode shapes for the first six free vibration modes of a 3.2 mm thick, pultruded GRP, square plate (C–F–F–F (45°)).

determined from Eq. (1), the MSC/NASTRAN FE frequency, the experimentally determined frequency and the LUSAS [6] FE frequency. However, for the plates with combinations of clamped (C) and free (F) edges, in general only three frequency values are given in Table 5, because a simple closed-form expression similar to Eq. (1) was not available. It is evident from Table 5 that both FE analyses predict similar frequency values for all cases and that the LUSAS values are slightly higher. This may be attributable to one or more of the following

factors: the use of a coarser mesh, an element based on thin plate theory and the Guyan reduction technique, which uses lumped masses at the master degrees of freedom. The experimentally determined frequencies appear, for the most part, to be in reasonable agreement with both the theoretical and FE frequency predictions, especially for the lower vibration modes and when all of the plate edges are supported. For plates with one or more free edges, some of the experimental frequencies for the first vibration mode differ significantly from the



(a)



(b)

Fig. 6. 3.2 mm thick, square, pultruded GRP plate (C-F-F-F (45°)): (a) comparison of MSC/NASTRAN and experimental frequencies and (b) sketches of experimental nodal line patterns for the first five free vibration modes.

FE values, but show much better agreement for higher modes. It is also evident that a number of the third mode frequencies were missed in the experiments, which is not altogether surprising given that only a simple experimental vibration test rig was available. The gaps in the sixth and seventh vibration mode columns of Table 5 arise, because only five frequencies were determined in the vibration tests. Due to some missed third mode frequencies and occasional difficulties in determining the nodal line patterns, vibration frequencies and mode shapes were computed for the first seven vibration modes in order to permit a more comprehensive comparison between theory and experiment. As an illustration of the correlation between the frequencies and mode shapes Figs. 5 and 6 are included. Fig. 5 shows the first six mode shapes for a (C-F-F-F) plate with the rovings oriented at 45° to the  $x$ - and  $y$ -axes of the plate. Sketches of the experimental mode shapes and a graph comparing the MSC/NASTRAN FE and experimental frequencies are shown in Fig. 6 for the same plate.

The difference between the theoretical/numerical and experimental frequencies in Table 5 is generally less than 10% and suggests that orthotropic/anisotropic thin plate theory provides a sound basis for modelling the free vibration response of pultruded GRP plates without cutouts under a variety of edge support conditions.

The second and last set of frequency results comparisons are for square pultruded GRP plates with central circular cutouts, with diameters varying from 25 to 125 mm and with three combinations of clamped (C) and simply supported (S) edge conditions. In this case, only MSC/NASTRAN FE frequencies were available for comparison with the experimental values. The frequency values are compared for the first six vibration modes in Table 6. In general, for each hole size and edge support combination, the two frequency values are in reasonably good agreement. However, it appears that some third mode frequencies were missed during the plate vibration tests. Figs. 7 and 8 illustrate, for the case of a (C-C-C-C) plate with a 50 mm diameter cutout,

Table 6

Comparison of numerical and experimental free vibration frequencies (Hz) for 3.2 mm thick, pultruded GRP, square, plates with central circular cutouts and with three combinations of clamped (C) and simply supported (S) edge conditions

Edge conditions (hole diameter (mm))	Anal./Exp.	Vibration mode number					
		1	2	3	4	5	6
C–C–C–C (25)	NASTRAN	147.91	281.49	325.14	437.22	494.78	597.85
	Exp.	134.00	266.00	296.00	404.00	457.00	
C–C–C–S (25)	NASTRAN	134.00	244.71	317.96	412.41	437.79	590.68
	Exp.	117.00	258.00		372.00	447.00	544.00
C–S–C–S (25)	NASTRAN	124.70	213.83	312.79	385.29	391.65	549.11
	Exp.	114.00	226.00		348.00	448.00	520.00
C–C–C–C (50)	NASTRAN	148.45	277.38	319.96	432.51	495.18	604.04
	Exp.	136.00	260.00	294.00	402.00	457.00	
C–C–C–S (50)	NASTRAN	134.23	241.95	313.55	407.90	436.83	581.77
	Exp.	120.00	254.00		364.00	451.00	
C–S–C–S (50)	NASTRAN	124.66	211.47	308.70	385.36	387.98	540.52
	Exp.	115.00	218.00		353.00	450.00	522.00
C–C–C–C (75)	NASTRAN	154.29	268.43	304.88	425.70	498.08	616.68
	Exp.	141.00	252.00	285.00	396.00	461.00	
C–C–C–S (75)	NASTRAN	137.99	236.57	299.70	401.56	441.54	570.57
	Exp.	121.00	246.00		361.00	464.00	558.00
C–S–C–S (75)	NASTRAN	127.66	205.86	295.58	382.83	394.65	529.04
	Exp.	116.00	208.00		355.00	456.00	529.00
C–C–C–C (100)	NASTRAN	168.02	259.39	288.17	414.42	489.25	612.66
	Exp.	146.00	246.00	270.00	385.00	463.00	
C–C–C–S (100)	NASTRAN	146.69	231.26	283.55	391.88	443.91	565.49
	Exp.	125.00	239.00		348.00	525.00	574.00
C–S–C–S (100)	NASTRAN	135.20	197.97	279.79	374.29	405.13	524.78
	Exp.	124.00	203.00		359.00	469.00	550.00
C–C–C–C (125)	NASTRAN	192.30	259.81	287.62	400.79	479.30	609.78
	Exp.	162.00	254.00	273.00	378.00	472.00	
C–C–C–S (125)	NASTRAN	160.26	234.39	282.08	379.75	444.62	564.16
	Exp.	140.00	238.00		348.00	525.00	574.00
C–S–C–S (125)	NASTRAN	148.36	192.17	277.73	362.47	413.35	525.89
	Exp.	128.00	186.00		375.00	480.00	573.00

the typical level of agreement between the FE and experimental free vibration frequencies and mode shapes.

In order to illustrate some general trends observed in both the experimental and FE vibration frequencies of 3.2 mm thick pultruded GRP plates, Figs. 9 and 10 have been compiled from the first mode vibration frequencies given in Tables 5 and 6. In Fig. 9, the fundamental frequencies are plotted against the six edge support combinations in order of decreasing edge rotational and translational restraint, i.e., as the edge supports are changed from C–C–C–C through C–S–C–S to C–F–F–F, for the three cases of material orthotropy/anisotropy. It is evident that the overall trend of reducing frequency with decreasing edge restraint applies irrespective of whether the rovings in the plate are oriented in the longitudinal, transverse or 45° directions. Perhaps the most striking feature of Fig. 9 is the dramatic reduction in frequency that arises on changing the edge support combination from 5 (C–F–C–F) to 6 (C–F–F–F). The experimental frequencies show the same overall trends as the FE frequencies. However, for plates with the rovings in the longitudinal direction and edge support combinations 4 (C–C–C–F) and 5 (C–F–C–F), the ex-

perimental frequencies are substantially lower than the FE values.

Fig. 10 shows a comparison of the first mode FE and experimental frequencies as a function of the hole size ratio for three combinations of clamped (C) and simply supported (S) edges. Both sets of results show that the frequency increases as the hole size ratio increases. In all cases, the experimental frequencies are lower than the theoretical values and the frequencies are also observed to reduce as the degree of rotational edge restraint is relaxed.

## 7. Concluding remarks

A series of small amplitude vibration tests have been carried out on 3.2 mm thick, square pultruded GRP plates with three orientations of the principal material axes and six edge support combinations. The free vibration frequencies and mode shapes observed in the tests have been compared with corresponding frequencies and mode shapes, obtained from approximate closed-form expressions and numerical FE analysis. The

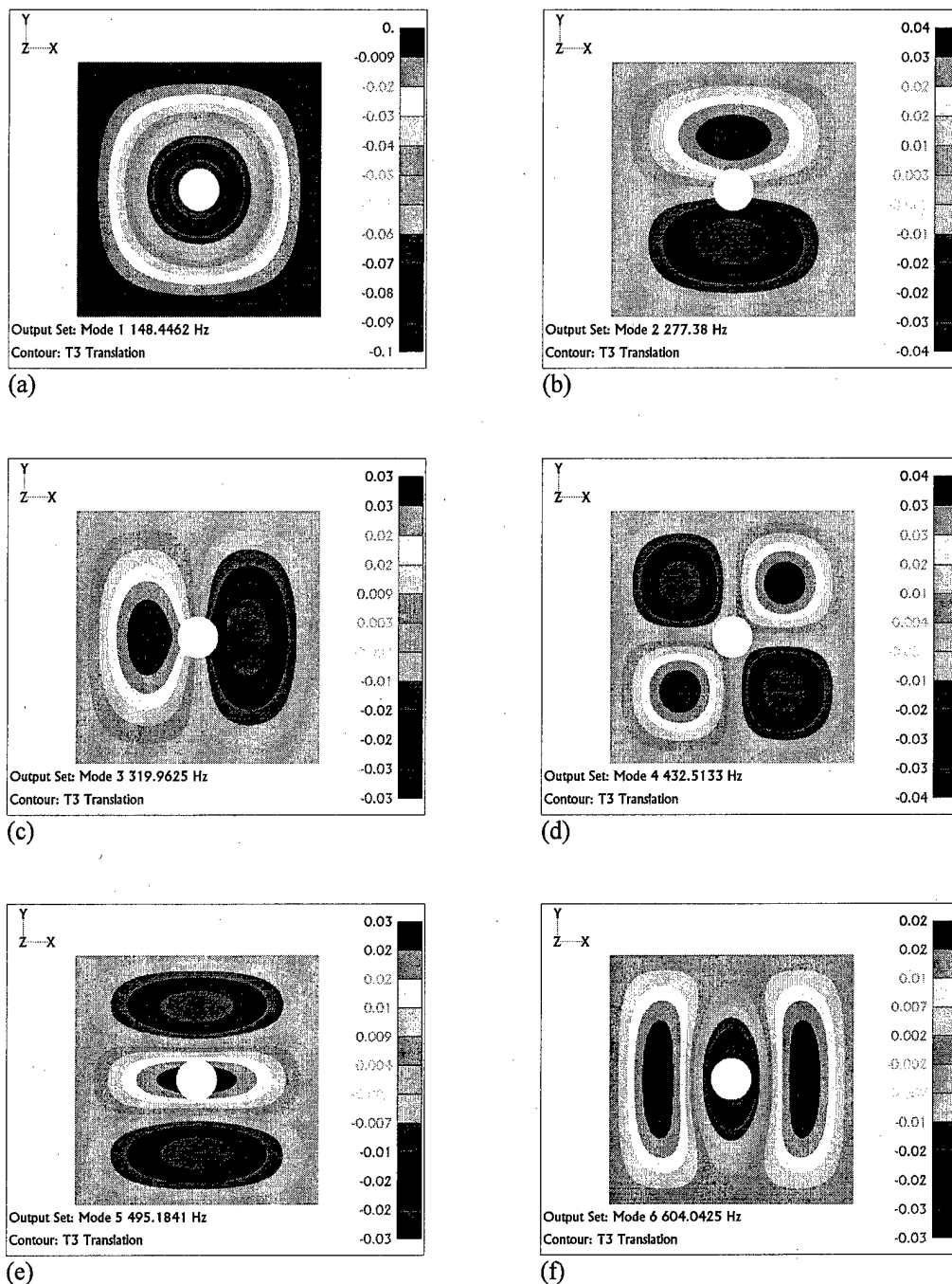


Fig. 7. MSC/NASTRAN modes shapes for the first six free vibration modes of a 3.2 mm thick, pultruded GRP, square plate with a 50 mm diameter, central circular cutout (C-C-C-C).

theoretical/numerical and experimental results have been shown to be in reasonably good agreement with, in general, corresponding frequency values differing by less than 10%. This suggests that thin orthotropic/anisotropic plate theory provides a sound basis for modelling the free vibration response of pultruded GRP plates, despite their relatively heterogeneous fibre architectures.

Free vibration frequencies and mode shapes were also determined experimentally for pultruded GRP plates

with central circular cutouts and three combinations of clamped (C) and simply supported (S) edge conditions. Again, it was shown that reasonably good approximations to the observed frequencies and mode shapes could be obtained with numerical FE analyses based on thin and moderately thick orthotropic/anisotropic plate theory.

It has also been shown, both numerically and experimentally, that, irrespective of the degree of material



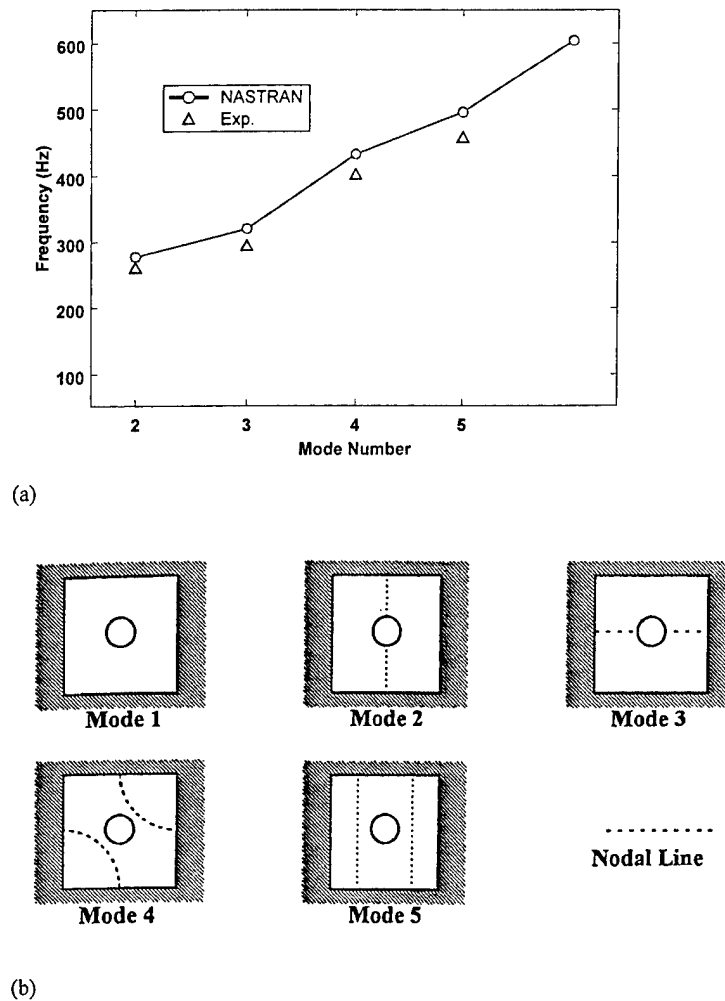


Fig. 8. 3.2 mm thick, square, pultruded GRP plate with a 50 mm diameter, central circular cutout (C–C–C–C): (a) comparison of MSC/NASTRAN and experimental frequencies and (b) sketches of experimental nodal line patterns for the first five free vibration frequencies.

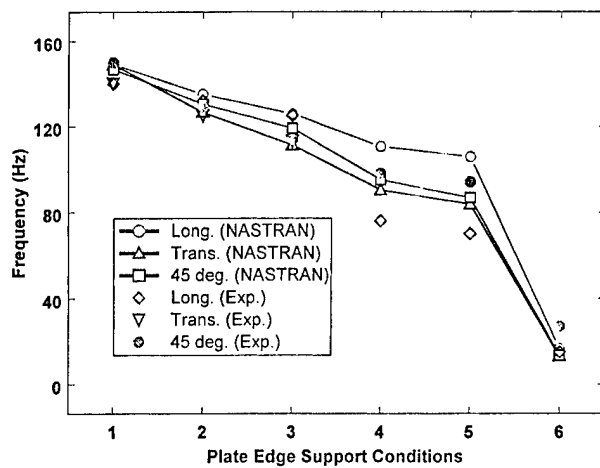


Fig. 9. Comparison of FE and experimental first mode vibration frequencies of 3.2 mm thick, pultruded GRP plates for three cases of material orthotropy/anisotropy and for successive relaxation of the edge restraints (1 = C–C–C–C, 2 = C–C–C–S, 3 = C–S–C–S, 4 = C–C–C–F, 5 = C–F–C–F and 6 = C–F–F–F).

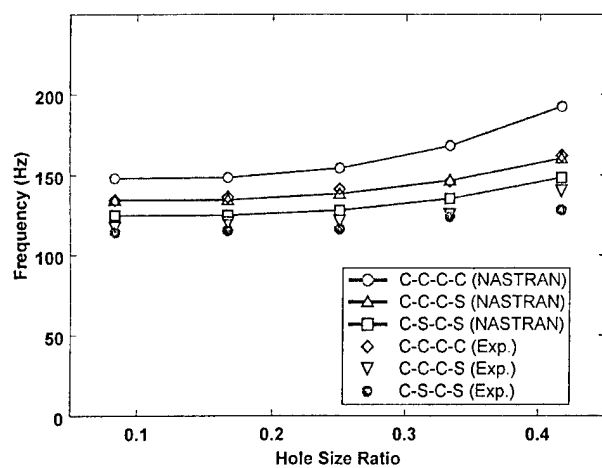


Fig. 10. Comparison of FE and experimental first mode vibration frequencies versus hole size ratio for 3.2 mm thick, pultruded GRP plates for three cases of material orthotropy/anisotropy and for three combinations of clamped (C) and simply supported (S) edge conditions.

orthotropy, the first mode vibration frequencies of square, pultruded GRP plates without cutouts decrease as the rotational and translational edge restraint is successively relaxed. Moreover, it has been demonstrated that there is a very large reduction in frequency when the number of supported edges reduces from two to one.

Finally, for pultruded GRP plates with central circular cutouts and with three combinations of clamped (C) and simply supported (S) edges, it has been shown that the first mode vibration frequencies increase more rapidly as the hole size ratio increases.

### Acknowledgements

The authors wish to record their appreciation of the contribution made to the research reported herein by Mr. Chi Kong Chung, who carried out the plate vibration tests, as part of his undergraduate final year project, under the direction of the first and third authors. They also wish to express their appreciation

to Ms. Patricia Eagling, who carried out the LUSAS FE analyses under the direction of the first author. And, last but by no means least, they wish to record their appreciation of the support of the technician staff of the Engineering Department, who manufactured the plate vibration test rig and other ancilliary equipment.

### References

- [1] Meyer RW. Handbook of pultrusion technology. New York: Chapman & Hall; 1985.
- [2] Anon. Extren fiberglass structural shapes design manual. Bristol, Virginia: Strongwell; 1989.
- [3] Hearmon RFS. The frequency of flexural vibration of rectangular orthotropic plates with clamped or simply supported edges. *J Appl Mech* 1959;26(3–4):537–40.
- [4] MSC/NASTRAN, The MacNeal-Schwendler Corporation, 815 Colorado Boulevard, Los Angeles, CA 90041-1777, USA.
- [5] MacNeal RH. A simple quadrilateral shell element. *Comput Struct* 1978;8(2):175–83.
- [6] LUSAS, FEA Ltd, Forge House, 66 High Street, Kingston upon Thames, Surrey KT1 1HN, UK.

# Optical fibre sensors for health monitoring of bonded repair systems

I. McKenzie<sup>a,\*</sup>, R. Jones<sup>a</sup>, I.H. Marshall<sup>a</sup>, S. Galea<sup>b</sup>

<sup>a</sup> DSTO Centre of Excellence for Structural Mechanics, Department of Mechanical Engineering, Monash University, Clayton, Vic. 3168, Australia

<sup>b</sup> Airframes and Engines Division, DSTO, 506 Lorimer St, Fishermens Bend, Vic. 3001, Australia

## Abstract

In the aircraft industry the use of externally bonded composite repairs has become an accepted way of repairing fatigue, or corrosion, damaged metallic structural components. However, current NDI and damage assessment techniques for composite repairs are passive and generally performed on ground. The challenge is to develop new techniques utilising recent analytical and experimental tools. This report examines the use of optical fibre sensors. Optical fibres offer a means of monitoring the load transfer process in these repairs, and can therefore be used to provide an indication of the integrity of the repair. This paper describes the use of an array of fibre Bragg grating strain sensors (FBGs) for the in situ monitoring of bonded repairs to aircraft structures and, in particular, the monitoring of crack propagation beneath a repair. In this work the FBGs have been multiplexed using a combination of wavelength and spatial techniques employing a tunable Fabry–Pérot (FP) filter to track individual gratings. The multiplexed FBGs were then surface-mounted on a boron–epoxy unidirectional composite patch bonded to an aluminium component. The sensors were located so as to monitor the changing stress field associated with the propagation of a crack beneath the patch. The ability of relating experimental results to sensor readings is then confirmed using both a thermo-elastic scan of the patch and 3D finite element analysis. © 2000 Published by Elsevier Science Ltd. All rights reserved.

**Keywords:** Bragg gratings; Fibre optics; Repairs

## 1. Introduction

The downturn of global economy coupled with the high acquisition cost associated with modern military and civilian aircraft has resulted in greater utilisation of the existing aircraft fleet. This trend, in operating aircraft to and beyond their intended design life, has been reflected in an increasing number of structurally significant defects and increases the possibility of a reduction, or loss of structural integrity due to fatigue. Recent disasters to both the civilian and military fleets have highlighted the importance and difficulties associated with the management of these ageing fleets.

The requirement for continued airworthiness of ageing aircraft has also fuelled the development of repair technology. The application of bonded composite patches to repair- and reinforce-damaged metallic structures is one such development that is widely becoming recognised as a versatile and effective repair procedure [1]. It has been applied to the primary structure of the F-111C, to repair cracking in the lower wing skin, and to damage in civil transport aircraft [2]. This

patching restores the strength and stiffness of the structure, and retards crack growth by reducing the stress intensities.

The Aloha incident focused public and government attention on the problem of ageing aircraft. The Aloha accident also revealed that multiple mechanical repairs, in close proximity, can compromise on structural integrity. However, continued airworthiness is of paramount importance and it is essential that structural integrity be maintained after repairs have been installed. Thus a methodology, and the associated documentation, must be prescribed against which (any) repair can be assessed and approved. This awareness has subsequently led to the requirement [3] that all repairs to RAAF (Royal Australian Airforce) aircraft must satisfy damage-tolerant requirements.

To assist in this task the current studies are focused on the assessment of new techniques in order to achieve in situ measurement of repair integrity and effectiveness. This would allow the operator to move away from current costly time-based maintenance procedures to real-time health condition monitoring of bonded repairs. Such a system would also permit timely decisions to be made on preventative and scheduled maintenance. In this work attention is focused on a fibre optic in situ

\* Corresponding author.

monitoring technique to detect and monitor crack growth and debonding under bonded repairs.

## 2. Optical fibre techniques

To evaluate the ability of optical fibre techniques to assess damage in composites an initial experimental programme was conducted on cracked aluminium skins 3.14 mm thick. Each plate had an edge crack 10 mm long which was repaired with a semicircular unidirectional boron/epoxy patch. The aluminium skins were tested back-to-back separated by a honeycomb sandwich core, see Fig. 1. The initial crack was then grown under constant amplitude fatigue loading to a length of 40 mm.

This test configuration was chosen to minimise the effects of bending and is widely used to represent the constraint conditions seen in a typical military aircraft structure [1].

### 2.1. Finite element analysis

To investigate the optimal placement of these sensors, and to validate the sensor readings, the specimen was modelled using finite element (FE) analysis. This analysis was also useful in examining the relative merit of sensor embedding versus surface mounting.

The FE model used iso-parametric 20-noded brick elements to model the 3.14 mm aluminium panel, the 0.9 mm adhesive layer and the boron repair. The material

properties used to model the various components of the specimen are given in Table 1.

Using the symmetry of the component it was only necessary to model half of one panel, see Figs. 2(a) and (b). To simplify geometry of the model, the boron repair was taken to be square rather than semicircular, and the tapered edges of the patch were also ignored. This simplification makes very little difference to the stresses near the crack face. The FE model was restrained such that it simulated a 45 mm edge crack in the aluminium panel and adhesive, with the boron repair covering it.

Due to the high stiffness of the boron patch in the direction of the boron fibres, it is clear that the stresses will be predominantly in the fibre direction. In this case the boron fibres lie in the  $y$ -direction therefore it is in this direction that the surface stresses and subsequently strains were highest. The loading condition applied to

Table 1  
Material properties used in the FE analysis

<i>Aluminium</i>	
Young's modulus	71 000 MPa
Poisson's ratio	0.33
<i>Adhesive</i>	
The values for the compliance matrix	
$S_{XX} = S_{YY} = S_{ZZ} = S_{XZ} = S_{XY} = S_{YZ} = S_{HXZ} = S_{HXY} = S_{HYZ}$	
$= 5.2632E - 4$	
<i>Boron repair</i>	
The values for the compliance matrix were	
$S_{XX} = 3.932E - 5, S_{YY} = 4.807E - 6, S_{ZZ} = 3.932E - 5,$	
$S_{XZ} = -6.558E - 6, S_{XY} = -8.8014E - 7, S_{XX} = -8.8014E - 7,$	
$S_{HXZ} = 1.381E - 4, S_{HXY} = 1.381E - 4, S_{HYZ} = 1.381E - 4$	

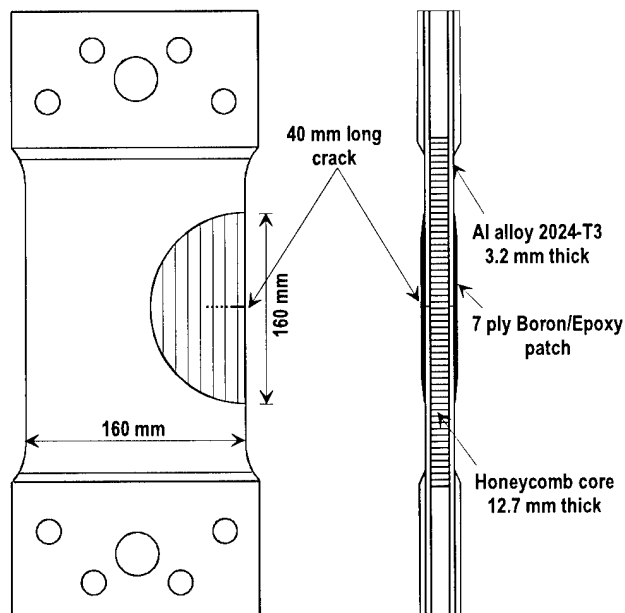


Fig. 1. Schematic of the specimen used for this experimental programme.

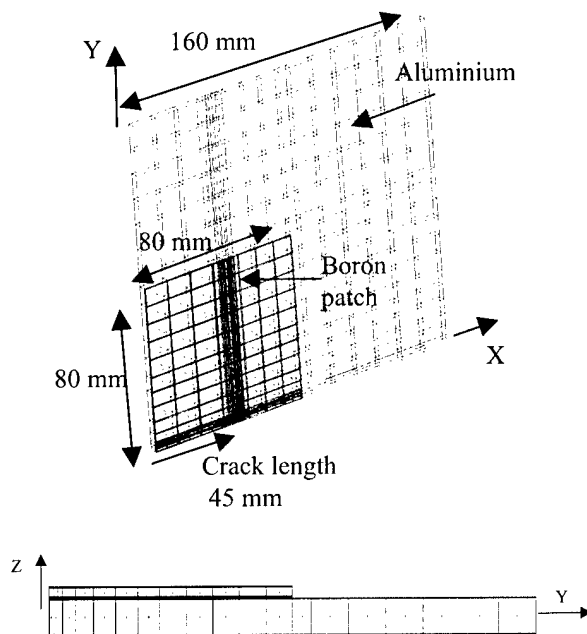


Fig. 2. FE mesh used to describe the specimen viewed from (a) above and (b) the side.

this model was a (remote) 70 kN surface load, in the  $y$ -direction, acting on at the edge of the specimen. The resultant  $\epsilon_{yy}$  strains on both the top and bottom surfaces of the repair are shown in Figs. 3 and 4.

## 2.2. Thermo-elastic analysis

Thermo-elastic emissions have been shown to be a useful tool for describing the structural significance of impact damage and other damage sites [11]. The thermal emissions can be related to the surface strains on the composite patch through the following equation [11]:

$$-\rho c_e \frac{\Delta T}{T_0} = (\alpha_{11} \Delta \sigma_{11} + \alpha_{22} \Delta \sigma_{22}), \quad (1)$$

where  $\Delta T$  is the local cyclic change in temperature,  $T_0$  the local absolute temperature,  $\rho$  the density,  $\alpha_{ii}$  the coefficient of thermal expansion,  $c_e$  the specific heat at constant strain and  $\Delta \sigma_{ii}$  is the cyclic principal stress amplitude. The subscripts 1 and 2 denote the directions parallel and perpendicular to the fibre. For specimens with unidirectional patches, as is the case here, stresses

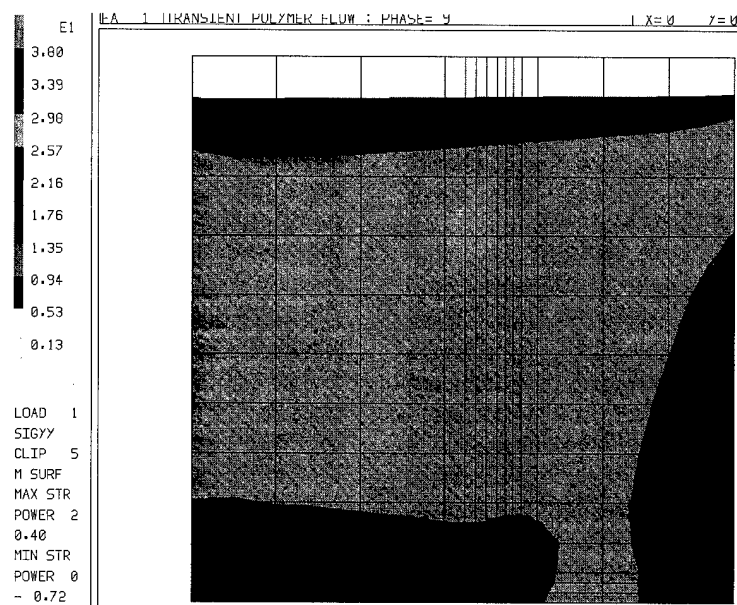
on the surface of the patch are predominantly in the fibre direction, therefore the thermo-elastic scan basically represents the  $\sigma_{11}$  surface stress distribution.

In the present investigation changes in the thermal emission signal are measured using a system marketed under the trade name SPATE 8000 which has a spatial temperature resolution of 0.25 mm<sup>2</sup> and 0.001 K, respectively. The infrared camera was placed approximately 0.5 m from the specimen and scans were performed, under cyclic loading of 40 ± 30 kN at 10 Hz, when the crack reached 40 and 50 mm. The resultant scans can be seen in Figs. 5(a) and (b).

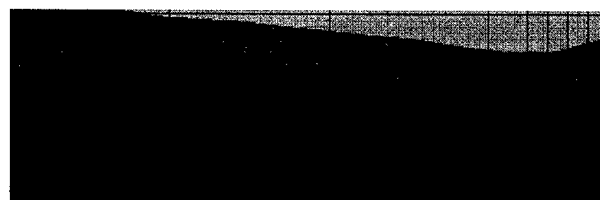
## 2.3. Sensor placement

It had been hoped to investigate both embedded and surface bonded FBGs. However, since the component was already fabricated with a bonded boron repair the analysis of the embedded sensors was limited to the results obtained from the FE analysis.

From both the SPATE and FE analyses of the cracked specimen the main features visible on the



Zoom in view of the region near the crack



Strain maximum is not over the crack but displaced due to shear lag.

Fig. 3. Surface  $\epsilon_{22}$  strains on the top surface of the boron repair when loaded axially by 70 kN.

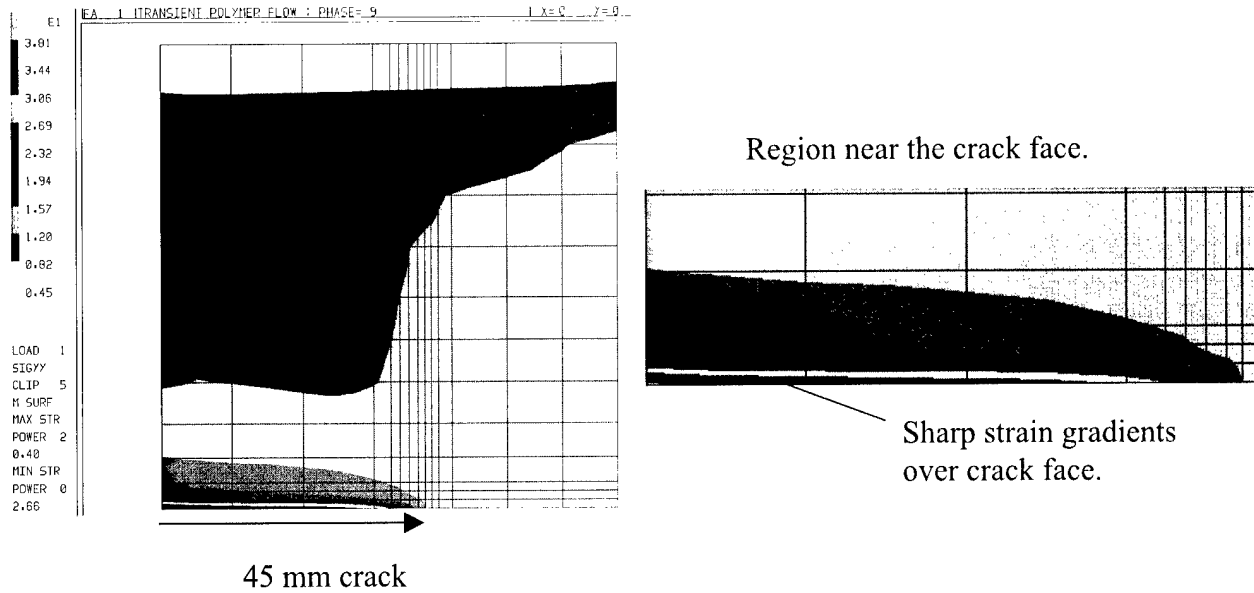


Fig. 4. Surface  $\epsilon_{22}$  strains on the bottom surface of the boron repair, axial load of 70 kN.

surface of the repair are a region of high stress on either side of the crack that extends  $\sim 7$ – $8$  mm in front of the crack tip. The SPATE scan also shows a region of low stress that lies behind the crack tip.

To pick up these features two gratings were written in a single optical fibre having Bragg wavelengths of  $\lambda_1 = 1534$  nm and  $\lambda_2 = 1536$  nm. These gratings had high reflectivities (80–90%), FWHM of approximately 0.5 nm, and a gauge length of around 5 mm. The gratings were located 7 mm apart, such that one grating would be placed in line with the crack tip and the second would be 7 mm off to the side of the crack, as can be seen illustrated in Fig. 6. A third FBG  $\lambda_3 = 1534$  nm on a separate optical fibre was used to compensate for the thermal drift and the drift associated with the instrumentation.

#### 2.4. Optical instrumentation

Temperature and strain both affect the Bragg wavelength as they affect the physical properties of the fibre, resulting in changes in the refractive index and the period of the grating. Thus FBGs can be used to give an absolute measurement of strain encoded in a wavelength shift. The wavelength shift  $\Delta\lambda_{BS}$ , for an applied longitudinal strain  $\Delta\epsilon$  is given by:

$$\Delta\lambda_{BS} = \lambda_B(1 - p_x)\Delta\epsilon, \quad (2)$$

where  $p_x$  is the photoelastic coefficient of the fibre.

$$p_x = n^2/2[p_{12} - \nu(p_{11} - p_{12})], \quad (3)$$

where  $p_{11}$  and  $p_{12}$  are the components of the fibre optic strain tensor and  $\nu$  is Poisson's ratio. Similarly for a

temperature change of  $\Delta T$ , the corresponding wavelength shift is given by

$$\Delta\lambda_{BT} = \lambda_B(1 + \xi)\Delta T, \quad (4)$$

where  $\xi$  is the fibre thermo-optic coefficient. For silica fibre, the wavelength sensitivities of a 1.55  $\mu\text{m}$  FBG have been measured as 1.15 pm/ $\mu\epsilon$ , and 13 pm/ $^\circ\text{C}$  [4].

The precise measurement of wavelength is therefore the key to strain measurement using FBGs. Many techniques for monitoring FBGs are available and have been discussed in depth in the literature, including edge filtering [5], tunable filters [6,7], and interrogation systems based on interferometric scanning [8]. For this work a tunable FP filter was used to track the Bragg wavelength, see Fig. 7. It was selected as it gives reasonable resolution  $\pm 25$   $\mu\epsilon$  and a large dynamic range.

To multiplex several FBGs onto a single optical fibre a broad band source is required. In this investigation an erbium doped-fibre amplifier (EDFA) was used, which had an FWHM of approximately 30 nm centred around 1550 nm. The light from this source was passed through a 3 dB coupler to the array of gratings. The two optical fibres were addressed by means of spatial multiplexing device, the York Switch master. This device can mechanically shift the coupling condition to address up to seven output optical fibres. The reflected signals from the FBGs were partially collected by the second arm of the coupler and directed to the tunable FP filter which was locked onto one of the Bragg reflections. The Micon Optics FP filter and controller can operate in one of the three modes, manual, locked or ramped. In the locked mode the controller outputs a 1.5 kHz dither signal which permits the tracking of the peak reflected Bragg wavelength. The feedback voltage controlling the

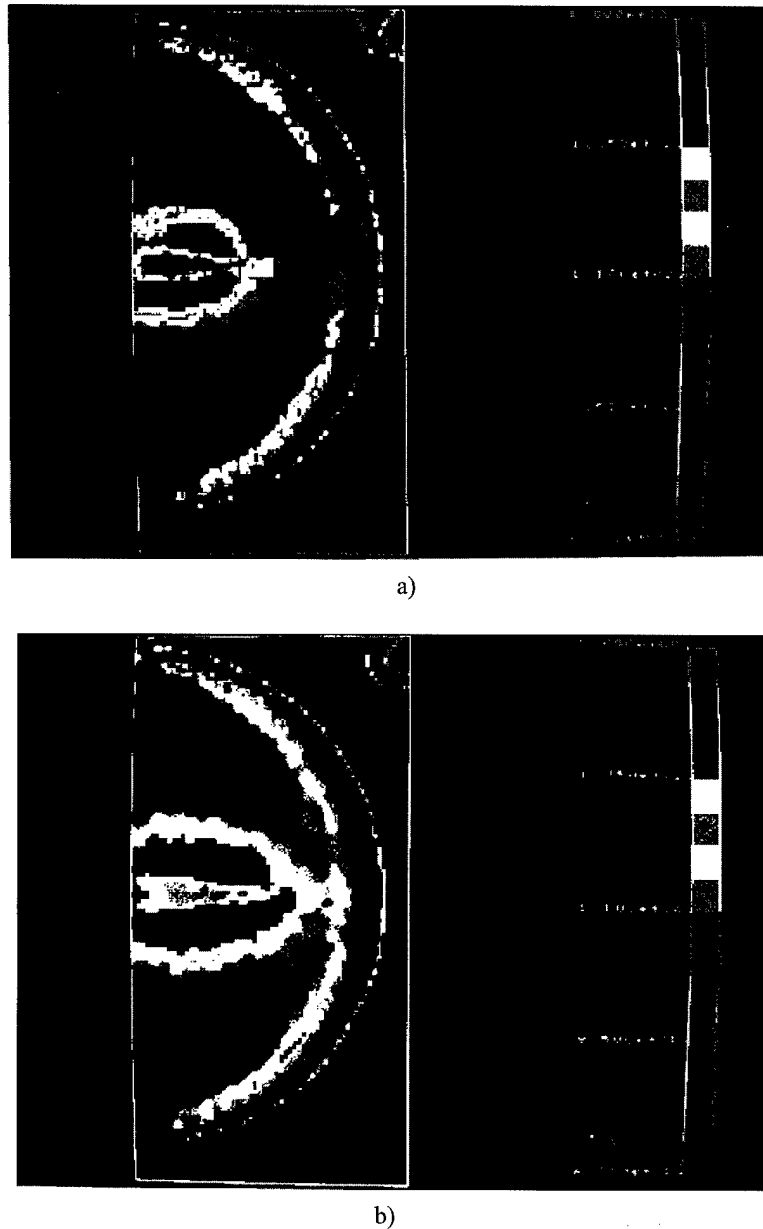


Fig. 5. SPATE scan of the bonded repair with: (a) 40 mm crack; (b) 50 mm crack.

FP was then used to calculate the strain since it is proportional to the shift in the wavelength of the FP filter and subsequently also the Bragg wavelength. The FBG sensors were calibrated by straining a grating by known amounts and measuring the change in feedback voltage. In this case the effect of temperature variations was ignored since these measurements were made in a controlled environment.

### 2.5. Experimental procedure

The specimen described above was instrumented with FBGs after it was fully fabricated. Hence only the strains due to the cyclic loads could be measured. The

cracks were grown under constant amplitude loading using two different loading conditions, see Table 2. Strain measurements were made, as the crack progressed, at load levels of 0 and 70 kN. Tests were conducted using a 500 kN MTS uni-axial hydraulic testing machine.

Loading condition 1 was maintained for 6000 cycles, interrupting the cyclic loading every 2000 cycles to carry out a strain survey and measure crack length. However, the crack growth rate was too low therefore the remainder of the test was performed at loading condition 2, interrupting the loading every 5000 cycles to make strain readings and to measure the crack length, as is illustrated in Fig. 8. The crack length was measured

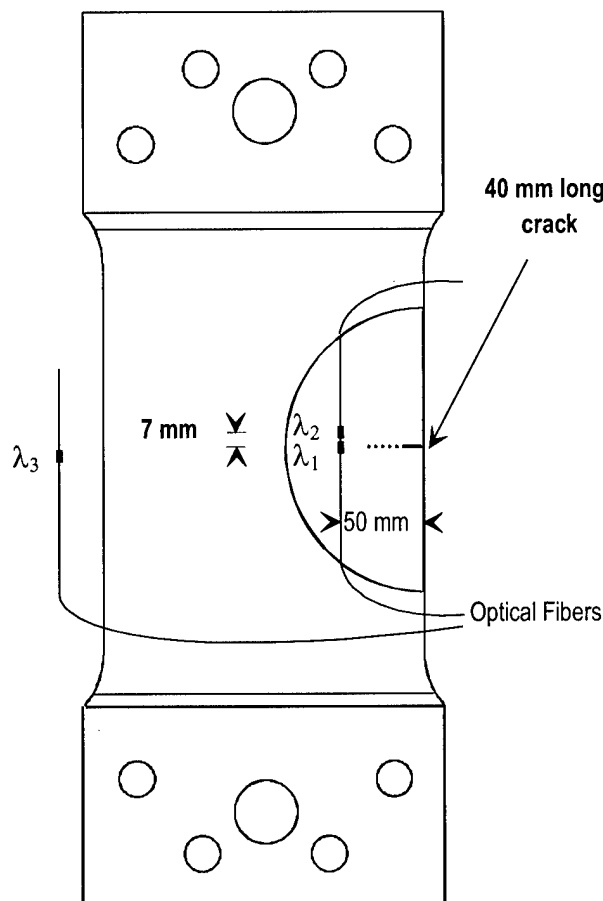


Fig. 6. Diagram of specimen showing the sensor placement.

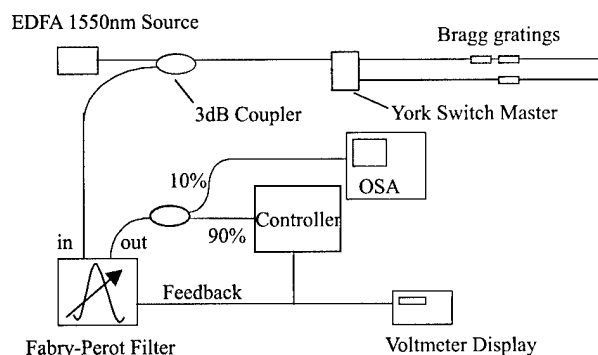


Fig. 7. Bragg grating sensor with a tunable filter for tracking.

Table 2  
Description of the applied stresses for each load case

Load condition	1	2
Stress (MPa), Max, $\sigma_{\max}$	120.0	180.0
Min, $\sigma_{\min}$	12.0	72.0
R ratio, $\sigma_{\min}/\sigma_{\max}$	0.1	0.4
Applied load		
$p_{\max}$	122.0	184.0
$p_{\min}$	13.0	3.0

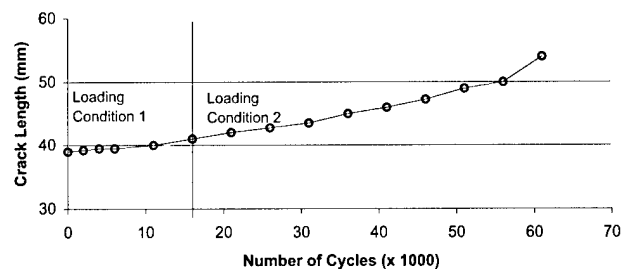


Fig. 8. Crack growth as a function of the number of fatigue cycles.

using a portable Zetec eddy-current instrument, with a 50–500 kHz differential probe.

After 61 000 cycles the testing was discontinued due to the unusual manner in which the specimen was deforming under the uniaxial loading. A closer examination of the specimen revealed that the aluminium panel on the reverse side (the side that had not been instrumented with gratings) had cracked right through thus changing the loading conditions.

## 2.6. Results and discussion

The specimen was tested under the loading conditions described above, and the edge crack was grown from 40–54 mm long. Fig. 9 shows the change in the strain, under a fixed 70 kN load, as seen by the two FBGs attached to the boron repair as the crack approaches and then passes underneath the sensors. The sensors were located 50 mm from the edge of the sample.

It is clear from Fig. 9 that as the crack approached sensor 1, which was located directly over the crack, the strain readings increased until the crack reaches the sensor (50 mm). At this point the strain readings dropped to a minimum. Sensor 2, however, lags sensor 1 and does not see this drop in strain but continues to rise. This result is entirely consistent with the thermo-elastic scan and partially consistent with the FE analysis both of which show that the maximum strains do not occur over the crack but reach a maximum on either side of the crack. This is illustrated in the detailed thermo-elastic scan shown in Fig. 10. The maximum strains occurring on either side of the crack are due to shear lag and the

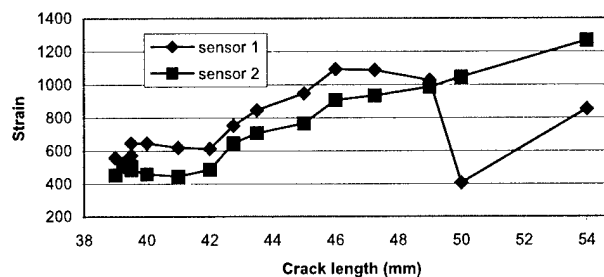


Fig. 9. Bragg sensor response versus crack length.



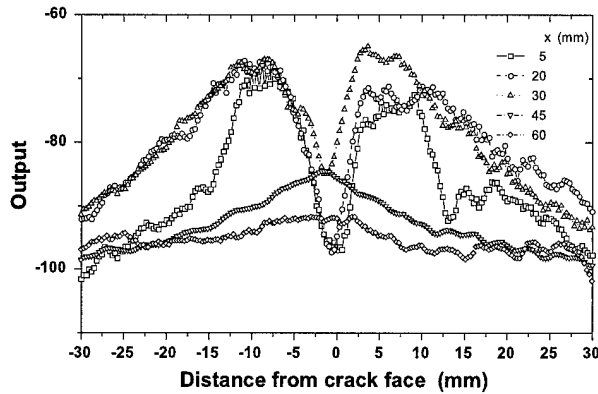


Fig. 10. Thermo-elastic scan of specimen with a 45 mm edge crack.

resulting load path eccentricity as the load passes up into the patch over the cracked region. The longer the crack becomes the higher the peaks and the lower the troughs will appear. Similar results were also reported in the previous work done on a similar test sample [9].

Another observation from the results is that the strain was picked up first by sensor 1, when the crack tip was

approximately 8 mm away, and then later by sensor 2. This was also consistent with the thermo-elastic scans which show a region of high strain preceding the crack tip. The FE model, however, failed to show either the region of high stress preceding the crack tip or the low stress region behind the crack tip, both of which are apparent in both the thermo-elastic scans and the sensor readings. The reason for the FE model not picking up these details was due to the constraint conditions in the  $z$ -direction imposed on the model differing from those in the test. It is also possible that a fair amount of debonding occurred around the cracked region. This debonding was also not modelled in the FE analysis.

### 3. Application of surface bonded fibre optic array on a cracked patched specimen

Following this initial test programme the use of an array of surface mounted optical fibres, OF1–OF4, was then investigated, see Fig. 11. To give a far-field reading fibre OF1, containing a single sensor S1, was bonded to

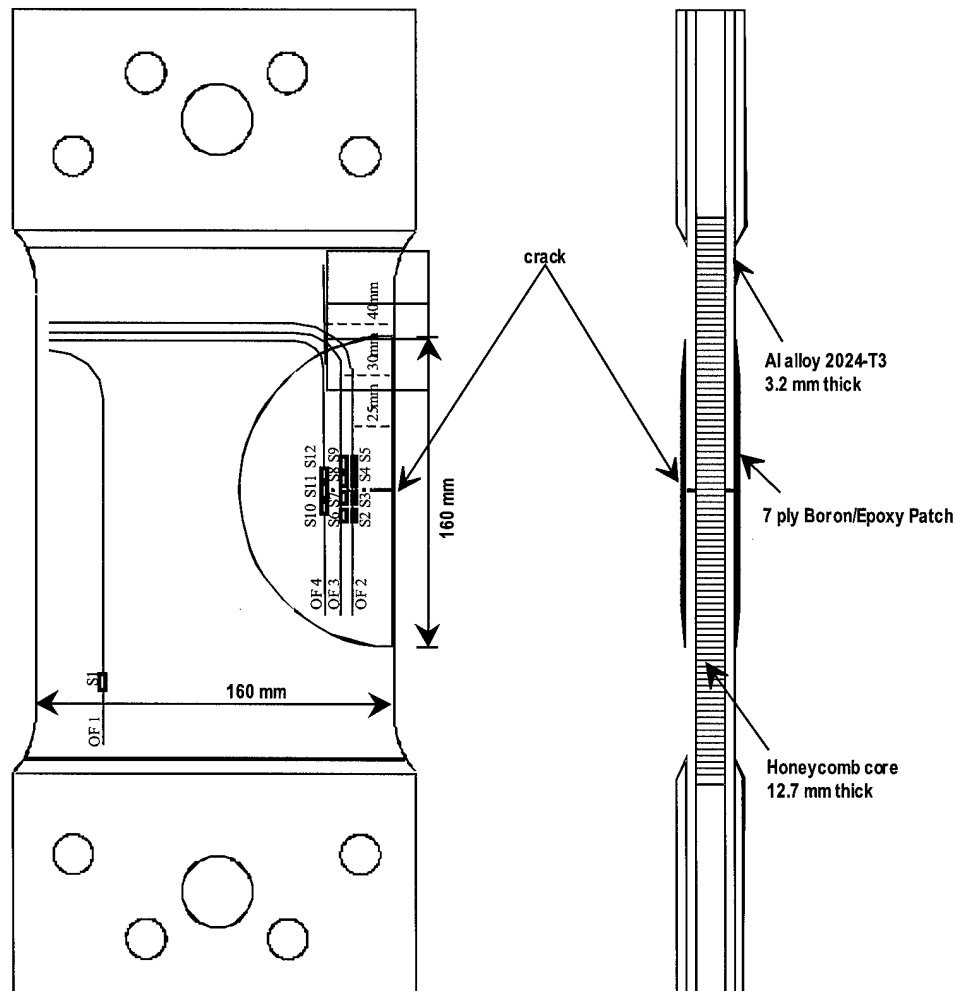


Fig. 11. Diagram showing sensor placement on the cracked patched specimen.

the aluminium skin using a cyano-acrylate adhesive. The remaining three optical fibres were bonded to the top surface of the boron repair also using a cyano-acrylate adhesive. These sensors were then completely buried beneath a thick layer of room temperature curing adhesive so as to protect the optical fibres and also provide a smooth surface for making the eddy current measurements of crack length.

### 3.1. Cracked patched specimen results

In this, second, test programme the crack was grown under a FALSTAFF fatigue load spectrum that attempts to simulate flight loads experienced by a military aircraft. As the crack progressed a series of static strain readings were periodically undertaken, the experimental set-up can be seen in Fig. 12, at load levels of 0 and 70 kN, see Figs. 13–16.

These results clearly demonstrate the ability of optical fibre sensor array to monitor crack growth under the bonded repair. This can be seen in the results from OF2 in Fig. 15, located 25 mm from the panel edge. The strain can be seen to initially increase as the crack approaches the sensors S2–S5. It continues to increase as the crack passes these sensors, with the exception of S4 which experiences a decrease as the crack passes directly under

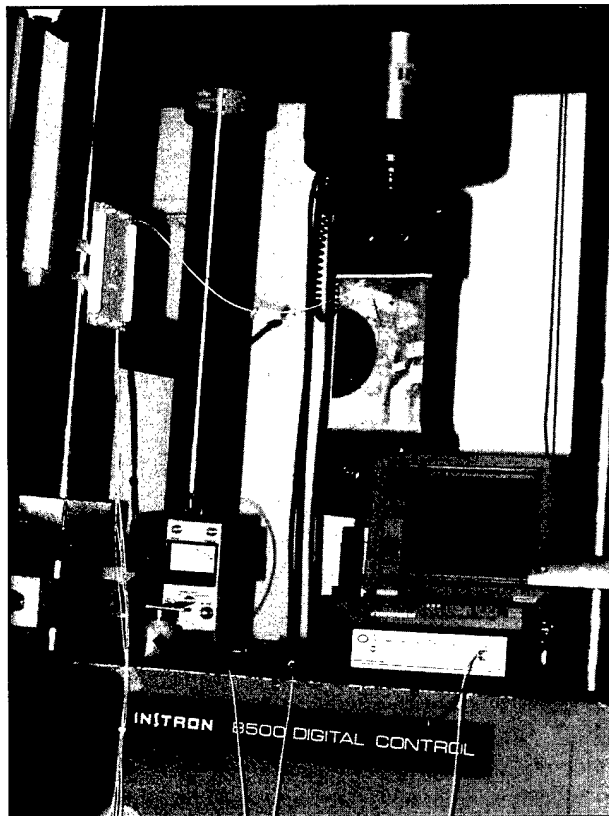


Fig. 12. Photograph of the experimental set-up.

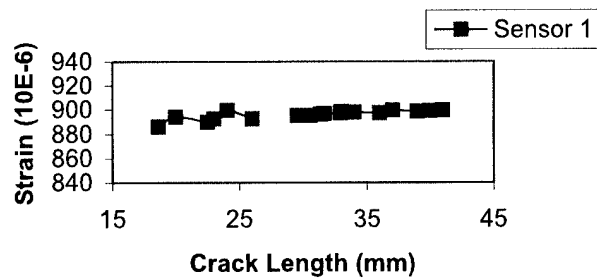


Fig. 13. Change in strain with crack length OF1.

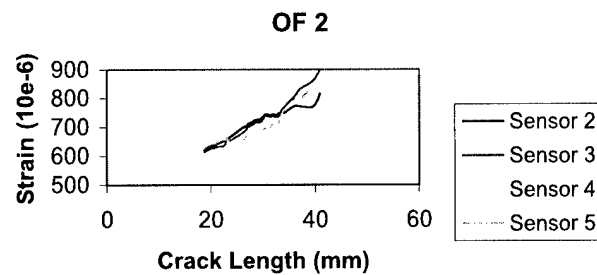


Fig. 14. Change in strain with crack length OF2.

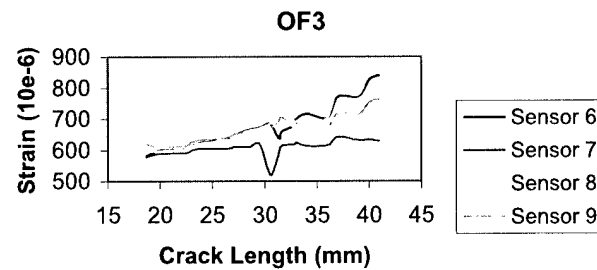


Fig. 15. Change in strain with crack length OF3.

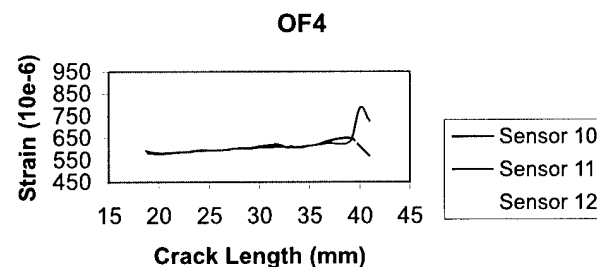


Fig. 16. Change in strain with crack length OF4.

this sensor. This is to be expected as a valley of low strain exists directly over the crack with ridges of high strain on either side. Such a shear lag effect is caused by the load flowing up into the patch causing local bending.

Sensors S6–S9, located 30 mm from the edge of the panel, exhibited a similar trend as can be seen in Fig. 16.

Here sensor S7 was located over the crack and experienced low strain readings as the crack passes underneath it. Sensors S6, S8 and S9 continued to increase as expected.

OF4 also exhibited a similar trend as the crack approaches the optical fibre sensors located 40 mm from the edge of the patch the strain increases. The initial decrease in S12 was attributed to debonding of the sensor. However, as the crack passes beneath S10 begins to decrease.

Residual strains in the specimen were also measured by tracking the absolute wavelength values of the Bragg gratings over the test period under a 0 kN load. These results are presented in Figs. 17–19 as a wavelength shift against crack length.

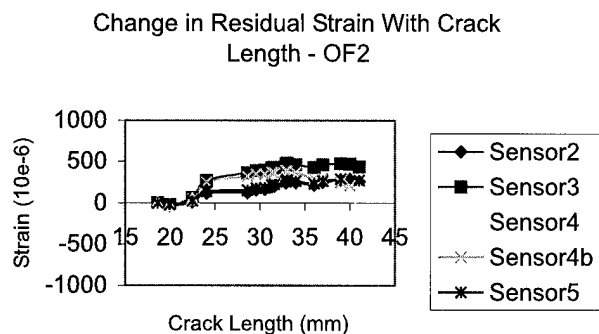


Fig. 17. Residual strain OF2.

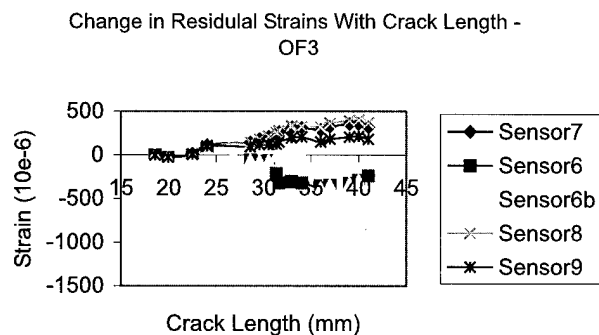


Fig. 18. Residual strain OF3.

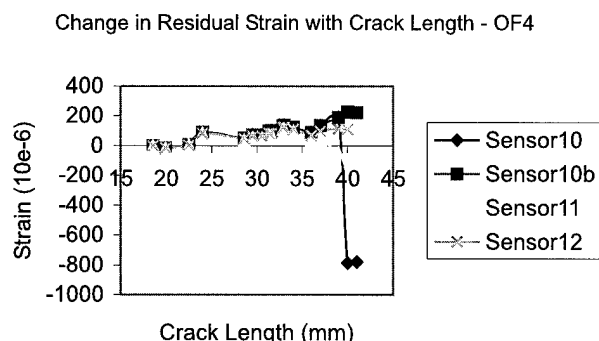


Fig. 19. Residual strain OF4.

The change in the residual strains appears to mimic the effect seen under load with the sensors over the crack having negative residual strains while those to the sides of the crack having positive residual strains. These results validate the previous work done using similar specimens instrumented with electrical strip strain gauges [2].

### 3.2. Problems encountered

While conducting this experiment several issues arose:

#### 3.2.1. Fibre-structure bond integrity

The bond between the optical fibre and the structure in two of the fibres degraded during the test programme. The first of these debonds occurred on OF4 and resulted in a drop in the strain seen by S12 from 590 to 490  $\mu\epsilon$ . The quality of the S4 bond is obviously in doubt for the remainder of this experiment even though it now appears to be consistently giving reasonable results.

The far-field optical fibre sensor S1 also debonded during the testing. This sensor was fixed by applying a layer of 5 min Araldite over it. When the Araldite was fully cured the sensor once again returned the same strain readings that it had given prior to debonding.

Since these problems were encountered experiments have been conducted which demonstrate that Araldite and AE10, a room-curing epoxy from M-bond, both provide adequate bonds up to at least 1500  $\mu\epsilon$ . The fatigue performance of these epoxies requires further evaluation. It is clear that, without a suitable surface treatment to the glass cyano-acrylate, super glue, is not a suitable adhesive for bonding optical fibres. Fibre glass manufacturers use a silane solution to treat the glass fibres before curing them in epoxy. A similar treatment may well be of benefit when bonding the optical fibre sensors to a structure.

#### 3.2.2. Bragg spectra distortion by strain gradients

In the conventional use of fibre Bragg gratings, the sensors are assumed to have uniform strains along their working length. In this case the shift in the Bragg wavelength is proportional to the change in length, and hence the strain, of the grating. The Micron Optics FBG-IS instrument uses this principle to measure the strain. A linear strain gradient over the sensing length produces a chirping of the grating and results in a change in both the Bragg wavelength and the shape of the Bragg reflection [10].

Strain gradients occur in many practical problems especially when cracks and flaws are present in the structure. FE analysis of the cracked patched specimen indicated the presence of large strain gradients on the surface of the patch over the crack<sup>3</sup>. As a result we would expect that for a sensor at this high strain location the

Micron Optics instrument should have problems proving a strain reading. This phenomenon was found to occur for a crack length of 25 mm, see Fig. 20, when attempting to read sensor OF2 at a load level of 70 kN.

The opportunities thus arising from severe strain gradients can best be understood by examining some of the Bragg spectra using an ANDO optical spectrum analyser as illustrated in Fig. 21.

Sensor S6, Fig. 21(a), clearly shows the effect of chirping of the grating period. In this case what was originally a fairly standard Bragg reflection spectra has become a complex spectra containing multiple peaks. Such a complex spectra can confuse the FBG-IS instrument, which relies on a simple peak detection algorithm.

This feature can be used to enable optic fibre technology to monitor delamination under the patch. In this case it will be possible to choose a sensor length such that without a delamination the severe strain gradient will result in there being no sensor readings for sensors located in this region. When the patch debonds the strain gradient will become more uniform and a sensor readings will be obtained.

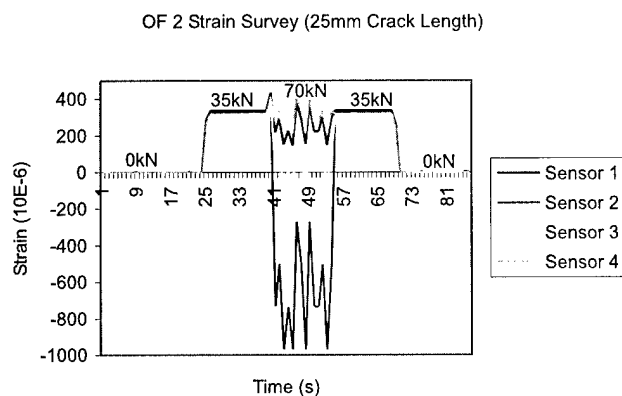


Fig. 20. Strain survey of OF2.

#### 4. Strain monitoring in a TTCP test specimen

To further evaluate the performance of smart sensors The Technical Cooperation programme (TTCP), which involves defence establishments from Australia, UK, US and New Zealand, has chosen to use a particular generic test specimen, see Fig. 22. The dimensions of the specimen are as shown in Fig. 22. The specimen had a 13-ply thick graphite epoxy doubler bonded to both the upper and lower surfaces of the specimen.

The specimen was used to evaluate the effect of delamination damage in both the adhesive and the composite doubler. To this end two different damage states have been considered, viz:

1. an edge debond in the adhesive layer;
2. an edge debond/delamination between the 2nd and 3rd plies of the doubler.

A range of disbond/delamination lengths were considered, viz: 0, 26, 31, 36, 41 and 46 mm, where the distance is measured from the edge of the patch, and the effect that these had on the axial strain, when the specimen was subjected to a remote tensile stress of 137 MPa, was studied using FE analysis. To evaluate the relative merits of in-built versus surface-mounted sensors the strains were computed on both the surface and in the 9th ply. The resultant strain profiles are presented in Figs. 23–26, where  $x = 0$  mm corresponds to the centre line of the specimen.

From these figures it can be seen that, for both cases (1) and (2), the sensors located in the 9th ply are more sensitive to small delaminations/disbonds. However, as the disbond length increases there is relatively little difference in the relative sensitivity of strains, as seen in the 9th ply or on the surface, to the delaminations/dibonds. This implies that, for the present problem, there would be relatively little difference in sensitivity between surface and embedded strain sensors. On the other hand the figures also show that sensors located between 0 and 30 mm from the centre line would have difficulty in as-

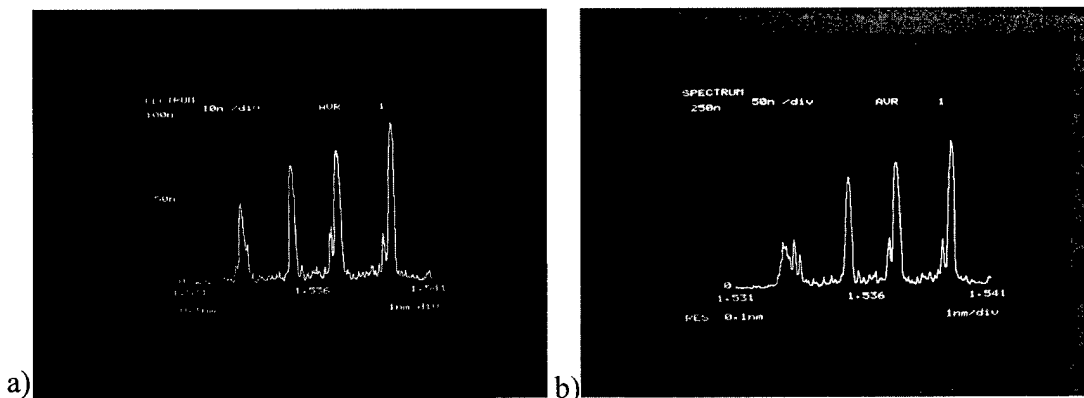


Fig. 21. Optical spectra of OF3: (a) before the crack; (b) after the crack passed under the sensor.

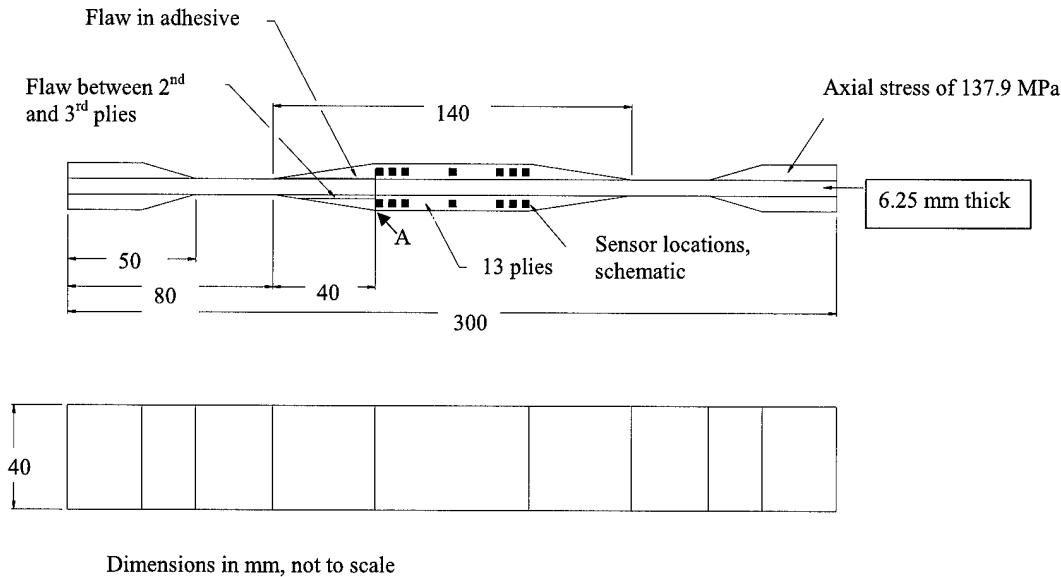


Fig. 22. Geometry of the TTCP test specimen.

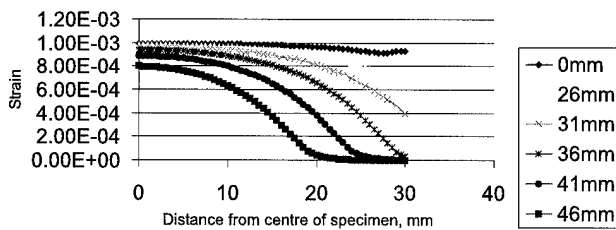


Fig. 23. Strain in the 9th ply of the composite for various disbond lengths in the adhesive.

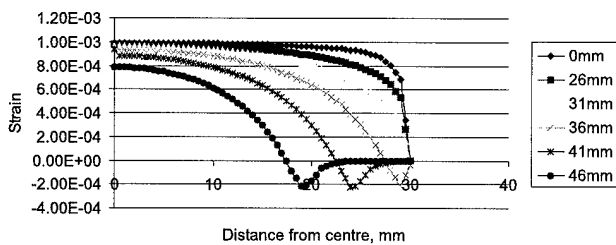


Fig. 24. Strain on the surface of the composite for various disbond lengths in the adhesive.

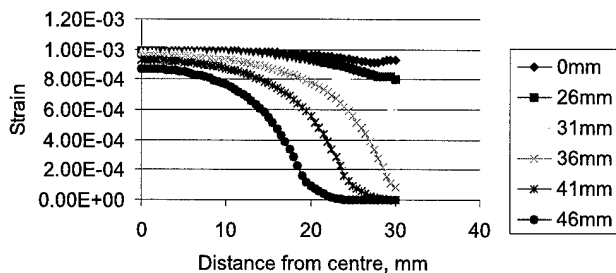


Fig. 25. Strain in the 9th ply of the composite for various disbond lengths in between the 2nd and 3rd plies.

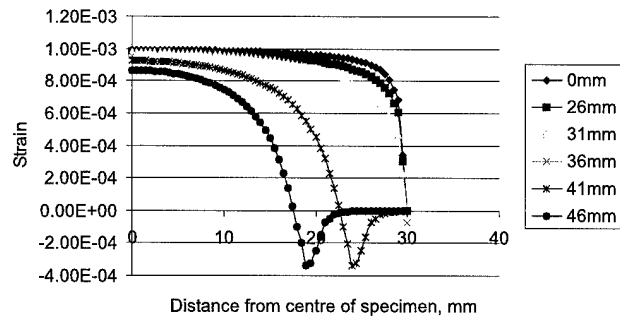


Fig. 26. Strain on surface of the composite for various disbond lengths in between the 2nd and 3rd plies.

sessing flaws less than 26 mm in length. This is not entirely unexpected as, for a 26 mm delamination, a sensor located 30 mm from the centre line would be ~14 mm from the end of the disbond/delamination. Furthermore, for the range of disbonds/delaminations under consideration, sensors located between 20 and 30 mm from the centre line are, in general, more likely to be able to sense the change in the strain field due to the disbond/delamination. For optimum detection of disbonds/delaminations in the taper sensors should be located in the region of the taper.

## 5. Conclusion

This study has demonstrated the ability of optical fibre sensor array to monitor crack growth and delamination under a bonded repair. Indeed, we have seen that OFS sensors have a unique feature that can be used to enable optic fibre technology to monitor delamination

under the patch. For example, in the present test programme it was possible to use a sensor length such that without a delamination the severe strain gradient on the upper surface of a patch over a crack, resulted in there being no sensor readings for sensors located in this region. When the patch debonded the strain gradient became more uniform and sensor readings were then obtained.

## References

- [1] Baker AA, Jones R. Bonded repair of aircraft structure. Hague: Martinus Nijhoff; 1988.
- [2] Jones R, Bartholomeusz R, Kaye R, Roberts J. Bonded-composite repair of representative multi-site damage in a full-scale fatigue-test article. *J Theoret Appl Fract Mech* 1994;21:41–9.
- [3] Technical airworthiness management manual, Defence Instruction (Air Force) AAP 7001.053, November 1994.
- [4] Rao YJ, Ribeiro ABL, Jackson DA, Zhang L, Bennion I. Combined spatial- and time-division-multiplexing scheme for fibre grating sensors with drift-compensated phase-sensitive detection. *Opt Lett* 1995;20:2149–51.
- [5] Melle SM, Liu K, Measures RM. A passive wavelength demodulation system for guided-wave Bragg grating sensors. *IEEE Photon Technol Lett* 1992;4:516–8.
- [6] Jackson DA, Ribeiro ABL, Reekie L, Archambault JL. Simple multiplexing scheme for a fibre-optic grating sensor network. *Opt Lett* 1993;18:1192–4.
- [7] Kersey AD, Berkoff TA, Morey WW. Multiplexed fibre Bragg grating strain-sensor system with a fibre Fabry P erot wavelength filter. *Opt Lett* 1993;18:1370–2.
- [8] Kersey AD, Berkoff TA, Morey WW. High resolution fibre grating based strain sensor with interferometric wavelength shift detection. *Electron Lett* 1992;28:236–8.
- [9] Galea SC. Monitoring damage in bonded composite repairs of cracked metallic components using surface strain measurements. In: Scott ML, editor. *Proceedings ICCM-11*, 14–18 July 1997; ISBN 185573, Australian Composite Society, Melbourne, 1997; p. 707–22.
- [10] Huang S, LeBlanc M, Ohn MM, Measures RM. Bragg intragrating structural sensing. *Appl Opt* 1995;34:5003–9.
- [11] Jones R, Heller M, Lombardo D, Dunn S, Paul J, Saunders D. Damage growth in composites. *Comp Struct* 1989;12:291–314.

# On the analysis of composite structures with material and geometric non-linearities

R. Jones <sup>\*</sup>, H. Alesi

*Department of Mechanical Engineering, Monash University, Wellington Road, Clayton, Vic. 3168, Australia*

## Abstract

If major weight saving is to be realised it is essential that composites be used in “primary” structural components, i.e., wing and fuselage skins. To this end it is essential that analytical tools be developed to ensure that composite structures meet the FAA damage tolerance certification requirements. For stiffened composite panels one potential failure mechanism is the separation of the skin from the stiffeners; resulting from excessive “through the thickness” stresses. This failure mechanism is also present in bonded composite joints and composite repairs. Currently failure prediction due to in-plane loading appears to be relatively well handled. Unfortunately, this is not yet true for matrix-dominated failures. Consequently, it is essential that a valid analysis methodology capable of addressing all of the possible failure mechanisms, including failure due to interlaminar failure, be developed. To aid in achieving this objective the present paper outlines the results of a series of experimental, analytical and numerical studies into the matrix-dominated failures of rib stiffened structures. © 2000 Published by Elsevier Science Ltd. All rights reserved.

**Keywords:** Failure; Buckling; Joints; Finite elements

## 1. Introduction

In the aeronautical field the design certification process for composite structures requires a damage tolerant evaluation of the structure to be performed [1,2]. In accordance with FAA AC's no. 20-107A and AC no. 25.571-1A [1,2] the damage tolerance evaluation of the structure is intended to ensure that should serious fatigue, corrosion, environmental degradation, impact damage, disbonding, delamination or accidental damage occur, then the remaining structure can withstand reasonable loads without failure or excessive structural deformation until the damage is detected. Indeed, to be consistent with the philosophy outlined in [2], AC no. 25.571-1A, ‘the evaluation should define the loading and the environmental conditions, extent of the damage and degradation of the structure, conduct of the associated structural tests or analyses, or both, used to substantiate that the design objective has been achieved, and establish data for the inspection programs necessary to ensure detection of damage’.

Following the current FAA procedures for damage tolerant assessment, as given in [2], the damage tolerant

assessment should be determined by analysis, supported by test evidence in the appropriate environment, unless (as stated in [2]) ‘it has been determined that the normal operating stresses are of such a low order that serious damage growth is extremely improbable’. In this process it must be shown that:

- (a) The residual strength of the damaged structure is not reduced below the specified design limit strength (considered as ultimate strength) over the operational life of the structure; and
- (b) The damage growth rate allowing for impact damage, interply delamination and adhesive debonding under the repeated loads expected in service (between the time the damage becomes initially detectable and the time the extent of damage reaches the value for residual strength evaluation) provides a practical basis for development of the inspection program.

Furthermore in accordance with [1], which deals with composite structure, the repeated loads should allow for load time effects, i.e., dwell time as in the F-111C cold proof load test (CPLT), certification tests (see [3–5] for details), and environmental, i.e., temperature and humidity fluctuations.

The damage tolerance characteristics can be shown analytically by reliable or conservative methods such as the following, see [2]:

<sup>\*</sup>Corresponding author. Tel.: +61-3-9905-4000; fax: +61-3-9905-1825.

E-mail address: rhys.jones@eng.monash.edu.au (R. Jones).

- (i) By demonstrating quantitative relationships with structures already verified as damage tolerant;
- (ii) By demonstrating that each damage event would be detected before it reaches the value for residual strength evaluation; or
- (iii) By demonstrating that the repeated loads and limit load stresses do not exceed those of previously verified designs of similar configuration, materials, and inspectability.

In this process, residual strength assessments to establish the shape of the residual strength-damage envelope, are essential. To this end residual strength evaluation by component testing, or by analysis supported by test evidence, should be performed for each specific damage state. The evaluation should demonstrate that the residual strength of the (damaged) structure is equal to or greater than the strength required for the specified design loads. It should be shown that stiffness properties have not changed beyond acceptable levels. For the no-growth concept residual strength testing should be performed after repeated load cycling.

In these processes the effects of temperature, humidity, and other environmental factors, which may result in material property degradation, should be addressed in the damage tolerance evaluation. These requirements directly reflect current FAA approaches for composite aircraft [1,2].

At the moment, the “Achilles” heel in this process is the lack of understanding of matrix-dominated failures. Failure due to in-plane loading appears to be relatively well handled. Unfortunately, this is not yet true for matrix-dominated failures. However, neglecting to allow for matrix-dominated failures in either the adherends or the adhesive, in the case of a bonded joint, may compromise the FAA certification requirements.

To accurately determine these interlaminar stresses for a complex structural component requires the use of advanced finite element techniques. To this end a number of finite element procedures have been developed for computing the 3D stresses at the stringer/skin interface of post-buckled composite panels. Hachenberg [3] proposed a method which used plate elements for determining the interfacial stresses between the stringer and skin. In other methods, quasi-3D models were employed for calculating these interfacial, i.e., interlaminar, stresses, see Davies [4] and Hyer et al. [5]. The previous techniques were computationally efficient but involved various approximation for the 3D stress state at the interface and did not allow for material non-linearities. This complicated the engineering interpretation of the interlaminar stresses and strains. To model full scale structural components with 3D elements is still a “dream” even with current supercomputer technology. An alternative global-2D/local-3D analysis methodology was suggested by Card et al. [6]. In this approach the

global proportion of a structure was modelled with 2D-plate finite elements and only a critical local domain was modelled with 3D-solid finite elements. The global and the local models were connected with global mesh refinement or other, regional, joining techniques and plate–solid coupling procedures.

One common approach for connecting plate and solid element models is to extend the plate model into the solid element region. This technique is well suited for connecting plate and solid models that have similar element mesh sizes. However, when strong changes in mesh density exist, between the 2D and 3D models, this technique requires extensive modelling of the transition zone. Liao et al. [7] and Surana [8] proposed an alternative means for coupling plate and solid models using 2D/3D transition elements. However, this technique had essentially the same modelling limitations as the classical approach. A regional joining technique for incompatible finite element subdomains, that does not suffer from the previous limitations, was presented by Aminpour et al. [9]. This technique has to be used in combination with transition elements when connecting 2D-plate models to 3D-solid models. However, with this approach modelling efficiency is achieved, although possibly at the expense of both computing time and significant implementation effort, see Housner [10].

An alternative group of coupling techniques based on multi-point constraints (MPCs) was regarded as being very difficult to implement. In disregard of this established opinion Alesi et al. [11] developed and implemented such a technique in the form of a user friendly computer program. The present paper uses this approach for the analysis of two geometrically non-linear structural problems and the results compare quite well with those obtained experimentally.

The majority of the analysis tools discussed above have assumed that the composite is behaving in the linear elastic regime. To illustrate the role that material non-linearities play in the failure of composite structural components the present paper outlines the results of a series of experimental and numerical studies into the failure of rib stiffened structures. Indeed, it will be shown that, when using a visco-plastic approach to the load history dependent response of the matrix material, it was possible to predict the matrix-dominated failure of the structure.

## 2. Background to interlaminar failure

At the stiffener run-out region in rib stiffened panels and when joining primary composite structures via a bonded joint, either secondary bonded, co-cured or co-bonded, the challenge is to transmit the load such that the resultant structure is damage tolerant. This often results in the creation of large interlaminar shear and



peel stresses. Indeed, this was one of the primary causes of the disbonding of the structural reinforcement of the F111C wing pivot fitting, see [12,13] (see Fig. 1).

In several respects the F/A-18 pioneered the use of composite to metal bonded joints as primary load carrying members. Here, the developmental test program included a fatigue test on a pre-production inner wing torque box, commonly referred to as the PTO1 test. This part of the aircraft structure includes the titanium to graphite epoxy step lap joint. During this test program problems were encountered with fasteners at the wing fold region and further examination revealed a large delamination at the second step from the titanium end of the wing root, see [14] for more details. A detailed test program, using representative structural detail specimens, was subsequently performed so as to evaluate the damage tolerance of this joint, see [14]. In this test program the dominant failure mechanism was observed to be interlaminar failure of the matrix material between the graphite epoxy plies bonded to the titanium rather than by failure of the adhesive, viz FM300, used to bond the graphite epoxy to the titanium, see Fig. 2. This failure process further highlighted the need to allow for interlaminar failure in the design process.

Consequently, as outlined above, safety and certification concerns therefore dictate that the matrix-dominated behaviour of both the composite(s) and the adhesive(s) be both understood, characterised and allowed for in the initial design process. The importance of accounting for material non-linearities was also a major finding in [15], which considered its effect on the buckling and post-buckling response of a range of composite structures. Indeed, [15] concluded that:

- (i) “The composite material non-linearity has a significant effect on the geometrically nonlinear, structural buckling load, post-buckling structural stiffness, and failure mode shape of composite plates and shells”.
- (ii) “The composite material nonlinearity also has an appreciable influence on geometric imperfection sensitivity of structural buckling and post-buckling deformations”.
- (iii) “Quantitative determination of these nonlinear effects requires advanced computational nonlinear material and structural mechanics”.

### 2.1. Inelastic response of composites under shear loading

When considering interlaminar failure analysis it should be noted that, when loaded in shear, composite laminates exhibit a similar non-linear stress strain behaviour and monotonic and typical cyclic load results, for AS4-35016, are shown in Figs. 3 and 4 (from [16]). Reference [16] found although there were quite distinct hysteresis loops the loading and unloading curves appeared to be parallel to the initial loading curve. Similar results have also been reported in [17,18] where the rate dependent behaviour of several composite laminates has been studied.

This monotonic and cyclic stress strain behaviour, as shown in Figs. 3 and 4 raises the question:

If a composite structure experiences large interlaminar stresses, which are below the static failure levels, will the structure experience fatigue failure under repetitive cyclic loading?

At the moment there are insufficient data to answer this question. The challenge is to develop both the

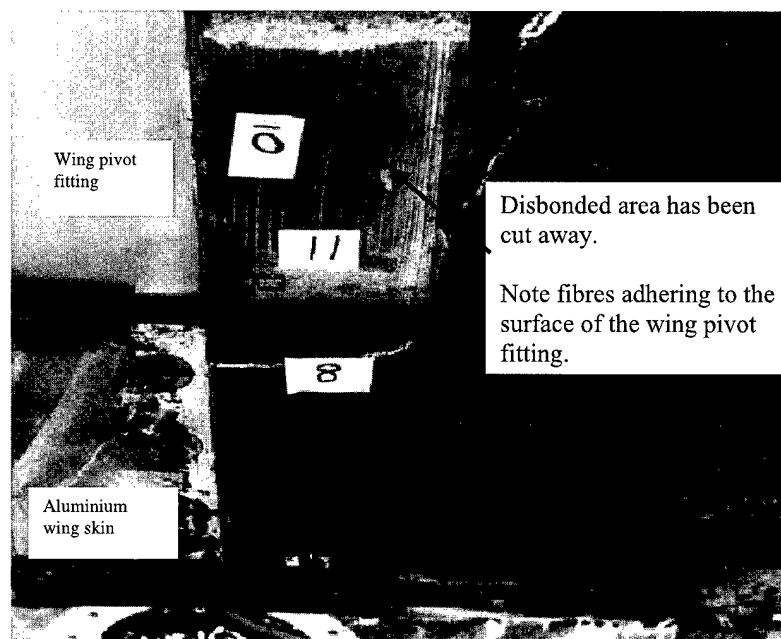


Fig. 1. Close of delaminated doubler on F111 aircraft showing boron fibres still attached to the wing pivot fitting.

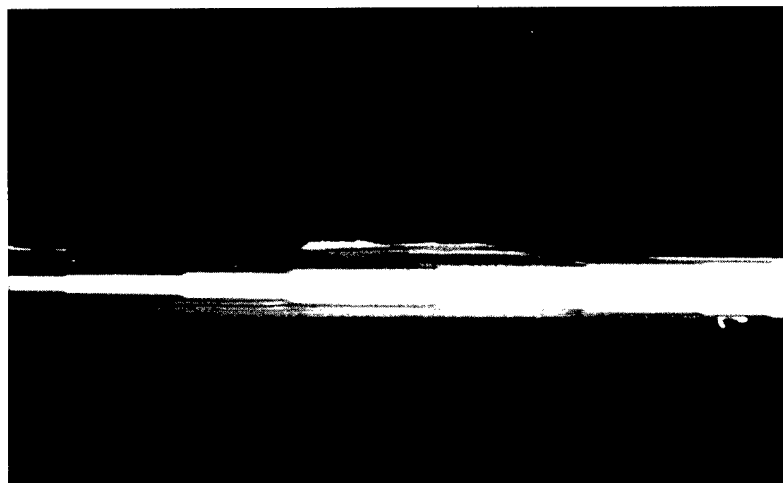


Fig. 2. Typical failure of F/A-18 step lap joint specimens.

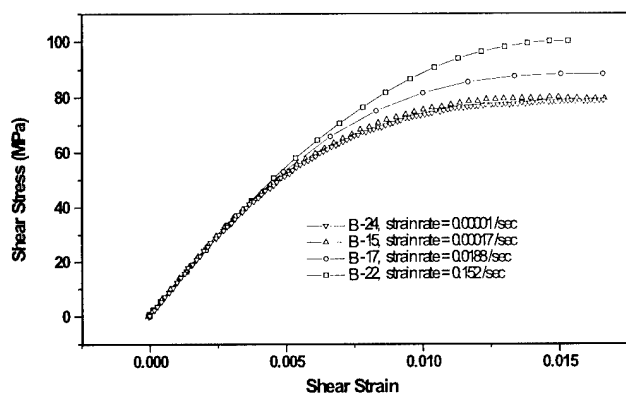
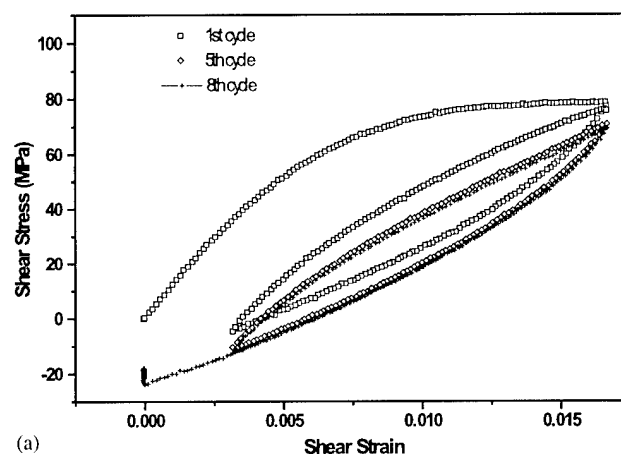


Fig. 3. Shear stress/shear strain behaviour of carbon fibre/epoxy resin system AS4/3501-6 at various strain rates, from [16].

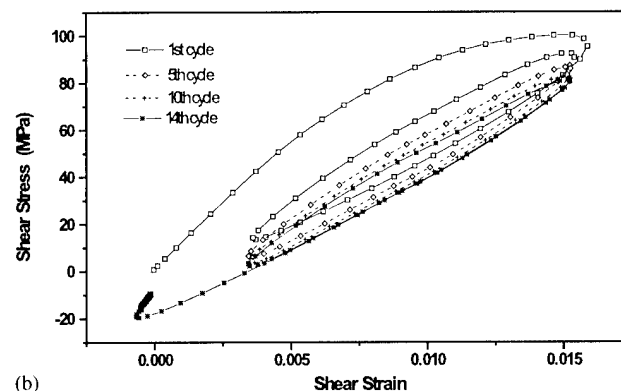
necessary test data and the engineering/mathematical required tools to assist in answering the question.

### 3. A local/global approach to determine 3D stress states

The accurate determination of the interlaminar stresses and strains requires a detailed 3D finite element analysis. One common approach is to use a local/global formulation where only the region of interest is modelled using 3D elements. This can be done using MPCs. The fundamental equations for the MPC coupling technique were developed for the general nodal point arrangement shown in Fig. 5. The 2D plate element nodes (A), (B) and (C) are assumed to be situated on the edge of a plate element that is adjacent to a region modelled using 3D solid elements and node (P) is an arbitrary node in one of the adjoining 3D elements. Point (i) is situated on the intersection between the line that connects (A) and (C) and the line through solid



(a)



(b)

Fig. 4. Shear stress/shear strain behaviour of carbon fibre/epoxy resin system AS4/3501-6 under cyclic loading at various strain rates. (a) 0.00001/s and (b) 0.152/s, from [16].

element node (P) that is orthonormal to line (A)–(C). The displacements of point (i) can be related to the displacements of nodes (A), (B) and (C) by employing the plate element shape functions

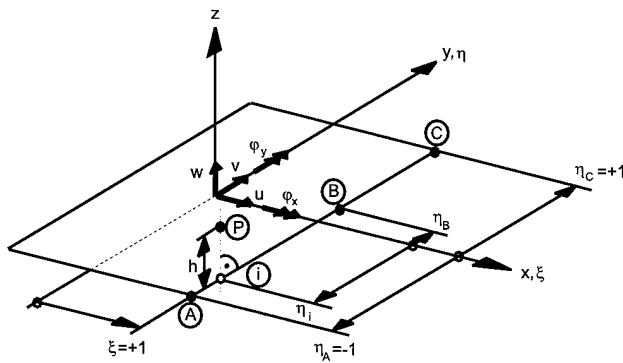


Fig. 5. General interface node arrangement.

$$\begin{aligned} N_A &= -0.25(1 + \xi_i \xi_A)(1 + \eta_i \eta_A)(1 - \xi_i \xi_C - \eta_i \eta_C), \\ N_B &= 0.50(1 + \xi_i \xi_B)(1 - \eta_i^2), \\ N_C &= -0.25(1 + \xi_i \xi_C)(1 + \eta_i \eta_C)(1 - \xi_i \xi_A - \eta_i \eta_A), \end{aligned} \quad (1)$$

where  $\eta$  and  $\xi_i$  are the local coordinates for the plate element. The effect of nodal point displacements at plate nodes (A), (B) and (C) on the displacements at point (i) can now be expressed using the following kinematic relations:

$$\begin{aligned} u_i &= N_A \cdot u_A + N_B \cdot u_B + N_C \cdot u_C, \\ v_i &= N_A \cdot v_A + N_B \cdot v_B + N_C \cdot v_C, \\ w_i &= N_A \cdot w_A + N_B \cdot w_B + N_C \cdot w_C, \\ \varphi_{xi} &= N_A \cdot \varphi_{xA} + N_B \cdot \varphi_{xB} + N_C \cdot \varphi_{xC}, \\ \varphi_{yi} &= N_A \cdot \varphi_{yA} + N_B \cdot \varphi_{yB} + N_C \cdot \varphi_{yC}. \end{aligned} \quad (2)$$

The kinematic relationship between the displacements at node (P) and at point (i) can be defined by applying the assumptions of Kirchhoff plate theory. In this case the displacements of node (P) can be expressed in terms of displacements and rotations on point (i), viz

$$\begin{aligned} u_P &= u_i + h \cdot \varphi_{yi}, \\ v_P &= v_i - h \cdot \varphi_{xi}, \\ w_P &= w_i. \end{aligned} \quad (3)$$

Substituting Eq. (2) into Eq. (3) yields a relationship between the degrees of freedom of the solid element node (P) and degrees of freedom of the plate element nodes (A), (B) and (C); viz

$$\begin{aligned} \begin{Bmatrix} u_P \\ v_P \\ w_P \end{Bmatrix} &= N_A \cdot \begin{Bmatrix} u_A \\ v_A \\ w_A \end{Bmatrix} + N_B \cdot \begin{Bmatrix} u_B \\ v_B \\ w_B \end{Bmatrix} + N_C \cdot \begin{Bmatrix} u_C \\ v_C \\ w_C \end{Bmatrix} \\ &\quad + N_A \cdot h \cdot \begin{Bmatrix} \varphi_{yA} \\ -\varphi_{xA} \\ 0 \end{Bmatrix} + N_B \cdot h \cdot \begin{Bmatrix} \varphi_{yB} \\ -\varphi_{xB} \\ 0 \end{Bmatrix} + N_C \cdot h \cdot \begin{Bmatrix} \varphi_{yC} \\ -\varphi_{xC} \\ 0 \end{Bmatrix}. \end{aligned} \quad (4)$$

This equation can be used to formulate a generic coupling program which can be used as a pre-processor for a variety of finite element codes, viz: MSC/NASTRAN, ABAQUS, etc. The present program reads a basic data input file and automatically identifies solid element nodes that are situated within their appropriate plate/solid interface control volumes. The program then generates, based on the physical location of plate nodes (A), (B) and (C), the coupling equations for every solid element node that is found within a user defined control volume. The resulting multi-point constraint statements are automatically added, in the required format, to the basic data input file.

### 3.1. Numerical validation

Two numerical examples were used to validate this coupling technique. The first was a plate-bending analysis of a composite plate whilst the second test case involved post-buckling analysis. In both cases the stress strain relationship was assumed to be linear.

#### 3.1.1. Interlaminar stress analysis

The first example involves the case of the simply supported rectangular laminated plate, previously analysed in [19], with a  $[0,90]_s$  stacking sequence and with dimensions  $a = b = 100$  mm and  $t = 1$  mm, see Fig. 6. The moduli of the individual layers (lamina) were assumed to be  $E_{11} = 138$  GPa,  $E_{22} = E_{33} = 9.3$  GPa,  $G_{12} = G_{13} = 4.6$  GPa,  $G_{23} = 3.2$  GPa,  $\nu_{12} = \nu_{13} = 0.3$ , and  $\nu_{23} = 0.3$ . The plate was subjected to a variable pressure load  $\sigma_{zz} = -P \cos(\pi x/a) \cos(\pi y/b)$ . Due to symmetry only a quarter section of the plate was modelled, see Fig. 7.

One plate element was removed from the 2D model and replaced with a local 3D model. The 3D model consisted of a  $10 \times 10 \times 12$  mesh of 20-noded solid elements. To achieve an accurate representation of the interlaminar stresses each ply of the plate was modelled

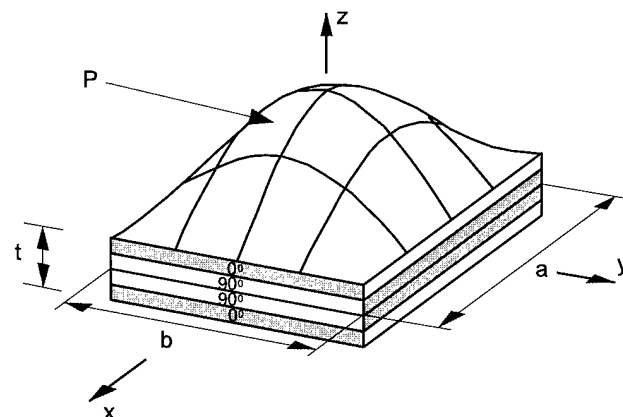


Fig. 6. Orthotropic plate.

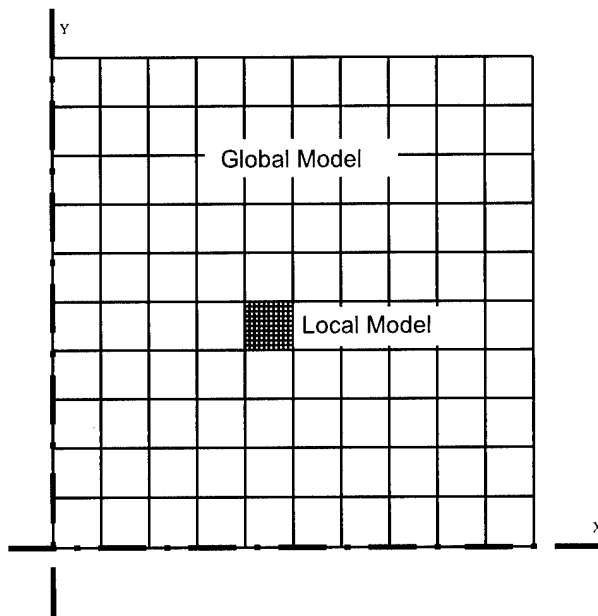


Fig. 7. Global/local model.

with three layers of solid elements. The in-plane stress results were almost identical to the analytical solution from classical laminated plate theory and as such are not presented here. The calculated interlaminar stresses were also in good agreement with those given in [19] as can be seen from Fig. 8 which shows these stresses slightly in-board (three elements) from the transition region. Here the maximum values for the interlaminar stresses  $\sigma_{xz}$ ,  $\sigma_{yz}$ , and  $\sigma_z$  were within 1%, 12%, and 1%, respectively, of the analytical solution, see Fig. 8.

### 3.1.2. Post-buckling deflection analysis

As a second illustration of this technique we first considered the post-buckling behaviour of a thin plate subjected to an in-plane force  $P(N)$ , see [20]. This test case consisted of a flat rectangular metal plate with dimensions  $a = 2$  m,  $b = 1$  m and  $t$  (thickness) = 0.01 m, see Fig. 9. The plate was assumed to be isotropic with moduli of  $E = 72,000$  MPa and  $\nu = 0.3$ . The loaded plate ends and the longitudinal unloaded plate sides were simply supported. Additional kinematic constraints were imposed that forced the ends and the sides to remain straight.

Three different finite element models were generated, see Fig. 10. The first model consisted of quadrilateral plate elements that had both membrane and bending stiffnesses. The second model was made from two layers of hexahedral solid elements. The third model had three quarters of the region modelled with plate elements and a quarter with 3D elements. The plate region and the solid region of the combined plate–solid model were connected as described above. The analysis used MSC-NASRAN which, at the time of the investigation, did

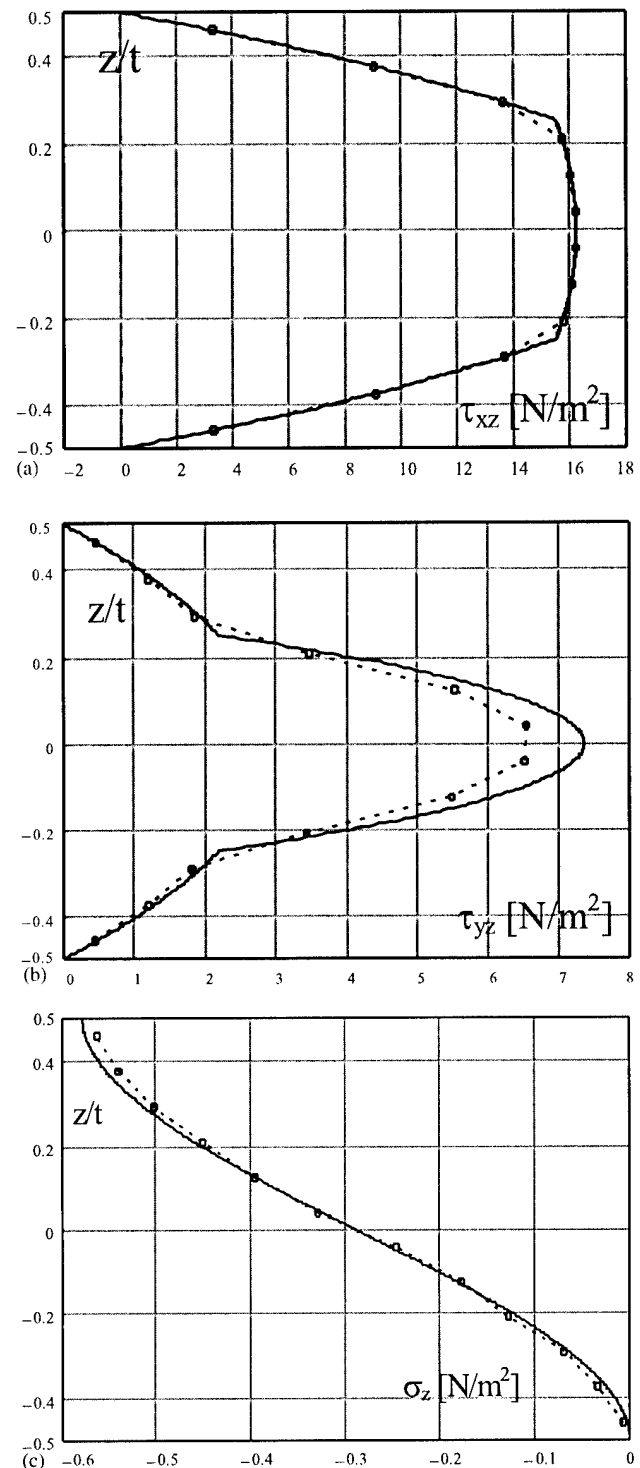


Fig. 8. Comparison of the computed interlaminar stresses with those from [19].

not support eight-noded plate-bending elements for geometric non-linear analysis. Consequently this analysis used four-noded and three-noded, triangular, plate-bending elements.

The three models were analysed, employing a standard incremental-iterative solution scheme, in displace-

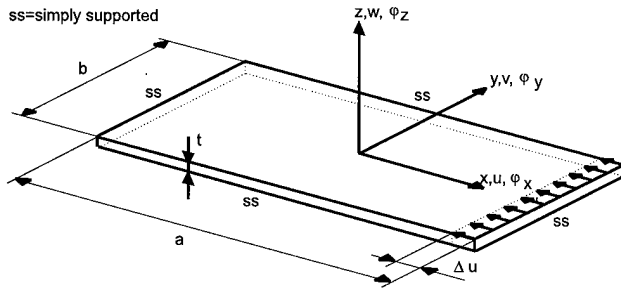


Fig. 9. Compression loaded plate.

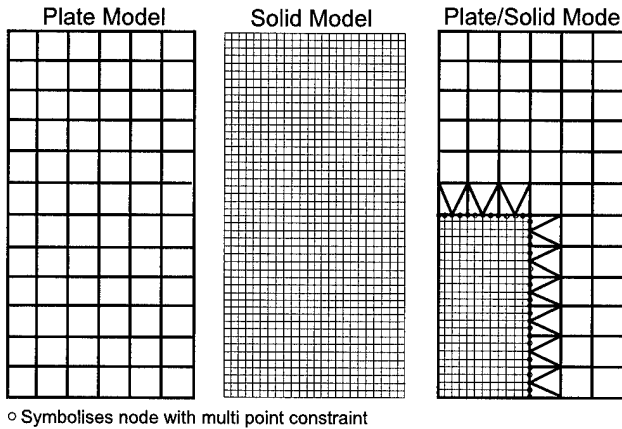


Fig. 10. The three finite element models.

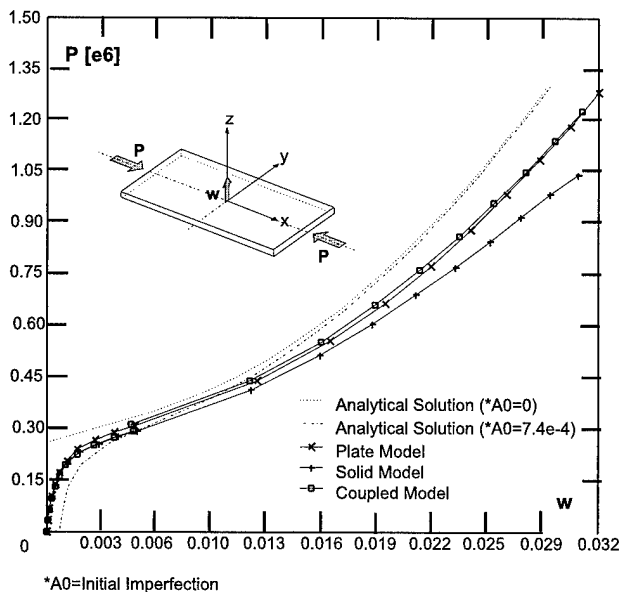


Fig. 11. Load-displacement curves for plate problem.

ment control mode. The resulting finite element load-deflection curves are compared in Fig. 11 along with Supple's [20] analytical solution.

Inspection of the load-displacement curves shows that the analytical plate model had the highest post-

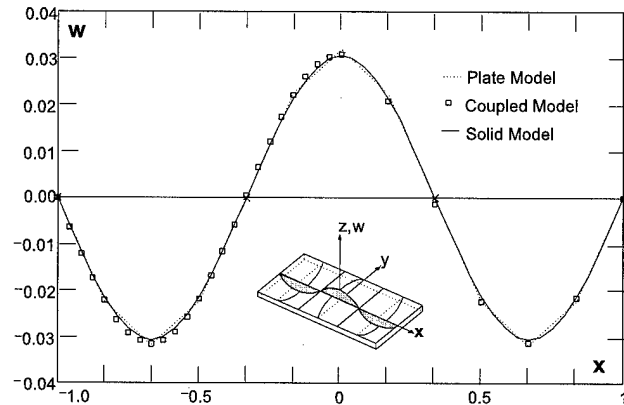


Fig. 12. Out-of-plane deflections.

buckling stiffness. This finding was not surprising considering that the analytical model was based on equations with only two generalised degrees of freedom associated to the first and second buckling mode. The 2D-plate finite element model and the combined 2D/3D finite element model were slightly more flexible. The 3D-solid finite element model was significantly more flexible than the analytical model. In general, the combined model results were in-between the plate and the solid model results.

The plate displacement results, obtained by the various techniques, along the  $x$ -axis are compared in Fig. 12. The maximum variation between the different models was  $\sim 3\%$ .

#### 4. Stiffened panel analysis

Having validated the global-2D/local-3D finite element methodology for a simple test case it was then employed for the investigation of a post-buckled composite stringer/skin panel. The panel under consideration was designed at the Co-operative Research Centre for Advanced Composite Structures (CRC-ACS) located in Melbourne, Australia. The CRC-ACS test panel was selected for the current investigation because a 2D finite element model, that could form a useful basis for the current work, was made available by the CRC-ACS. The particular panel was designed by Thomson et al. [21] and consisted of a quasi-isotropic composite skin and three composite blade stiffeners that were equally spaced across the working section, see Fig. 13.

##### 4.1. The finite element model

The 2D finite element model of the shear panel is shown in Fig. 14. In this model, the stringers and the skin were modelled with four-noded quadrilateral plate-bending elements and the shear fixture was modelled with beam-type elements.

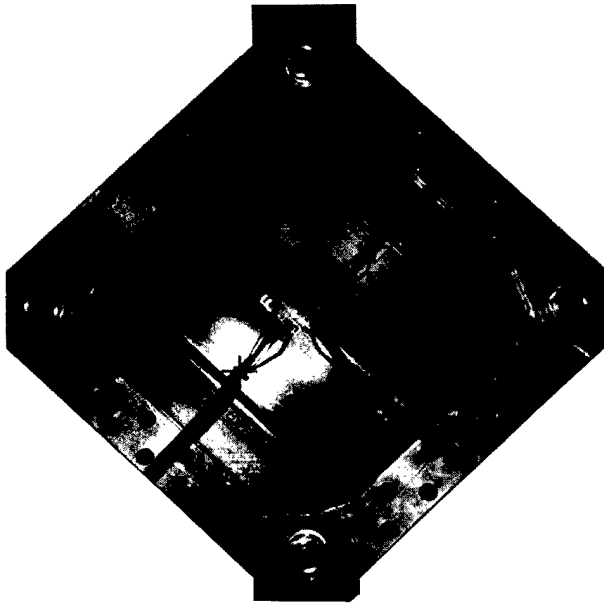


Fig. 13. Composite shear panel and test configuration.

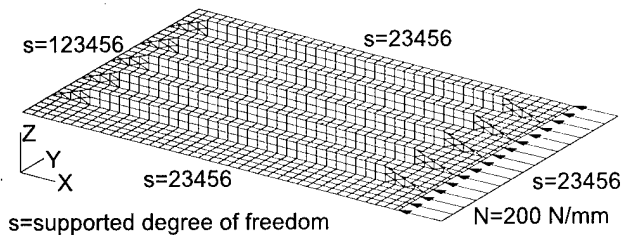


Fig. 14. Global 2D-plate finite element model.

To represent the test conditions a point load, acting in the plane of the panel skin, was applied to the right corner of the beam frame. The loaded node was kinematically constrained in order to move in the direction

of the applied load. The translations at the opposite corner of the beam frame were suppressed. The out-of-plane translations and rotations on the four edges were suppressed in order to simulate the clamping conditions in the test fixture.

The local 3D model of the critical skin/stiffener region in the centre of the panel is shown in Fig. 15. Individual plies of the skin/stiffener interface were modelled with discrete layers of hexagonal solid elements. Pentagonal solid elements were employed for the ply drop-off areas. The critical skin/stiffener interface regions, such as the stiffener web/flange transition and the ply drop-offs, were also modelled. The various elastic moduli and strengths used in this analysis are given in Tables 1 and 2, respectively.

#### 4.2. The experimental test

A shear test rig was employed for the experimental model verification and a total of three panels were tested, see Fig. 9. The picture frame test fixture had a working area of  $250 \times 250$  mm. and was designed to avoid stress concentrations in the specimen corners which can lead to pre-mature panel failure. In the current design the pinned corners were free to pivot but not able to move out-of-plane. Six high precision electrical resistance strain gauges were bonded to each panel in order to record the surface strains in the critical skin/stiffener region during load application.

The tests were performed using a 200 kN MTS servo-hydraulic uniaxial testing machine. The machine was configured to load in tension by using a constant ramp-loading generator in displacement control mode. The uniaxial quasi-static load was applied diagonally through the top and bottom pins and was transferred to the panel sides by the edge members of the fixture. This

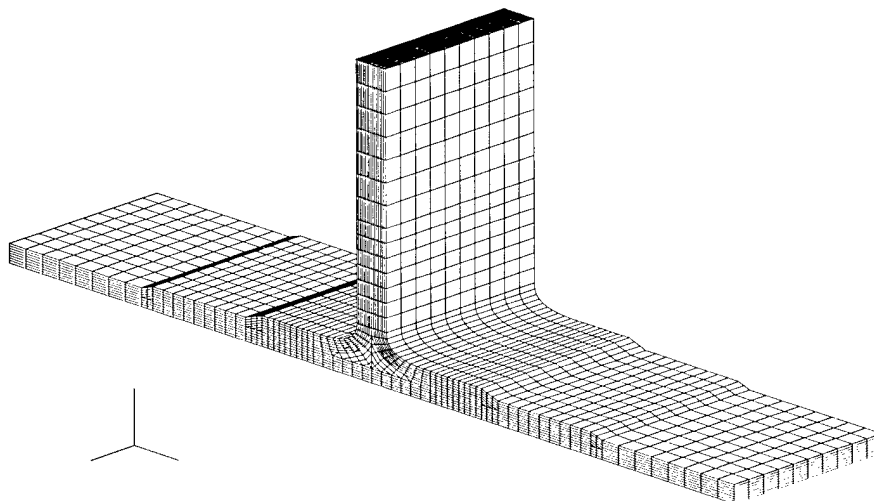


Fig. 15. Local 3D-solid finite element model.

Table 1  
Material constants for T300/914C, from [22]

$E_{11}$	$E_{22}$	$E_{33}$
131.90 GPa	9.51 GPa	9.43 GPa
$G_{12}$	$G_{13}$	$G_{23}$
5.27 GPa	7.03 GPa	3.39 GPa
$\nu_{12}$	$\nu_{13}$	$\nu_{23}$
0.326	0.341	0.485

Table 2  
Material allowables for T300/914C (MPa), from [22]

Material allowable	Symbol	Value
Tensile strength in fibre direction	$X_T$	1328.0
Compression strength in fibre direction	$X_C$	1064.0
In-plane transverse tensile strength	$Y_T$	70.9
In-plane transverse compression strength	$Y_C$	221.0
Interlaminar peel strength	$Z_T$	97.6
Interlaminar compression strength	$Z_C$	242.0
In-plane shear strength	$S_{12}$	71.2
Interlaminar 1–3 shear strength	$R_{13}$	94.5
Interlaminar 2–3 shear strength	$T_{23}$	52.9

was equivalent to applying a pure in-plane shear load at the panel sides.

#### 4.3. Test results

This section compares the results from the geometric non-linear finite element analysis to the results obtained from the experimental program. A plot of the (computed) deformed shape of the panel is given in Fig. 16. A qualitative inspection of the deformations experienced by the panel shows that the local solid element model, in the centre of the panel, deformed consistently with respect to the global plate element model. This figure also shows the complexity of the post-buckled shape.

The combined global-2D/local-3D finite element model was further validated by comparing computed and measured strains within the critical skin/stiffener

region, see Fig. 17. Inspection of the load-strain curves shows that the onset of buckling was observed, both in the analysis and the experiments, at approximately 30 kN. The computed post-buckling strains were consistent with the experimental results up to two times the critical buckling load, i.e., up to approximately 60 kN. At this load level there were a series of loud noises indicative of failure initiation and as a consequence, at higher loads, a significant amount of scatter was observed in the experimental strain readings.

In the post-buckling domain the strain results from the individual panel tests showed some variation, i.e., scatter. It was initially thought that the differences were caused by small changes during panel manufacture. However, inspection of the panels and the analysis revealed that the major contribution towards the scatter in the experimental results came from variations in the precise location of the strain gauges. The scatter was small at pre-buckling loads where the panels deformation was essentially in-plane and resulted in a relatively homogeneous strain field. The pre-buckling strain results were therefore only marginally sensitive to the location of the strain gauges. The strain scatter was larger in the post-buckling regime where the post-buckled shape was particularly complex, see Fig. 16, and the resultant strain distribution in the panels was extremely non-uniform with large localised strain gradients around the buckles. In this regime small differences in the location of the gauges resulted in large variations in the strain gauge readings.

The finite element model gave a structural representation that was somewhat stiffer than the physically observed panel behaviour. A possible explanation for this mismatch was given by Wang et al. [15]. They found that the post-buckling behaviour of composite structures can be affected if individual plies exhibit material non-linearity. However, this potential effect was not modelled in the current simulation.

The stresses resulting from the 3D finite element model were substituted into the Tsai-Wu [24] failure theory. This approach predicted failure initiation to commence at approximately 58 kN. This prediction

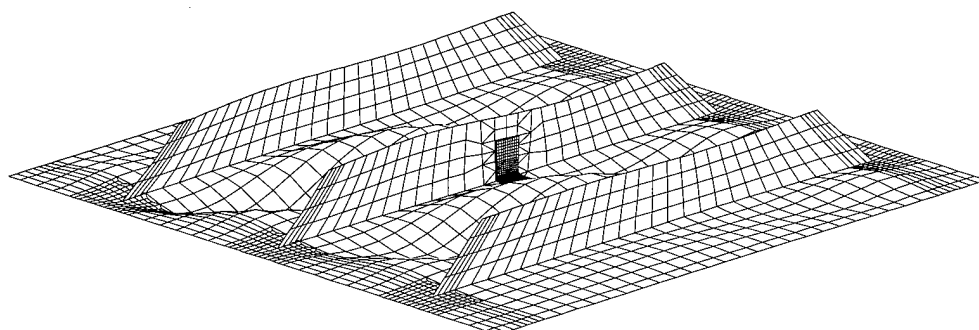


Fig. 16. Deformed geometry of combined plate–solid model.

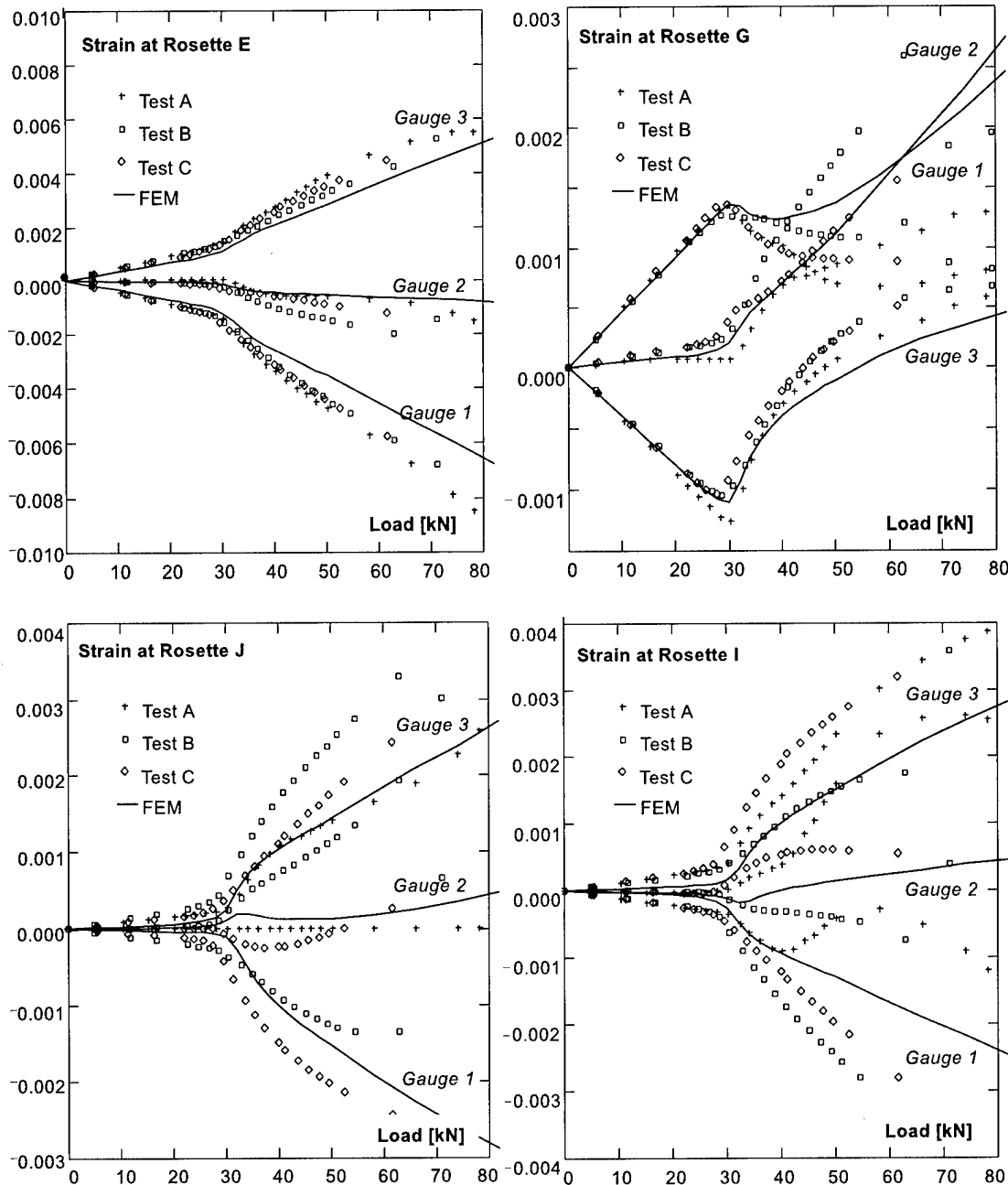


Fig. 17. Comparison of computational and experimental surface strains.

correlated very well with the experimental results where failure initiation occurred at load levels, which ranged between 62 and 64 kN.

No post-(initial) failure analysis was performed to determine the ultimate strength of the panels. It was therefore not possible to explain why one panel that underwent continuous loading failed at an ultimate load 15% less than the panels that were loaded incrementally. In the absence of more test data it could not be determined whether the apparent drop in ultimate strength was caused by a manufacturing defect or by time dependent, i.e., visco-plastic behaviour of the panels. The

overall shear test conditions and observations are summarised in Table 3.

### 5. Post-buckled stiffened panels under axial loading

In the previous test failure was essentially due to the in-plane stresses. However, to illustrate the role of interlaminar failure and the need to accurately compute the associated interlaminar stresses let us consider the post-buckling behaviour of the composite stringer/skin panel discussed in [22]. In this paper the composite panel



Table 3  
Shear test conditions and observations

	Experiment A	Experiment B	Experiment C	FEM
Load rate	0.3 mm/min	0.3 mm/min	0.3 mm/min	
Temperature	21°C	25°C	25°C	
Humidity	30%	30%	30%	
Initial bending	~26 kN	~25 kN	~25 kN	~25 kN
Initial buckling	30 kN	31 kN	30 kN	30 kN
First crack	63 kN	62 kN	64 kN	58 kN
Ultimate failure	78 kN	68 kN	79 kN	
Comments	Load hold at 10 kN Inc.	Continuous loading	Load hold at 10 kN Inc.	

under investigation was fabricated from unidirectional carbon/epoxy CIBA GEIGY/FIB-REDUX 914-TS-534 tape that contained T300 high tensile TORAYACA carbon fibres. The panels consisted of a quasi-isotropic skin with the blade-type stiffeners equally spaced across the working section. A description of the panel geometry is given in Fig. 18, see [22] for more details.

The skin regions between the stiffeners were made from eight plies and the stiffeners were made from sixteen plies of unidirectional tape. A symmetric stiffener lay-up was employed. This resulted in a skin lay-up that alternated between being symmetric in some skin bays and unsymmetric in other skin bays. The top three skin plies were wrapped from the skin on to the stiffener in order to make the stiffener form a more integral part of the skin, see Fig. 19.

Five stringer/skin panels were tested using a box beam test rig which consisted of a three bay aluminium box beam, a supporting steel frame and two 20,000 lb load jacks operated in load control. The jack loads induced a constant bending moment into the middle bay where the test panel was located, see Fig. 20. The test panel was loaded by a distributed force,  $N$ , that acted in the plane of the box beam covers, see [22] for more details.

### 5.1. Numerical analysis

The loading and support conditions, together with the global 2D finite element used in [22] are shown in

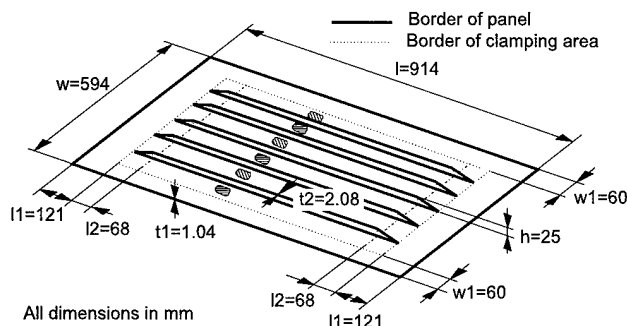


Fig. 18. Test panel geometry, from [22].

Fig. 21. In the local 3D model the individual plies were modelled with separate layers of 3D solid elements, see Fig. 22.

### 5.2. The material model

The finite element analysis used a particular form of the general purpose visco-plastic material model developed in [24–26]. In this analysis a number of simplifying assumptions were made, viz:

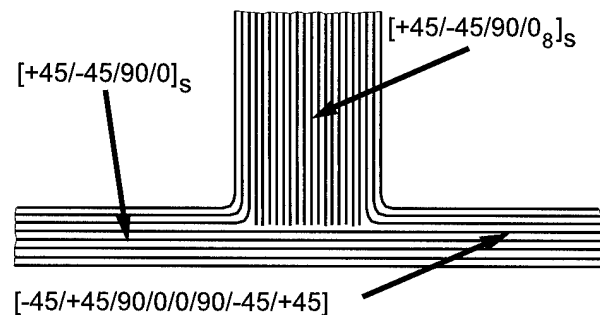


Fig. 19. Schematic of ply stacking sequence, from [22].

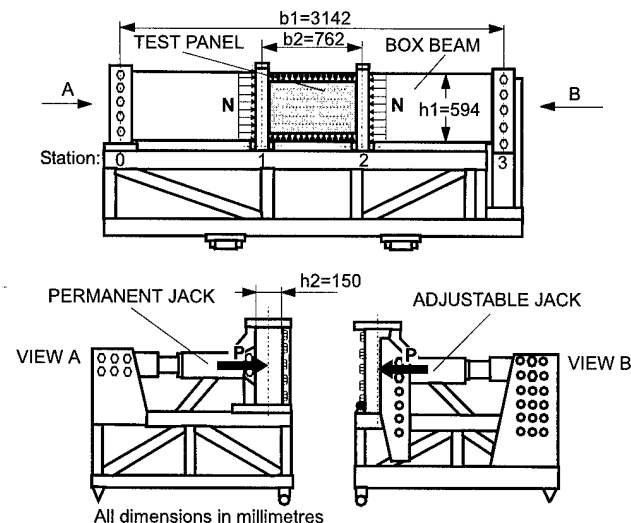


Fig. 20. Box beam test rig, from [22].

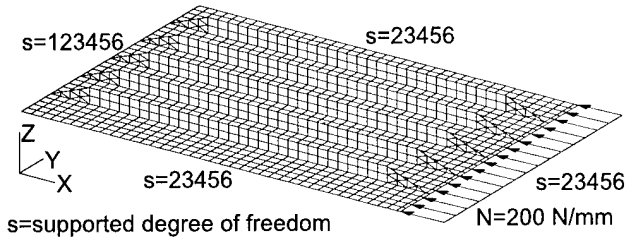


Fig. 21. The initial global 2D finite element model, from [22].

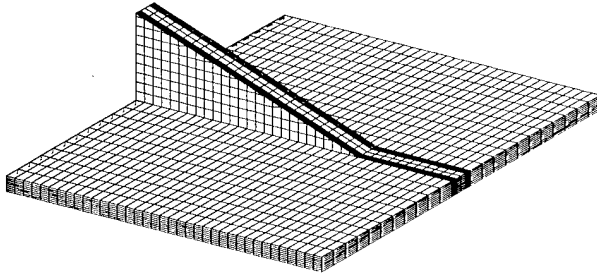


Fig. 22. The local 3D finite element model, from [22].

1. only the matrix-dominated stress terms  $\sigma_{22}$ ,  $\sigma_{33}$ ,  $\sigma_{12}$ ,  $\sigma_{13}$  and  $\sigma_{23}$  were considered to contribute to the visco-plastic response;
2. as a first order approximation it was assumed that, at room temperature, the direct stresses  $\sigma_{11}$ ,  $\sigma_{22}$  and  $\sigma_{33}$  were linear functions of the direct strains;
3. as a first order approximation the inelastic shear behaviour was taken to be similar in each of the three principal material planes.

These assumptions lead to a constitutive model that contained a linear elastic/orthotropic representation for the direct stress components, the associated elastic constants are given in Table 4, and a non-linear inelastic representation for the shear stress components. The resultant formulation essentially consisted of three equations. The first equation represented the constitutive relation between the inelastic shear strain rate  $\dot{\epsilon}_{ij}^I$ , the shear stress  $\tau_{ij}$ , the 'back (shear) stress'  $\Omega_{ij}$ , the 'drag stress'  $Z$  and the effective value of the 'overstress'  $K_2$

$$\dot{\epsilon}_{ij}^I = D_0 \cdot \exp \left[ -\frac{A}{2} \cdot \left( \frac{Z^2}{3 \cdot K_2} \right)^n \right] \cdot \frac{(\tau_{ij} - \Omega_{ij})}{\sqrt{K_2}}, \quad (5)$$

where

$$K_2 = \frac{1}{2} (\tau_{ij} - \Omega_{ij})(\tau_{ij} - \Omega_{ij}). \quad (6)$$

The 'back stress' was computed via the evolution; viz

$$\dot{\Omega}_{ij} = \frac{2}{3} \cdot f_1 \cdot \dot{\epsilon}_{ij}^I - f_1 \cdot \frac{\Omega_{ij}}{\Omega_s} \cdot \dot{\epsilon}_c^I + f_2 \cdot \dot{\tau}_{ij}, \quad (7)$$

where  $\dot{\epsilon}_c^I$  was the effective inelastic strain rate. As in [25,26] the 'drag stress'  $Z$  was defined to be a function of accumulated inelastic work  $W^I$ , viz

$$Z = Z_1 + (Z_0 - Z_1)e^{-mW^I}. \quad (7)$$

The resultant material parameters  $A$ ,  $D_0$ ,  $n$ ,  $f_1$ ,  $f_2$ ,  $m$ ,  $Z_0$ ,  $Z_1$ ,  $\Omega_s$  used in [22] to describe the shear stress strain behaviour of T300/914C are presented in Table 4, see [22] for more details. The various elastic moduli and strengths used in this analysis are as given in Tables 1 and 2.

This simplified model for the inelastic shear response coincides with that used in [24,25] for modelling the shear performance of structural epoxies. At this point it should be stated that this particular visco-plasticity model was primarily used due to the authors' familiarity with the formulation rather than a belief that it was inherently superior to other competitive formulations, i.e., [15,27–29].

Reference [22] then used this material law in conjunction with the ABAQUS finite element program. Prior to the analysis of the particular test program outlined the numerical model was validated by comparison with a series of shear strain shear stress coupon tests, on a (+/–45°)s T300/914C laminate 40 mm wide and 120 mm long. These coupon tests were performed, in accordance with ASTM standard D3518-76. The numerical implementation was also validated by comparison with a prior 1-D solution [30] for an adhesively bonded lap joint which used the same constitutive law.

### 5.3. Stress and failure analysis

When assuming that the material behaved in a linear elastic fashion an apparent "stress singularity" occurred at the stiffener run-out region. This interpretation was implied when numerical convergence tests with different stiffener tip mesh sizes were performed. In this process it was found that some tip stress components increased dramatically when the mesh size reduced. The problem did not arise in the material non-linear analysis. In this case the material behaved in an inelastic fashion and load was shed to other areas.

Having obtained a solution for the stress and strain states at the stiffener run-out several of the more commonly used 3D composite failure theories, see [23,31–35], were then employed in an attempt to predict failure.

Table 4  
Material parameters for T300/914C, from [22]

$A$	$D_0$	$n$	$f_1$	$f_2$	$m$	$Z_0$ (MPa)	$Z_1$ (MPa)	$\Omega_s$ (MPa)
1	$5 \times 10^9/s$	0.237	$2.4 \times 10^4$	0	0	$2.9 \times 10^5$	$2.9 \times 10^5$	65

The material strength allowables for T300/914C, used in [22], are presented in Table 4. A comparison between the predicted and experimental failure initiation loads is given in Table 5.

From this analysis it was found [22] that, at the design load of  $N = 200$  N/mm, the critical stress levels were only exceeded in a very small region in the vicinity of the stiffener run-out tip. The critical regions were found to occur in  $0^\circ$  plies within the stiffener and the skin and also within the  $90^\circ$  degree plies in the stiffener. This result was consistent with a c-scan image that was taken after the panels had failed. Here it was found that delamination mainly occurred around the stiffener run-outs. Reference [22] stated that the delaminations in the far left skin bay were formed during final panel collapse. The stress components and the associated failure indices for the critical elements are shown in Table 6.

Post-failure inspection of the area showed that failure was due to the stiffener run-out separating from the skin. The stiffener run-out also split at the interface between the 'block' of  $0^\circ$  stringer plies and the top three stringer/skin cover plies. Both of these experimentally observed failure mechanisms were consistent with the computationally predicted failure modes.

Table 5  
Comparison of failure loads (N/mm), from [22]

Failure theory	$P_{\text{limit}}^a$	$P_{\text{limit}}^b$	$P_{\text{limit}}^c$ (test panel)
Max. stress	106.85	153.74	204.00 (BP01)
Hoffman	91.22	178.49	211.00 (BP06)
Tsai-Wu	84.26	150.79	187.00 (BP06B)
Hashin	75.84	157.98	158.00 (BP10)
Quad. stress	101.49	158.08	
Average values	89.13	154.50	188.80

<sup>a</sup>FEM material linear analysis.

<sup>b</sup>FEM nonlinear material.

<sup>c</sup>Experiment.

Table 6  
Critical element stresses (MPa), in the local ply axis system, from [22]

Element	$\sigma_{11}$	$\sigma_{22}$	$\sigma_{33}$	$\sigma_{12}$	$\sigma_{13}$	$\sigma_{23}$	$f^a$
3030	-1376	-15	-74	55	9	-2	1.8
3252	-1384	-40	-86	44	33	13	1.7
6582	-1375	-15	-74	56	-8	2	1.8
6804	-1382	-40	-85	45	-33	-13	1.7
3031	-891	-15	-62	66	10	-4	1.2
6583	-891	-15	-62	66	-9	4	1.2
1515	-313	-12	-37	81	9	-10	1.2
2130	-313	-12	-37	81	-9	10	1.2
12310	-817	-31	-60	82	32	-6	1.6
12311	-709	-18	-58	90	6	-7	1.7
12312	-709	-18	-58	90	-5	7	1.7
12313	-818	-32	-60	82	-32	6	1.6
2747	57	-26	-13	-15	-25	-65	1.3
2752	54	-26	-13	-15	25	65	1.3
12309	84	-82	-76	-42	-26	-62	1.2
12314	84	-82	-76	-42	26	62	1.2

<sup>a</sup> $f$  = Failure index.

#### 5.4. Discussion

The material non-linear analysis performed in [22] produced physically meaningful stress values that could be employed for a quantitative prediction of failure initiation. In general the computed results for both the buckling and the failure initiation loads represented conservative estimates of the experimentally observed values, see Fig. 23. These findings support the findings presented in [15] that, for composite structures undergoing geometrically non-linear deformations, failure initiation can be effectively modelled and that sometimes it may be necessary to allow for material non-linearities in the analysis. As previously mentioned the particular visco-plasticity model used in this investigation was primarily due to the authors' familiarity with this formulation rather than a belief that it was inherently superior to other competitive formulations.

Given that the shear stress shear strain response of many composite materials can exhibit significant inelastic behaviour, see Figs. 3 and 4 and Refs. [15–18,22,24,27–29], this work raises the question of the

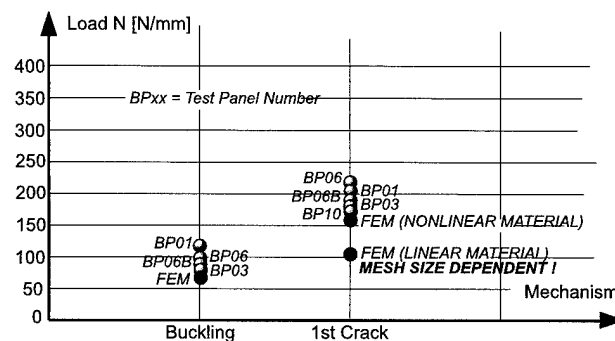


Fig. 23. Summary of results, from [22].

need to evaluate the fatigue performance of composite structural components with large interlaminar stresses which are beneath static failure levels but which are subjected to repetitive cyclic load spectra.

## 6. Conclusion

On the basis of the examples presented in this paper it is clear that when evaluating the structural integrity of composite structural components it may sometimes be necessary to take the potential for matrix-dominated failures, with its implicit load history and time dependency, into account. This paper has illustrated this conclusion via a series of studies ranging from the post-buckling behaviour of a rib stiffened composite panel to failures on F111 aircraft.

To assist with this requirement the present paper has presented a methodology for the finite element analysis of composite structures undergoing both geometric and material non-linearities. The methodology has been validated using two (relatively) simple test cases and then applied for analysing two quite different composite stringer/skin panels. In both the finite element results from the analysis correlated quite well with experimental test results.

Whilst this work has focused on failures due to static loading it raises the question:

If a composite structure experiences large interlaminar stresses, which are below the static failure levels, will the structure experience fatigue failure under repetitive cyclic loading?

At the moment there are insufficient data to answer this question. The challenge is to develop both the necessary test data and to validate the engineering/mathematical required tools to assist in answering the question.

## References

- [1] Composite aircraft structure. Federal Aviation Administration Advisory Circular, 20-107A; 1984.
- [2] Damage tolerance and fatigue evaluation of structure. Federal Aviation Administration Advisory Circular, 25.571-1A; 1986.
- [3] Hachenberg D, Kossira H. Theoretical and experimental investigation of stringer peeling effects at stiffened shearloaded composite panels in the postbuckling range. ICAS-90-4.3.1; 1990. p. 511-21.
- [4] Davies GAO, Robinson P. Predicting failure by debonding/delamination. Dept of Aeronautics, Imperial College, London, Report on Brite Euram Programs BE 3159 & BE 3160; 1992. p. 5-1-5-28.
- [5] Hyer MW, Loup DC, Starnes JH. Stiffener/skin interactions in pressure-loaded composite panels. AIAA J 1989;28(3):532-7.
- [6] Card MF, Starnes JH. Current research in composite structures at NASA's Langley research centre. In: Proceedings of the International Conference on Composite Materials and Structures, Madras; 1988. p. 1-17.
- [7] Liao CL, Reddy JN, Engelstad SP. A solid-shell transition element for geometrically non-linear analysis of laminated composite structures. Int J Numer Meth Eng 1988;26:1843-54.
- [8] Surana KS. Transition finite elements for three-dimensional stress analysis. Int J Numer Meth Eng 1980;15:991-1020.
- [9] Aminpour MA, Ransom JB, McCleary SL. Coupled analysis of independently modelled finite element subdomains. AIAA Report no. 92-2235-CP; 1992. p. 109-20.
- [10] Housner JM, Aminpour MA, Dávila CG, Schiermeier JE, Stroud WJ, Ransom JB, Gillian RE. An interface element for global/local and substructuring analysis. Paper no. 25, MSC World Users Conference; 1995.
- [11] Alesi H, Jones R, Mileshkin, N. A technique for coupling plate and solid elements. In: Atluri SN, Yagawa G, Cruise TA. Proc Comp Mech Springer 1995;95(1):702-7.
- [12] Molent L, Callinan RJ, Jones R. Design of an all boron epoxy doubler for the F-111C wing pivot fitting: structural aspects. J Compos Struct 1989;11(1):57-83.
- [13] Jones R, Chiu WK, Smith R. Airworthiness of composite repairs. Eng Failure Anal 1995;2(2):117-28.
- [14] van Blaricum TJ, Bates P, Jones R. An experimental investigation into the effect of impact damage on the compressive strength of step lap joints. J Eng Fract Mech 1989;32(5):667-74.
- [15] Wang S, Srinivasan S, Hu HT, Haj Ali R. Effect of material nonlinearity on buckling and postbuckling of fiber composite laminated plates and cylindrical shells. Compos Struct 1995;33:7-15.
- [16] Chiu WK, Galea SC, Jones R. The role of material non-linearities in composite structures. J Compos Struct 1997;38:71-81.
- [17] Gates S. Matrix dominated stress/strain behaviour in polymeric composites: effect of hold time, nonlinearities and rate dependent stress-strain behaviour of advanced polymer matrix composites. NASA Technical Memorandum 104070; 1991.
- [18] Gates S. Rate dependent stress-strain behaviour of advanced polymer matrix composites. NASA Technical Memorandum 104070; 1991.
- [19] Rohwer K. Application of higher order theories to the bending analysis of layered composite plates. Int J Solids Struct 1992;29(1):105-19.
- [20] Supple WJ. Structural instability. Report from Department of Civil Engineering, University of Surrey; 1973. p. 64-82.
- [21] Thomson RS, Scott ML. Testing and analysis of thin stiffened composite shear panels. PICAST2-AAC6, Proc, Melbourne; 1995. p. 655-62.
- [22] Alesi H, Nguyen VM, Jones R, Mileshkin N, Kelly D. Postbuckling failure analysis of carbon/epoxy compression panel. In: Scott ML. Proceedings of the ICCM-11, ISBN 185573. Melbourne: Australian Composite Society; 14-18 July 1997. p. 707-22.
- [23] Tsai SW, Wu EM. A general theory of strength for anisotropic materials. J Compos Mater 1971;5:58-80.
- [24] Chiu WK, Chalkley PD, Jones R. Effects of temperature on the shear stress-strain behaviour of structural adhesives (FM73). J Comput Struct 1994;53(3):483-9.
- [25] Chiu WK, Jones R, Chao M. A visco-plastic analysis of bonded joints under complex loading. J Polym Polym Compos 1998;6:15-24.
- [26] Chiu WK, Jones R. The role of rate effects in adhesives and graphite epoxy in structural design. J Polym Polym Compos 1996;4(1):1-12.
- [27] Mignery LA, Schapery RA. Viscoelastic and nonlinear adherend effects in bonded composite joints. J Adhesion 1991;34:17-40.
- [28] Gates TS. Effect of elevated temperature on the visco-plastic modelling of graphite/polymeric composites. In: Harris CE, Gates TS, editors. ASTM STP 1174; 1993. p. 201-21.
- [29] Weeks CA, Sun CT. Nonlinear rate dependent response of thick section composite laminates. In: Rajapase YDS, Vinson JR, editors. High Strain Rate Effects on Polymeric, Metal and

Ceramic Matrix Composites and Other Advanced Materials, ASME, AD-Vol 48; 1995. p. 81–95.

- [30] Jones R, Trippit B, Chiu WK, Tomas J. Lap joint theory revisited. *J Polym Polym Compos* 1995;3(1):11–9.
- [31] Zocher MA, Allen DH. Evaluation of first ply failure in a three dimensional loadsapce. *J Compos Mater* 1995;29(12):1649–65.
- [32] Hoffman O. The brittle strength of orthotropic materials. *J Compos Mater* 1967;1:200–6.
- [33] Tsai S, Wu E. A general theory of strength for anisotropic materials. *J Compos Mater* 1971;5:58–78.
- [34] Hashin Z. A failure criteria for unidirectional fiber composites. *J Appl Mech* 1980;47:329–34.
- [35] Brewer J, Lagace P. Quadratic stress criterion for initiation of delamination. *J Compos Mater* 1988;22:114–1153.

## Smart structure application in bonded repairs

W.K. Chiu <sup>a,\*</sup>, Y.L. Koh <sup>a</sup>, S.C. Galea <sup>b</sup>, N. Rajic <sup>b</sup>

<sup>a</sup> Department of Mechanical Engineering, DSTO-Monash Centre of Expertise (Structural Mechanics), Monash University, Wellington Road, Clayton, Vic. 3168, Australia

<sup>b</sup> Aeronautical and Maritime Research Laboratory, Defence Science and Technology Organisation, Airframes and Engines Division 506, Lorimer Street, Fishermens Bend, Vic. 3207, Australia

### Abstract

In the aerospace industries bonded composite patches are being increasingly used to extend the operational life of aging aircraft. The application of bonded composite patches to repair or reinforce defective metallic structures is widely acknowledged as an effective and versatile procedure. Such patches have been successfully applied to the repair of cracked structures, to the reinforcement of components subject to material loss due to corrosion damage and as a general means of stress reduction through the provision of a supplementary load path. However, certification requirements mandate the need for a methodology for monitoring the damage state of both the defective underlying structure and of the repair. In this case, the concept of smart structures can be used to detect damage in the repair itself as well as monitor damage growth in the parent structure.

This paper will report on the development of a 'perceptive repair' or 'smart' system which will provide information on the in-service performance of the repair and the associated structure. In this respect, this paper will focus on the detection of disbond in the adhesive layer between adherend and the metallic parent structure. Since this is a relatively new area, a series of numerical studies were initially performed to reveal the salient features of the signals expected. These numerical findings were subsequently confirmed experimentally. Crown Copyright © 2000 Published by Elsevier Science Ltd. All rights reserved.

**Keywords:** Composite structures; Composite repairs; Structures; Health monitoring

### 1. Introduction

Spillman et al. [11] defined smart material and/or structure as a system that is designed for a specific functional purpose, and in fulfilling this purpose, it operates at a higher level of performance than its conventional counterpart. The system senses its internal state and external environment, and makes decisions and/or responds based on data obtained to meet the functional requirements. These decisions and adaptations are made through the use of feedback and memory. One of the primary purposes of implementing smart structure is to promote life extension and to prevent catastrophic failures. The research outcomes in smart structures/materials are applicable to the following industries:

1. Aerospace industries, which includes aging aircraft, space vehicles, satellites and space stations.
2. Maritime industries, which includes ocean going vessels, light-weight high-speed vessels, floating platforms in the oil and gas industries.

3. Civil infrastructures, which includes buildings (both new and old), pipelines, pressure vessels.

The condition monitoring of operational health and performance condition and the diagnosis of any faults as they occur is a relatively new technology that is being developed globally to provide advantages of safer and more reliable structures. Monitoring can be achieved by placing a sensor system on a structure/machine to measure a physical quantity, e.g. vibration signature, power flow, strain, acoustic emissions, etc. The measurements from sensor systems can be interpreted to provide five possible levels of diagnosis:

1. damage detection,
2. damage location,
3. damage force magnitude,
4. partial self-repair of the damage, and
5. the remaining life of the structure.

In an effort to utilise smart structures concepts for these and other related applications, attention has focussed on the use of surface mounted sensors and actuators [6], embedded sensors and actuators [7] and a combination of both [10].

Chaudhry et al. [6] reported on the monitoring of the integrity of composite repairs to aluminium structures.

\* Corresponding author.

They used a series of surface mounted piezoceramic sensors/actuators on the aluminium surface in the vicinity of the repair as a means to detect possible degradation of the patch. Here, the piezoceramic patches acted both as a sensor as well as an actuator. They reportedly were able to detect delamination of the patch. In another application of surface mounted sensor/actuator systems, Lichtenwalner et al. [8] bonded a series of piezoceramic patches on a flexbeam of an MD-900 Explorer. Whilst the piezoceramic patches can act both as an actuator and as a sensor, a series of strain gauges were also located at strategic locations. A series of notches were cut into the test specimen to simulate damage. They also reported a simple data processing system for the analysis of the test results to determine the state of damage. The frequency range used in their study spanned from 200 Hz to 20 KHz. They were able to quantify the existence of damage induced in the test specimen.

In a bid to determine the presence of delaminations in a fibre reinforced composite test specimen, Islam and Craig [7] embedded a series of piezoceramic patches onto the test specimen. The frequency at which the investigation was performed ranged from 100 Hz to 2 KHz. This work found that the frequency response of the system was able to detect the presence of the delamination in their test specimen.

The use of piezoceramics to produce Lamb waves for damage detection has been reported by numerous authors [5,9]. These devices are designed to operate at higher frequencies in order to detect damage (i.e. in the order of 1 MHz). Lamb waves can propagate over long distances, giving the possibility of inspecting several metres of structure in a single test. By controlling the frequency of the excitation, a single non-dispersive mode of wave can be achieved. Peirce et al. [10] used a combination of this technique, together with an optical fibre sensor embedded in a composite structure to determine the presence of delamination due to impact damage.

## 2. Statement of problem

One of the main thrusts of smart structures/materials technology is to develop techniques, for both new and ageing structures, which can assess structural integrity. In the area of new structures, these concepts can be used to both identify critical regions and to quantify the structural significance of any damage developing on these new structures. Similar strategies can be applied to existing/aging structures.

In the aerospace industries composite patches, used to repair or reinforce defective metallic structures, are being increasingly used to extend the operational life of aging aircraft [1,2]. It is recognised as a very effective and versatile procedure for repairing many types of

problems, for example repairs of cracking, localised reinforcement after removal of corrosion damage and for reduction of fatigue strain. For repairs to critical components (primary aircraft structure), certification requirements mandate a rigorous repair validation procedure as well as a methodology for monitoring the damage state both of the structure and of the repair [3]. Baker et al. [4] argue that a smart patch approach using in situ structural health monitoring (i.e. smart materials/structures) approach for the patched system may be necessary to alleviate certification concerns. Here, smart structures concepts can be used to determine the damage growth under these patches and in the repair itself. This paper addresses the suitability of some sensing techniques which can be employed to determine the state of damage in a structure which has been repaired with an adhesively bonded composite doubler.

This paper will report on the development of a 'perceptive repair' or 'smart' system which will provide information on the in-service performance of the repair and the associated structure. These systems would then provide information on in-service problems and therefore would allow timely decisions on preventative and schedule maintenance before failure of the repair or the repaired structure. In this respect, this paper will focus on the detection of disbond in the adhesive layer between adherend and the metallic parent structure. Some of the criteria of this smart system are that it must be economical, reliable and preferably self-powered. To this end, it was proposed that piezoceramic or piezoelectric material be utilised because of their ease of application. These materials were chosen because they can be used both as an actuator and as a sensor. This paper will present a set of numerical investigations performed to highlight the viability of using this material system, and the associated signal analysis that can be employed to detect the presence or the development of disbonds in the adhesive in a bonded repair situation. These numerical findings will be supported experimentally.

## 3. Numerical study

### 3.1. Numerical model

Fig. 1 shows a schematic diagram of the problem which simulates a bonded repair of an aluminium structure. Here the parent material is made from aluminium and the doubler is made from boron/epoxy, which is a typical repair material for aluminium structures. Fig. 2 show the mesh used in the analysis. The aluminium structure is 3 mm thick, the adhesive layer is 0.2 mm thick and the boron/epoxy (unidirectional) is five layers thick (approximately 0.6 mm). The material properties of the material used are as follows:

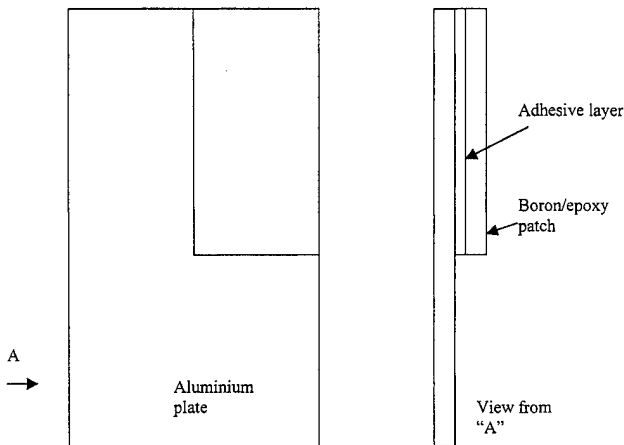


Fig. 1. Schematic of a typical repair situation.

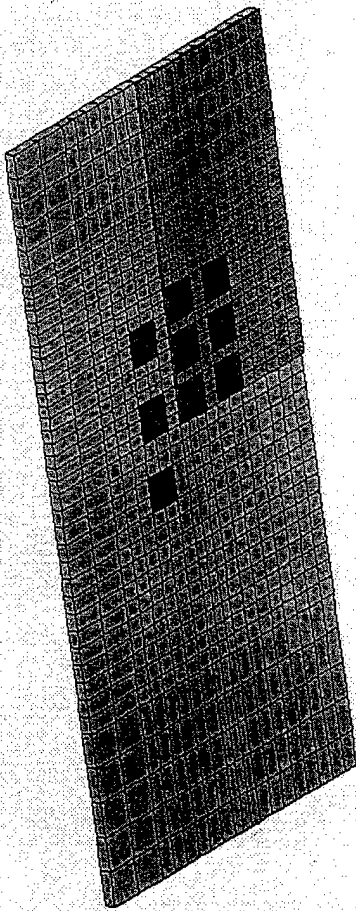


Fig. 2. Finite element model of bonded repair system with PZT elements.

Modulus of elasticity of aluminium = 71 GPa

Poissons ratio of aluminium = 0.3

Compliance of boron/epoxy;

$$S_{xx} = 3.932 \times 10^{-11} \text{ Pa}^{-1},$$

$$S_{yy} = 4.807 \times 10^{-12} \text{ Pa}^{-1},$$

$$S_{zz} = 3.932 \times 10^{-11} \text{ Pa}^{-1}.$$

Five different models were created to simulate:

- specimen without disbond in the adhesive layer (no damage)
- specimen with a  $5 \times 5$  mm disbond in the adhesive layer (damage 1)
- specimen with a  $10 \times 10$  mm disbond in the adhesive layer (damage 2)
- specimen with a  $13 \times 13$  mm disbond in the adhesive layer (damage 3)
- specimen with a  $20 \times 20$  mm disbond in the adhesive layer (damage 4)

One of the aims of this investigation is to determine the viability of using piezoelectric type devices for detecting the disbonds in the adhesive layer in these repair situations. To achieve this, the model contains an array of piezoceramic elements (actuators/sensors) located over the boron/epoxy patch and the aluminium structure. Fig. 3 shows the location of these actuator/sensors. The modulus of elasticity of the piezoceramic was assumed to be 64 GPa. The disbond, modeled in cases b–e, is located in the adhesive layer at the corner of the patch under piezoceramic element A.

In the investigation, each piezoceramic actuator/sensor was given a constant force sinusoidal excitation with frequencies ranging from 250 to 100 000 Hz. This force is only applied in the  $y$ -direction (i.e. in-plane excitation). This input is used to simulate a broadband excitation given to the actuator. The average strain levels (i.e. output) of the other sensors were determined for this given input. Two different signal analysis technique were assessed to determine if the signal from the sensor/actuator can be used to determine the presence of any disbond in the adhesive layer. In the first technique, the individual sensors will be used both as a sensor and as an actuator (i.e. a single piezoceramic element approach). This is one of the advantages of the using piezoceramic materials. In the second technique, a single piezoceramic element will be excited and the average strain of the other sensors will be determined. A transfer function between the actuator and a sensor will be calculated.

In the first set of analysis, the mechanical impedance at the location of the active piezoceramic element will be analysed. Given that the actuator is provided with a constant force over the entire frequency range (250 Hz–100 kHz), the impedance at the drive point (i.e. at the active piezoceramic element) can be written as

$$\text{Impedance} = \text{force/strain rate.} \quad (1)$$

Here the force can be written as

$$\text{Force} = Fe^{i\omega t}, \quad (2)$$

where  $\omega$  is the angular frequency and  $t$  is the time.



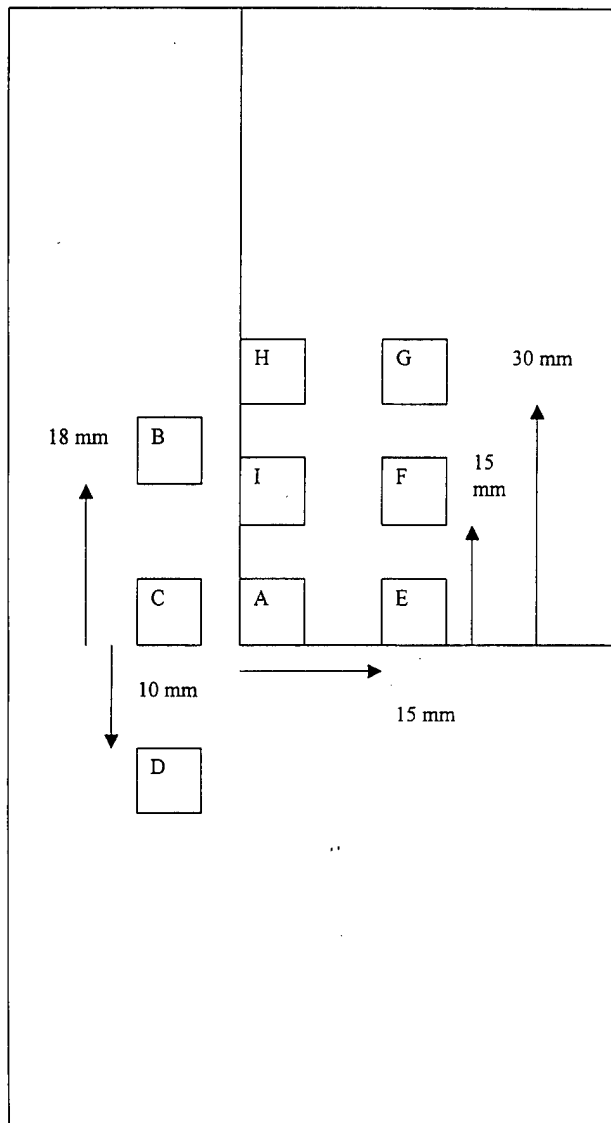


Fig. 3. Schematic of the bonded repair system with PZT elements.

If we are only interested in the  $y$ -direction response of the piezoceramic element, the expected voltage output at the piezoceramic elements due to this excitation can be expressed as

$$V_s = (d_{32})_s (\varepsilon_2)_s e^{i\omega(t+\phi)}, \quad (3)$$

where  $V_s$  is the expected voltage output from sensor and the actuator, respectively,  $d_{32}$  the piezoelectric coefficient,  $\phi$  the phase difference between the excitation and the response and  $\varepsilon_2$  is the average strain of the sensor in the  $y$ -direction. For the purpose of this analytical study, the value of  $d_{32}$  was taken as unity and from Eq. (1), the magnitude of the impedance can be written as

$$Z = F / (i\omega\varepsilon_2). \quad (4)$$

In the analysis of the piezoceramic sensor/actuator distributed over the repaired structure is actuated in turn

and the mechanical impedance at the drive point is determined using Eq. (2). In this respect, the technique is similar to that reported by Chaudhry et al. [6]. This investigation will demonstrate if this method can be used to, firstly, detect the presence of disbond in the adhesive layer and, secondly, monitor the development of the disbond.

In the second analysis technique, the transfer functions between the sensors and the actuator is evaluated. Changes in these transfer functions will indicate if damage can be detected using this technique. It must be emphasised at this stage that we are not attempting to use modal analysis to determine the presence of damage in the structure. Here the transfer function is defined as

$$\text{Transfer function, } TF = V_s / V_a, \quad (5)$$

$$V_s = (d_{32})_s (\varepsilon_2)_s e^{i\omega(t+\phi)}, \quad (6)$$

$$V_a = (d_{32})_a (\varepsilon_2)_a e^{i\omega(t+\phi)}. \quad (7)$$

Here,  $V_s$  and  $V_a$  are the expected voltage output from sensor and the actuator, respectively,  $d_{32}$  the piezoelectric coefficient,  $\phi$  and  $\alpha$  are the phases of the response due to the forcing provided in Eq. (1) and  $\varepsilon_2$  is the average strain of the sensor/actuator in the  $y$ -direction.

### 3.2. Numerical results and discussions

#### 3.2.1. Electromechanical impedance measurements

Fig. 4(a)–(f) show the impedance plots obtained from the finite element analysis. When the sensor/actuator was located on the damage location (Fig. 4(a)), the impedance measurement (as in Eq. (2)) decreases with increasing disbond size. The impedance plot for sensor/actuator E is shown in Fig. 4(e) and (f). Here it is evident that the impedance measurement did not show appreciable changes until the disbond develops into the sensor/actuator. Take Fig. 4(f) as an example, the impedance of the sensor/actuator did not show any appreciable change when the disbond is limited to 13 mm × 13 mm. However, as soon as the disbond (20 mm × 20 mm) grew under the sensor/actuator, there is a decrease in the local impedance. These results show that the impedance technique has a potential for use in detecting disbond in bonded repairs.

Fig. 4(c) and (d) show the impedance plots of sensor/actuator located outside the damage area. It can be seen from these figures that the predicted impedance did not show any changes with damage size. This revealed that if the impedance measurements are to be sensitive to the presence of disbond in the adhesive layer, then the sensor/actuator has to be placed over or close to the location of the damage.

### 3.2.2. Transfer function technique

In this section of the investigation, the piezoceramic actuators distributed over the repair were actuated individually and the transfer function between the actuator and the rest of the sensors were calculated. Fig. 5(a) and (b) show some examples of transfer functions when A was used as an actuator. It is evident from this figure that the magnitude of the transfer functions was observed to decrease when the size of the damage increases. Given that the size of the actuator was 10 mm × 10 mm, it is interesting to note a significant decrease in the magnitude of the transfer function when the disbond developed past the sensor (i.e. disbond sizes of 13 mm × 13 mm and 20 mm × 20 mm). It must be emphasised at this stage that this numerical study as-

sumed a zero stiffness adhesive layer in the region of the disbond. This dramatic decrease in the magnitude of the transfer function may not be quite as drastic in reality because the stiffness over the disbond may not be 0 due to friction and other factors. However, the trend observed in this set of numerical analysis does show that there is a potential of using this transfer function technique to monitor the development of disbond in the bonded repair situation.

Fig. 6(a) and (b) show the transfer functions when the piezoceramic element at A was used as a sensor and the excitation was provided by the other piezoceramic elements (i.e. at locations D and E). It is evident from these plots that the size of the disbond can also be inferred from these transfer functions. A, similar trend of a

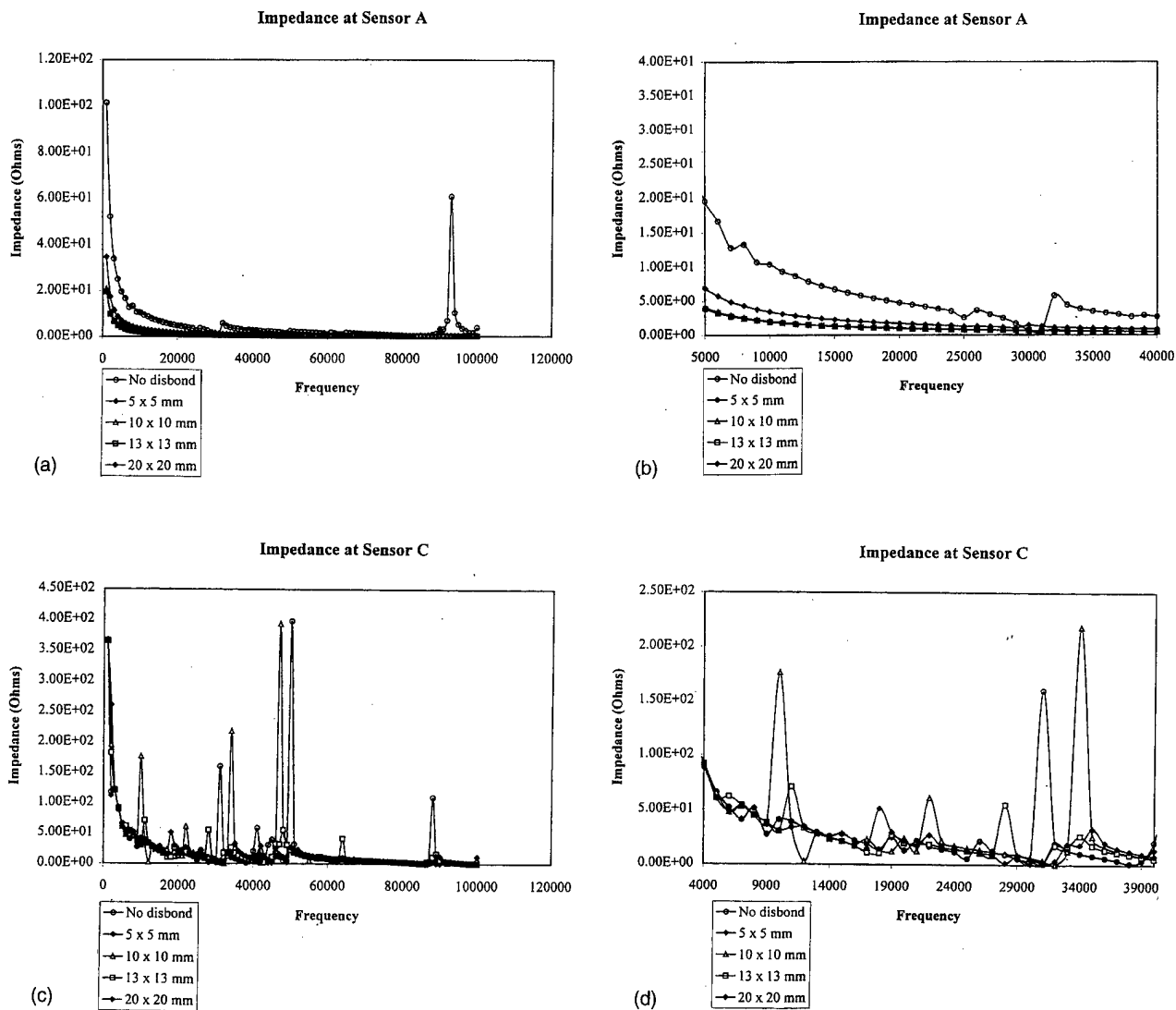


Fig. 4. (a) Impedance plot for sensor/actuator A. (b) Impedance plot for sensor/actuator A (narrow frequency band; 4000 to 40 000 Hz). (c) Impedance plot for sensor/actuator C (next to the damage area). (d) Impedance plot for sensor/actuator C (narrow frequency band; 4000 to 40 000 Hz). (e) Impedance plot for sensor/actuator E. (f) Impedance plot for sensor/actuator E (narrow frequency band; 4000 to 40 000 Hz).

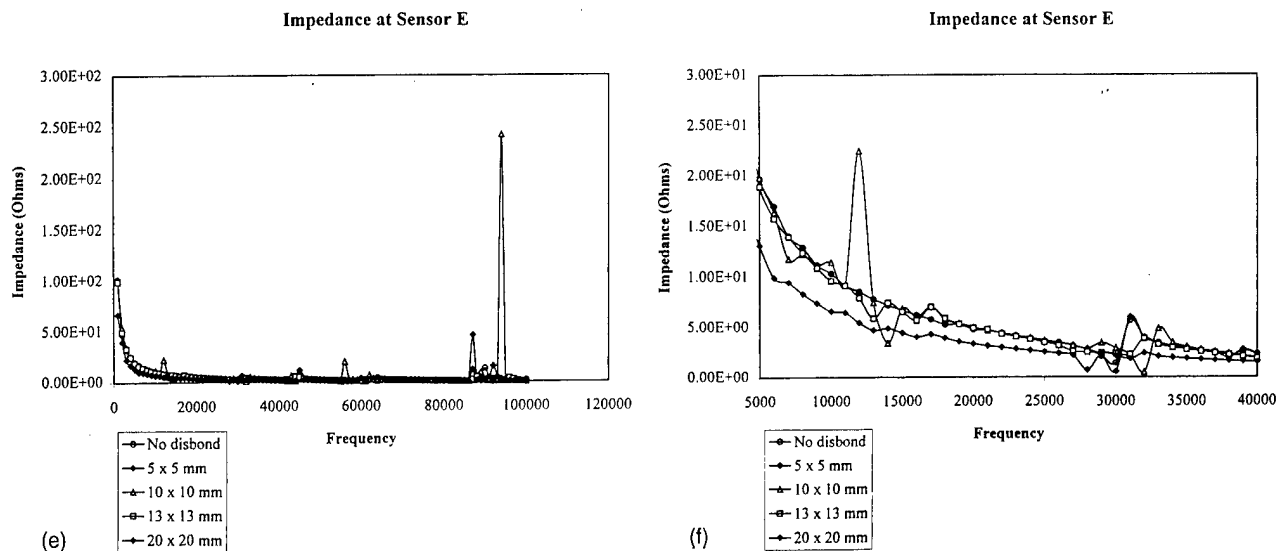


Fig. 4. (Continued).

decrease in the magnitude of the transfer function was observed. Like the result shown in Fig. 5(a) and (b), the results shown in Fig. 6(a) and (b) show that the decrease in magnitude of the transfer function may provide an indication of the developing disbond in the adhesive layer.

Fig. 7(a) and (b) show the transfer functions when the piezoceramic element at E was used as an actuator. As discussed earlier, the disbond will only develop partially into sensor E when the damage grew to 20 mm x 20 mm. These results are similar to those obtained earlier, which show that the magnitude of the transfer function is relatively unchanged until the damage begins to de-

velop under the piezoceramic element used as an actuator or that used as the sensor.

Fig. 8 show the transfer functions obtained when the sensor interrogated was located outside the damage area. These results show that there is little change in the transfer function when the sensor/actuator pair is located outside the damage area. This unchanging transfer function may be used to assess the integrity of sensor/actuator pairs in practice. More research is required for the development of a suitable algorithm to utilise this information to determine the reliability of the sensor/actuator pair and to discriminate sensor degradation from actual structural damage detected.

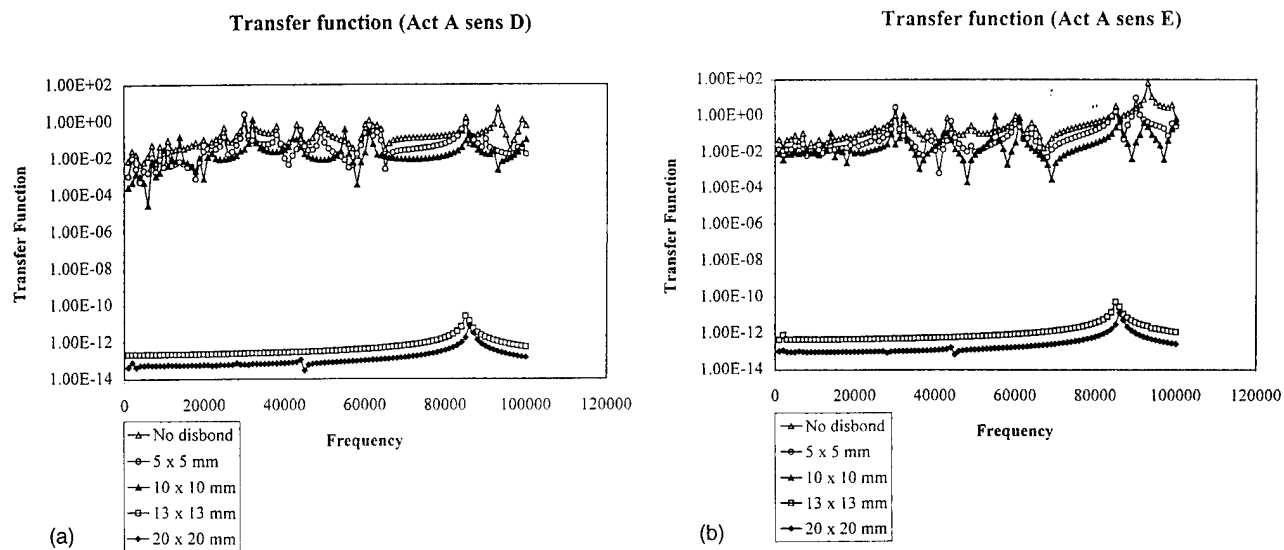


Fig. 5. (a) Magnitude of the transfer function between actuator A and sensor D. (b) Magnitude of the transfer function between actuator A and sensor E.

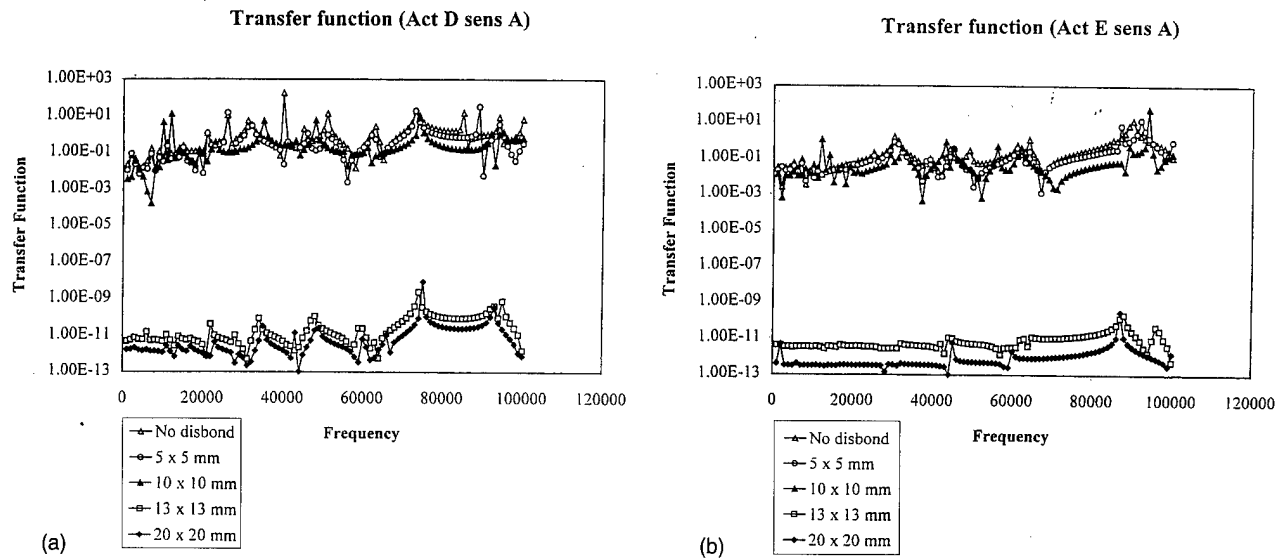


Fig. 6. (a) Magnitude of the transfer function between actuator D and sensor A. (b) Magnitude of the transfer function between actuator E and sensor A.

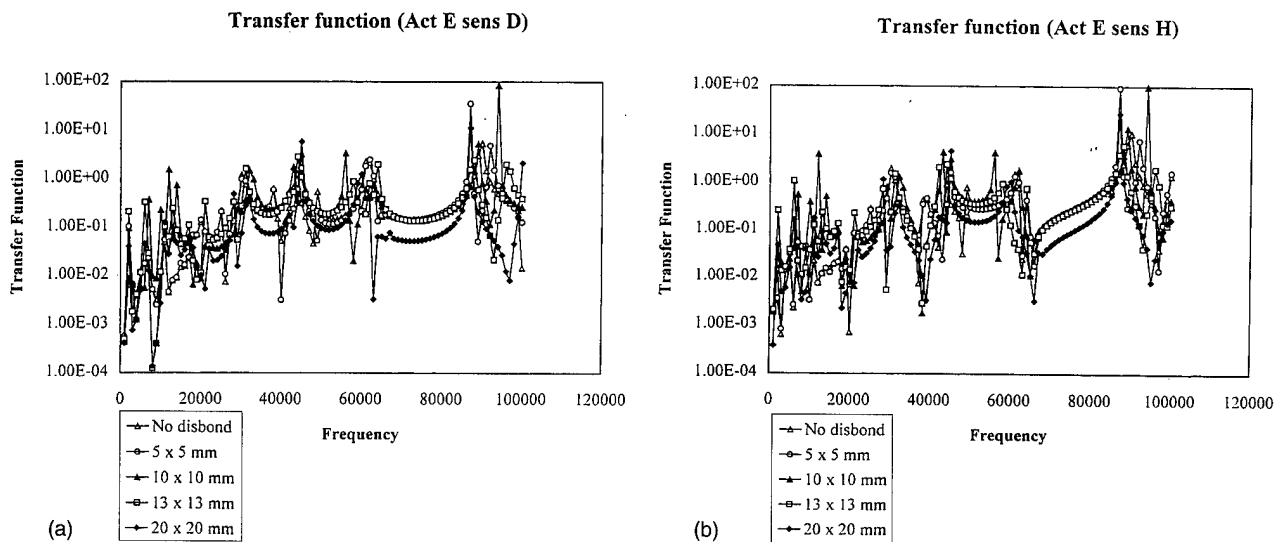


Fig. 7. (a) Magnitude of the transfer function between actuator E and sensor D. (b) Magnitude of the transfer function between actuator E and sensor H.

## 4. Experimental study

### 4.1. Experimental test specimen and setup

Fig. 9 illustrates schematically the repair configuration considered in this paper. It involves a 5-ply unidirectional Boron/Epoxy patch bonded onto an aluminium plate with a Teflon strip inserted into the bondline at the location marked 'A'. Four such specimens were prepared each with a different Teflon strip size: 5 mm × 5 mm, 10 mm × 10 mm, 15 mm × 15 mm and 20 mm × 20 mm so as to simulate the progressive enlargement of a disbond as might occur

during active service. A further specimen was prepared without a Teflon insert to serve as a reference against which comparisons could be made. Three PZT elements were bonded onto the specimen as shown in Fig. 9. Whilst element 1 was bonded directly over the disbond, elements 2 and 3 were bonded on the aluminium host. The intention in this study was to examine whether PZT elements bonded in such an arrangement could be interrogated so as to provide indication of the extent of simulated disbonding at the glue line.

The Transfer Function approach and the Electromechanical Impedance Method described in the numerical

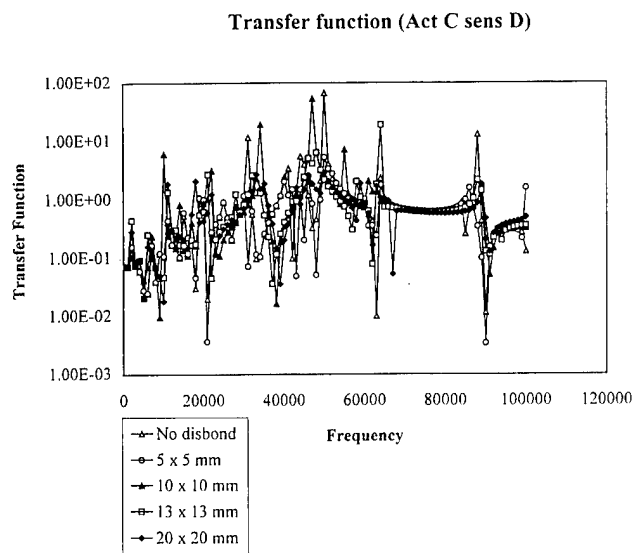


Fig. 8. Magnitude of the transfer function between actuator C and sensor D.

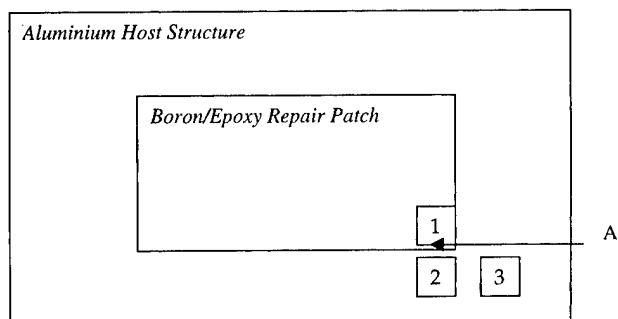


Fig. 9. Schematic of test specimen.

section of this paper were employed to detect the presence of disbond in the repaired system.

## 4.2. Experimental results

### 4.2.1. Electromechanical impedance method

The degree of disbond of the composite patch was successfully monitored with microprocessor-based electrical impedance analysers on the specimen (Fig. 9). High-resolution amplitude and phase measurements were made in the 400 Hz to 1 kHz and 1 to 25 kHz bands. The experimental results for the repair patch are presented in Figs. 10 and 11 when impedance was taken from sensor/actuator (1).

In Fig. 10 it was found that the changes were clear and distinctive. Progressive disbonds produce downward translation in the  $y$ -direction in increasing frequencies. The frequency shift and degree of modulation depends on the location of damage as well as the actuator-sensor PZT patch location. Here the frequency range of 400 to 1000 Hz was used. When a higher frequency range used, the impedance curve tends to bend together (see Fig. 11). It is obvious from these results that the choice of frequency range is important.

It was also found that in order to detect a disbond the PZT needs to be located on the patch. Placing the element on the host structure for example yields no measurable indication of the disbond (Figs. 12 and 13).

When the PZT located on the aluminium structure (i.e. sensor/actuator 2) was used, the responses are shown in Figs. 12 and 13. It is clear from these figures that the Impedance Method is particularly effective when the sensor/actuator was located directly over the damage area.

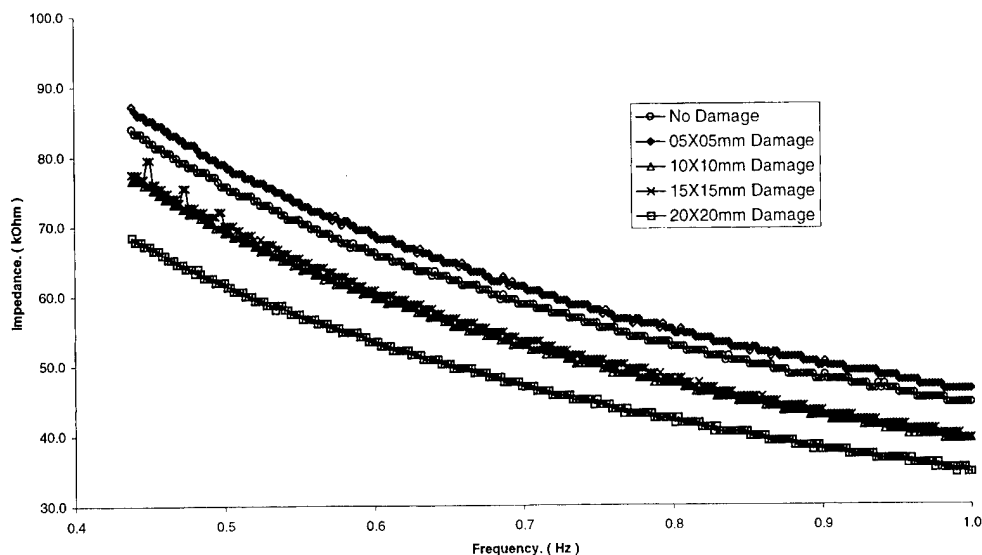


Fig. 10. Effect of disbonding on impedance magnitude (low frequency).

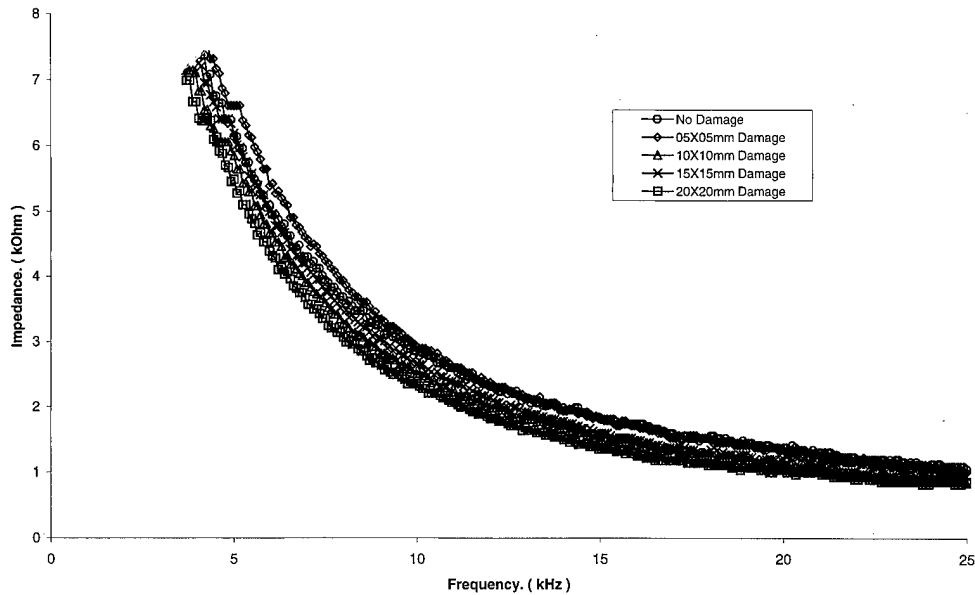


Fig. 11. Effect of disbonding on impedance magnitude (high frequency).

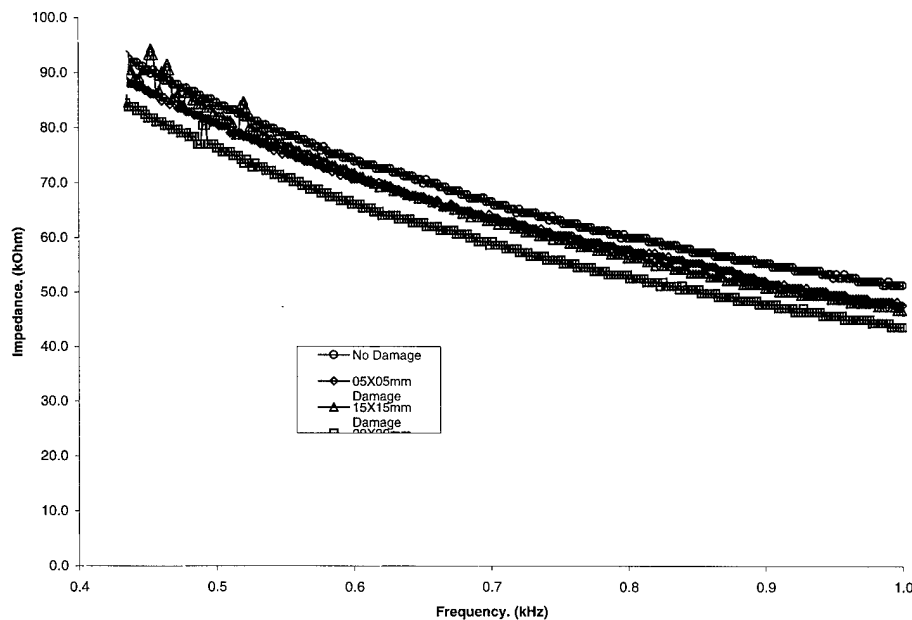


Fig. 12. Effect of distance on impedance magnitude (low frequency).

#### 4.2.2. Transfer function technique

The specimens that were used in the Impedance Method were used to demonstrate the effectiveness of the Transfer Function Method. This method was found to be very sensitive to the presence of disbond.

In this investigation, three sets of experiments were conducted (referring to Fig. 9):

1. When PZT (1) was used as a sensor and PZT (2) was used as an actuator.
2. When PZT (2) was used as a sensor and PZT (1) was used as an actuator.

3. When PZT (2) was used as a sensor and PZT (3) was used as an actuator.

The acquisition of data done using the transfer function between the sensor and actuator can be described as follows:

1. A broadband signal using an AND AD-3525 FFT Analyser was used to evaluate the transfer function and to provide the broadband input signal to the actuator. The frequency bandwidth used was 250 Hz to 100 kHz and the RMS amplitude of signal input was set at 2 V.

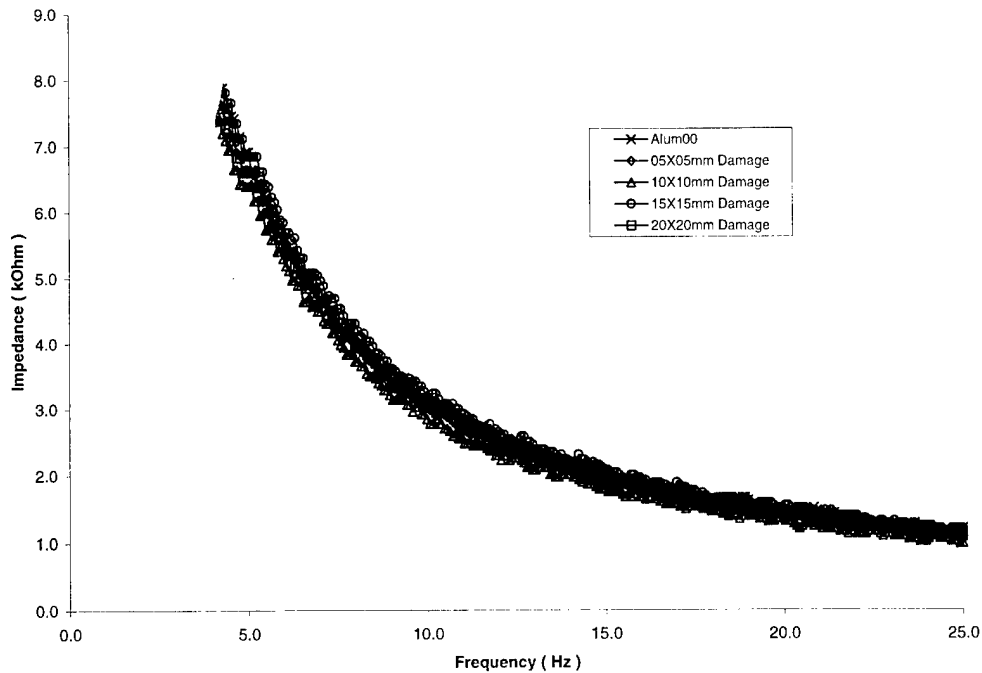


Fig. 13. Effect of distance on impedance magnitude (high frequency).

2. Thirty averages are taken to obtain a single frequency response function.
3. The real and imaginary transfer function of the current drawn by the sensor is recorded and converted to magnitude and phase.

In this manner, the transfer function for the various damage state was obtained, disbond sizes can be easily observed. In the case whereby PZT (1) was used as a sensor and PZT (2) was used as an actuator, Fig. 14 shows the amplitude of the Transfer Function obtained. When this spectrum was integrated over the entire frequency band in a similar fashion to that of [8] the effects

of the size of disbond under the patch on the frequency response can clearly be seen.

Fig. 15 shows the results obtained when PZT (2) was used as a sensor and PZT (3) was used as an actuator. This figure that indicates the sensor has to be located over the damage area for integrity assessment. When PZT (2) (i.e. on aluminium structure) was used as sensor and PZT (1) (i.e. over damage) was used as an actuator the results shown in Fig. 16 are similar to that in Fig. 14. This shows that this method is capable of detecting the disbond as long as a sensor or an actuator is located over the damage area.

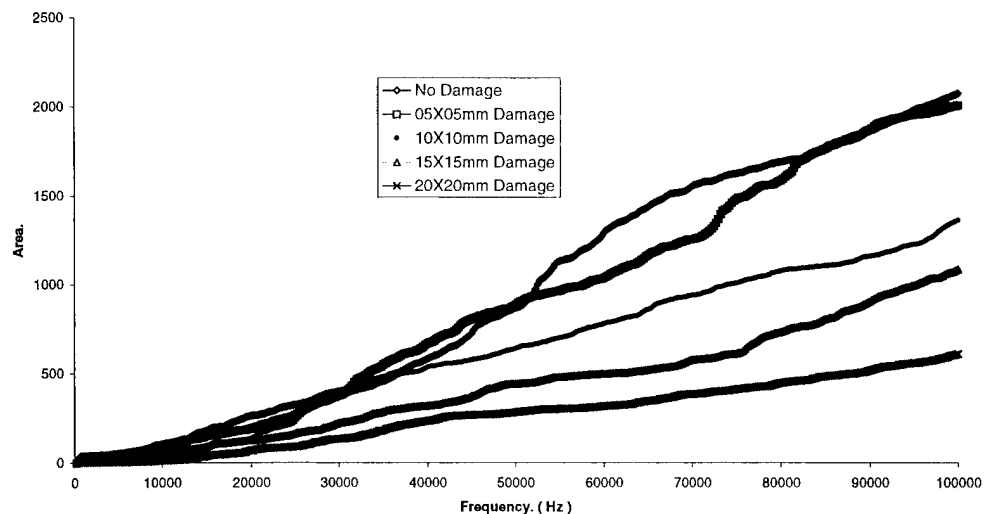


Fig. 14. Effect of debonding on transfer function magnitude area (actuator on aluminum).

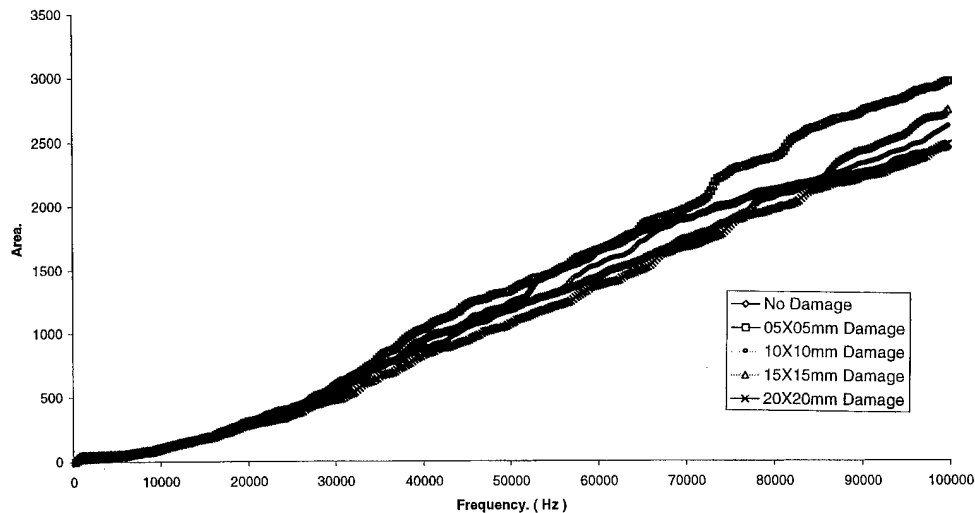


Fig. 15. Effect of aluminium structure on transfer function magnitude area.

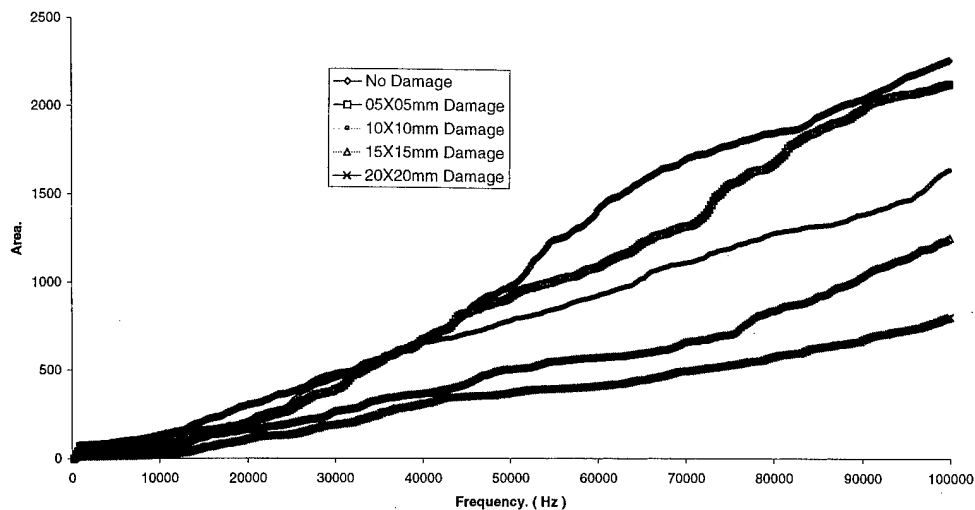


Fig. 16. Effect of debonding on transfer function magnitude area (actuator on patch).

## 5. Conclusions

The results presented in this paper show the possibility of using piezoelectric elements for the development of a 'smart' patch. The main conclusions of this paper are:

- Impedance measurement can be used to determine the presence of damage.
- When impedance measurements are used, the sensor/actuator must be located close to the damage area.
- Transfer function technique may be used to quantify the extent of disbond in a bonded repair.
- This technique may also be used to determine the integrity of the 'smart' system.

From the results obtained above, it is clear that both methods should be in conjunction with one another to determine the size of disbond. This provides a particularly attractive monitoring system/strategy as they can

be used to compare the readings from one method to another. It transpires that when the critical location is in a region of high stresses the transfer function method is particularly attractive because the actuating PZT can be located in a low stress region, while the sensor placed in the high stress region can be made from a more fatigue resistant PVDF.

## References

- [1] Baker AA, Jones R. Bonded repair of aircraft structure. The Hague: Martinus Nijhoff; 1988.
- [2] Baker AA. Bonded Composite repair of metallic aircraft components. AGARD-CP-550 Composite Repair of Military Aircraft Structures, Paper 1, 1994.
- [3] Baker AA. On the certification of bonded composite repairs to primary aircraft structures. In: Proceedings of 11th International



- Conference on Composite Materials (ICCM-11), Gold Coast Australia, 1997.
- [4] Baker AA, Galea SC, Powlesland IG. A smart patch approach for bonded composite repairs to primary airframe structures. In: *Proceedings of Second Joint NASA/FAA/DoD Conference on Aging Aircraft*, Williamsburg, Virginia, 31 August–3 September, 1998, pp. 328–38.
- [5] Badcock RA, Birt EA. The use of 0–3 piezocomposite embedded Lamb wave sensors for damage detection in advanced fibre composites. In: *Proceedings of the Fourth ESSM and Second MIMR Conference*, Harrogate, 1998, pp. 373–80.
- [6] Chaudhry Z, Frederic L, Ganino A, Rogers CA. Monitoring the integrity of composite patch structural repair via piezoelectric actuators/sensors. In: *Proceedings of the AIAA/ASME/AHS/ASC 36th SDM Conference*, vol. 4, New Orleans, LA, 1995, pp. 2243–48.
- [7] Islam AS, Craig KC. Damage detection in composite structures using piezoelectric materials. *Smart Mater Struct* 1994;3:318–26.
- [8] Lichtenwalner PF, Dunne JP, Becker RS, Baumann EW. Active damage interrogation system for structural health monitoring. *SPIE* 1997;3044:186–94.
- [9] Monkhouse RSC, Wilcox PD, Cawley WP. Flexible interdigital PVDF transducers for the generation of Lamb waves in structures. *Ultrasonics* 1997;35:489–98.
- [10] Pierce SG, Staszewski WJ, Gachagan A, James IR, Philp WR, Worden K, Culshaw B, McNab A, Tomlinson GR, Hayward G. Ultrasonic condition monitoring of composite structures using a low profile acoustic source and an embedded optical fibre sensor. *SPIE* 1997;3041:437–48.
- [11] Spillman WB, Sirkis JS, Gardiner PT. Smart materials and structures: What are they? *Smart Mater Struct* 1996;5:247–54.

## CONTENTS OF VOLUMES 48–50

### Volume 48 Number 1-3

#### Special Issue: Second International Conference on Composite Science & Technology (ICCST/2)

Guest Editors: S. Adali, E.V. Morozov & V.E. Verijenko

- v Preface
- 1 Recent developments in the modeling and behavior of advanced sandwich constructions: a survey  
L. LIBRESCU & T. HAUSE (USA)
- 19 Modeling the statistical lifetime of glass fiber/polymer matrix composites in tension  
S. L. PHOENIX (USA)
- 31 Developments in thermopiezoelectricity with relevance to smart composite structures  
T. R. TAUCHERT (USA), F. ASHIDA, N. NODA (Japan), S. ADALI & V. VERIJENKO (South Africa)
- 39 Modern conceptions of plate theory  
V. V. VASILIEV (Russia)
- 49 Mechanical and morphological behavior of polyolefin blends in the presence of  $\text{CaCO}_3$   
C. ALBANO, J. GONZÁLEZ, M. ICHAZO, C. ROSALES, C. URBINA DE NAVARRO & C. PARRA (Venezuela)
- 59 Development of a numerical model for the damage identification on composite plate structures  
J. V. ARAÚJO DOS SANTOS, C. M. MOTA SOARES, C. A. MOTA SOARES & H. L. G. PINA (Portugal)
- 67 Closed-form analysis of the thickness effect of regular honeycomb core material  
W. BECKER (Germany)
- 71 Detection of cracks in ceramic matrix composites based on surface temperature  
L. W. BYRD & V. M. BIRMAN (USA)
- 79 Influence of metallic fillers on the thermal and mechanical behaviour in composites of epoxy matrix  
Z. BRITO & G. SÁNCHEZ (Venezuela)
- 83 Optimization of fiber reinforced composites  
G. DUVAUT, G. TERREL, F. LÉNÉ (France) & V. E. VERIJENKO (South Africa)
- 91 Dynamic analysis of orthotropic shells by the grid-characteristic method  
E. G. EVSEEV (Russian Federation) & E. V. MOROZOV (South Africa)
- 95 Impact perforation of thin stiffened CFRP panels  
M. S. FOUND, I. C. HOWARD & A. P. PARAN (UK)
- 99 Optimal temperature profiles for minimum residual stress in the cure process of polymer composites  
A. K. GOPAL, S. ADALI & V. E. VERIJENKO (South Africa)
- 107 Effect of trigger geometry on energy absorption in composite profiles  
M. A. JIMÉNEZ, A. MIRAVETE, E. LARRODÉ & D. REVUELTA (Spain)
- 113 Simulation of thermo-mechanical behavior and interfacial stress of metal matrix composite under thermal shock process  
D.-Y. JU (Japan)
- 119 Composite pressure vessels with higher stiffness  
A. A. KRIKANOV (Russia)

- 129 Thermoelasticity of spatially reinforced composite plates  
E. V. MOROZOV (South Africa)
- 135 Nonlinear fracture analysis of hybrid polymer composite materials and structures  
E. V. MOROZOV (South Africa), S. A. SYLANTIEV, E. G. EVSEEV & H. G. LESSMANN (Russian Federation)
- 139 Design of composite plates under cyclic loading  
A. MUC & Z. KRAWIEC (Poland)
- 145 Buckling and failure analysis of FRP faced sandwich plates  
A. MUC & P. ZUCHARA (Poland)
- 151 Some aspects of ultrasonic testing of composites  
E. G. NESVIJSKI (Brazil)
- 157 The effect of strain rate and fibre content on the Poissons ratio of glass/epoxy composites  
O. I. OKOLI (USA) & G. F. SMITH (UK)
- 163 Dynamics and buckling of a multilayer composite plate with embedded SMA wires  
W. OSTACHOWICZ, M. KRAWCZUK & A. ŻAK (Poland)
- 169 High-order model of the stress-strain state of composite bars and its implementation by computer algebra  
V. G. PISKUNOV, A. V. GORYK, A. L. LYAKHOV & V. N. CHEREDNIKOV (Ukraine)
- 177 Stress concentration in bending of sandwich orthotropic panels under point forces  
V. POLYAKOV (Latvia)
- 183 A new approach to fatigue analysis in composites based on residual strength degradation  
D. REVUELTA, J. CUARTERO, A. MIRAVETE & R. CLEMENTE (Spain)
- 187 Overall properties of composites with physically non-linear discrete phase  
I. SEVOSTIANOV (USA), V. E. VERIJENKO & C. J. VON KLEMPERER (South Africa)
- 197 Mathematical model of cavitation during resin film infusion process  
I. SEVOSTIANOV (USA), V. E. VERIJENKO & C. J. VON KLEMPERER (South Africa)
- 205 Linear analysis of laminated composite plates using single layer higher-order discrete models  
Dj. VUKSANOVIĆ (Yugoslavia)
- 213 A method for optimally designing laminated plates subject to fatigue loads for minimum weight using a cumulative damage constraint  
M. WALKER (South Africa)

**Volume 48 Number 4 2000**

- 219 Vibrations of and sound radiation from sandwich plates in heavy fluid loading conditions  
S. V. SOROKIN (Russian Federation)
- 231 Vibration and stability of cross-ply laminated composite plates according to a global higher-order plate theory  
H. MATSUNAGA (Japan)
- 245 A priori vs. a posteriori evaluation of transverse stresses in multilayered orthotropic plates  
E. CARRERA (Italy)
- 261 Evaluation of the residual strength degradation in composite laminates under fatigue loading  
H. A. WHITWORTH (USA)
- 265 The effect of rotatory inertia on the dynamic response of laminated composite plate  
Y. Y. WANG, K. Y. LAM & G. R. LIU (Singapore)
- 275 Effects of truncation and elimination on composite fatigue life  
T. NYMAN, H. ANSELL & A. BLOM (Sweden)

- 287 Dynamic equilibrium equations of composite anisotropic beams considering the effects of transverse shear deformations and structural damping  
C.-N. CHEN (ROC)
- 305 Analysis of active damping in composite laminate cylindrical shells of revolution with skewed PVDF sensors/actuators  
C. SARAVANAN, N. GANESAN & V. RAMAMURTI (India)

**Volume 49 Number 1 2000**

- 1 Optimal dimension of PQFP by using Taguchi method  
R.-S. CHEN, H.-C. LIN & C. KUNG (ROC)
- 9 Elastic–plastic stress analysis and expansion of plastic zone in clamped and simply supported aluminum metal–matrix laminated plates  
C. ATAS & O. SAYMAN (Turkey)
- 21 Fabrication and testing of thin composite isogrid stiffened panel  
T. D. KIM (Japan)
- 27 A general solution for stress resultants and moments around holes in unsymmetric laminates  
V. G. UKADGAONKER & D. K. N. RAO (India)
- 41 A general solution for moments around holes in symmetric laminates  
V. G. UKADGAONKER & D. K. N. RAO (India)
- 55 Stiffening effects on the free vibration behavior of composite plates with PZT actuators  
J. A. HERNANDES, S. F. M. ALMEIDA & A. NABARRETE (Brazil)
- 65 Estimation of transverse/interlaminar stresses in laminated composites – a selective review and survey of current developments  
T. KANT & K. SWAMINATHAN (India)
- 77 Thermal buckling analysis of skew fibre-reinforced composite and sandwich plates using shear deformable finite element models  
T. KANT & C. S. BABU (India)
- 87 Random field formulation of composite laminates  
W.-F. WU, H.-C. CHENG & C.-K. KANG (ROC)
- 95 Overall behaviour of singly curved shallow sandwich panels: the case of general boundary conditions  
V. SKVORTSOV, E. BOZHEVOLNAYA & A. KILDEGAARD (Denmark)
- 111 Errata

**Volume 49 Number 2 2000**

- 115 Nonlinear analysis of composite laminated thin plates subjected to lateral pressure and thermal loading and resting on elastic foundations  
H.-S. SHEN (People's Republic of China)
- 129 Nonlinear transient analysis of rectangular composite laminated plates  
J. CHEN, D. J. DAWE & S. WANG (UK)
- 141 Analysis and testing of a prototype pultruded composite causeway structure  
S. J. SMITH, L. C. BANK, T. R. GENTRY, K. H. NUSS, S. H. HURD, S. J. DUICH & B. OH (USA)
- 151 On damage development in mechanically fastened composite laminates  
T. IREMAN, T. RANVIK & I. ERIKSSON (Sweden)
- 173 Structural failure study of laminated composites: the bundle optimization approach  
D. N. KAZIOLAS & C. C. BANIOTOPOULOS (Greece)

- 183 Determination of elastic constants of materials by vibration testing  
S.-F. HWANG & C.-S. CHANG (Taiwan, ROC)
- 191 Experimental study of CFRP-prestressed high-strength concrete bridge beams  
F. STOLL, J. E. SALIBA & L. E. CASPER (USA)
- 201 Elastic–plastic stress analysis in thermoplastic composite laminated plates under in-plane loading  
R. ÖZCAN (Turkey)
- 209 Finite element analysis of low-velocity impact on composite sandwich plates  
A. N. PALAZOTTO, E. J. HERUP & L. N. B. GUMMADI (USA)
- 229 Free-edge strength analysis in composite laminates by the extended Kantorovich method  
H. S. KIM, M. CHO & G.-I. KIM (South Korea)

**Technical Note**

- 237 Experimental and theoretical analyses of first-ply failure of laminated composite pressure vessels  
R. R. CHANG (Taiwan, ROC)
- 245 Erratum

**Volume 49 Number 3 2000**

- 247 Finite element analysis of composite pressure vessels with a load sharing metallic liner  
M. Z. KABIR (Iran)
- 257 Non-linear thermal effects on the bending response of cross-ply laminated plates using refined first-order theory  
M. E. FARES, A. M. ZENKOUR & M. Kh. EL-MARGHANY (Egypt)
- 269 An asymptotic characterisation of the moisture diffusion in polymer matrix composites with cyclic environmental conditions  
E.-A. ADDA-BEDIA (Algeria), W. S. HAN & G. VERCHERY (France)
- 275 Boundary value problems for unsymmetric laminates, occupying a region with elliptic contour  
D. D. ZAKHAROV (Russian Federation) & W. BECKER (Germany)
- 285 Optimum design of symmetric composite patch repair to centre cracked metallic sheet  
A. MAHADESH KUMAR & S. A. HAKEEM (India)
- 293 On the stochastic nature of thermomechanical properties in glass reinforced polyester laminates  
T. P. PHILIPPIDIS, D. J. LEKOU & G. A. KALOGIANNAKIS (Greece)
- 303 Process induced stress for woven fabric thick section composite structures  
X. HUANG, J. W. GILLESPIE Jr. & T. BOGETTI (USA)
- 313 Investigation of the rotary inertia and shear deformation effects on the out-of-plane bending and torsional natural frequencies of laminated beams  
V. YILDIRIM & E. KIRAL (Turkey)
- 321 Predicting the penetration and perforation of FRP laminates struck normally by projectiles with different nose shapes  
H. M. WEN (UK)
- 331 Strain monitoring in composite patched structures  
F. FINDIK (Turkey), N. MRAD & A. JOHNSTON (Canada)
- 339 A general solution for stresses around holes in symmetric laminates under inplane loading  
V. G. UKADGAONKER & D. K. N. RAO (India)

**Volume 49 Number 4 2000**

- 355 Validation of FE models for buckling analysis of woven GFRP shells  
M. K. CHRYSSANTHOPOULOS, A. Y. ELGHAZOULI & I. E. ESONG (UK)

- 369 Viscoelastic failure analysis of composite plates and shells  
B. F. OLIVEIRA & G. J. CREUS (Brazil)
- 385 Analysis of debonding fracture in a sandwich plate with hexagonal core  
S. GOSWAMI & W. BECKER (Germany)
- 393 On the importance of cross-sectional warping in solid composite beams  
O. RAND (Israel)
- 399 Analytic extraction of the elastic coupling mechanisms in composite blades  
J. ALKAHE & O. RAND (Israel)
- 415 Investigation of the size effect of composite patching repaired on edge-cracked plates  
W.-C. WANG & J.-S. HSU (Taiwan, ROC)
- 425 Development of Benson–Mayers theory on the wrinkling of anisotropic sandwich panels  
B. K. HADI (Indonesia) & F. L. MATTHEWS (UK)
- 435 Matrix cracking behavior of K3B/IM7 composite laminates subject to static and fatigue loading  
X. HUANG, J. W. GILLESPIE Jr., R. F. EDULJEE & Z. SHEN (USA)
- 443 Wavelet analysis of plate wave propagation in composite laminates  
H. JEONG & Y.-S. JANG (South Korea)
- 451 Mechanics of three-dimensional braided structures for composite materials – part I: fabric structure and fibre volume fraction  
Z. X. TANG & R. POSTLE (Australia)

#### Volume 50 Number 1 2000

- 1 First-order zig-zag sublaminar plate theory and finite element model for laminated composite and sandwich panels  
Y. B. CHO & R. C. AVERILL (USA)
- 17 Experimental and numerical analysis of transverse stitched T-joints in bending  
P. B. STICKLER, M. RAMULU & P. S. JOHNSON (USA)
- 29 Three-dimensional elasticity solution for buckling of composite laminates  
H. GU & A. CHATTOPADHYAY (USA)
- 37 Composite rotor for high-speed induction motors  
S. H. CHANG, D. G. LEE & J. K. CHOI (South Korea)
- 49 Finite element implementation of a new sandwich homogenization procedure  
R. TANOV & A. TABIEI (USA)
- 59 Frequency characteristics of a rotating truncated circular layered conical shell  
LI HUA (Singapore)
- 69 Reliability assessment of pultruded FRP reinforcements with embedded fiber optic sensors  
A. L. KALAMKAROV, D. O. MACDONALD, S. B. FITZGERALD & A. V. GEORGIADIS (Canada)
- 79 Material and structural failure criterion of corrugated board facings  
U. NYMAN & P. J. GUSTAFSSON (Sweden)
- 85 Secondary effects in the analysis of the post-buckling bending test  
I. KALLEL-KAMOUN (France, Tunisia), A. CHATEAUMINOIS & F. SIDOROFF (France)
- 93 Buckling behaviour of composite shells  
A. J. M. FERREIRA & J. T. BARBOSA (Portugal)

#### Technical Note

- 99 Analytical and finite element comparisons of stress intensity factors of composite materials  
M. HÜSNÜ DIRIKOLU & A. AKTAŞ (Turkey)

**Volume 50 Number 2 2000**

- 103 In-plane vibration of laminated curved beams with variable curvature by dynamic stiffness analysis  
Y. P. TSENG, C. S. HUANG & M. S. KAO (Taiwan, ROC)
- 115 Analysis of axisymmetrically-loaded filament wound composite cylindrical shells  
F. G. YUAN, W. YANG & H. KIM (USA)
- 131 Nonlinear bending of shear deformable laminated plates under transverse and in-plane loads and resting on elastic foundations  
H.-S. SHEN (People's Republic of China)
- 143 Three-dimensional nonlinear orthotropic finite element material model for wood  
A. TABIEI & J. WU (USA)
- 151 Prediction of compressive strength of carbon–epoxy laminates containing delamination by using a mixed-mode damage model  
M. F. S. F. DE MOURA, J. P. M. GONÇALVES, A. T. MARQUES & P. M. S. T. DE CASTRO (Portugal)
- 159 Laminated composite open profile sections: non-uniform torsion of I-sections  
S. S. MADDUR & S. K. CHATURVEDI (USA)
- 171 Predictor–corrector procedures for analysis of laminated plates using standard Mindlin finite element models  
K. Y. SZE, L.-W. HE & Y. K. CHEUNG (People's Republic of China)
- 183 An assessment of mixed and classical theories on global and local response of multilayered orthotropic plates  
E. CARRERA (Italy)
- 199 An elastic–plastic stress analysis of thermoplastic composite beams loaded by bending moments  
O. SAYMAN & H. ÇALLIOĞLU (Turkey)
- 207 Static indentation and impact behaviour of reformed bamboo/aluminium laminated composites  
J. Y. ZHANG, T. X. YU, J. K. KIM & G. X. SUI (Hong Kong)

**Volume 50 Number 3 2000**

- 217 Damping characteristics of 0° and 90° AS4/3501-6 unidirectional laminates including the transverse shear effect  
J. H. YIM (South Korea) & J. W. GILLESPIE JR (USA)
- 227 High-order theory for the analysis of multi-layer plate assemblies and its application for the analysis of sandwich panels with terminating plies  
O. T. THOMSEN (USA)
- 239 Experimental investigation of low-velocity impact characteristics of sandwich composites  
T. ANDERSON & E. MADENCI (USA)
- 249 Compressive buckling analysis of rectangular composite laminates containing multiple delaminations  
M. A. KOUCHAKZADEH & H. SEKINE (Japan)
- 257 Impact testing and simulation of composite sandwich structures for civil transportation  
L. TORRE & J. M. KENNY (Italy)
- 269 Vibration response of laminated plates containing spheroidal inclusions  
J. H. HUANG (Taiwan, ROC)
- 279 An innovative technique for measuring the high strain rate response of sandwich composites  
H. MAHFUZ, W. AL MAMUN, A. HAQUE, S. TURNER, H. MOHAMED & S. JEELANI (USA)
- 287 Stress and failure analysis of mechanically fastened joints in composite laminates  
M.-L. DANO, G. GENDRON & A. PICARD (Canada)

- 297 Development of concurrent engineering system for design of composite structures  
J.-S. KIM, C.-G. KIM, C.-S. HONG (South Korea) & H. T. HAHN (USA)
- 311 Indentation failure analysis of sandwich beams  
A. PETRAS & M. P. F. SUTCLIFFE (UK)
- 319 Effect of the longitudinal to transverse moduli ratio on the in-plane natural frequencies of symmetric cross-ply laminated beams by the stiffness method  
V. YILDIRIM (Turkey)

**Volume 50 Number 4 2000**

**Special Issue: Experimental Validation of Theoretical Predictions for Composite Structures**

**Guest Editors: R. Jones & T. D. Kim**

- 327 Foreword  
T. D. KIM (Japan)
- 329 Preface  
I. H. MARSHALL (Australia), T. D. KIM (Japan) & R. JONES (Australia)
- 331 Experience with the finite element modelling of a full-scale test of a composite aircraft control surface  
R. S. THOMSON & M. L. SCOTT (Australia)
- 347 Material characterization of laminated composite plates via static testing  
W. T. WANG & T. Y. KAM (ROC)
- 353 Evaluating the soundness of bonding using shearography  
Y. Y. HUNG, W. D. LUO, L. LIN (USA) & H. M. SHANG (Singapore)
- 363 Combined numerical–experimental model for the identification of mechanical properties of laminated structures  
A. L. ARAÚJO, C. M. MOTA SOARES, M. J. MOREIRA DE FREITAS (Portugal), P. PEDERSEN (Denmark) & J. HERSKOVITS (Brazil)
- 373 Control of beam vibrations by means of piezoelectric devices: theory and experiments  
P. GAUDENZI, R. CARBONARO & E. BENZI (Italy)
- 381 Impact energy absorption characteristics of composite structures  
D. G. LEE, T. S. LIM & S. S. CHEON (South Korea)
- 391 Experimental and computed natural frequencies of square pultruded GRP plates: effects of anisotropy, hole size ratio and edge support conditions  
G. J. TURVEY, N. MULCAHY & M. B. WIDDEN (UK)
- 405 Optical fibre sensors for health monitoring of bonded repair systems  
I. MCKENZIE, R. JONES, I. H. MARSHALL & S. GALEA (Australia)
- 417 On the analysis of composite structures with material and geometric non-linearities  
R. JONES & H. ALESI (Australia)
- 433 Smart structure application in bonded repairs  
W. K. CHIU, Y. L. KOH, S. C. GALEA & N. RAJIC (Australia)



# Composite Structures — Instructions to Authors

## Submission of Papers

Authors are requested to submit their original manuscript and figures with three copies to the Editor: Prof. I. H. Marshall, 36 Gogoside Road, Largs, Ayrshire, Scotland KA30 9LX, UK or to any member of the Editorial Board.

All papers should be written in English and will be independently refereed.

Submission of a paper implies that it has not been published previously, that it is not under consideration for publication elsewhere, and that if accepted it will not be published elsewhere in the same form, in English or in any other language, without the written consent of the publisher. All papers should be written in English. All papers will be independently refereed.

## Types of Contributions

Research papers; review articles; case studies; technical notes; book reviews; reports of conferences and meetings; letters to the Editor.

## Manuscript Preparation

**General:** Manuscripts must be typewritten, double-spaced with wide margins on one side of white paper. Good quality printouts with a font size of 12 or 10 pt are required. The corresponding author should be identified (include a Fax number and E-mail address). Full postal addresses must be given for all co-authors. Authors should consult a recent issue of the journal for style if possible. An electronic copy of the paper should accompany the final version. The Editors reserve the right to adjust style to certain standards of uniformity. Authors should retain a copy of their manuscript since we cannot accept responsibility for damage or loss of papers. Original manuscripts are discarded one month after publication unless the Publisher is asked to return original material after use.

**Paper Length:** Generally, the size of the manuscript should not exceed 6000 words or about 12 printed pages.

**Abstracts:** The Abstract should be of about 100–150 words, reporting concisely on the purpose and results of the paper.

**Text:** Follow this order when typing manuscripts: Title, Authors, Affiliations, Abstract, Keywords, Main text, Acknowledgements, Appendix, References, Vitae, Figure Captions and then Tables. Do not import the Figures or Tables into your text. The corresponding author should be identified with an asterisk and footnote. All other footnotes (except for table footnotes) should be identified with superscript Arabic numbers.

**Symbols:** The SI system should be used for all scientific and laboratory data; if, in certain instances, it is necessary to quote other units, these should be added in parentheses. Temperatures should be given in degrees Celsius. The unit billion' ( $10^9$  in America,  $10^{12}$  in Europe) is ambiguous and should not be used.

**References:** All publications cited in the text should be presented in a list of references following the text of the manuscript. In the text refer to references by a number in square brackets on the line (e.g. Since Sonti[1]), and the full reference should be given in a numerical list at the end of the paper. References should be given in the following form:

1. Sonti SS, Davalos JF, Zipfel MG, Gang Rao HVS. A review of wood cross tie performance. *Forest Products Journal* 1995;45(9):55–58.
2. Hetenyi M. *Beams on elastic foundation*. Ann Arbor, MI: University of Michigan Press, 1946.
3. Adali S. Lay-up optimization of laminated plates under buckling loads. In: Turvey GJ, Marshall IH, editors. *Buckling and postbuckling of composite plates*. London: Chapman and Hall, 1995. p. 329–365.
4. Adali S, Verijenko VE, Galileev SM, Matrosov AV. Method of initial function in three-dimensional analysis of laminated composite structures. In: *Composites Modelling and Processing Science, Proceedings of the 9th International Conference on Composite Materials (ICCM/9)*, Madrid, 12–16 July 1993. p. 23–30.

**Illustrations:** All illustrations should be provided in camera-ready form, suitable for reproduction (which may include reduction) without retouching. Photographs, charts and diagrams are all to be referred to as

'Figure(s)' and should be numbered consecutively in the order to which they are referred. They should accompany the manuscript, but should not be included within the text. All illustrations should be clearly marked on the back with the figure number and the author's name. All figures are to have a caption. Captions should be supplied on a separate sheet.

**Line drawings:** Good quality printouts on white paper produced in black ink are required. All lettering, graph lines and points on graphs should be sufficiently large and bold to permit reproduction when the diagram has been reduced to a size suitable for inclusion in the journal. Dye-line prints or photocopies are not suitable for reproduction. Do not use any type of shading on computer-generated illustrations.

**Photographs:** Original photographs must be supplied as they are to be reproduced (e.g. black and white or colour). If necessary, a scale should be marked on the photograph. Please note that photocopies of photographs are not acceptable.

**Colour:** Where colour figures are required, the author will be charged accordingly. Further details of cost are available from Author Services, at Elsevier Science.

**Tables:** Tables should be numbered consecutively and given a suitable caption and each table typed on a separate sheet. Footnotes to tables should be typed below the table and should be referred to by superscript lowercase letters. No vertical rules should be used. Tables should not duplicate results presented elsewhere in the manuscript, (e.g. in graphs).

## Electronic Submission

**Authors should submit an electronic copy of their paper with the final version of the manuscript. The electronic copy should match the hardcopy exactly.** Always keep a backup copy of the electronic file for reference and safety. Full details of electronic submission and formats can be obtained from Author Services at Elsevier Science.

## Proofs

Proofs will be sent to the author (first named author if no corresponding author is identified of multi-authored papers) and should be returned within 48 hours of receipt. Corrections should be restricted to typesetting errors; any others may be charged to the author. Any queries should be answered in full. Please note that authors are urged to check their proofs carefully before return, since the inclusion of late corrections cannot be guaranteed. Proofs are to be returned to the Log-in Department, Elsevier Science, The Boulevard, Langford Lane, Kidlington, Oxford OX5 1GB, UK.

## Offprints

Fifty offprints will be supplied free of charge. Additional offprints and copies of the issue can be ordered at a specially reduced rate using the order form sent to the corresponding author after the manuscript has been accepted. Orders for reprints will incur a 50% surcharge. Authors who pay for colour illustrations will receive an additional 100 offprints free of charge.

## Copyright

All authors must sign the 'Transfer of Copyright' agreement before the article can be published. This transfer agreement enables Elsevier Science Ltd to protect the copyrighted material for the authors, but does not relinquish the author's proprietary rights. The copyright transfer covers the exclusive rights to reproduce and distribute the article, including reprints, photographic reproductions, microfilm or any other reproductions of similar nature and translations. Includes the right to adapt the article for use in conjunction with computer systems and programs, including reproduction or publication in machine-readable form and incorporation in retrieval systems. Authors are responsible for obtaining from the copyright holder permission to reproduce any figures for which copyright exists.

## Author Services

For queries relating to the general submission of manuscripts (including electronic text and artwork) and the status of accepted manuscripts, please contact Author Services, Log-in Department, Elsevier Science, The Boulevard, Langford Lane, Kidlington, Oxford OX5 1GB, UK. E-mail: authors@elsevier.co.uk, Fax: +44 (0) 1865 843905, Tel: +44 (0) 1865 843900.



(Abstracted/indexed in: *Applied Mechanics Reviews*; *Current Contents/Engineering, Computing and Technology*; *Engineering Index*; *Materials Information*; *Materials Science Citation Index*; *Metals Abstracts*; *Polymer Contents*; *Science Citation Index*)

The Elsevier Science Catalogue can be accessed in <http://www.elsevier.nl> or [gopher.elsevier.nl](mailto:gopher.elsevier.nl)

## CONTENTS

**Volume 50 Number 4 2000**

**Special Issue: Experimental Validation of Theoretical Predictions for Composite Structures**

**Guest Editors: R. Jones & T. D. Kim**

- 327 Foreword  
T. D. KIM (Japan)
- 329 Preface  
I. H. MARSHALL (Australia), T. D. KIM (Japan) & R. JONES (Australia)
- 331 Experience with the finite element modelling of a full-scale test of a composite aircraft control surface  
R. S. THOMSON & M. L. SCOTT (Australia)
- 347 Material characterization of laminated composite plates via static testing  
W. T. WANG & T. Y. KAM (ROC)
- 353 Evaluating the soundness of bonding using shearography  
Y. Y. HUNG, W. D. LUO, L. LIN (USA) & H. M. SHANG (Singapore)
- 363 Combined numerical-experimental model for the identification of mechanical properties of laminated structures  
A. L. ARAÚJO, C. M. MOTA SOARES, M. J. MOREIRA DE FREITAS (Portugal), P. PEDERSEN (Denmark) & J. HERSKOVITS (Brazil)
- 373 Control of beam vibrations by means of piezoelectric devices: theory and experiments  
P. GAUDENZI, R. CARBONARO & E. BENZI (Italy)
- 381 Impact energy absorption characteristics of composite structures  
D. G. LEE, T. S. LIM & S. S. CHEON (South Korea)
- 391 Experimental and computed natural frequencies of square pultruded GRP plates: effects of anisotropy, hole size ratio and edge support conditions  
G. J. TURVEY, N. MULCAHY & M. B. WIDDEN (UK)
- 405 Optical fibre sensors for health monitoring of bonded repair systems  
I. MCKENZIE, R. JONES, I. H. MARSHALL & S. GALEA (Australia)
- 417 On the analysis of composite structures with material and geometric non-linearities  
R. JONES & H. ALESÌ (Australia)
- 433 Smart structure application in bonded repairs  
W. K. CHIU, Y. L. KOH, S. C. GALEA & N. RAJIC (Australia)



This journal is part of **ContentsDirect**, the *free* alerting service which sends tables of contents by e-mail for Elsevier Science books and journals. You can register for **ContentsDirect** online at: [www.elsevier.nl/locate/contentsdirect](http://www.elsevier.nl/locate/contentsdirect)



ELSEVIER

02017